Modeling, understanding, and screening fast lithium-ion conductors for solid-state electrolytes

Thèse N° 7375

Présentée le 6 décembre 2019

à la Faculté des sciences et techniques de l'ingénieur
Laboratoire de théorie et simulation des matériaux
Programme doctoral en science et génie des matériaux

pour l'obtention du grade de Docteur ès Sciences

par

Leonid KAHLE

Acceptée sur proposition du jury

Prof. A. Fontcuberta i Morral, présidente du jury
Prof. N. Marzari, directeur de thèse
Prof. G. Hautier, rapporteur
Prof. T. Vegge, rapporteur
Prof. M. Ceriotti, rapporteur

2019

ÉCOLE POLYTECHNIQUE
FÉDÉRALE DE LAUSANNE

The good life is inspired by love and guided by knowledge.

Bertrand Russell

This thesis is dedicated to my greatest teachers — my parents

Acknowledgements

Verily, whoever exists, he, in being born, is born as owing a debt
to the gods, to the saints, to the fathers, and to men.
When he sacrifices, it is for the reason he is born as owing a debt to the gods.
And further, inasmuch as he is bound to study the Veda,
it is for the reason he is born as owing a debt to the saints.
And further, inasmuch as he is bound to wish for offspring,
for that reason he is born as owing a debt to the fathers.
And further, inasmuch as he is bound to practise hospitality,
it is in discharge of his debt to men that he does so.

Satapatha Brâhmana 1:7:2

I am deeply indebted to my thesis advisor Nicola Marzari for his trust, guidance, and words of motivation during these incredible four years that passed. Many thanks to Aris Marcolongo, the best colleague to start this journey with; 'grazie mille' for your many patient explanations, the exemplary rigor of your work, and our countless insightful discussions. I also learned a lot from the AiiDA team, and would like to thank especially Giovanni Pizzi, Martin Uhrin, and Sebastiaan Huber; working on this fantastic software project was a delight, and our coding retreats were always something to look forward to. My fellow PhD students have provided for pleasant respite from work, and special thanks go to Antimo Marrazzo and Gianluca Prandini: we started and finish this journey together, and I could not have wished for better comrades. I'm grateful to have worked with Giuliana Materzanini, Loris Ercole, and Sokseiha Muy. Alby Musaelian was the best student one could wish for, and I greatly enjoyed working with him. My sincere thanks to all (former) colleagues of the Theory and Simulations Laboratory, especially Thibault Sohier, Marco Gibertini, Iurii Timrov, Nicolas Hörmann, and Nicolas Mounet. Whenever I required help or advice, no-one hesitated; when it was time to celebrate, all cherished; and when things needed to get done, everyone gave 100%!

Regarding colleagues and friends outside the laboratory: Boris Kozinsky deserves much credit for introducing me to the exciting topic of solid-state electrolytes, and so does Michele Ceriotti for his lessons on statistical mechanics and his genuine (and contagious) enthusiasm. The members of

my thesis committee, Tejs Vegge, Geoffroy Hautier, and (the same) Michele Ceriotti, contributed to this work thanks to their thorough reading and many thoughtful, deep, and very useful comments, questions, discussions, and suggestions; I would never have imagined my defense to be so enjoyable and scientifically stimulating. I feel indebted to Brandon Wood, Nicole Adelstein, and their colleagues for our wonderful discussions and my inspiring scientific visit to California. To my colleagues within the MARVEL incubator at IBM and the Paul Scherrer Institute: thanks for the thoughtful discussions, eloquent explanations, and undeterred motivation.

A PhD thesis requires some downtown; on this regard, many thanks to the committee members of the Club Montagne EPFL, and especially to Florian, Nadine, Sylvain, and Alexis, for our unforgettable adventures in the mountains of Switzerland. Thanks to Elodie for being by my side during the last two years, always cheerful and motivated! I am very grateful for my great flatmates to return to after work: Martin, Irene, Luca, Daniel, and Anna, thanks for all the laughs, ideas, food, and beer we shared.

Finally, I would like to express how much I owe my family – especially my parents – for their continuous encouragement, unconditional trust, and their shining example of how to live the good life, inspired by love and guided by knowledge.

L. K.

Abstract

The Li-ion batteries within the consumer electronics used in our everyday life suffer from well-known deficiencies due to the prevalent use of organic liquid electrolytes: the narrow electrochemical stability windows of the organic solvents used in these electrolytes prevent the use of high-voltage cathodes, and the flammability and volatility of the solvent molecules constitute a safety hazard. Replacing the organic liquid electrolytes with inorganic solid-state electrolytes could lead to significantly safer batteries with a higher energy density. However, most known solid-state Li-ion conductors are not yet suitable for application as electrolytes, since no material satisfies the stringent requirements for safety in a high-performance battery: a wide electrochemical stability window, high mechanical stability, very low electronic mobility, and fast Li-ion conduction.

Searching for materials that satisfy those requirements by via experiment is too human-labor intensive to be done on a large scale due to the time-consuming materials synthesis and experimental characterization. Computational approaches can be easily parallelized, enabling the screening of thousands of materials to find new solid-state electrolytes for Li-ion batteries. Such a computational high-throughput screening requires an automated framework and methods that are accurate enough to predict the quantities of interest but also of sufficient computational efficiency to be applied on many materials. However, known methods to predict the Li-ion conductivity in a material are either computationally too expensive to be applied on a large scale, as is the case for first-principles molecular dynamics, or are not general enough to be performed across a wide range of materials.

We present a model to calculate the Li-ion diffusion coefficient and conductivity efficiently by applying physically motivated approximations to the Hamiltonian of density-functional theory. The results obtained using this "pinball model" compare well to those from accurate first-principles molecular dynamics. This agreement provides interesting insights into the dependence of the valence electronic charge density of an ionic system on the motion of Li ions and suggests that the model can be used for screening applications. After its derivation and validation, we use the pinball model in a computational high-throughput screening to find structures with promising Li-ion diffusion. These candidate solid-state electrolytes are characterized with first-principles molecular dynamics to obtain more accurate predictions of the diffusion coefficients and pathways in these materials.

The pinball model, combined with the efforts to automate molecular dynamics simulations, results in a large quantity of data stored in the form of molecular dynamics trajectories, motivating a

framework to analyze these in an unsupervised manner. We describe a method to investigate the diffusion mechanism in molecular dynamics simulations by performing similarity measurements between local atomic neighborhood descriptors to detect diffusive pathways and jumps of diffusing particles in an automatic and unbiased fashion.

The efforts on new methods for modeling Li-ion conductors, analyzing diffusion pathways in solid-state ionic conductors, and screening for new ceramic electrolytes are summarized in the concluding chapter, which also outlines promising possibilities for future research.

Keywords: atomistic simulation, molecular dynamics, density-functional theory, Li-ion battery, solid-state electrolyte, high-throughput screening, computational screening

Zusammenfassung

Die Li-Ionen-Akkumulatoren oder Li-Ionen-Batterien in den vielen elektronischen Gebrauchsgegenständen, die wir alltäglich verwenden, leiden an Mängeln, die auf die weit verbreitete Verwendung von organischen, flüssigen Elektrolyten zurückzuführen sind. Das elektrochemische Stabilitätsfenster der organischen Lösungsmittel verhindert die Verwendung von Kathoden mit hohem Redox-Potenzial und die Entflammbarkeit und Flüchtigkeit der Moleküle stellen ein Sicherheitsrisiko dar. Der Ersatz der organischen Flüssig-Elektrolyte durch anorganische Festkörper-Elektrolyte könnte zu deutlich sichereren Batterien mit höherer Energiedichte führen. Bekannte inorganische Li-Ionen-leitende Festkörper sind jedoch noch nicht zur Anwendung geeignet, da kein Material alle strengen Anforderungen erfüllt, um sicher und kostengünstig als Elektrolyt in einer kommerziellen Batterie eingesetzt zu werden. Solche Anforderungen sind hohe mechanische Stabilität, ein breites elektrochemisches Stabilitäts-Fenster, leichte Verarbeitbarkeit, sehr geringe Elektronen-Mobilität, jedoch vor allem schnelle Li-Ionen-Leitfähigkeit.

Die experimentelle Suche nach Materialien, die diese Anforderungen erfüllen, ist aufgrund der zeitaufwendigen Synthese und der experimentellen Charakterisierung zu arbeitsintensiv, um in großem Maßstab durchgeführt zu werden. Computergestützte Ansätze können parallelisiert werden, um Tausende von Materialien auf ihre Li-Ionen-Leitfähigkeit zu untersuchen. Ein solches rechnergestütztes Hochdurchsatz-Screening erfordert eine automatisierte Plattform und Methoden, welche genau genug sind, um die physikalischen Eigenschaften zu berechnen, aber auch ausreichend effizient sind, um bei der heutigen Rechenleistung parallel auf viele Materialien angewendet zu werden. Bekannte Methoden zur Vorhersage der Li-Ionen-Leitfähigkeit in einer beliebigen Struktur sind jedoch entweder zu rechenintensiv, um in großem Maßstab durchgeführt zu werden, wie zum Beispiel die quantenmechanische *ab initio* Molekulardynamik, oder sind nicht genau genug, um über ein breites Spektrum an Materialien angewendet zu werden.

Wir präsentieren ein Modell, welches den Li-Ionen-Diffusionskoeffizienten eines ionischen Festkörpers sehr effizient berechnet, indem wir durch physikalisch motivierte Näherungen den Hamilton-Operator der Dichtefunktionaltheorie vereinfachen. Die Ergebnisse, die mit diesem "Pinball-Modell" erzielt werden, sind sehr gut mit genauen Resultaten der quantenmechanischen *ab initio* Molekulardynamik vergleichbar. Dieser Befund liefert interessante Einblicke in die Abhängigkeit der elektronischen Ladungsdichte eines ionischen Festkörpers von der Bewegung der Li-Ionen, und belegt das Potenzial des Modells für Screening-Anwendungen. Nach der Ableitung und

Validierung verwenden wir das Pinball-Modell für ein rechnergestütztes Hochdurchsatz-Screening, um unter vielen experimentell bekannten ionischen Strukturen solche mit vielversprechender Li-Ionen-Diffusion zu finden, die als Festkörperelektrolyte verwendet werden könnten. Wir charakterisieren diese Festkörperelektrolyt-Kandidaten mit der *ab initio* Molekulardynamik, und erhalten genaue Vorhersagen der Diffusionskoeffizienten und Diffusionswege in den ausgesuchten Materialien.

Das Pinball-Modell, kombiniert mit unseren Bemühungen, atomistische Simulationen zu automatisieren, führt zu einer großen Menge von Daten in Form von molekulardynamischen Trajektorien, was die Entwicklung eines Modells motivierte, diese unbeaufsichtigt zu analysieren. Wir beschreiben eine neue Methode zur Bestimmung des Diffusionsmechanismus in molekulardynamischen Simulationen über Vergleiche lokaler Nachbarschaftsdeskriptoren zur Detektion von Diffusionswegen und Sprüngen diffundierender Partikel, was eine genaue, unverzerrte und automatisierte Analyse der Trajektorien ermöglicht.

Unsere Methoden zur Modellierung von Li-Ionen-Leitern, zur Analyse von Diffusionswegen und für effizientes Hochdurchsatz-Screening für neue inorganische Elektrolyte sind im abschließenden Kapitel zusammengefasst, welches vielversprechende Ansätze für künftige Forschung skizziert.

Stichwörter: Atomistische Simulation, Molekulardynamik, Dichtefunktionaltheorie, Lithium-Ionen-Batterie, Hochdurchsatz-Screening, computergestütztes Screening

Résumé

Les accumulateurs lithium-ion utilisés dans les produits électroniques au quotidien souffrent de carences bien connues dues à l'utilisation d'électrolytes liquides organiques: les fenêtres de stabilité électrochimique étroites des solvants organiques utilisés dans ces électrolytes empêchent l'utilisation de cathodes à haut potentiel et l'inflammabilité et la volatilité des molécules de solvant constituent un risque pour la sécurité. Le remplacement des électrolytes liquides organiques par des électrolytes inorganiques à l'état solide pourrait améliorer considérablement la sécurité des batteries avec une densité d'énergie plus élevée. Cependant, la plupart des conducteurs ionique de lithium connus à l'état solide ne sont pas encore adaptés à une application comme électrolytes, puisque aucun matériau ne satisfait les exigences strictes de sécurité dans une batterie de haute performance: une large fenêtre de stabilité électrochimique, une stabilité mécanique élevée, une très faible mobilité électronique et une conduction rapide aux ions de lithium.

La recherche expérimentale de matériaux qui répondent à ces exigences demande trop de main-d'œuvre à réaliser à grande échelle a cause de la synthèse fastidieuse des matériaux et de la caractérisation expérimentale. Les approches informatiques peuvent être facilement parallélisées, ce qui permet de cribler des milliers de matériaux pour trouver des nouveaux électrolytes à l'état solide pour les batteries Li-ion. Un tel criblage informatique à haut débit nécessite un cadre automatisé et des méthodes suffisamment précises pour prédire les quantités d'intérêt, mais aussi une efficacité de calcul suffisante pour être appliquée sur de nombreux matériaux. Cependant, les méthodes connues pour prédire la conductivité Li-ion dans un matériau sont trop onéreuses en termes de calcul pour être appliquées à grande échelle, comme c'est le cas pour la dynamique moléculaire *ab initio*, ou ne sont pas assez généraux pour être effectués sur une large gamme de matériaux.

Nous présentons un modèle permettant de calculer efficacement le coefficient de diffusion de lithium et la conductivité ionique en appliquant des approximations à motivation physique à l'hamiltonien de la théorie de la fontionelle de la densité. Les résultats obtenus avec ce "modèle pinball" se comparent bien à ceux obtenus avec la dynamique moléculaire *ab initio*. Cet accord fournit des informations intéressantes sur la dépendance de la densité de charge électronique d'un système ionique sur le mouvement des ions lithium, mais aussi suggère que le modèle peut être utilisé pour des applications de criblage. Après sa dérivation et validation, nous utilisons le modèle pinball dans un criblage informatique à haut débit pour trouver des structures offrant une diffusion de lithium prometteuse. Ces électrolytes solides candidats sont caractérisés par la dynamique

moléculaire quantique afin d'obtenir des prévisions plus précises des coefficients de diffusion et des chemins de propagation dans ces matériaux.

Le modèle pinball et nos efforts d'automatisation des simulations de dynamique moléculaire produisent une grande quantité de données stockées sous la forme de trajectoires de dynamique moléculaire, ce qui motive le développement d'un cadre pour les analyser de manière non-supervisée. Nous décrivons une méthode pour étudier le mécanisme de diffusion dans les simulations de dynamique moléculaire en effectuant des mesures de similarité entre les descripteurs de voisinage atomique locaux afin de détecter les chemins de diffusion et les sauts de particules diffusées de manière automatique et non biaisée.

Les efforts sur de nouvelles méthodes de modélisation des conducteurs de lithium, l'analyse des voies de diffusion dans les conducteurs ioniques solides et le dépistage de nouveaux électrolytes céramiques sont résumés dans le chapitre de conclusion, qui souligne également les possibilités prometteuses pour la recherche future.

Mots-clés: simulation atomistique, dynamics moleculaires, théory de la fonctionnelle de la densité, batterie lithium-ion, electrolytes solides, criblage à haut débit, criblage numerique

Contents

1 Introduction

And let us, as nature directs, begin first with first principles.

Ἀριστοτέλης – *Aristotle, Poetics*

1.1 Li-ion batteries

Lithium (Li), from the Greek word for stone, λίθος, is the lightest solid element at ambient conditions, with a density of 0.53 g cm^{-3}, and has the third-lightest atomic weight in the periodic table, 6.94 g mol^{-1}; only hydrogen and helium have lighter atoms. The reaction of Li to $Li^+ + e^-$ is one of the most electropositive, at -3.04 V versus the standard hydrogen electrode [1, 2]. Thanks to its lightness and reactive chemistry, large amounts of energy can be stored within the Li/Li^+ chemistry per unit of weight, making Li/Li^+ an optimal choice for electrochemical storage of energy in a battery.

The advantages that the Li-ion chemistry entails for batteries were already recognized in the 70s. Whittingham presented in 1976, in a forward-looking work, a TiS_2 cathode to be used in Li-ion batteries "for electric vehicle propulsion" [3–5]. However, the poor cyclability of Li-ion batteries and concerns for their safety impeded the introduction of this technology to the market. Especially the dendritic growth of metallic Li from anode to cathode was one of the major challenges for Li-ion batteries [5, 6]. Li-metal dendrites form when Li is driven faster to the anode than it can be incorporated, resulting in the anode being plated with Li metal [7, 8], which prevented commercialization of this technology for many years. One breakthrough for Li-ion batteries can undoubtedly be credited to research on oxide intercalation materials resulting in new cathode materials, most notably by John B. Goodenough [9–13]. Research of graphitic carbon for the anode by Akira Yoshino led to an intercalation anode [14]. The Sony corporation was the first to successfully commercialize a Li-ion battery in 1991, with a $Li_xT^MO_2$ (T^M =Co, Ni, Mn) cathode and a graphitic anode in 1991 [2, 15–19].

Now, nearly three decades later, the importance of rechargeable Li-ion batteries can hardly be overstated. Almost all our portable electronics are powered by Li-ion battery cells. In 2015 alone, ~2.5 billion such cells were produced for laptops and cell phones [20]. The importance of Li-ion batteries for portable electronics was also remarked by the Royal Swedish Academy of Sciences,

which awarded aforementioned John B. Goodenough, M. Stanley Whittingham, and Akira Yoshino with the Nobel Prize in Chemistry this year (2019) "*for the development of lithium-ion batteries*" [21].

Looking ahead, Li-ion batteries are currently the major competitor for the succession of fossil-fuel usage in road transport [22–25]. The electrification* of our vehicle fleet would have important beneficial effects: road transport accounts for 81% of the energy used in the transport sector [26, 27], and, due to the prevalent use of fossil-fueled vehicles, is a major contributor to the green-house effect and climate change [28]. In addition, burning fossil fuels in vehicle engines is unsustainable, since crude oil and its derivatives (such as gasoline) are non-renewable resources [29]. Fully electric vehicles, powered only by electricity stored in rechargeable Li-ion batteries, could mitigate the carbon footprint of road transport, especially if combined with a substantial increase in renewable electricity production, and help transition this sector to a more sustainable use of energy resources. The necessity and potential of a wide-spread introduction of electric vehicles has been understood by automobile manufacturers, policy makers, and consumers: in 2018 the global electric vehicle fleet reached 5.1 million cars, two million cars more than in 2017 [30]. The International Energy Agency (IEA) expects annual sales to reach between 23 and 43 million electric cars by 2030, partly due to the intention of several European governments to forbid fossil-fueled vehicles in the next decades [19, 31].

In order to replace internal-combustion automobiles entirely with fully electric vehicles, major technological hurdles need to be overcome: First, the driving range of an electric vehicle at one single charge is determined by the gravimetric or volumetric energy density of its battery, which is the energy stored (at full charge) per unit of weight or unit of volume, measured in $\mathrm{Wh\,kg^{-1}}$ or in $\mathrm{Wh\,L^{-1}}$, respectively [32, 33]. Most electric vehicles currently on the market have a driving range of 100 – 200 km [18], which is below what consumers are accustomed to from gasoline-powered vehicles (400 – 600 km). Second, the safety of Li-ion batteries remains – thirty years after their first commercialization – a major concern [18, 25], exemplified by the substantial financial losses suffered by the international corporations Samsung and Boeing due to safety issues in the Li-ion batteries contained in their products Galaxy Note 7 and 787 Dreamliner, respectively [34, 35].

In order to understand the shortcomings of Li-ion batteries, I will explain how they function in the following. A battery has three major necessary components, whose assembly is illustrated in Fig. 1.1, namely an anode, an electrolyte, and a cathode. The two current collectors, one for the cathode and one for the anode, are needed to complete the electric circuit. They are usually made of a metal that does not dissolve or corrode in the chemical environment of a battery, the most cost-effective and common choice being aluminum [36].

* Re-electrification, one should say, since in the beginning of the twentieth century batteries were supposed to power electric vehicles [2, 19].

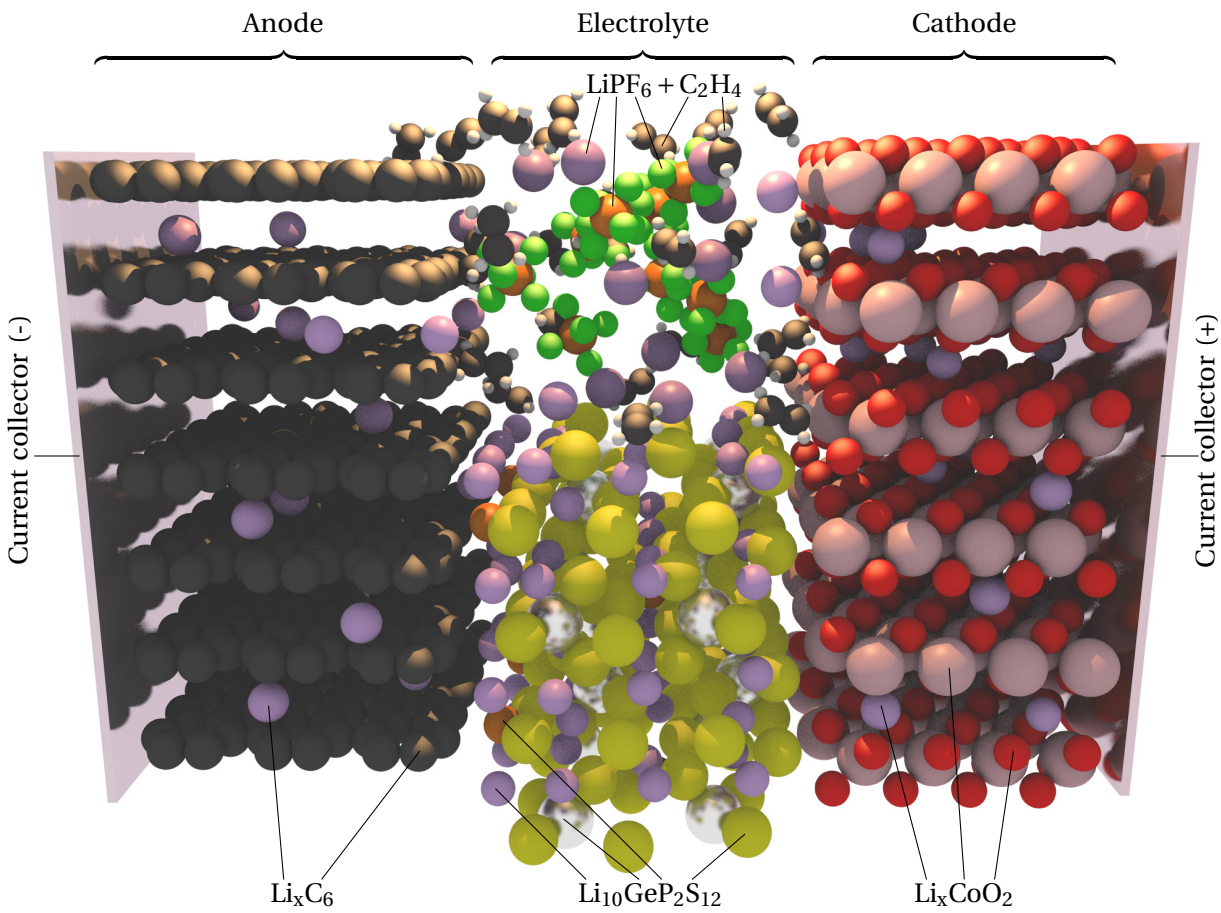

Fig. 1.1: Schematic of a Li-ion battery: during discharge Li ions travel from the anode (Li_xC_6, left) to the cathode (Li_xCO_2, right). In between anode and cathode is the electrolyte; two examples of electrolytes are shown, an organic liquid ($LiPF_6$ in organic solvent, top) and an inorganic solid-state electrolyte ($Li_{10}GeP_2S_{12}$, bottom). Electronic current collectors connect the electrodes via the outer circuit.

1.1.1 Anode

On the left side of Fig. 1.1 is the anode, where a chemical oxidation takes place during discharge, freeing electrons that are passed to the outer circuit. In the case of a Li-ion battery, metallic Li, intercalated into graphitic layers of carbon (C), gets oxidized, resulting in free Li ions, in a +1 charged state, and free electrons:

$$\overset{0}{\mathrm{Li}}_x C_6 \underset{\text{charge}}{\overset{\text{discharge}}{\rightleftharpoons}} x\,\mathrm{Li}^+ + x\,\mathrm{e}^- + \mathrm{C}_6, \quad 0 < x < 1, \tag{1.1}$$

where $\rightleftharpoons$ denotes a reversible reaction. Soft disordered graphitic carbon, as shown in Fig. 1.1 and given in Reaction (1.1), is the major anode material used nowadays due to its excellent cyclability [19, 20, 37, 38]. However, only one Li can be intercalated for every six carbon atoms, which severely limits the capacity of a battery with a graphitic anode.

Other anode materials, such as silicon, are being investigated to obtain higher capacities and energy densities [20, 39–41]. Pure Li metal would provide the best anode material, since the volume/weight of any additional host material is eliminated. However, using pure Li has two major drawbacks: first, metallic Li is very reactive, and decomposes most electrolytes, and second, using it as an anode would foster the formation of Li-metal dendrites upon charging. By intercalating Li within layers of carbon, no Li-metal dendrites form as long as the rate of discharge does not surpass the rate of Li intercalation.

1.1.2 Cathode

The (reversible) reduction of Li ions upon discharge takes place in the cathode. The widely employed cathode material Li_xCoO_2 [10, 11] is shown in Fig. 1.1, and it reacts with Li^+ as [23]:

$$x\,Li^+ + x\,e^- + Li_y\overset{+III}{Co}O_2 \underset{\text{charge}}{\overset{\text{discharge}}{\rightleftharpoons}} Li_{x+y}\overset{+II}{Co}O_2, \quad y > 0.5, \quad x + y \leq 1. \tag{1.2}$$

In this cathode material, Li^+ is intercalated into layers of the cobalt oxide CoO_2, while the additional electron changes the oxidation state of cobalt (Co). In cathode materials, some species need to change their oxidation state during charge/discharge, which is why cathodes usually contain transition metals such as iron (Fe), manganese (Mn), or nickel (Ni). Besides $LiCoO_2$, the olivine Li_xFePO_4 ($1 < x < 2$), the spinel $Li_xMn_2O_4$ ($0 < x < 1$), the layered $Li_xNi_yMn_zCo_{1\text{-}y\text{-}z}O_2$ (NMC-cathode) [32, 42–53], and organic cathode materials [54], are used in common Li-ion batteries or being investigated, especially since there are strong incentives to reduce the amount of cobalt in the cathode due to the high cost, limited availability, and toxicity of this conflict mineral [55].

The optimal choice – in terms of energy density – would be the cathode being the atmosphere, more precisely the O_2 in it, leading to a Li-air battery or Li-air fuel cell [56], where Li^+ reacts with atmospheric oxygen to lithium oxide (Li_2O) or lithium peroxide (Li_2O_2). If we also assume metallic Li on the anode side, the Li-air battery has a very high theoretical energy density (~10 kWh kg^{-1}) rivaling that of gasoline (12 – 13 kWh kg^{-1}, of which only ~15% are used for propulsion, on average), and much higher than today's consumer batteries with an energy density of 100 – 300 Wh kg^{-1} [57, 58]. However, how to make a cyclable Li(-metal) air battery is still under investigation [59–64].

To summarize so far: the anodic Reaction (1.1) frees electrons, while Reaction (1.2) in the cathode absorbs electrons during the discharge of a battery. The electrons are transported to and from the active material via metallic collectors, as illustrated in Fig. 1.1, one for the anode and one for the cathode, and travel in the outer circuit where they can perform work. The open-circuit voltage of the battery is determined by the difference in the electrochemical potential of the anodic and cathodic reactions [65]. As an example, Reactions (1.1) and (1.2) have potentials of ~0.5 V and ~4 V vs Li/Li^+, respectively [46]. The difference is ~3.5 V, which is therefore the open-circuit voltage of a battery built with the anode and cathode shown in Fig. 1.1, namely Li_xC_6 and Li_xCoO_2.

1.1.3 Electrolyte

The electrolyte is the last missing component of a battery; it does not store metallic Li, Li ions, or energy, but separates the anode from the cathode. As illustrated in Fig. 1.1, the electrolyte can be either liquid or solid, and needs to fulfill several requirements:

(1) One function of the electrolyte is to hinder electrons from taking the shortcut through the battery, directly from the cathode to the anode; the electrolyte has to be an electronic insulator.

(2) Li ions, produced by Reaction 1.1 during discharge, need to diffuse through the electrolyte to the cathode, where Reaction 1.2 takes place; to ensure sufficient power density (power per unit of weight or volume) the electrolyte needs to display high Li-ion conductivity across the operating-temperature range of the battery.

(3) The electrolyte should be chemically stable in contact with the electrodes to guarantee a long battery life.

(4) In order to ensure a high number of charge/discharge cycles, the electrolyte should display no contact loss during charge or discharge [66] and resist the growth of Li-metal dendrites.

Environmental friendliness, non-hygroscopicity and ease of preparation are of additional advantage in application [66]. In the following, I will discuss common electrolytes that are used in today's batteries or are under investigation for future Li-ion battery technology.

Organic liquids are the most widely employed electrolytes and consist of organic solvents such as propylene, ethylene, or diethyl carbonates that dissolve Li salts; commonly employed salts are $LiClO_4$, $LiAsF_6$, $LiBF_4$, or $LiPF_6$ (shown in Fig. 1.1, dissolved in ethylene). Organic liquid electrolytes are generally fast ionic conductors [46, 63, 67], but also flammable due to the organic solvent. In addition, the solvent molecules are often volatile and can evaporate in case of battery damage, leading to further deterioration. Furthermore, the organic solvents limit the voltage of a battery [2, 20, 55], as the molecules decompose in contact with high-voltage cathode materials such as $LiMn_{1.5}Ni_{0.5}O_4$, $LiNiVO_4$, or $LiCoPO_4$, at over 4.5 V vs Li/Li^+ [19, 68–70]. Most organic solvents used in state-of-the-art electrolytes react at both the anode and the cathode side, and are only stabilized by the formation of solid/electrolyte interfaces [36, 46, 71]. Furthermore, aforementioned Li salts react with water, requiring the battery to be sealed tightly. For all above reasons, employing organic liquid electrolytes in Li-ion batteries commonly results in high power densities (high charge/discharge rates), but presents a safety hazard [72], requiring flame-retardant additives inside the battery [71], and current-limiting devices and safety vents at device level [72, 73]. In addition, the liquid electrolyte presents no resistance to the growth of Li-metal dendrites from the anode to the cathode, which makes the introduction of separators necessary [23, 74].

Inorganic liquids employ inorganic solvents, such as sulphur dioxide (SO_2), where Li salts, e.g. $LiAlCl_4$, are dissolved. Just as organic liquids, they generally display high ionic conductivities, but have the advantage of using non-flammable solvents [75–77]. Water (H_2O), an obvious inorganic electrolyte, cannot be used with standard cathodes because of the reaction $2\,H_2O + 2\,e^- \rightleftharpoons H_2 +$

2 OH^- at 2.2 V vs. Li/Li^+ and its narrow stability window of 1.23 V [78]. Despite the stability window of SO_2 being wider than that of water, the solvent is still not suitable for the most common anode or cathode materials. In addition, as for all liquid electrolytes, resistance to dendrites remains a challenge for inorganic liquids.

Ionic Liquids are non-flammable, non-volatile liquids that contain mobile Li ions and do not require the addition of solvents, which makes them interesting candidates for future electrolytes because they are, in general, electrochemically more stable than solvent-based liquid electrolytes, with stability windows reaching 5 V vs Li/Li^+ [20, 23, 46, 78–80]. Their high viscosity, however, limits the power density of a battery. Some ionic liquids display lower viscosity, but these possess too narrow electrochemical stability windows [81]. Furthermore, whether ionic liquids can be used with graphitic anodes remains an open question, because other cations than Li^+ are also present and intercalate into the graphite sheets [23, 36].

Solid polymer electrolytes employ long and branched polymers, such as the widely used polyethylene oxide (PEO), polyvinylidene fluoride (PVDF), or polyacrylonitrile (PAN), as a solid matrix. A mixing or reaction with lithium salts, for example $LiPF_6$ or $LiClO_4$, makes the solid polymer ionically conducting [58, 82, 83]. Solid polymer electrolytes have beneficial mechanical properties that can be fine-tuned by controlling the degree of cross-linking [84]. As a result they retain excellent contact with the electrodes during the charge-discharge volume changes [46]. Despite their solid nature, polymer electrolytes also require separators to prevent dendrite growth [46, 74]. The additional safety advantage of solid polymer electrolytes largely stems from the usage of non-volatile molecules: in case of battery damage no electrolyte leaks out, preventing further deterioration. However, solid polymer electrolytes generally suffer from poor ionic conductivities.

Inorganic solid-state electrolytes employ ceramic or glassy ionic conductors, and generally show high thermal and exceptional electrochemical stability [58, 85–91]. While the ionic conductivity in inorganic solid-state electrolytes is generally lower than in liquid electrolytes, their high transference number is an advantage. The disadvantage of lower ionic conductivities can be overcome in solid-state thin-film batteries due to the small dimensions of the electrolyte [90, 92], capable of high charge/discharge rates [93]. The increased elastic modulus and high density, compared to all other electrolytes, are beneficial for the suppression of dendritic growth of metallic lithium, a major source of battery failure [94]. Disadvantages, besides the lower ionic conductivity, are the lack of mechanical flexibility and the brittleness of the ceramic [95].

Hybrid/composite electrolytes combine the advantages and – unfortunately – disadvantages of different classes of electrolytes. For example, ionic liquids can be mixed with organic solvents to improve their viscosity, but this decreases the width of their stability window [96]. Polymers can be swelled with organic liquids or with ionic liquids to form polymer gels, combining the excellent mechanical properties (regarding contact retention) of solid polymers with the high ionic conductivity of liquid electrolytes, but also displaying the aforementioned safety concerns due to the

use of small solvent molecules [58, 84, 97]. When ionic liquids are used to swell the solid polymers, the resulting electrolytes become solid and non-flammable [98]. As another example, inorganic solid electrolytes dispersed in a polymer matrix combine the dendrite-preventing hardness of the former with the adhesiveness and softness of the latter, which helps to preserve good contact between the electrolyte and the electrodes during cycling [78, 95, 99–101]. In addition, the ionic conductivity of the inorganic electrolyte is improved, since voids between grain boundaries in the ceramic are filled with the polymer [99].

Which type of electrolyte future high-performance batteries will contain is still undecided, but the properties of their electrolyte will determine to a large extent their performance. Currently, none of the known electrolyte formulations excel at meeting all aforementioned requirements to be used safely in a high-performance Li-ion battery. The organic and inorganic solvents of liquid electrolytes limit the voltage of a battery due to their narrow electrochemical stability windows. Ionic liquids, and solid polymer or inorganic electrolytes suffer from low ionic conductivities, which limit the power density of batteries and is due to slow diffusion of Li^+ ions through the electrolyte. Diffusion, and how to calculate this important figure of merit, will be described in the following sections.

1.2 Diffusion

Diffusion describes the transport of atoms as a result of random molecular motion and was first studied with experiments on gases, liquids, and the uptake of hydrogen in metals [102]. Thomas Graham discovered in the 19th century the connection between the diffusion of gases and their thermal motion (temperature) and established the concept of the mean free path, the average distance that particles in a gas travel between collisions [102]. The mathematical framework to describe diffusion is attributed to Adolf Eugen Fick. Fick's first law of diffusion states that the flux of particles $\boldsymbol{J}$ is proportional to the gradient of the concentration C of particles:

$$\boldsymbol{J} = -\bar{D}\boldsymbol{\nabla} C, \tag{1.3}$$

where $\boldsymbol{J}$ is the flux of particles and $\bar{D}$ the 3×3 diffusion coefficient matrix, most often expressed in units of $\mathrm{cm}^2\,\mathrm{s}^{-1}$. The empirical observation given in Eq. (1.3) assumes that $\bar{D}$ is independent of the concentration. If we also assume that diffusing particles do not undergo chemical reactions, we can write the continuity equation for the conserved quantity C:

$$\frac{\partial C}{\partial t} + \boldsymbol{\nabla}\boldsymbol{J} = 0. \tag{1.4}$$

In other words, the change of concentration at any point in space has to be offset exactly by the divergence of the particle flux $\boldsymbol{J}$. We multiply Eq. (1.3) from both sides with $\boldsymbol{\nabla}$ and obtain:

$$\boldsymbol{\nabla}\boldsymbol{J} = -\boldsymbol{\nabla}\left(\bar{D}\boldsymbol{\nabla} C\right). \tag{1.5}$$

By inserting Eq. (1.5) into Eq. (1.4) we obtain Fick's second law of diffusion:

$$\frac{\partial C}{\partial t} = \boldsymbol{\nabla}\left(\bar{D}\boldsymbol{\nabla}C\right), \tag{1.6}$$

which allows to solve for the concentration as a function of time [103]. If we only consider the dimension x, we obtain the more common expression for Fick's second law in one dimension:

$$\frac{\partial C}{\partial t} = D_{xx}\frac{\partial^2 C}{\partial x^2}. \tag{1.7}$$

In parallel, the concept of Brownian motion was discovered by the Scottish botanist Robert Brown in the early 19th century. He observed that pollen in water showed random motion that was not due to currents in the liquid. The explanation of Brownian motion and its connection with macroscopic diffusion took nearly a hundred years and was given by Albert Einstein [104] in one of his four *Annus Mirabilis* papers of 1905. The link between macroscopic diffusion and microscopic Brownian motion is the mean-square displacement (MSD) of the particles. If we observe a system of N particles that move independently, we can track the squared distance traveled on average in a time window τ:

$$\mathrm{MSD}(\tau) = \frac{1}{N}\sum_{I}^{N}\langle \boldsymbol{R}_I(t+\tau) - \boldsymbol{R}_I(t)\rangle_t, \tag{1.8}$$

where $\boldsymbol{R}_I(t)$ is the position of atom/particle I at time t, and the angular brackets $\langle\cdots\rangle$ indicate that an average in the thermodynamic ensemble is taken by considering different starting times t of the measurement. I derive in detail how the MSD relates the macroscopic diffusion coefficient to Brownian motion in Sec. A.1 and only report the result for the diffusion coefficient of a single particle, called the tracer diffusion coefficient:

$$D_{tr} = \frac{1}{N}\sum_{I}^{N}\lim_{\tau\to\infty}\frac{1}{6\tau}\left\langle\left(\boldsymbol{R}_I(t+\tau) - \boldsymbol{R}_I(t)\right)^2\right\rangle_t. \tag{1.9}$$

The tracer diffusion coefficient can be also calculated from an integral of the velocity auto-correlation function, which is derived in Sec. A.2:

$$D_{tr} = \frac{1}{3N}\sum_{I}^{N}\int_{t'=0}^{\infty}\left\langle \boldsymbol{V}_I(t)\boldsymbol{V}_I(t'+t)\right\rangle_t \mathrm{d}t', \tag{1.10}$$

where $\boldsymbol{V}_I(t)$ is the velocity of particle I at time t.

The tracer diffusion coefficient is a measure of how fast a single particle diffuses, but several properties, among which is the ionic conductivity σ of a material, depend on how fast particles move collectively, which is derived in Sec. A.3. If particles diffuse in a correlated manner, the observed charge diffusion will differ from the diffusion of the individual particles [105]. The difference between the charge diffusion coefficient D_σ (see Eq. (A.19) for definition) and the tracer diffusion coefficient

D_{tr} is expressed via the Haven ratio $H = \frac{D_{tr}}{D_\sigma}$. The latter is a measure of how collective the diffusion is, reaching $H = 1$ when particles of a species do not diffuse together (the so-called dilute limit), and $H \to 0$ the stronger the correlation is. The ionic conductivity σ is calculated from the tracer diffusion coefficient D_{tr} or the charge diffusion coefficient D_σ using the Nernst-Einstein equation:

$$\sigma = \frac{N(Ze)^2}{\Omega k_B T} D_\sigma = \frac{N(Ze)^2}{\Omega k_B T} \frac{D_{tr}}{H}, \tag{1.11}$$

where N is the number of particles of charge Ze, Ω and T are the system volume and temperature, respectively, k_B is the Boltzmann constant, and H is the Haven ratio.

In summary, the diffusion coefficient and the ionic conductivity of Li ions in a structure can be calculated from a trajectory, that is the positions (and velocities) of atoms as a function of time. How to obtain the trajectory is described in the next section.

1.3 Molecular dynamics

Molecular dynamics (MD) resemble closely real experiments, but are performed *in silico*, i.e., within a computer. The essential principle is to prepare the system of atoms in a certain microscopic state, and evolve it in real time from this state onwards. A basic assumption is that we can treat the atomic nuclei as classical particles with well-defined positions $\boldsymbol{R}_I$ and momenta $\boldsymbol{P}_I$, represented in a phase-space vector $\boldsymbol{X}(t) = \{\boldsymbol{R}_1(t), \boldsymbol{R}_2(t), \ldots, \boldsymbol{R}_N(t), \boldsymbol{P}_1(t), \boldsymbol{P}_2(t), \ldots, \boldsymbol{P}_N(t)\}$. To evolve the system, we do not need to know anything about other regions in phase space, but only how to get from one point in phase space to the next point in a very small step. Since we treat the system as classical particles, this can be done by integrating Newton's classical equation of motion:

$$M_I \frac{\mathrm{d}^2 \boldsymbol{R}_I}{\mathrm{d}t^2} = \frac{\mathrm{d}\boldsymbol{P}_I}{\mathrm{d}t} = \boldsymbol{F}_I\big(\boldsymbol{R}_1, \boldsymbol{R}_2, \ldots, \boldsymbol{R}_N\big) = -\frac{\partial U\big(\boldsymbol{R}_1, \boldsymbol{R}_2, \ldots, \boldsymbol{R}_N\big)}{\partial \boldsymbol{R}_I}, \tag{1.12}$$

where U is the potential energy, a function of the positions of all atoms. The Hamiltonian of the system is given by the sum of kinetic and potential energies:

$$\mathscr{H} = K\big(\boldsymbol{P}_1, \boldsymbol{P}_2, \ldots, \boldsymbol{P}_N\big) + U\big(\boldsymbol{R}_1, \boldsymbol{R}_2, \ldots, \boldsymbol{R}_N\big) = \sum_I \frac{\boldsymbol{P}_I}{2M_I} + U\big(\boldsymbol{R}_1, \boldsymbol{R}_2, \ldots, \boldsymbol{R}_N\big), \tag{1.13}$$

where K is the kinetic energy of the system, which depends on the momenta of the atoms. The connections between Eq. (1.12) and Eq. (1.13) is that the equation of motion conserves the Hamiltonian during the evolution in time:

$$\frac{\mathrm{d}\mathscr{H}}{\mathrm{d}t} = \sum_I \frac{\boldsymbol{P}_I \dot{\boldsymbol{P}}_I}{M_I} + \sum_I \frac{\partial U}{\partial \boldsymbol{R}_I} \dot{\boldsymbol{R}}_I = \sum_I \dot{\boldsymbol{R}}_I \Big(\dot{\boldsymbol{P}}_I + \frac{\partial U}{\partial \boldsymbol{R}_I}\Big) = 0, \tag{1.14}$$

where I inserted Eq. (1.12) in the last step. The equation of motion given in Eq. (1.12) preserves therefore the total energy of the system, and can be used to sample the microcanonical ensemble,

where the number of particles N, the volume V, and total energy E are conserved.

It is straightforward to couple a thermostat to Eqs. 1.12 and 1.13, leading to an equation of motion that conserves the temperature, and samples the canonical ensemble with constant N, V, and temperature T [106–113], and/or a barostat to evolve a system at constant pressure [106, 114]. With an ensemble defined, the evolution of the system in phase space is – in principle – predetermined, given a starting point in phase space, but usually, with the exception of very simple systems such as the harmonic oscillator, no analytical solution is possible. Therefore we integrate Eq. (1.12) numerically, using a discrete time step Δt and a numerical integration method, for example the common Verlet integrator [115]:

$$\boldsymbol{R}_I(t+\Delta t) = 2\boldsymbol{R}_I(t) - \boldsymbol{R}_I(t-\Delta t) + \Delta t^2 \frac{\boldsymbol{F}_I(\boldsymbol{R}_1(t), \boldsymbol{R}_2(t), \ldots, \boldsymbol{R}_N(t))}{M_I}. \tag{1.15}$$

In order to obtain the position of the atomic nucleus at the next step $t+\Delta t$, we need to know the force $\boldsymbol{F}_I(t)$ acting on particle I at time t, which depends on the position of some (or all) other atoms or particles in the system. Performing this operation in succession results in a trajectory of the N particles and constitutes the essential principle of an MD simulation.

The interaction of particles were originally described by interatomic pair potentials, where the potential energy of a system is obtained as the sum of the energetic contributions of each pair of particles, which is a function of the distance between them: $U_{pot} = \sum_{I \neq J} U(|\boldsymbol{R}_I - \boldsymbol{R}_J|)$. The first MD simulations were performed by Alder and Wainwright in the 1950s, studying the phase transition in a system of hard spheres [116], where the interaction between two spheres was given by:

$$U(r_{ij}) = \begin{cases} 0, & r_{ij} > 2r_s \\ \infty, & r_{ij} \leq 2r_s, \end{cases} \tag{1.16}$$

where $r_{ij} = |\boldsymbol{R}_I - \boldsymbol{R}_J|$ is the distance between spheres I and J and r_s is the radius of the spheres. The integration of this discontinuous interatomic potential was performed by calculating analytically the trajectory until the next collision, assuming free/ballistic movement between collisions.

To study more realistic atomic systems such as liquid argon at low temperature, a continuous interatomic force field such as the 12-6 Lennard-Jones potential was needed [117]:

$$E = \sum_{I \neq J} \epsilon_0 \left[\left(\frac{r_0}{r_{ij}} \right)^{12} - \left(\frac{r_0}{r_{ij}} \right)^{6} \right], \tag{1.17}$$

where r_{ij} is the distance between atoms I and J, and r_0 and ϵ_0 are parameters of the force field, which is well suited to describe non-covalent and non-ionic interatomic effects: the r_{ij}^{-6} term describes van der Waals interactions very well and the r_{ij}^{-12} term represents the repulsive interaction due to Pauli exclusion [118, 119]. The parameters of the model (r_0 and ϵ_0) were usually fitted to reproduce experimental observables, for example lattice constants or elastic moduli.

Force fields were continuously improved since the Lennard-Jones potential, adding flexibility with

more parameters [119]. The development of machine-learning (ML) potentials is a direct consequence, offering huge flexibility at the cost of being prone to overfitting [120–127]. The flexibility offered by ML potentials means that they need to be fitted on a large amount of data, usually originating from electronic-structure methods such as density-functional theory, that I will introduce in the next section.

Instead of using electronic-structure methods to fit classical force fields, one can benefit from the quantum-mechanical treatment of the electrons to calculate the energies and forces during the molecular dynamics on the fly [128]. No parameters are needed in such an approach, which explains the commonly employed term of first-principles molecular dynamics (FPMD).

1.4 Density functional theory

In principle, we know how to obtain energies and forces of a system consisting of atomic nuclei and electrons without resorting to parametrized interatomic force fields such as the Lennard-Jones potential of Eq. (1.17), namely by solving the Schrödinger equation $\hat{H}|\Psi_{tot}\rangle = E|\Psi_{tot}\rangle$, where $\hat{H}$ is the quantum-mechanical Hamiltonian operator which sums over all the contributions to the energy of a system: the quantum kinetic energy of electrons and nuclei and the electrostatic interaction between nuclei, between electrons, and between nuclei and electrons. $|\Psi_{tot}\rangle$ is the wave function describing the system and E is its energy.

To simplify this very complex mathematical problem, the system is studied in the adiabatic approximation; the weight of the nuclei is much larger than the weight of an electron, so that the electrons can be assumed to follow instantaneously the nuclei. Therefore, the nuclei and the electrons can be treated independently. In addition, we describe the nuclear degrees of freedom using classical equations, leading to the Born-Oppenheimer approximation [129]. The Schrödinger equation for the electrons in this clamped-nuclei approximation is:

$$\hat{H}|\Psi_{el}\rangle = \left(-\frac{\hbar^2\boldsymbol{\nabla}^2}{2m} + \frac{1}{2}\sum_{i\neq j}\frac{e^2}{4\pi\epsilon_0|\boldsymbol{r}_i-\boldsymbol{r}_j|} + V_{ext}\right)|\Psi_{el}\rangle\,, \quad V_{ext} = -\sum_{I,i}\frac{Z_I e^2}{4\pi\epsilon_0|\boldsymbol{R}_I-\boldsymbol{r}_i|}, \tag{1.18}$$

where V_{ext} stands for the Coulomb interaction of the electrons (in a state $|\Psi_{el}\rangle$) with the "external system" of nuclei, $\hbar$ is the reduced Planck constant, ϵ_0 the permittivity of vacuum, e the electron charge, m the electron mass, and Z_I the atomic number of atom I. As customary, all quantities are represented with lowercase characters for electrons and with uppercase characters for nuclei, i.e., the position of the nucleus of atom I is given by $\boldsymbol{R}_I$, while the position operator of electron i is given by $\boldsymbol{r}_i$. In atomic units, where $\hbar = e = m = 4\pi\epsilon_0 = 1$, the Schrödinger-equation for electrons in the Coulomb potential of atomic nuclei is:

$$\hat{H}|\Psi_{el}\rangle = \left(-\frac{1}{2}\boldsymbol{\nabla}^2 + \frac{1}{2}\sum_{i\neq j}\frac{1}{|\boldsymbol{r}_i-\boldsymbol{r}_j|} - \sum_{I,i}\frac{Z_I}{|\boldsymbol{R}_I-\boldsymbol{r}_i|}\right)|\Psi_{el}\rangle\,. \tag{1.19}$$

The wave function $|\Psi_{el}\rangle$ depends on the coordinates and spins of all electrons. The presence of

the electron-electron repulsion term in Eq. (1.19) rules out the possibility to find any exact analytical solution for the ground-state wave function of a system with more than one electron. However, this so-called many-body problem can be solved numerically, e.g., by exploiting the Rayleigh–Ritz variational principle, which states that by minimizing the energy with respect to all possible wave functions we converge to the ground-state energy:

$$E_0 = \min_{\Psi_{el}} \left(\frac{\langle \Psi_{el} | \hat{H} | \Psi_{el} \rangle}{\langle \Psi_{el} | \Psi_{el} \rangle} \right). \tag{1.20}$$

However, $|\Psi_{el}\rangle$ is still an extremely complex object to use for the minimization and computationally too expensive for many practical applications [130].

Another simplification is to express the wave function $|\Psi_{el}\rangle$ as a single Slater determinant of single-particle wave functions $|\psi_i\rangle$, since a Slater determinant abides to the Pauli exclusion principle. Applying a mean-field approximation allows one to iteratively solve for each ψ_i until convergence, i.e., $\frac{\delta E}{\delta \psi_i} = 0$, while imposing the orthonormality constraint $\langle \psi_i | \psi_j \rangle = \delta_{ij}$. These two simplifications result in the Hartree-Fock equation for the single-particle wave function:

$$\left[-\frac{1}{2}\nabla_i^2 - \sum_I \frac{Z_I}{|\boldsymbol{R}_I - \boldsymbol{r}|} + \int \frac{n(\boldsymbol{r}')}{|\boldsymbol{r} - \boldsymbol{r}'|} \mathrm{d}\boldsymbol{r}' \right] \psi_i(\boldsymbol{r}) - \sum_j \left[\int \frac{\psi_j^*(\boldsymbol{r}')\psi_i(\boldsymbol{r}')}{|\boldsymbol{r} - \boldsymbol{r}'|} \mathrm{d}\boldsymbol{r}' \right] \psi_j(\boldsymbol{r}) = \epsilon_i \psi_i(\boldsymbol{r}), \tag{1.21}$$

where the charge density $n(\boldsymbol{r}) = \sum_i |\psi_i(\boldsymbol{r})|^2$ is a function of all wave functions ψ_i, and the last term on the left hand side of Eq. (1.21) is the Fock exchange, imposing the correct behavior for a system of fermions. The non-locality of this term gives rise to a significant computational cost, namely a N^4 scaling, where N is the number of wave functions. In addition, the approximation of $|\Psi_{el}\rangle$ as a single Slater determinant means that dynamical correlation between electrons is lost, leading to an overestimation of the total energy of the system.

In density-functional theory (DFT) the electronic charge density is used instead of the the wave functions of the system for the minimization, which is possible thanks to the first Hohenberg–Kohn theorem [131], which states that ground-state properties of a system of interacting electrons in a local external potential are uniquely determined by its ground-state charge density $n(\boldsymbol{r})$ (and not only by the external potential). The second Hohenberg–Kohn theorem [131] states that for any external potential V_{ext}, a functional $E[n]$ exists that can be minimized, which allows for the application of the Raleigh–Ritz variational principle, see Eq. (1.20). In order to approximate the unknown functional, the physical system of electrons $|\Psi_{el}\rangle$ is mapped to an auxiliary system of non-interacting particles, the Kohn–Sham (KS) system $|\Phi\rangle$, with the Kohn–Sham potential of this auxiliary system adjusted to result in the same charge density n [132]. The resulting set of equations for the single-particle Kohn-Sham wave functions ϕ_i can be solved iteratively until convergence:

$$\left[-\frac{1}{2}\nabla_i^2 - \sum_I \frac{Z_I}{|\boldsymbol{R}_I - \boldsymbol{r}|} + \int \frac{n(\boldsymbol{r}')}{|\boldsymbol{r} - \boldsymbol{r}'|} \mathrm{d}\boldsymbol{r}' + V_{xc}[n] \right] \phi_i(\boldsymbol{r}) = \epsilon_i \phi_i(\boldsymbol{r}), \tag{1.22}$$

where the last term is the exchange-correlation potential $V_{xc}(\boldsymbol{r}) = \frac{\delta E_{xc}[n(\boldsymbol{r})]}{\delta n(\boldsymbol{r})}$, which has several important functions: it captures exchange, but also accounts for electron-electron correlations [133], and corrects for the assumption of independent electrons.

Kohn–Sham DFT (KS-DFT) is still in principle an exact theory, but the exchange-correlation functional is not known, which led to Richard Feynman calling this term the "stupidity energy", because everything unknown (or too expensive to calculate exactly) is put into it [133]. The functional has to be approximated, for example by fitting the local density to accurate Quantum Monte Carlo results for the homogeneous electron gas, resulting in the local-density approximation (LDA) [134]. The generalized-gradient approximation (GGA) adds a gradient correction. The Perdew-Burke-Enzerhof (PBE) exchange-correlation functional is one of widely used flavors of GGA [135, 136]. Three charge densities calculated with the PBE functional are shown in Fig. 1.2 to illustrate the different behavior of the charge density in different systems.

DFT is in principle only applicable to ground-state properties but it is very successful there, despite short-comings in the treatment of correlated electrons or the famous self-interaction error in DFT [65, 134, 137, 138]. The number of papers on the topic of DFT has increased substantially in the last 20 years, shown in Fig. 1.3, where I also compare to the topics "molecular dynamics" and "Li-ion battery". The success of DFT led to Walter Kohn being awarded the Nobel prize in chemistry in 1998.

To this day, many "flavors" of DFT remain parameter-free, demonstrating good reproducibility of materials' properties across different implementation of basis sets and potentials [136, 139]. Several efforts attempt to increase the accuracy of DFT, for example via the re-introduction of exact exchange from Hartree-Fock in so-called hybrid functionals, but include, to a certain degree, parameters that stem from fits to experiment or higher-order theories [140–143]. For many applications in materials science, however, DFT is very accurate and is computationally affordable [144]; examples include the prediction of lattice constants and bulk moduli [145], ground-state structures and

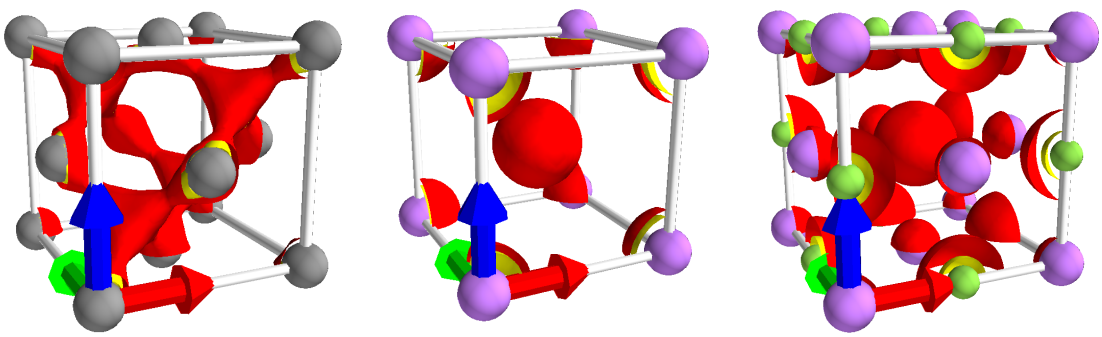

Fig. 1.2: The charge density of the valence electrons of diamond (left), lithium in its BCC phase (center), and LiF (right), shown as isosurfaces of two isovalues, yellow depicting a higher charge density than red (different isovalues for each system). Carbon in the diamond structures bonds covalently, visibly in the sp^3-type distribution of the charge density in the region between atoms. A metallic bond as for BCC lithium displays no directionality, and the charge density for Li is spread out. An ionic bond, as in LiF, is also not directional, but the charge density around Li^+ is reduced.

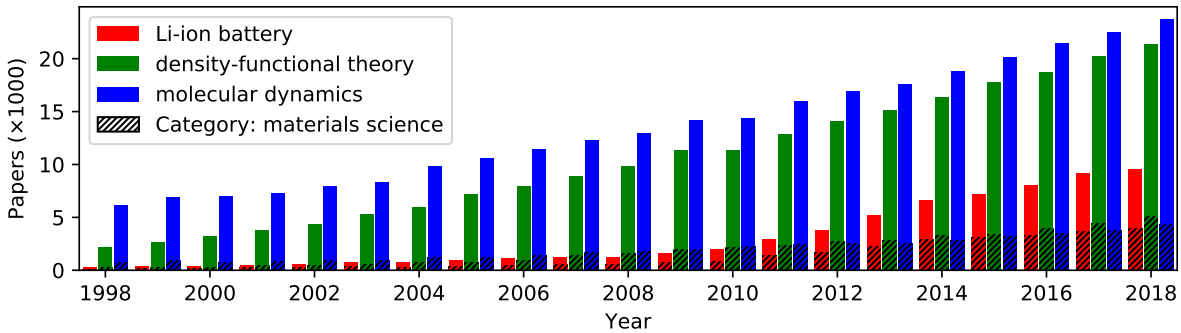

Fig. 1.3: The number of papers that appeared in the last 20 years on the topic of 'Li-ion battery' (or 'lithium-ion battery'), 'density-functional theory' (or 'density functional theory', or 'DFT'), and 'molecular dynamics' is shown in red, green, and blue, respectively. The subset of papers that appeared in the category 'materials science' are marked with striped lines, showing that these three topics are on a par in that category. The statistics originate from the Web of Science platform.

phase diagrams [146–149], or nuclear magnetic resonance (NMR) and Raman spectra [150–156]. Since energetics are well reproduced, the application of DFT to drive molecular dynamics is a straightforward choice, resulting in first-principles molecular dynamics (FPMD) [128, 157–162]. Forces on the ionic nuclei, needed to propagate the atoms using Eq. (1.15), can be calculated from the electronic ground state using the Hellman-Feynman theorem [163]:

$$F_I = -\frac{\partial E}{\partial \boldsymbol{R}_I} = -\left\langle \Psi_0 \middle| \frac{\partial \hat{H}_{el}}{\partial \boldsymbol{R}_I} \middle| \Psi_0 \right\rangle - \frac{\partial E_{\text{ion-ion}}}{\partial \boldsymbol{R}_I}, \tag{1.23}$$

where Ψ_0 is the ground-state wave function and $\hat{H}_{el}$ the Hamiltonian of the electrons. In DFT, the only term that depends on the ionic positions is the external potential, which yields the following expression for the forces in DFT:

$$\boldsymbol{F}_I = -\frac{\partial E_{\text{ion-ion}}}{\partial \boldsymbol{R}_I} - \int \frac{\partial V_{ext}}{\partial \boldsymbol{R}_I} n_0(\boldsymbol{r}) \mathrm{d}\boldsymbol{r}, \tag{1.24}$$

where n_0 is the ground-state charge density. The forces in DFT depend purely on electrostatic interactions, and are easy to compute once the ground-state charge density is known, leading to first-principles Born-Oppenheimer molecular dynamics, since the system remains on the Born-Oppenheimer surface, where the electrons are always in the ground state for the atomic configuration. Another (computationally more efficient) implementation of FPMD is the Car-Parrinello approach, where electrons and nuclei are propagated together [128].

1.5 Computational materials screening

Materials screening refers to the search for materials satisfying specific properties that might be important for a certain application, e.g., a band gap of ~1.5 V for a light-harvesting semiconductor or a Young's modulus above 200 GPa for a metal alloy. These properties, if not known beforehand,

must be either experimentally determined during the screening or need to be computed, e.g., with DFT. The former is referred to as experimental screening, the latter as computational screening, and undoubtedly both approaches can be combined.

Experimental screenings for materials that are optimal for a specific application have been done successfully in the early days of materials science: the inventor Thomas Edison and his team tested thousands of materials in the 1870s to find the perfect filament for the incandescent light bulb [164, 165], performing the first "high-throughput" materials screening that we know of, where high-throughput generally refers to testing several thousand structures [166]. Clearly, testing thousands of materials in the laboratory is generally very human-labor intensive, since each material has to be procured or synthesized, and have its property measured. Nevertheless, experimental high-throughput screening has become an established method as early as twenty years ago in chemistry [167] and in the bio-medical field, where high-throughput screening of molecules for drug applications is so established that the term "beyond high-throughput" has been coined [168]. Also the field of materials science saw successful applications of experimental screening in the search for superconductors, materials' synthesis, and sensors [169–171].

Despite aforementioned successes of experimental searches, and partly due to the development of DFT, a general, accurate, and – for most problems and systems – computationally affordable technique to calculate materials' properties, high-throughput materials screening has lately shifted towards computational approaches [17, 165, 172–175], for several reasons. First, Moore's law, which describes the empirical observation that the density of transistors per unit area doubled about every 18 months, until recently [176–178], resulted in an exponential increase in the computing power available to the scientific community. With the advent of codes that implemented DFT for high-performance computing (HPC) architectures [179–182], scientists can calculate the properties of materials in a highly parallelized manner, faster than the corresponding experiment would take. Second, the simulation of materials offers more control, as also non-synthesizable structures can be calculated [173], chemical substitutions can be performed in a straightforward manner, and conditions that are difficult to achieve in experiment can be obtained easily in simulation, e.g., to discover new phases at very high pressures [148, 183]. As a recent example of computational materials screening, Castelli *et al.* studied all possible perovskite structures ABO_3, with A and B being any of 52 non-radioactive metals, resulting in a total of 2704 oxides. Their formation energy was estimated with DFT and their electronic band gap was calculated with a hybrid functional in order to find perovskites for photo-induced water splitting, resulting in ten candidates [184]. A second example is by Hautier *et al.*, who screened for possible cathode materials for Li-ion batteries among all structures in a large experimental database and derivatives created from those structures using a machine-learned substitution model. Their DFT calculations (with a Hubbard-U correction) to estimate the stability of the compounds and calculate their redox potential resulted in candidate cathodes from the sidorenkite family [48, 185, 186]. A third example is the discovery of exfoliable 2D-materials by Mounet *et al.*: after a pre-screening using geometric criteria to find layers, DFT (including van der Waals dispersion) was employed to select materials with a low binding energy

between the layers, that are most likely be exfoliated into single atomic layers [187].

It is generally accepted [174] that high-throughput materials screening is not about simply scaling up the traditional way of calculating materials' properties, where the approach can be tailored to the distinct material investigated, taking into consideration whether it is metallic or insulating, magnetic or non-magnetic, solid or liquid, and where every parameter of the simulation is converged for the specific case. A different paradigm is required, where convergence tests are automated and material-independent, and where the scientific knowledge of how to treat different cases are encoded into computational workflows, ensuring an automated and reproducible sequence of calculations. In addition, in a high-throughput calculation scenario results cannot be simply stored in human-readable text files, to be interpreted by the scientist, but need to be parsed automatically and stored in a queryable manner within databases [174].

Several materials' informatics platforms have been implemented in the past, and used for screening projects, notably the atomic simulation environment (ASE) [188], AFLOW [189], FireWorks[190], and the Automated Interactive Infrastructure and Database for Computational Science (AiiDA) [191]. I will briefly explain the automation and storage in the case of AiiDA, that was used extensively in the work presented in the following chapters. The platform implements the ADES model, where ADES is an acronym for Automation, Data, Environment, and Sharing, that are viewed as pillars on which a high-throughput computational screening can be built upon.

The first pillar, automation, requires a high-throughput platform to have all the functionality needed to run any number of calculations without human intervention, given a well-defined sequence of steps to follow. Steps that normally require such human intervention are: (1) the creation of input files for a calculation, (2) copying the files to a remote high-performance computer where the calculation will run, and submitting the jobs, (3) checking for completion of the calculation, (4) copying the results back to the local computer, and (5) analyzing the results for the properties of interest. Depending on the results, new calculations might need to be performed, bringing us back to step (1). These steps are automated in AiiDA with the daemon (for job submission, retrieval, parsing), shown in the left panel of Fig. 1.4, and workflows that orchestrate the sequence of calculations to perform.

Data, the second pillar of the ADES model, calls for the storage of data in a queryable format. The central part of the AiiDA architecture consists of the object relation mapper (ORM), that maps calculation or data instances between storage (database and file repository) and Python instances that users can interact with via command line, Python scripts, or an interactive shell (see left panel of Fig. 1.4; more details are given in Sec. B.1). Additional functionality necessary for specific types of calculations or data instances can be inserted into AiiDA via plugins. Due to the ORM, every object that a user (or the daemon) creates within AiiDA is stored directly in a database. In addition, AiiDA provides for every record, data or calculation, the history of its creation (provenance). AiiDA is inspired by the Open Provenance Model [192] and views every calculation as a function, returning

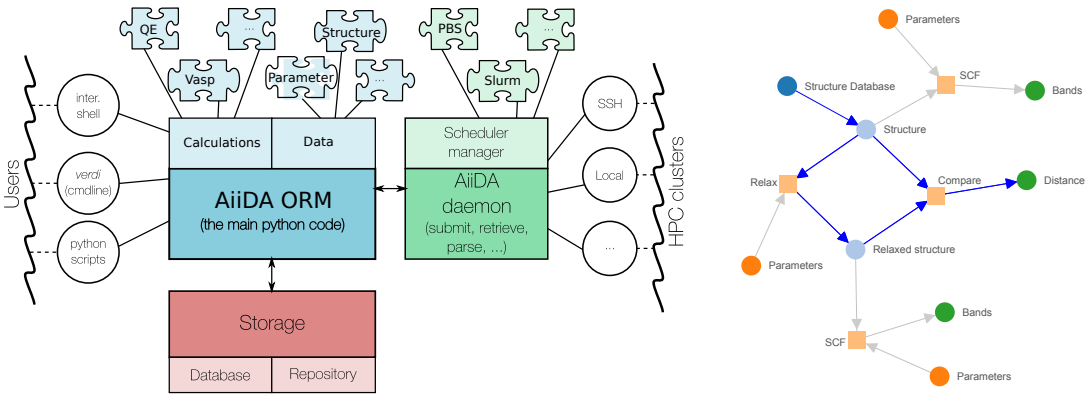

Fig. 1.4: (Left) The architecture of AiiDA consists of the object relation mapper (ORM) that maps between Python entities and database storage. The user and the AiiDA daemon interact with these stored calculation and data instances, with plugins allowing for specialized functionality. (Right) Exemplary graph illustrating the provenance model of AiiDA: data instances, represented by circles, are input to calculations (squares), that create new data instances. Data being input to, or created by, a calculation is presented by arrows, resulting in a directed acyclic graph. As an example, the blue subgraph shows a structure (downloaded from an external database) being relaxed, and compared to the unrelaxed structure, resulting in a distance. Adapted from Pizzi *et al.* [191].

output data as a function of its input data:

$$\text{output}_1, \text{output}_2 = \text{calculation}(\text{input}_1, \text{input}_2, \text{input}_3), \tag{1.25}$$

where the output of one calculation can be the input to another calculation, leading to a directed acyclic graph, as illustrated in the right panel of Fig. 1.4. The provenance of a result can be obtained by walking from this node in the graph in reverse direction along the edges (which are stored in the database). This way, every data and calculation instance that led to a specific result can be explored (how to explore the graph is described in Sec. B.2). In addition, if we assume that the calculations are pure functions (output uniquely determined by input), the results are also fully reproducible: one can take the same type of calculation, apply the same input, and will obtain the same output. Given the recent and ongoing reproducibility crisis in science [193–195], having everything to reproduce a result safely stored in a database is an important feature.

Environment, the third pillar, covers higher-level functionality that enables a scientist to focus primarily on the scientific question at hand. AiiDA allows for modular workflows that can be independent of a code, allowing a decoupling of the calculation of a property and the specific DFT (or any other) code employed. As an example, calculating the diffusion coefficient requires a workflow that only needs to have the functionality to calculate and converge the diffusion coefficient. Producing the trajectory can be outsourced to a different workflow and calculation plugin specific to a molecular dynamics code.

Finally, AiiDA facilitates the sharing (last pillar of ADES model) of data between projects or between

scientists due to the underlying standardization of data storage, and provides easy functions to import to and export from any AiiDA database. In addition, data can also be shared with the public via graphical interfaces on platforms such as the MaterialsCloud. Also the workflows (encoding scientific knowledge and best practices) can be shared by scientists that work on a variety of projects, since workflows can be independent of the specific codes used, and should be completely independent of the hardware architecture the codes will execute on.

1.6 Outline of the thesis

Inorganic solid-state electrolytes, introduced in Sec. 1.1.3, form a class of promising electrolyte materials for Li-ion batteries, due to their high mechanical stiffness and their wide electrochemical stability windows, preventing dendritic growth of metallic lithium from the anode side effectively and allowing for the use of high-voltage cathodes. As a result, they have the potential to increase safety and energy density of Li-ion batteries significantly. One disadvantage of solid-state electrolytes is their generally lower Li-ion diffusion or, equivalently, lower Li-ionic conductivity, compared to liquid electrolytes, motivating further research to understand Li-ion diffusion in solid-state ionic conductors [196]. Diffusion and ionic conductivity, introduced in Sec. 1.2, can be calculated for a material without resorting to experiment by simulating the movement of atoms via molecular dynamics (see Sec. 1.3). Using DFT, introduced in Sec. 1.4, to drive the evolution of atoms results in accurate predictions, making first-principles molecular dynamics (FPMD) an invaluable tool to study diffusion properties of Li-ion conductors. However, FPMD is still too expensive to simulate large systems, long time scales, or a large number of systems. A computational screening (see Sec. 1.5) to discover new Li-ionic conductors requires cheaper models.

We worked on approximations to DFT that were physically motivated by what we know about the effects that Li ions have on the electronic charge density of ionic systems. This resulted in the so-called “pinball model”, derived and validated in Chap. 2, which can be used to evolve Li ions in molecular dynamics simulations. Due to its derivation from a first-principles framework it retains good accuracy, compared to first-principles molecular dynamics, but at a fraction of the computational cost. Having a model of such computational efficiency resulted in a large quantity of trajectories of Li-ionic conductors, too many to analyze using the standard methods in the literature. Chap. 3 describes a new method to analyze molecular dynamics simulations in a highly automated fashion to detect jumps or hops of Li ions during the simulations. The computationally efficiency of the pinball model, combined with our automation efforts, permitted us to perform a computational screening for new Li-ionic conductors that can be used as solid-state electrolytes for next generation batteries, and the methods employed and results obtained are presented in Chap. 4. All these techniques were applied in the finding and characterization of a fast-ionic conductor found in the screening, namely Li_7TaO, which is presented in Chap. 5. The conclusion and outlook are given in Chap. 6.

2 The pinball model

I thought I was the bally table king.
but I just handed my pinball crown to him.

Even my usual table, he can beat my best.
His disciples lead him in and he just does the rest.

He's got crazy flipper fingers, never seen him fall...
That deaf, dumb, and blind kid sure plays a mean pinball.

The Who – Pinball Wizard

For a high-throughput computational screening for solid-state electrolytes, the calculation of the Li-ion diffusion coefficients of thousands of systems would be necessary. First-principles molecular dynamics (FPMD), introduced in Chap. 1, are computationally very costly, limiting the application of this method to the study of few, selected materials for intermediate time scales (hundreds of picoseconds).

To overcome the computational cost of FPMD, but retain its generality and accuracy needed for a high-throughput screening, we applied physically motivated approximations to density-functional theory (DFT), resulting in the pinball model for Li-ionic systems. The approximations stem from two observations: first, that Li ions only negligibly perturb the valence electronic charge density of an ionic system, and second, that in many solid-state Li-ion conductors the host lattice vibrates around equilibrium positions, but does not diffuse. Approximating the charge density as independent of Li-ion positions and the host lattice as frozen to equilibrium positions (see Fig. 2.1) results in a computationally very inexpensive model, that is presented and validated in the remainder of this chapter. I note that the pinball model can be derived in a different manner, namely via a Taylor expansion of the Hamiltonian around the ground state of the host lattice, which I present in Appendix C. By including higher order terms, the latter derivation allows to formulate a "flexible" model, where the charge density is updated as a response to the host-lattice vibrations. Latter approach has not been fully implemented and validated, therefore is not part of the main work.

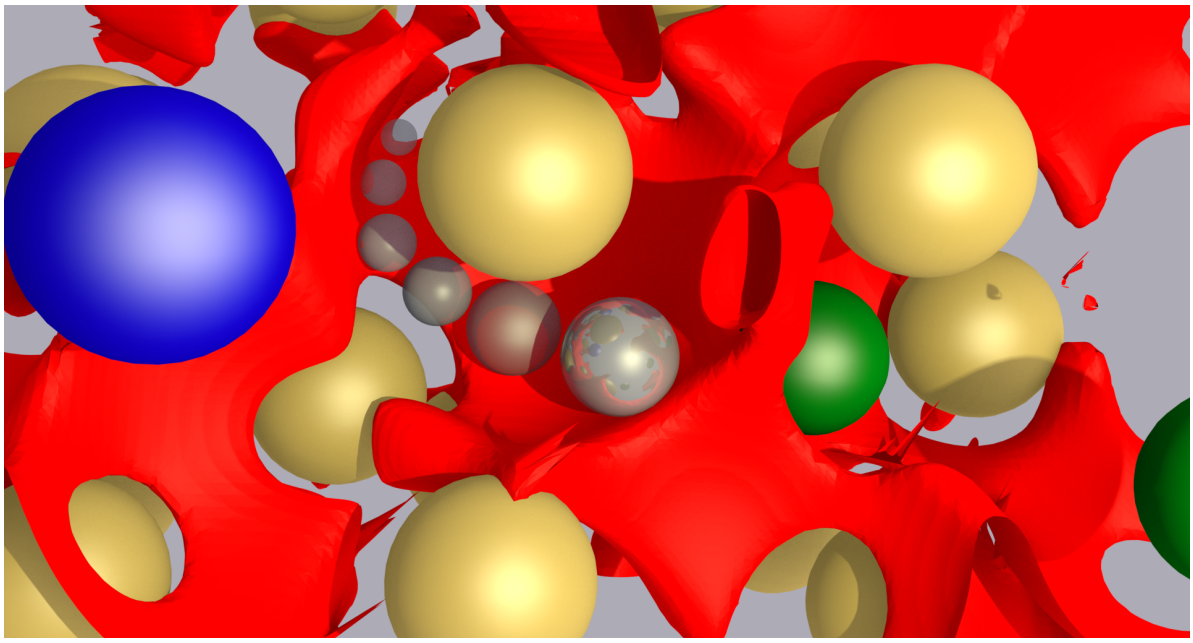

Fig. 2.1: The pinball (metallic sphere) is moving on a potential energy surface given by a frozen charge density (one isosurface shown in red) and the frozen host-lattice ions (large spheres).

The "frozen-host" pinball model was conceptualized and derived by all authors of the resulting publication and was implemented by Aris Marcolongo and myself. I conducted all simulations presented in the following post-print, and wrote the manuscript with Aris Marcolongo and Nicola Marzari.

Authors	Leonid Kahle, Aris Marcolongo, and Nicola Marzari
Title	Modeling lithium-ion solid-state electrolytes with a pinball model
Journal reference	*Physical Review Materials* **2**, 065405, 2018
DOI	10.1103/PhysRevMaterials.2.065405
arXiv	1805.10263

Modeling lithium-ion solid-state electrolytes with a pinball model

Leonid Kahle,[a] Aris Marcolongo,[a†] and Nicola Marzari[a]

Abstract: We introduce a simple and efficient model to describe the potential energy surface of lithium diffusing in a solid-state ionic conductor. First, we assume that the Li atoms are fully ionized and we neglect the weak dependence of the electronic valence charge density on the instantaneous position of the Li ions. Second, we freeze the atoms of the host lattice in their equilibrium positions; consequently, also the valence charge density is frozen. We thus obtain a computational setup (the "pinball model") for which extremely inexpensive molecular dynamics simulations can be performed. To assess the accuracy of the model, we contrast it with full first-principles molecular dynamics simulations performed either with a free or frozen host lattice; in this latter case, the charge density still readjusts itself self-consistently to the actual positions of the diffusing Li ions. We show that the pinball model is able to reproduce accurately the static and dynamic properties of the diffusing Li ions – including forces, power spectra, and diffusion coefficients – when compared to the self-consistent frozen-host lattice simulations. The frozen-lattice approximation itself is often accurate enough, and certainly a good proxy in most materials. These observations unlock efficient ways to simulating the diffusion of lithium in the solid state, and provide additional physical insight into the respective roles of charge-density rearrangements or lattice vibrations in affecting lithium diffusion.

2.1 Introduction

Overcoming safety challenges and reaching performance targets in rechargeable Li-ion batteries will be key to the deployment of mobile applications such as electric vehicles [16]. The electrically insulating, ion-conducting electrolyte is a critical component in the quest to improve the power density, time stability, and safety of batteries [58, 73], and replacing the current state-of-the-art organic electrolytes with solid-state electrolytes (SSEs) offers an attractive alternative [197, 198]. Despite the urgent need of new SSEs, only a small number of crystal structures with a sufficient ionic conductivity [196] have been discovered so far, and large regions of materials' space remain unexplored, highlighting the need and opportunity to find efficient ways to screen experimental or theoretical repositories of crystal structures for good ionic conductors. Accurate first-principles molecular dynamics (FPMD) simulations of diffusion properties are resource-limited to a few selected cases. The first FPMD simulations of fast-ion or superionic conductors date to 1999 [159] (H_2O and NH_3) and 2006 [162] (AgI), with few works specifically tackling Li-ion diffusion and Li-ion migration barriers with static [105, 199–203] and dynamic [51, 204–211] first-principles methods.

[a] Theory and Simulation of Materials (THEOS), and National Centre for Computational Design and Discovery of Novel Materials (MARVEL), École Polytechnique Fédérale de Lausanne, CH-1015 Lausanne, Switzerland
†Present address: IBM Research–Zurich, CH-8803 Rüschlikon, Switzerland

More efforts employ classical force-fields to study diffusion phenomena in specific crystal families, such as the garnets [212–216] and the lithium superionic conductors (LISICONs) [217, 218], but empirical methods often lack the generality to deal with large compositional variety.

In addition to direct dynamical simulations, several descriptors or design principles for ionic conductivity in solid-state materials have been suggested. As a first example, Wakamura and Aniya correlated optical phonon frequencies and the activation energy for diffusion in selected classes of materials [219, 220]. Another example is the importance of accessible volume for the diffusing species, which has been confirmed by experiments and simulations [221, 222]. This observation resulted in the bond-valence method [223] which accounts, in a static single-particle picture, for volume and energy effects and has already been used in large-scale screening for ionic conductors [224, 225]. Wang *et al.* [208] could relate superionicity to the bcc-like topology of the underlying anionic sublattice, as was also discussed by Wood and Marzari [162] for AgI. Work by Adelstein and Wood [226] showed how the mixed ionic-covalent nature of lithium bonds and frustration of the bonding during transition can explain superionic behavior observed in Li_3InBr_6. In addition to the search for descriptors, very recent work also highlights the importance of the collective nature of superionic diffusion [211, 214, 227]. An emerging trend is to tackle the descriptor search with machine-learning [228], which could automatically detect combinations of descriptors and the intricate correlations between them, although the lack of training data and interpretation of the results remain a major hurdle.

Consequently, the discovery of new ionic conductors has been driven up to now mostly by chemical intuition, as for example the discovery of the garnet family of structures [229] and of the argyrodites [230], and incremental improvements of known ionic conductors, for example by anionic and cationic substitutions of known ionic conductors, as in the $Li_{4-x}Ge_{1-x}P_xS_4$ thio-LISICON system [231], and equivalently in the $Li_{4\pm x}Si_{1-x}Y_xO_4 \quad (Y = Al, Ge, P)$ LISICON system [232].

The varying and complex ionic diffusion mechanisms in diverse materials challenge the efforts to relate diffusion properties to simple descriptors, and this work explores a different approach. Instead of looking for descriptors, we try to directly compute the bulk diffusion coefficients for every material, at a cost compatible with screening applications. The goal is to combine the accurate framework of FPMD with physically motivated approximations that can tackle the time-limitations of this rather expensive technique. This is achieved by simulating lithium ions in a potential energy landscape defined by the electrostatic and non-local interactions with a frozen host lattice and its charge density. Li-ions moving through an environment of static obstacles recall the game of pinball, and we refer to the model as the pinball model. We will show that it correctly models the interaction of diffusing particles with the host lattice as well as the ion-ion interactions between diffusing particles, and is therefore a promising approach in the search for predictive models for ionic conductivity. The pinball model does not account for lattice vibrations, and we discuss how much this limitation can influence the results. In addition, by comparing to first-principles simulations, we get novel insight on the correlation of lithium motion with the vibrations of the host lattice.

In Sec. 2.2 we present the model, while Secs. 2.3 and 2.4 discuss the validation strategy and results. The conclusions are presented in Sec. 2.5.

2.2 The pinball approximation

We aim to model the diffusion of lithium ions through an ionic crystal. In these systems the ions move through a host lattice containing anions of highly electronegative character, such as oxygen, sulfur, nitrogen or halides. Due to the large difference in electronegativity, the cations lose their 2s-valence electrons, which are accommodated by the host-lattice anions, while keeping the 1s-states in their core configuration. As a consequence, the valence electronic charge density depends weakly on the position of the diffusing cations. Such effect is shown in Fig. 2.2, where the charge density of one of the fastest known Li-ionic conductors, $Li_{10}GeP_2S_{12}$ (LGPS), is illustrated. We show the electronic charge density for one molecular dynamics snapshot computed in the explicit presence of lithium and compare it with the charge density obtained when all lithium ions are removed, while leaving their valence electrons in the simulation cell. The difference between the two charge densities is quite minor. In order to exploit this behavior for modeling purposes it is convenient to separate the ionic conductor into two subsystems:

(1) A system of electropositive Li ions, treated as electrostatic/quantum charges stripped of their

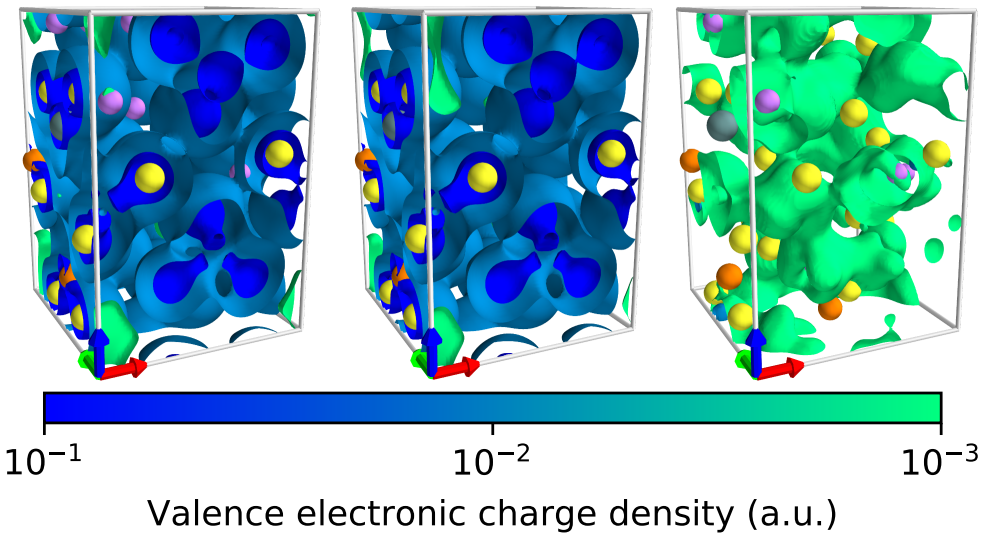

Fig. 2.2: The left image shows a unit cell of $Li_{20}Ge_2P_4S_{24}$ and 3 isosurfaces at 10^{-3}, 10^{-2} and 10^{-1} of its ground-state valence electronic charge density. The center image displays the same isosurfaces for the charge density of $Ge_2P_4S_{24} + 20e^-$, which is the former structure without the lithium cores but in the presence of lithium valence electrons. The same isosurfaces for the difference between the two previous charge densities are shown in the right image, showing that the error from the approximation is about two orders of magnitude lower than its characteristic values. Lithium, germanium, phosphorus and sulfur positions are shown as purple, olive, orange and yellow spheres, respectively, and the crystallographic directions a, b and c as red, green and blue arrows, respectively.

valence electrons, but carrying a local and non-local effective pseudopotential taking into account the interaction of the entire electronic valence manifold with the Li 1s core states. All members of this system will be called *pinballs* (P) in the remainder of this work.

(2) The host lattice (H), consisting of the remaining, non-diffusing atoms and the valence electrons coming from the ionized Li; this is negatively charged.

We study the dynamics of the system using Born-Oppenheimer molecular dynamics (BOMD) in the framework of Kohn-Sham density functional theory (KS-DFT) [131, 132]. In the following, atomic units are used, where Planck's constant $\hbar$, the mass of the electron and the elemental charge are of unity. For an ionic conductor with a sublattice H of host ions at positions $\boldsymbol{R}_H$ and a sublattice P of pinballs at positions $\boldsymbol{R}_P$, the Hamiltonian reads:

$$\mathscr{H} = \frac{1}{2}\sum_h^H M_h \dot{\boldsymbol{R}}_h^2 + \frac{1}{2}\sum_p^P M_p \dot{\boldsymbol{R}}_p^2 + U(\boldsymbol{R}_H, \boldsymbol{R}_P), \tag{2.1}$$

where the potential energy surface U in the pseudopotential formulation of KS-DFT is given by:

$$\begin{aligned} U(\boldsymbol{R}_H, \boldsymbol{R}_P) =& E_N^{P-P} + E_N^{H-H} + E_N^{H-P} + \int n(\boldsymbol{r}) V_{LOC}^H(\boldsymbol{r}) d\boldsymbol{r} + \int n(\boldsymbol{r}) V_{LOC}^P(\boldsymbol{r}) d\boldsymbol{r} \\ &+ \sum_i \langle \psi_i | \hat{V}_{NL}^H | \psi_i \rangle + \sum_i \langle \psi_i | \hat{V}_{NL}^P | \psi_i \rangle + F[n], \end{aligned} \tag{2.2}$$

where E_N^{A-B} is the electrostatic interaction between the nuclei dressed by the frozen core electrons of species A and species B, $V_{LOC/NL}^A(r)$ are the external local and non-local components of the pseudopotential of species A that act on the valence electronic charge density $n(\boldsymbol{r}) = \sum_i \psi_i^*(\boldsymbol{r})\psi_i(\boldsymbol{r})$, and where $F[n]$ is the universal functional of the charge density composed of the quantum kinetic energy operator, the Hartree contribution and the exchange-correlation term:

$$F[n] = -\frac{1}{2}\sum_i \langle \psi_i | \nabla^2 | \psi_i \rangle + \frac{1}{2}\int\int \frac{n(\boldsymbol{r}) n(\boldsymbol{r}')}{|\boldsymbol{r} - \boldsymbol{r}'|} d\boldsymbol{r}' d\boldsymbol{r} + E_{XC}[n]. \tag{2.3}$$

In Eq. (2.2), we assume a negligible contribution from non-linear core corrections [233] and therefore do not account for the nonlinearity of the exchange and correlation interactions of the valence and core charge densities.

We apply two approximations to Eq. (2.2), motivated by physical intuition. First, due to the weak dependence of the self-consistent valence electronic charge density on the Li-ion positions, we approximate the fully self-consistent valence wave functions ψ_i and valence charge density $n(\boldsymbol{r})$ with the wave functions and charge density that are computed only in the presence of the host lattice, adding the additional electrons coming from the valence shell of the pinballs. Technically, this results in a charged cell computation compensated by a neutralizing background. We will denote the new wavefunctions and charge density with ψ_{i,R_H} and n_{R_H}, respectively, because they depend parametrically solely on the host-lattice positions and are independent of the positions

of the pinballs. Second, we neglect any motion of the host lattice and pin the host ions to their equilibrium positions R_{H_0}. The application of these two approximations to Eq. (2.2) and the removal of all constant terms results in:

$$\mathscr{H}_P = \frac{1}{2}\sum_p^P M_p \dot{\boldsymbol{R}}_p^2 + E_N^{P-P} + E_N^{H-P} + \int n_{R_{H_0}}(\boldsymbol{r}) V_{LOC}^P(\boldsymbol{r}) d\boldsymbol{r} + \sum_i \langle \psi_{i,R_{H_0}} | \hat{V}_{NL}^P | \psi_{i,R_{H_0}} \rangle . \tag{2.4}$$

By definition $n_{R_{H_0}}$ and $\psi_{i,R_{H_0}}$ are time independent, leading to a massive reduction of computational costs compared to FPMD, since the self-consistent calculations of $\psi_i(\boldsymbol{r})$ and $n(\boldsymbol{r})$ at every ionic step are eliminated and are calculated once, prior to the dynamics, in a single self-consistent calculation.

In order to improve further the accuracy of the model we introduce four phenomenological coefficients $\alpha_1, \alpha_2, \beta_1$, and β_2 in the Hamiltonian of Eq. (2.4), accounting for a potentially different screening of each contribution to the total energy due to charge polarization:

$$\begin{aligned}\mathscr{H}_P = &\frac{1}{2}\sum_p^P M_p \dot{\boldsymbol{R}}_p^2 + \alpha_1 E_N^{P-P} + \alpha_2 E_N^{H-P} + \beta_1 \int n_{R_{H_0}}(\boldsymbol{r}) V_{LOC}^P(\boldsymbol{r}) d\boldsymbol{r} \\ &+ \beta_2 \sum_i \langle \psi_{i,R_{H_0}} | \hat{V}_{NL}^P | \psi_{i,R_{H_0}} \rangle .\end{aligned} \tag{2.5}$$

The Hamiltonian framework is important for the resulting dynamics, permitting to extract dynamical properties under a well defined statistical ensemble. The corresponding forces are:

$$\begin{aligned}\boldsymbol{F_p} = &-\frac{d}{d\boldsymbol{R}_p}\left(\alpha_1 E_N^{P-P} + \alpha_2 E_N^{H-P}\right) - \beta_1 \int n_{R_{H_0}}(\boldsymbol{r}) \frac{d}{d\boldsymbol{R}_p} V_{LOC}^P(\boldsymbol{r}) d\boldsymbol{r} \\ &- \beta_2 \sum_i \langle \psi_{i,R_{H_0}} | \frac{d\hat{V}_{NL}^P}{d\boldsymbol{R}_p} | \psi_{i,R_{H_0}} \rangle .\end{aligned} \tag{2.6}$$

The coefficients are obtained from a force-matching procedure [234]: a standard multilinear-regression fit permits one to determine the 4 coefficients by minimizing the error with respect to exact KS-DFT forces in selected snapshots. Deviation from unity of these parameters, as is generally observed, is due to the polarizability of the host matrix. The fitting procedure is very inexpensive compared to the simulation times required for the computation of transport properties with FPMD, and technical details are discussed in Sec. 2.6.1.

We note in passing that in the present work the last terms in Eq. (2.4), (2.5), or (2.6) represents a norm-conserving pseudopotential, rather than an ultrasoft one or a PAW projector. The extension to PAW and ultrasoft projectors, while feasible, is more cumbersome and provides a negligible advantage, since the cutoff for the charge density is broadly unaltered, and the additional efficiency in computing the ultrasoft or PAW projections due to a lower wave function cutoff is nullified by the larger prefactor in the calculation of the projection.

2.3 Validation strategy

We validated the pinball model in several systems characterized by different mechanisms of lithium diffusion and interactions with the host lattice. For every system three statistical setups are simulated, associated to different approximations of the underlying dynamics, and compared against each other:

(1) The "free" setup corresponds to standard FPMD of the full system, allowing both pinballs and the host lattice to move freely, with full self-consistency in the charge density.

(2) In the "constrained" setup the host lattice is frozen in an equilibrium configuration, while the electronic charge density is allowed to relax self-consistently according to the instantaneous positions of the pinballs.

(3) Finally, in the "pinball" setup, with its Hamiltonian given by Eq. (2.5), any temporal variation of the electronic charge density and wave functions is neglected and replaced by $n_{R_{H_0}}$ and $\psi_{i,R_{H_0}}$.

For all three cases we compute diffusion properties under microcanonical evolution. In addition to serve as a test bed, these simulations bring further physical insight into the diffusion mechanisms. The comparison between the free and constrained dynamics allows for an assessment of the role of host lattice vibrations in lithium diffusion. Instead, comparing the constrained with the pinball setup enables us to quantify the importance of charge density fluctuations and self-consistency during the motion of lithium through the crystal.

We chose several systems from four different structural families to allow for general conclusions. The first set of structures are represented by $Li_{10}GeP_2S_{12}$ (LGPS) and derivatives, studied extensively with FPMD by Ong *et al.* [204] and forming a set of highly conductive structures with variations in composition and volume. As a second benchmark, we considered the LISICON structure $Li_{3.75}Si_{0.75}P_{0.25}O_4$. Unlike the LGPS family, it shows a 3-dimensional conduction pathway [218] for lithium, while still having a high conductivity that allows for treatment with full FPMD in reasonable timescales. The third case is that of the layered vacancy conductoLi$_3$Nr [235–237], very different from the LISICON and LGPS-like structures both in composition and morphology. The high lithium content of Li_3N makes it an ideal testing case for the limits of the pinball model, since in this material 75% of the atomic constituents are treated as pinballs. In addition, the lower electronegativity of nitrogen (compared to oxygen or halides) suggests a lower degree of ionicity in this system when comparing to oxides, implying that lithium is more likely to affect its valence electron. Therefore Li_3N is included as a worst-case study. Last, we included the non-conducting material Li_3NbO_4, since experiments by McLaren et al. [238] show that undoped Li_3NbO_4 is a poor ionic conductor, but also that the ionic conductivity increases upon doping with Ni^{2+}. A more detailed discussion on the selection of materials is given in Sec. 2.6.2 together with technical details on the supercells used, chosen where necessary to reduce the effect of spurious correlations with periodic images. For clarity, we will use the chemical formulas of the supercells in the remainder of this work.

The screening parameters needed to calculate energies and forces in the pinball model (Eqs. (2.5) and (2.6)) are obtained from a force-matching procedure. For each material, several configura-

tions from a training set are calculated fully self-consistently and in the pinball model without the screening parameters ($\alpha_1 = \alpha_2 = \beta_1 = \beta_2 = 1$). Using least-squares linear regression we find the material-specific parameters that minimize the error of the pinball forces against self-consistent forces in this training set. In this work, we take the training configurations to be the snapshots of the constrained simulation taken every $10ps$ of all the runs performed, since we did not observe any dependence of the parameters on the mean kinetic energy of the ensemble, i.e. the screening parameters are temperature independent. We give additional details on the fitting procedure and the resulting parameters in Sec. 2.6.1, together with an alternative procedure for the fitting that is of comparable accuracy but computationally much less expensive.

The "free" and "constrained" simulations were performed using the PWscf code of the Quantum ESPRESSO distribution [181] . Dynamics in the pinball model required instead the development of an add-on functionality, in order to avoid the self-consistent cycle for the charge density optimization. For high-throughput capabilities, we wrote a plugin for the AiiDA materials' informatics platform [191] that is used in this work. Technical details regarding the protocols for the molecular dynamics are given in Sec. 2.6.2, and figures of merit regarding the computational speedup of the pinball model are presented in Sec. 2.6.3.

2.4 Numerical results and discussion

A good reproduction of Hellmann-Feynman forces, determining the time evolution of the system and *a fortiori* the ensembles spanned, is a prerequisite for accurate dynamics. In Fig. 2.3 we show forces as resulting from the pinball model against those obtained with fully self-consistent calculations for all systems studied. Configurations in this validation set originate from snapshots taken every time step from trajectories calculated in the constrained setup at temperatures ranging from $600K$ to $1200K$. Overall, forces in the pinball model are in excellent agreement with their DFT counterparts

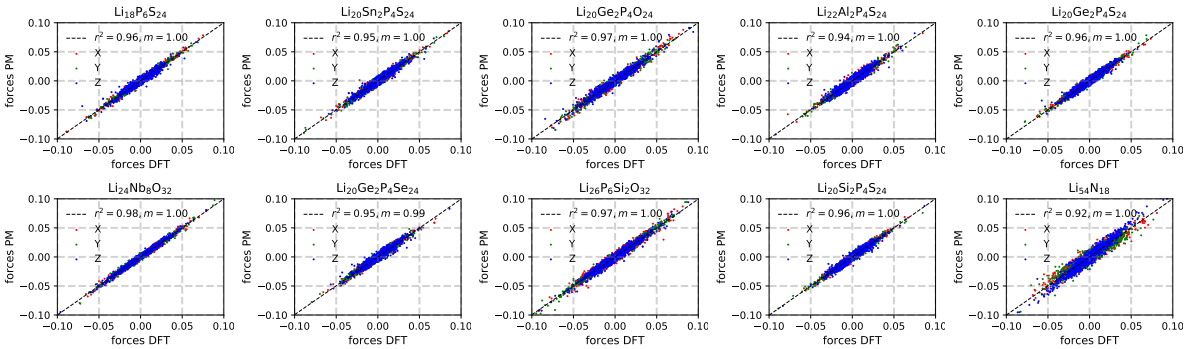

Fig. 2.3: We show the forces (in Rydberg atomic units) in the pinball model on the y-axis against the forces calculated with KS-DFT on the x-axis. Every point represent one component of the force vector for a lithium ion in a configuration from our validation set. The best fit is shown as a dashed black line and in the legend its slope m and the r^2 correlation coefficient are given as a quality measure of the fit.

for all structures studied, indicating that the "pinball" setup can serve as a good approximation for the "constrained" one, for the temperature ranges spanned in this work. The best fit ($r^2 = 0.984$) is produced for Li_3NbO_4, as expected, since the lower polarizability of oxygen reduces the error made when freezing the electronic charge density. The worst fit ($r^2 = 0.916$) can be seen in Li_3N, also expected because three quarters of the atoms in this structure are treated in an approximate way as pinballs.

Careful reproduction of the forces on the pinballs is a first step to show that the pinball model reproduces correctly static and dynamical properties. In order to ensure that the model leads also to the correct distribution of the diffusing cation, we show the probability densities for the pinballs from each setup, calculated as:

$$n_{\mathrm{P}}(\boldsymbol{r}) = \left\langle \sum_{p}^{P} \delta(\boldsymbol{r} - \boldsymbol{R}_p) \right\rangle_{N,E,V}, \tag{2.7}$$

where the index p runs over all pinballs in the simulation cell and angular brackets indicate a microcanonical mean over the molecular dynamics simulation. In practice, the delta function is replaced by a gaussian of 0.2Å standard deviation.

To estimate whether the vibrational properties of the pinballs are reproduced, we calculate the vibrational density of states from the Fourier transform of the velocity-velocity autocorrelation function $C_v(\omega)$:

$$C_v(\omega) = \frac{1}{N_P} \sum_{p}^{P} \int_{-\infty}^{+\infty} \langle \boldsymbol{V}_p(t) \cdot \boldsymbol{V}_p(0) \rangle_{N,E,V} \, e^{i\omega t} \, dt, \tag{2.8}$$

where $\boldsymbol{V}_p$ is the velocity of a pinball p. In addition, the tracer diffusion coefficient is computed, which is a more delicate property to reproduce, strongly dependent on the time evolution of the system:

$$D_{\mathrm{tr}} = \lim_{t\to\infty} \frac{1}{N_P} \sum_{p}^{P} \frac{1}{6t} \langle |\boldsymbol{R}_p(t) - \boldsymbol{R}_p(0)|^2 \rangle_{N,E,V}, \tag{2.9}$$

where $\boldsymbol{R}_p(t)$ is the position of a pinball p at time t. An estimate of the error of the tracer diffusion coefficients is obtained from a block analysis, with further details given in Appendix 2.6.2

A discussion of these figures-of-merit for the pinball model, ordered by material, follows. The vibrational density of states and the isosurfaces shown in this work are always calculated from the simulation equilibrated, as explained in Appendix 2.6.2, at $635K$, and isovalues are reported in the respective caption.

The *LGPS* family. The tetragonal structure of $Li_{20}Ge_2P_4S_{24}$, discovered by Kamaya *et al.* [239], is well-known for its high and predominantly unidimensional transport. The isosurfaces of ionic density for the free setup, shown in Fig. 2.4, give clear evidence for the presence of unidimensional

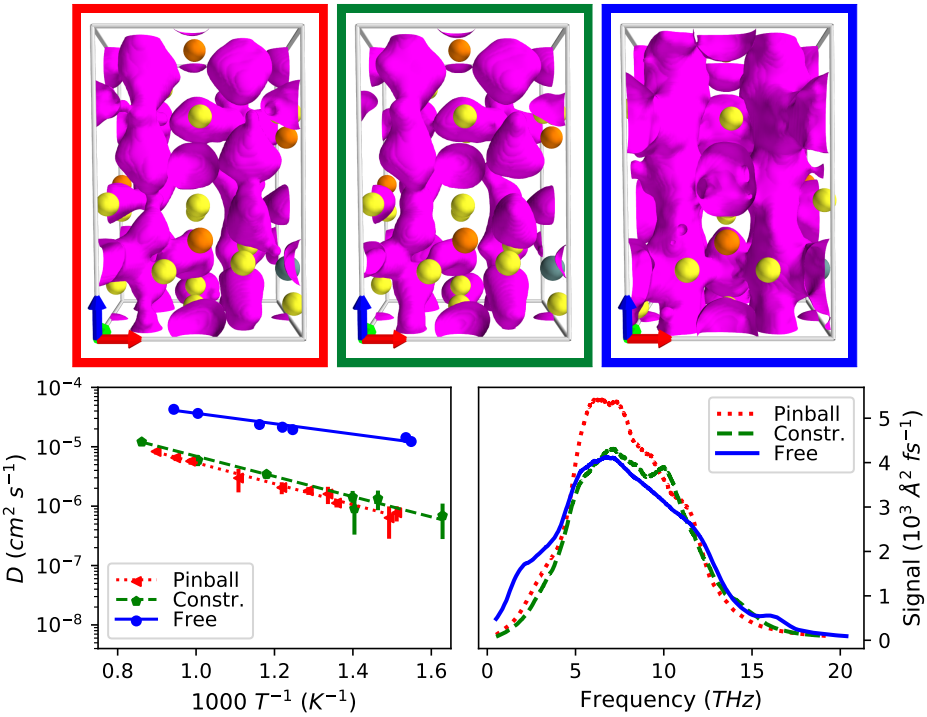

Fig. 2.4: Results for $Li_{20}Ge_2P_4S_{24}$: In the top row, the isosurfaces of the probability density of Li-ions for the same isovalue (0.01 $Å^{-3}$) are displayed: on the left for the pinball model, in the center for the constrained setup and on the right for the free simulations. Ge, P and S are represented as green, orange and yellow spheres, respectively, at their equilibrium position. In the bottom left panel, the tracer diffusion coefficients are represented as a function of inverse temperature for the pinball, constrained and free setup with red dotted, blue dashed and green solid lines, respectively. Error bars indicate the 2σ-standard error of the mean. On the bottom right panel we report the vibrational density of states of the Li-ions, with the same color coding.

channels. The same channels form in the constrained case, shown in the upper center panel, evidence that the topology of the carrier density is not affected by freezing the host lattice. The ionic densities derived from the pinball, shown in the upper left panel, display very small differences when compared with the constrained setup, proving that the potential energy surfaces sampled in the two cases are very similar. The bottom left panel displays the tracer diffusion coefficients calculated in the different setups and temperatures. Lithium is more diffusive in the free setup than in the constrained one by about an order of magnitude in the temperature range studied, leading to an activation barrier of 0.33 eV in the constrained setup against 0.17 eV in the free setup. Instead, the diffusion coefficients calculated in the pinball model agree well with the constrained simulations, with an activation barrier to diffusion of 0.35 eV. In the bottom right panel we present the vibrational density of states for the Li-ions. Apart from the $\omega \to 0$ limit, proportional to the diffusion coefficient, the spectra show very good agreement, which becomes almost perfect when comparing the constrained and pinball setups. In summary, the pinball reproduces accurately dynamical and static properties

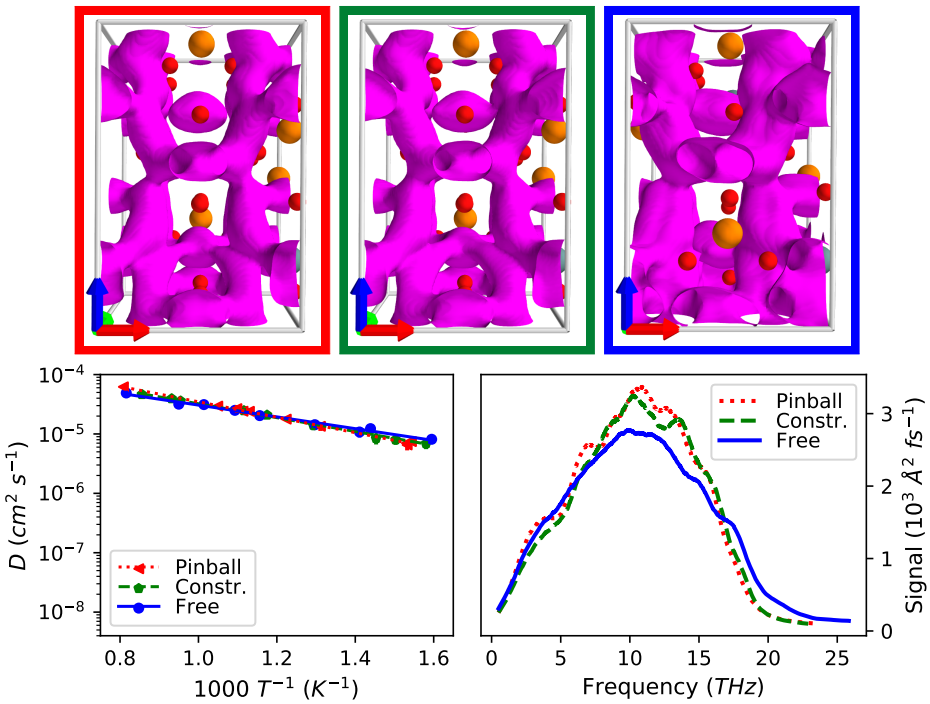

Fig. 2.5: Results for $Li_{20}Ge_2P_4O_{24}$, as in Fig. 2.4, with an isovalue of 0.01 $Å^{-3}$ for the Li-ion probability density; Ge, P and O are represented as green, orange and red spheres, respectively, at their equilibrium position.

of the constrained setup in LGPS. Freezing the charge density and switching to the pinball framework has a smaller effect on the resulting dynamics than constraining the movement of the host lattice. We observed the same behavior for all sulfur and selenium derivatives.

$Li_{20}Ge_2P_4O_{24}$ was obtained by Ong *et al.* [204] by replacing sulfur in $Li_{20}Ge_2P_4S_{24}$ with oxygen and relaxing the resulting cell. We include this structure in the analysis due to the interesting differences with respect to LGPS. Here, the isosurfaces in Fig. 2.5 agree very well between the three different setups at each respective isovalue, as do the diffusion coefficients and the vibrational density of states, without the differences between free and constrained setups observed in LGPS.

As discussed by Bachman *et al.* [196], there is an understanding that the conductivity of a material can be enhanced by either softer vibrational modes or a higher polarizability of the host lattice that lithium is moving through. The results on LGPS/LGPO suggest that the effect of freezing the host lattice has a significant effect for the sulfur containing compounds of the LGPS family, but not for their oxygen counterparts.

The LGPS-derivatives studied by Ong *et al.* [204] display small variations in the composition and volume, and the effect of these is discussed in the reference. In order to estimate whether the pinball model correctly accounts for these variations, we plot the diffusion coefficients we obtained in this family in Fig. 2.6. The diffusion coefficients obtained in constrained setup span three orders of magnitude, and pinball simulations are able to reproduce the diffusion coefficients with remarkable

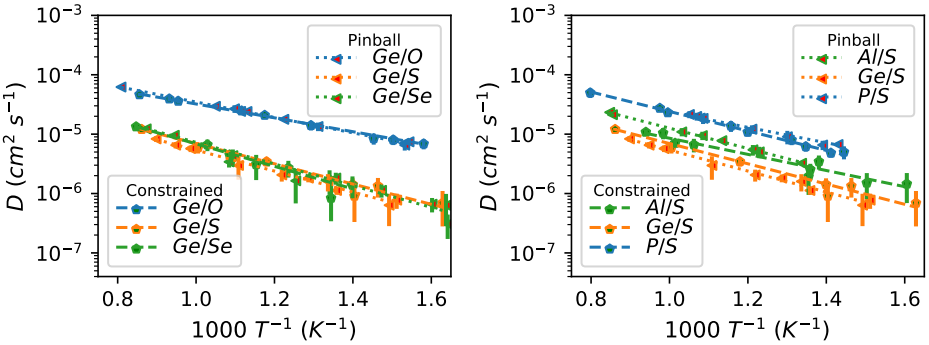

Fig. 2.6: Arrhenius behavior of the tracer diffusion coefficient for the constrained and the pinball setup (dashed and dotted lines of the same color). On the left for $Li_{20}Ge_2P_4S_{24}$ and anionic substitutions with O and Se, on the right for $Li_{20}Ge_2P_4S_{24}$ and aliovalent cationic substitutions.

accuracy both for aliovalent and anionic substitutions, indicating that the model can account for subtle variations in lithium-ion density and anionic effects. Display of the Si and Sn-substitutions of Ge was omitted since no effect on the diffusion was found, regardless of the setup studied.

$Li_{26}P_6Si_2O_{32}$. This LISICON compound was reported as a three-dimensional conductor by Deng *et al.* [218], possessing the highest conductivities in the $Li_4SiO_4 - Li_3PO_4$ system. Our FPMD results confirm that this material has a high conductivity and forms a 3-dimensional diffusion network highlighted by the isosurfaces of the lithium probability density in the left panel of Fig. 2.7. The pinball, constrained, and free setups produce a very similar distribution of the lithium ions, as apparent from the shape of the isosurfaces. The diffusion coefficients are in good agreement, although the pinball model produced marginally higher values. Finally, the vibrational density of state in the pinball and constrained setups agree very closely: a small discrepancy is observed between the free and the constrained setup, where some modes are softened. Overall, similar to the case study of $Li_{20}Ge_2P_4O_{24}$, all setups are in very good agreement between each other.

$Li_{54}N_{18}$. This compound forms a layered structure of Li_2N^-, with Li^+ intercalated between the layers, resulting in 2-dimensional transport along mentioned layers [235–237]. The principal reason for inclusion of $Li_{54}N_{18}$ (a $3 \times 3 \times 2$ supercell of Li_3N) in this set is the high ratio of Li to the respective anion N: 75% of the constituents of this system are abstracted away in the pinball model. In fact, in Fig. 2.8 discrepancies appear between the constrained and free setups in the ionic densities, diffusion coefficients, and vibrational densities of states, highlighting how motion of the lithium ions in this system is assisted by vibrations of the host lattice. Nevertheless, the ionic densities in the constrained and pinball setup are in good agreement. Diffusion in the pinball model is underestimated when comparing with the constrained simulations, but the slopes of the logarithm of the diffusion with respect to inverse temperature are compatible. In summary, the pinball approximation reproduces reasonably well the constrained case, despite the fact that the charge density is obtained in the presence of just 25% of the atomic constituents. The pinball model is not able to reproduce the free

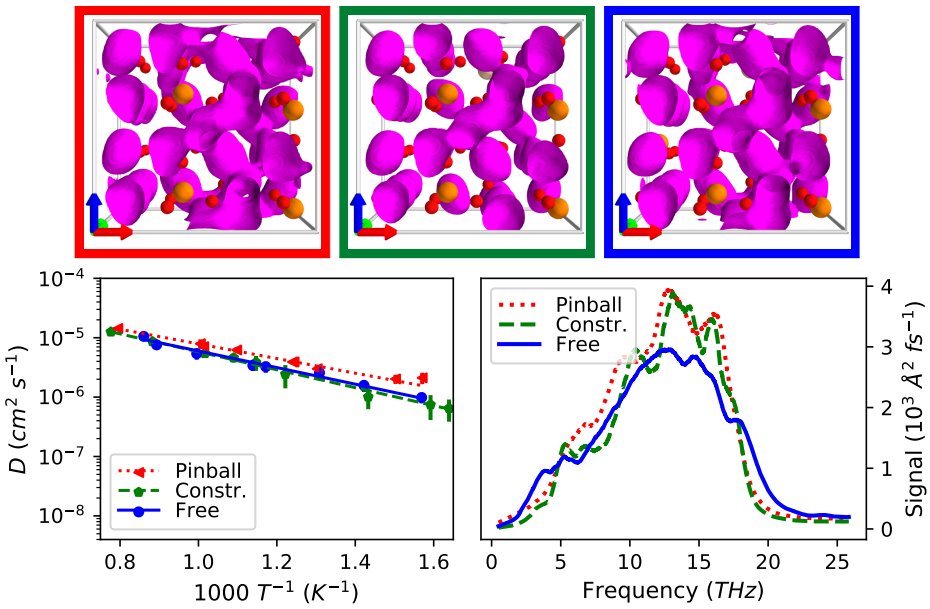

Fig. 2.7: Results for $Li_{26}P_6Si_2O_{32}$, as in Fig. 2.4, with an isovalue of 0.001 Å^{-3}. Host lattice ions (P, Si, O) are shown at equilibrium as orange, yellow and red spheres, respectively.

setup due to the constraint of frozen anions, and not the constraint on the charge density.

$Li_{24}Nb_8O_{32}$. This structure was refined by Grenier and Bassi [240] and also by Ukei et al. [241] with a different space group but similar positions. McLaren et al. [238] reported the structure as a poor conductor, with the conductivity sharply increasing after doping with Ni, due to the creation of vacancies. Our FPMD simulations of $Li_{24}Nb_8O_{32}$ confirm that the structure is not conducting,

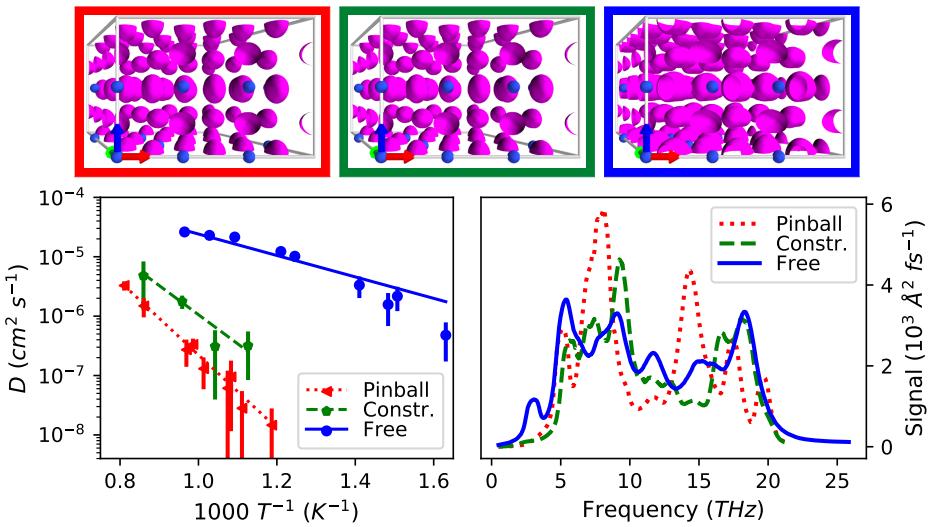

Fig. 2.8: Results for $Li_{54}N_{18}$, as in Fig. 2.4. The isovalue for the Li-ion probability density is 0.05 Å^{-3}, the host structure, consisting of nitrogen, is shown as blue spheres.

as there is no diffusion of the lithium ions over the observed time of roughly 200 ps, for all the simulations performed. The Li-ion densities, shown in Fig. 2.9, agree perfectly between the pinball model, free and constrained setups and suggest that the undoped compound is saturated in lithium, inhibiting vacancy-mediated ionic transport. The vibrational density of states of the constrained setup and the pinball model are very similar, proving that the pinball model correctly captures the much more structured vibrational modes in this system. As in previous materials, the distinct peaks of the vibrational spectrum in the constrained case are washed out when allowing the host lattice to move.

Instead of the Arrhenius behavior, which cannot be resolved due to the non-conducting nature of this material, the bottom left panel shows the estimated tracer diffusion coefficient of $Li_{24-x}Nb_8O_{32}$ in the pinball model as a function of concentration. The concentration of the pinballs can be changed without updating the charge density or the pinball parameters α_1, α_2, β_1 and β_2, if we assume that the only effect of the dopant atoms is to produce Li-ion vacancies to keep charge neutrality and that they do not affect the valence electronic charge density or the screening. We vary the lithium concentration by removing lithium from the original structure, and calculate the diffusion coefficient of that partially delithiated structure at 1000 K. As shown in the bottom left panel of Fig. 2.9, the diffusivity increases sharply after the removal of lithium. The same behavior is reported in McLaren's

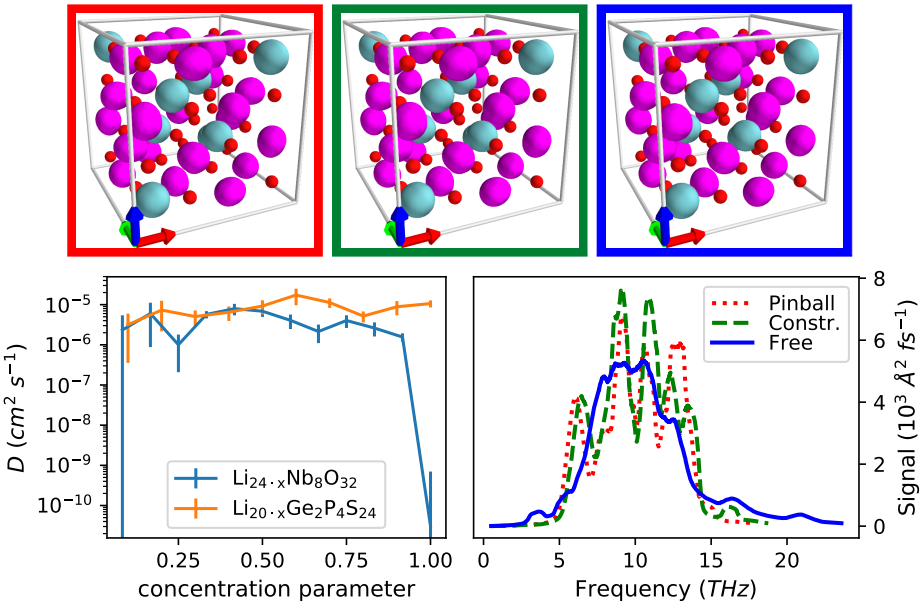

Fig. 2.9: Results for $Li_{24}Nb_8O_{32}$: as in Fig. 2.4, we plot in the top row the isosurfaces (at 0.05 $Å^{-3}$) of the lithium-ion density for the pinball, constrained and free simulations, with the host structure of Nb and O illustrated as turquoise and red spheres, respectively, and the vibrational density of states in the bottom right panel. In the bottom left panel we show the diffusion coefficient for $Li_{24-x}Nb_8O_{32}$ and $Li_{20-x}Ge_2P_4S_{24}$, calculated in the pinball model at $1000K$, against the concentration parameter x ranging from 0 (corresponding to no lithium) to 1 (fully lithiated structure).

experimental study [238], where doping with Ni^{2+} sharply increases the ionic conductivity of this structure. Out of interest we repeated this exercise for LGPS, shown in orange, finding good diffusion at all concentrations. The case of $Li_{24}Nb_8O_{32}$ proves that the pinball model can correctly account for the effect of variations in the concentration and compares qualitatively with experimental findings. We expect the calculated diffusion coefficient in the niobate to be an overestimate with respect to the experiments since the simulations do not capture the trapping and channel blocking effect of the dopant, but the qualitative agreement suggests that the pinball model can be used to study efficiently also the effects of concentration changes.

Interpretation The reported results can suggest general trends. For the three oxides studied in this work, the error made by the approximations of the model for the properties studied are quite minor. While cancellations of errors cannot be excluded, they are unlikely, since we compared different structures and different properties. We conclude therefore that lithium-ion dynamics within a rigid solid-state structure of high ionic character are likely to be treated very accurately by the pinball model. As one moves to less ionic systems, for example by replacing oxygen with sulfur, or moving to nitride systems, errors are introduced, as can be seen from a smaller r^2-value in the force comparison and a less accurate reproduction of the vibrational density of states and diffusion coefficients when comparing the pinball with the constrained setup. However, this error is small compared to the error made by freezing the host lattice. Already in LGPS, there is clear evidence for dynamic correlations between the anionic framework with the lithium ions. An estimate of the ionic diffusion in the pinball model for structures that exhibit a close coupling between long-range diffusional modes and rotational modes of the host lattice, such as shown for *closo*-borates [242], is unlikely to work with the pinball model. The same can be concluded for the treatment of liquid systems, where the model can capture neither the correlations between anion and cation diffusion, nor the configurational degrees of freedom that can lead to enhanced diffusion. Based on these considerations, we speculate that the frozen host approximation most often leads to an underestimate of transport coefficients, since more degrees of freedom give the system access to lower barriers, and because host-pinball dynamical correlations are neglected. This variational behavior of the pinball model is compatible with its use as a screening criterion, where the estimate of the diffusion in the model can be seen as a lower bound for the actual diffusivity.

2.5 Conclusions

We proposed a “pinball” model to simulate efficiently the dynamics of lithium ions at frozen host lattice and reported excellent agreement between this model and the corresponding constrained FPMD simulations with regards to the topology of the carrier density, characteristic vibrational frequencies and diffusion coefficients. The qualitative behavior of the diffusion, as compared to fully unconstrained simulations, is always reproduced, and non-diffusive materials can clearly be distinguished from diffusive ones; this makes the model suitable for screening applications. An ongoing line of research is the extension of the model to allow for vibrations of the host lattice,

based on linear-response theory, leading to an even more faithful reproduction of the lithium-ion dynamics.

In addition, we show that the vibrations of the host lattice are an important contribution to the diffusion coefficients of sulfide/nitride/selenide compounds, since constraining the host lattice leads to a decrease of conductivity by an order of magnitude in the temperature range studied for LGPS and sulfur/selenium derivatives, and several orders of magnitude for Li_3N. For the three oxides studied, we observe no significant effect from freezing the host lattice on the static or dynamical properties of lithium. This observation suggests that the enhancement of lithium diffusivity in sulfides with respect to oxides is primarily due to different vibrational properties, especially the softer vibrational modes of the former, although this aspect could be investigated further. Last, it is very unlikely that superionic conductivity in the compounds studied originates from complex bond rearrangements during the transitions, since the pinball model cannot, by construction, account for fluctuations in the charge density, but is nevertheless able to predict accurately the dynamical behavior of lithium ions in the frozen-lattice setup.

Acknowledgements

This research was supported by the Swiss National Science Foundation, through project 200021-159198 and the NCCR MARVEL. We acknowledge computational support from the Swiss National Supercomputing Centre (CSCS).

2.6 Method details

2.6.1 Fitting procedure

The parameters α_1, α_2, β_1 and β_2 in the pinball Hamiltonian Eq. (2.4) are determined by matching the forces for a training set of configurations between the pinball Hamiltonian and fully self-consistent calculations (Table 2.1). This is done by finding the parameters that minimize the error in a training

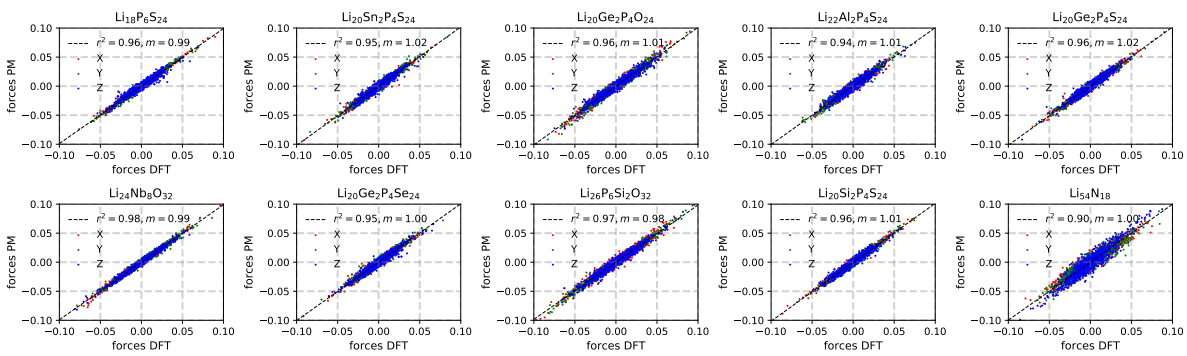

Fig. 2.10: As in Fig. 2.3, we show forces in Rydberg atomic units in the pinball model on the y-axis against the forces calculated with KS-DFT on the x-axis, where the screening parameters have been determined using the smaller set discussed in Sec. 2.6.1. Quality of the fits remains excellent.

set of size M:

$$S(\alpha_{1,2},\beta_{1,2}) = \sum_k^M \sum_p^P \Bigg\| F_{k,p}^{DFT} - \Bigg[-\frac{d}{d\boldsymbol{R}_{k,p}} \left(\alpha_1 E_N^{P-P} + \alpha_2 E_N^{H-P}\right) - \beta_1 \int n_{R_{H_0}}(\boldsymbol{r}) \frac{d}{d\boldsymbol{R}_{k,p}} V_{LOC}^P(\boldsymbol{r}) d\boldsymbol{r} - \beta_2 \sum_i \langle \psi_{i,R_{H_0}} | \frac{d\hat{V}_{NL}^P}{d\boldsymbol{R}_{k,p}} | \psi_{i,R_{H_0}} \rangle \Bigg] \Bigg\|^2$$

in a single shot using least-square regression. The training set used in this work is a subset of the configurations from the constrained dynamics, selected every 10 ps from our simulations. We found no dependence of the converged parameters on the mean kinetic energy (i.e. temperature), which enables us to use a large training set of configurations from all the simulations between 600 K and 1200 K.

The primary reason to chose a large training set was to neglect any error coming from unconverged parameters, rather than a need from the model itself. For resource critical-applications it is not needed to run long dynamics to obtain uncorrelated snapshots to be used for fitting. We investigated a faster fitting procedure: Starting from the relaxed positions, we randomly displace the lithium-ions and create training configurations. We observe the parameters of the model to be well converged when obtained from 100 random configurations of the respective supercells with the pinball's displacements from equilibrium taken from a Gaussian distribution centered at 0 and with a standard deviation of 0.1 Å. The forces we obtain for the validation set using this protocol are compared with DFT-forces in Fig. 2.10, also showing very good agreement indicating that the this fitting procedure is equally good. We also note that in resource-critical applications, the non-local projectors can be omitted, but the error made with this additional approximation needs to be assessed for each system.

Structure	β_1	β_2	α_1	α_2
$Li_{20}Ge_2P_4O_{24}$	1.08481	2.18597	1.09664	0.52106
$Li_{20}Ge_2P_4S_{24}$	0.88117	1.50166	0.88354	0.32560
$Li_{20}Ge_2P_4Se_{24}$	0.85610	1.40126	0.85348	0.27956
$Li_{20}Sn_2P_4S_{24}$	0.95740	1.80620	0.96590	0.31865
$Li_{20}Si_2P_4S_{24}$	0.88896	1.55215	0.89317	0.33272
$Li_{18}P_6S_{24}$	0.90096	1.56215	0.90261	0.29648
$Li_{22}Al_2P_4S_{24}$	0.91360	1.62639	0.91756	0.34469
$Li_{24}Nb_8O_{32}$	1.14716	2.36787	1.16180	0.44543
$Li_{26}P_6Si_2O_{32}$	0.95224	1.76575	0.95931	0.52586
$Li_{54}N_{18}$	0.55120	0.31873	0.43687	0.58825

Table 2.1: Pinball parameters (used in this work).

2.6.2 Molecular dynamics simulations

The structure of $Li_{10}GeP_2S_{12}$ (LGPS) and its derivatives are taken from the Supplementary Information of Ong *et al.* [204]. The structure of $Li_{3.75}Si_{0.75}P_{0.25}O_4$, as studied by Deng *et al.* [218], comes from the corresponding ICSD entry 238600. The structure of Li_3N is taken from COD entry 4311893

and that of Li_3NbO_4 is taken from the Materials Project [243], entry 31488. Supercells are created by replicating the corresponding unit cells to ensure a minimum image distance of at least 6.4 Å. A subsequent relaxation of the host lattice geometry is performed in the absence of lithium ions. The cell is not allowed to relax, so that the lattice vectors are still compatible with the reference structures.

Every system is thermalized at temperatures ranging from 600 K to 1200 K, a standard choice in FPMD simulations of solid-state ionic conductors. Thermalization is performed using a velocity rescaling thermostat [244] for 20 ps, after that it is switched off to recover microcanonical dynamics and to rule out any possible influence of the thermostat on the system dynamics. Microcanonical simulation times vary according to the computational cost of each model. In the case of the "free" and "constrained" first-principles simulations, 400–500 ps simulations are performed with a timestep of 1.93 fs. Half that timestep is used for the pinball model with simulation times of 750 ps. We calculate the mean square displacements as a time average over all configurations in the microcanonical trajectories. The diffusion coefficient is calculated from a linear fit of the mean square displacement between 2 and 4 ps. The error on the diffusion coefficient is estimated with a block analysis, where each trajectory is split into 8 independent blocks, each of at least 50 ps. The activation energies are estimated from a linear fit on the Arrhenius plot (logarithm of the diffusion coefficient versus inverse temperature).

The exchange-correlation used in the DFT-calculations is PBE [135]; pseudopotentials are those of the Standard Solid-state Pseudopotential (SSSP) library version 0.7 for efficiency, with the recommended cutoffs [245], with the exception of lithium for all pinball model simulations, which required the construction of a custom pseudopotential using the atomic module of the Quantum ESPRESSO package. This pseudopotential includes the 1s states in the core, and pseudizes the wave functions for the 2s and 2p states with a cutoff radius of 2.45 a.u. for both. Non-linear core corrections have not been included.

2.6.3 CPU-timings

To apply pinball model in a screening scenario, the computational cost of simulating time evolution via molecular dynamics is of paramount importance. In Table 2.2 we report the average CPU time per node for a single ionic step in the pinball model and compare this to BOMD for all calculations that have been used in this work. The speedup of the pinball model is at least 2 orders of magnitude for every structure studied. All calculations are run on an Intel Xeon cluster, on one or two nodes each, equipped with two Ivy Bridge processors with eight cores each. The computational efficiency is mostly due to avoiding a call to the routines for the self-consistent minimization. Further improvements stem from avoiding the recalculation of structure factors for non-diffusive species, and the recalculation of the reciprocal-space charge density before evaluating the forces and total energy.

Whereas the calculation of the forces is parallelized with MPI, the propagation of ions is still done in serial. Together with other possible optimizations, the efficiency of the pinball model can most likely be further improved, and Table 2.2 should be seen as a lower bound for the speedup of the model. Regarding scaling, the pinball model scales linearly with the number of local and quadratically with the number of non-local projectors, and linearly with the grid size for the charge density and wave functions. Therefore, a worst-case cubic scaling with system size at constant grid point density and Li-stochiometry is found with non-local projectors, and quadratic scaling if only local projections are included.

Structure	$t_{CPU}^{BO}(s)$	$t_{CPU}^{PM}(s)$	$t_{CPU}^{BO}/t_{CPU}^{PM}$
$Li_{20}Ge_2P_4O_{24}$	$2.31 \cdot 10^1$	$7.59 \cdot 10^{-2}$	$3.05 \cdot 10^2$
$Li_{20}Ge_2P_4S_{24}$	$3.18 \cdot 10^1$	$1.07 \cdot 10^{-1}$	$2.97 \cdot 10^2$
$Li_{20}Ge_2P_4Se_{24}$	$3.26 \cdot 10^1$	$1.30 \cdot 10^{-1}$	$2.50 \cdot 10^2$
$Li_{20}Sn_2P_4S_{24}$	$2.17 \cdot 10^1$	$9.72 \cdot 10^{-2}$	$2.23 \cdot 10^2$
$Li_{20}Si_2P_4S_{24}$	$1.76 \cdot 10^1$	$7.74 \cdot 10^{-2}$	$2.28 \cdot 10^2$
$Li_{18}P_6S_{24}$	$1.49 \cdot 10^1$	$7.20 \cdot 10^{-2}$	$2.07 \cdot 10^2$
$Li_{22}Al_2P_4S_{24}$	$2.65 \cdot 10^1$	$8.43 \cdot 10^{-2}$	$3.14 \cdot 10^2$
$Li_{24}Nb_8O_{32}$	$3.07 \cdot 10^1$	$1.18 \cdot 10^{-1}$	$2.59 \cdot 10^2$
$Li_{26}P_6Si_2O_{32}$	$1.86 \cdot 10^1$	$1.19 \cdot 10^{-1}$	$1.56 \cdot 10^2$
$Li_{54}N_{18}$	$3.21 \cdot 10^1$	$2.85 \cdot 10^{-1}$	$1.13 \cdot 10^2$

Table 2.2: CPU time t per ionic step is given for Born-Oppenheimer MD and for the pinball model dynamics in columns 2 and 3, respectively, for each structure. The last column shows the ratio of the timings and represents the computational speedup of the pinball model with respect to DFT-based BOMD. The timings are normalized by the number of nodes used in the respective calculation, assuming linear scaling.

3 Unsupervised landmark analysis

If you want to build a ship,
don't drum up the men to gather wood,
divide the work, and give orders.
Instead, teach them to yearn for the
vast and endless sea.

Antoine de Saint-Exupéry

The previous Chap. 2 described the pinball model, which can be used to run molecular dynamics for Li-ionic systems in a computationally substantially more efficent manner, compared to first-principles molecular dynamics. The next Chap. 4 will illustrate our efforts to run molecular dynamics simulations in an automated high-throughput fashion, relying on the AiiDA platform and computational workflows to ensure automation. The pinball model and the automation efforts have facilitated the production of large amounts of data in the form of trajectories, calling also for an automated and efficient analysis in order to obtain scientific results. For some quantities, such as the estimate of the diffusion coefficient in a structure, the analysis can be automated reasonably well. However, to understand the microscopic origin of diffusion, it is necessary to detect significant events, such as diffusive jumps. No published framework we looked at could be easily automated and was accurate enough for the analysis of molecular dynamics trajectories for such events.

The following article introduces a method to analyze molecular dynamics trajectories to detect jumps of diffusing particles within a stable host lattice, as for example Li ions diffusing in the cubic garnet $Li_7La_3Zr_2O_{12}$, depicted in Fig. 3.1. In order to reduce noise due to thermal motion, we transform the atomic positions into a new vector space, where we perform the operations measuring similarity between environments. We use unsupervised clustering to detect the significant states in a Li-ion trajectory, and no prior information about the system is required, making the framework an efficient tool for analyzing the dynamics of ill-characterized systems.

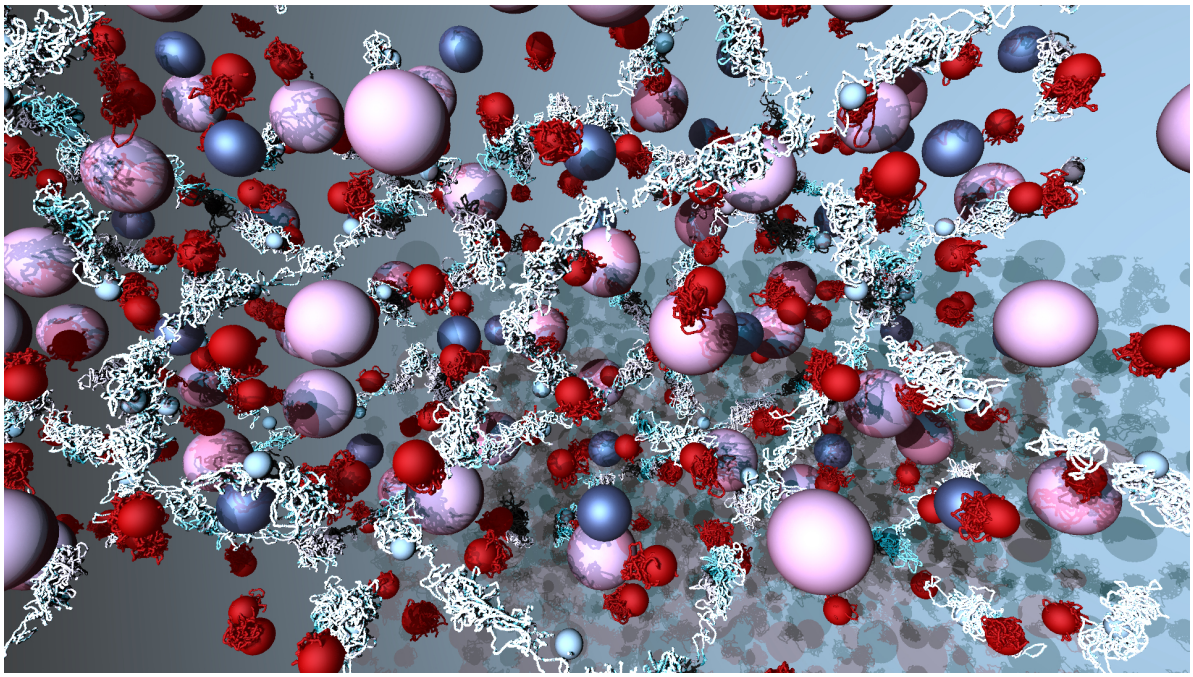

Fig. 3.1: A snapshot from a molecular-dynamics simulation of $Li_7La_3Zr_2O_{12}$, with Li shown in white, oxygen in red, zirconium in blue, and lanthanum in violet. Previous positions of lithium and oxygen ions are shown as dots, highlighting the differences between the two species: while lithium is diffusing, oxygen ions remain close to their equilibrium positions.

I conceptualized this work with Boris Kozinksy, and Albert Musaelian is credited with the implementation of the underlying code. The analysis of LLZO, LGPS and LASO was done by me, and the analysis of the seven non-diffusive structures by Albert Musaelian. I ran all simulations in this work, except for LGPS. All authors contributed to the discussion and revision of the following post-print.

Authors	Leonid Kahle, Albert Musaelian, Nicola Marzari, Boris Kozinsky
Title	Unsupervised landmark analysis for jump detection in molecular dynamics simulations
Journal reference	*Physical Review Materials* **3**, 055404, 2019
DOI	10.1103/PhysRevMaterials.3.055404
arXiv	1902.02107

Unsupervised landmark analysis for jump detection in molecular dynamics simulations

Leonid Kahle,[a,*] Albert Musaelian,[a,*] Nicola Marzari,[a] and Boris Kozinsky[b]

Abstract: Molecular dynamics is a versatile and powerful method to study diffusion in solid-state ionic conductors, requiring minimal prior knowledge of equilibrium or transition states of the system's free energy surface. However, the analysis of trajectories for relevant but rare events, such as a jump of the diffusing mobile ion, is still rather cumbersome, requiring prior knowledge of the diffusive process in order to get meaningful results. In this work, we present a novel approach to detect the relevant events in a diffusive system without assuming prior information regarding the underlying process. We start from a projection of the atomic coordinates into a landmark basis to identify the dominant features in a mobile ion's environment. Subsequent clustering in landmark space enables a discretization of any trajectory into a sequence of distinct states. As a final step, the use of the smooth overlap of atomic positions descriptor allows distinguishing between different environments in a straightforward way. We apply this algorithm to ten Li-ionic systems and perform in-depth analyses of cubic $Li_7La_3Zr_2O_{12}$, tetragonal $Li_{10}GeP_2S_{12}$, and the β-eucryptite $LiAlSiO_4$. We compare our results to existing methods, underscoring strong points, weaknesses, and insights into the diffusive behavior of the ionic conduction in the materials investigated.

3.1 Introduction

Lithium-ion batteries power an increasingly broad and critical set of technologies [16]. Commercially available batteries use organic electrolytes that impose constraints on their safety, power and energy density [78] and can introduce chemical instabilities that require the incorporation of fuses and safety vents [73]. Solid-state electrolytes are widely considered to be a promising alternative for next-generation batteries: many structural families of candidate solid-state ionic conductors have been identified and are under investigation [196]. While a good solid-state electrolyte must meet several criteria, such as low electronic mobility, easy device integration, and electrochemical and mechanical stability [198], it must first be a fast Li-ion conductor, and consequently optimization of conductivity and analysis of the mechanisms of Li-ion diffusion has been the focus of a large body of literature [196].

Atomistic modeling techniques, and in particular molecular dynamics (MD), have been used to study a wide variety of candidates for solid-state electrolytes and the factors that influence their

[a] Theory and Simulation of Materials (THEOS), and National Centre for Computational Design and Discovery of Novel Materials (MARVEL), École Polytechnique Fédérale de Lausanne, CH-1015 Lausanne, Switzerland
[a] John A. Paulson School of Engineering and Applied Sciences, Harvard University, Cambridge, Massachusetts 02138, USA
* These two authors contributed equally to this work.

ionic conductivity. Classical/empirical force fields were chosen in several studies [212–218, 246] due to their computational efficiency and access to the time and length scales required to characterize ionic transport. Accurate, yet expensive, first-principles simulations have also been employed for selected systems [51, 162, 204–211, 247]. The necessary compromise between the transferability of first-principles potential energy surfaces and the computational efficiency of force fields has also motivated the development of novel hybrid quantum/classical approaches [248] to model diffusion. The estimate of transport coefficients from the Green-Kubo or Einstein relations using molecular dynamics can be done in a straightforward yet expensive way, though improved methods for obtaining accurate estimates from short trajectories are being developed [249]. In addition to computing ionic conductivity, design and characterization of new materials requires detailed understanding of the atomistic mechanisms of ionic transport. The central challenge is to develop automated methods for accurately analyzing the structure and dynamics of lithium's local atomic environments and for detecting rare transitions and subtle correlations in large amounts of data.

In many solid-state Li-ion conductors, Li ions form a mobile, often disordered, sublattice within a non–diffusive sublattice of the other species, which we refer to as the host lattice hereafter. In the jump-diffusion model, the mobile ions spend the majority of their time in the local minima of the potential energy surface and vibrate within such sites for a sufficiently long time to lose memory of their previous locations while intermittently acquiring sufficient kinetic energy to overcome the barrier separating them from a different potential well. This formulation of Li-ion diffusion as occupation of and exchange between well-defined crystallographic sites can be used to model diffusion as a Markov-chain model using kinetic Monte Carlo [105]. Also, using this discrete formulation to understand the microscopic origin of diffusion is a common theme in the literature, and site analysis tools have been used to explore the effects of site volume [208, 242] and anion sublattice structure [208] on ionic conductivity, to identify conduction pathways and rate-limiting steps [214, 250], and correlated diffusion events [251], and to design new descriptors for conductiv-

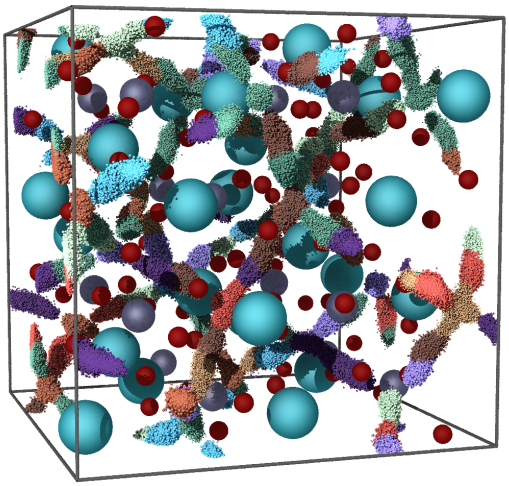

Fig. 3.2: The site analysis is exemplified above for $Li_7La_3Zr_2O_{12}$, based on the results discussed in Sec. 3.3.1. The equilibrium positions of lanthanum are shown as large blue spheres, those of zirconium as grey spheres, and those of oxygen as red spheres. The positions of lithium during the trajectory are collapsed into the same frame and shown as small spheres, with color and reflectivity being chosen according to the site associated with the ion in that frame.

ity [242]. Ideally, an automated site analysis (see Fig. 3.2) approach should: (1) automatically identify relevant Li sites, (2) accurately track migration of mobile ions through those sites, (3) require no prior knowledge of the material, and (4) work with the same parameters over a broad range of materials.

Existing approaches fall mostly into three classes: distance-based, topology-based, and density-based methods. Distance-based methods [242, 250, 252] use preexisting knowledge of the equilibrium positions of all Li-ion sites and consider a Li ion to be resident at a site when it comes within a given cutoff distance from the site's position. Cutoffs can be smooth [242] or discrete [250], but in both cases, they need to be tailored to the structure at hand and are uniform across all sites within it. The positions of sites can also be coupled to the instantaneous positions of nearby host-lattice atoms [242] to decrease sensitivity to thermal noise. Nevertheless, such methods rely on the crystallographic information they are given and also do not account for the varied or non-spherical geometry of sites [253]. Starting from a prior knowledge of the host structure and possible Li sites, mobile ions can also be automatically assigned to sites based on convex-hull analysis of site polyhedra [214, 254]. This topology-based method deals with arbitrary site geometries, eliminates thermal noise and does not require arbitrary distance cutoffs, but does require the site polyhedra to be specified. Density-based methods [251] identify regions of high Li-ion density separated by areas of low Li-ion density, as determined by a threshold, and define each high-density region as a site. These methods thus do not require prior knowledge about the material and can resolve sites with different geometries. In materials with nearby or rapidly exchanging sites, however, choosing a density threshold that can distinguish such sites from one another can be difficult. Richards *et al.* [255] used a k-means clustering of Na-ion positions in $Na_{10}GeP_2S_{12}$, initialized with known ionic positions for the similar ionic conductor $Li_{10}GeP_2S_{12}$, combining prior information with a density based method.

In order to overcome some of these challenges, this work introduces an algorithm for accurately and automatically analyzing molecular dynamics trajectories and detecting jumps of the mobile ion through the host lattice with minimal human supervision and no prior knowledge. This algorithm can be combined with the automatic detection of important structural motifs [256, 257], leading to a versatile tool for the unsupervised analysis of trajectories and detection of diffusion events. The algorithm will be discussed in Sec. 3.2; in Sec. 3.3 we apply it to three known ionic conductors and to seven non-diffusing materials and discuss the results; some details of the implementation are given in Sec. 3.4; and our final conclusions are presented in Sec. 3.5.

3.2 Algorithm

Landmarks are persistent local features in an environment and therefore can be used to describe positions in the absence of global information (i.e. real-space coordinates). Landmark-based navigation explains the homing of social insects [258] and has been applied in the field of autonomous navigation and artificial intelligence [259]. Landmark models employ a vector-based description of the environment via a landmark vector $\boldsymbol{l}$. Such a vector representation is useful for navigation if the distances between the landmark vectors corresponding to two states or positions A and B decrease

with reducing distances in real space: $|\boldsymbol{r}_A - \boldsymbol{r}_B| = f(|\boldsymbol{l}_A - \boldsymbol{l}_B|)$, where f is a monotonically increasing function of its input.

When analyzing trajectories, the real-space positions are obviously known beforehand. However, atomic coordinates are inefficient descriptors for most properties since they are not invariant under rigid translation or rotation of the structure. We will describe the positions of mobile ions through landmarks that encode all the information necessary to detect changes in the ions' environments and are invariant under these transformations.

First, we deduce that the descriptors should only encode local information since the local environment mostly defines the potential energy landscape for the mobile ion, a principle reminiscent of the nearsightedness of electronic matter [260]. In addition, we know from Pauling's rules in crystal structures [261] that ionic systems minimize their energy by packing into coordination numbers that are determined, among other factors, by the ratio of the radii of the cations and anions. Therefore, possible coordination polyhedra in the local environment are meaningful features. Checking all the possible polyhedra in a crystal is not feasible because of the combinatorial complexity this induces, so we need to restrict the description via a meaningful subset of convex hulls or polyhedra formed by the host lattice. A site description and trajectory discretization via pre-selected convex hulls has been previously developed and applied [214] to study Li-ion diffusion in garnets.

Using polyhedra defined by host-lattice atoms as landmarks relies on the assumption that these atoms fluctuate around equilibrium positions, such that well-defined coordination polyhedra persist throughout the simulation. Equivalently, the host lattice is not changing in a way that causes sites to appear or disappear. Due to this assumption, the present landmark analysis cannot be applied to systems with liquid-like host structure such as polymers, where inter-site hopping happens on a longer time scale than the host motion, and dynamic coordination tracking must be used [262]. It also cannot be applied to systems with a "paddle-wheel" diffusion mechanism, where the slow rotation of polyatomic anions creates a constantly changing set of local potential minima, such as shown for proton diffusion in $CsHSO_4$ [263] or lithium- and sodium-ionic diffusion in the closoborate structures [242]. Similar to the site analysis presented in the literature, our method does not assume that the occupation a given site are Markovian, i.e. whether a mobile ion completely loses memory of its past at any site: We define and find a site based on stable and persistent features in the environment of mobile ions, described by the landmark vectors, without considering information in the time domain. Whether the underlying process is Markovian can be determined by analyzing the resulting statistics [251, 264].

The basic algorithm has three steps: (1) definition of suitable landmarks, (2) expression of the coordinates of the mobile ions during their trajectory in the landmark basis, and (3) clustering of the landmark vectors to reveal sites and discretize the trajectory of each mobile atom. We also implemented, as an option, the possibility to: (4) merge nearby sites that have high exchange rates and that fulfill some distance criteria and (5) determine site types based on the geometry and chemistry of the local environment.

While the two last steps are optional and independent from each other, we always apply them in

the analysis that we show in Sec. 3.3. Step 4 reduces significantly the noise in the data, and step 5 supplies information on the local geometry and chemistry. In the following we explain each of the steps in greater detail and finish with a discussion on why certain design choices were taken.

3.2.1 Step 1: Define Landmarks

The landmark analysis we introduce here is based on the Voronoi tessellation of the equilibrium configuration of the host lattice and its geometric dual, the Delaunay triangulation. Given a set of points in space, termed seeds, a Voronoi tessellation divides space into regions such that all points in each region are closer to the region's seed than to any other seed [265]. Formally, the Voronoi region determined by the seed point $s_i \in \mathbb{R}^n$ is given by:

$$R_i = \{x \in \mathbb{R}^n : |\vec{x} - \vec{s}_i| \leq |\vec{x} - \vec{s}_j| \text{ for all } j \neq i\}$$

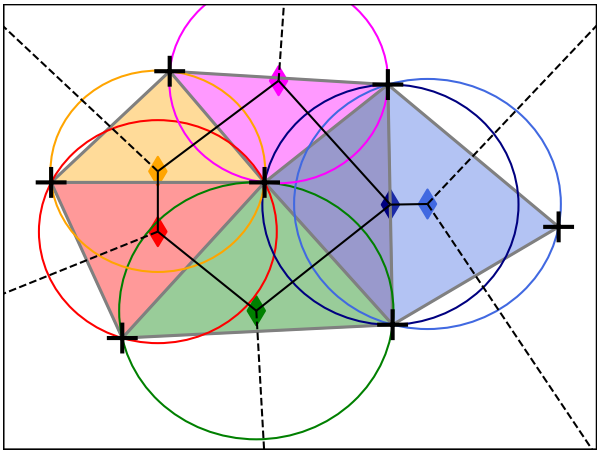

Fig. 3.3: Schematic of the Voronoi tessellation in two dimensions of seven seed points (black crosses). The resulting Voronoi facets are shown as black solid lines; dashed black lines are Voronoi facets that are not bounded by a Voronoi node. The Voronoi nodes are shown as coloured diamonds, and the associated Delaunay triangles formed by their seeds are filled with the same color. The circumcircles of each Delaunay triangle are shown in the same color, demonstrating that no seed point is inscribed in them and that the associated Voronoi node is at its center.

Voronoi regions connect at Voronoi facets, as shown in the schematic in Fig. 3.3. Any point on such a facet is equidistant to the seeds of the adjacent Voronoi regions. Voronoi nodes are, in a space of D dimensions, points where at least D facets intersect and therefore are equidistant to at least $D+1$ seed points. It follows that each Voronoi node locally maximizes the distance to its adjacent seed points. The geometric dual of the Voronoi tessellation is the Delaunay triangulation. Such a triangulation or simplicial * decomposition is obtained by connecting seed points that share a Voronoi facet. The Delaunay triangulation has the useful property that the circumcircles of all formed triangles have empty interiors, i.e. there are no seed points inside any circumcircle. It follows from the duality between the two tessellations that every Voronoi node is associated to exactly one Delaunay simplex. The Voronoi node lies at the center of the circumcircle of the associated Delaunay simplex. In the remainder of the text we will work in three dimensions unless otherwise specified; in three dimensions a Voronoi node is equidistant to at least four coordinating seeds.

* A simplex in $\mathbb{R}^D$ is the convex hull of $D+1$ points that do not lie on a hyperplane.

While a Voronoi node is a reasonable guess for a low-energy position since it maximizes the distance to its coordinating seeds, the associated Delaunay simplex corresponds to the coordinating polyhedron of the site or a subset thereof. A Voronoi node and its coordinating host-lattice atoms are together referred to as a landmark. The coordinating host-lattice atoms of a landmark are the host-lattice atoms that are vertices of the Delaunay simplex – dual to the Voronoi node – in the equilibrium configuration.

3.2.2 Step 2: Landmark Vectors

We start from a molecular dynamics trajectory that gives the real-space positions $\vec{r}_i(t) \in \mathbb{R}^3$ of each atom i at time $t = N\Delta t_s$, an integer multiple of the sampling timestep Δt_s. In the remainder, we will use the index h for host-lattice atoms and m for mobile ions. First, we calculate the time-averaged positions for host-lattice atoms $\bar{\vec{r}}_h = \langle \vec{r}_h \rangle_t$ and use these as seed points for a Voronoi decomposition, resulting in Voronoi nodes $\bar{\vec{r}}^{\mathrm{A}}_{\mathrm{VN}}$. The instantaneous position of a mobile particle, $\vec{r}_m(t)$, is expressed in terms of a proximity or similarity to each landmark in the system. That is to say, any real space position $\vec{r}_m$ can be transformed into a vector in the N-dimensional landmark space, where N is the number of landmarks in the system, equal to the number of Voronoi nodes and also equal to the number of Delaunay simplices, due to the duality discussed in Sec. 3.2.1. We index landmarks with capital latin characters. For a landmark A, we first define the normalized instantaneous distance between a mobile particle m and a host lattice atom h, where atom h is one of the coordinating seed atoms of the landmark A:

$$d^{\mathrm{A}}_{m,h}(t) = \frac{|\vec{r}_m(t) - \vec{r}_h(t)|}{\left|\bar{\vec{r}}^{\mathrm{A}}_{\mathrm{VN}} - \bar{\vec{r}}_h\right|}, \quad h \in \mathrm{A}, \tag{3.1}$$

where $\vec{r}_h(t)$ and $\vec{r}_m(t)$ are the instantaneous real-space positions of host-lattice atom h and mobile ion m, respectively, $\bar{\vec{r}}_h$ is the time-averaged position of host-lattice atom h, and $\bar{\vec{r}}^{\mathrm{A}}_{\mathrm{VN}}$ is the position of the landmark's Voronoi node. The corresponding component of the landmark vector is then computed as:

$$l^m_{\mathrm{A}} = \prod_h^{N_{\mathrm{coord}}} \left[f\left(d^{\mathrm{A}}_{m,h}\right)\right]^{\frac{1}{N_{\mathrm{coord}}}}, \tag{3.2}$$

where h ranges over the set of N_{coord} coordinating host-lattice atoms and $f(d)$ is a cutoff function that smoothly goes from 1 to 0. We base the cutoff function on the logistic function $\sigma(d; d_0, k)$, a sigmoid curve that goes from 0 to 1 around a midpoint d_0, with a steepness k:

$$\sigma(d; d_0, k) = \frac{1}{1 + e^{-k(d-d_0)}}. \tag{3.3}$$

To obtain a cutoff function suitable for Eq. (3.2), we subtract the logistic function from 1:

$$f(d; d_0, k) = 1 - \sigma(d; d_0, k) = \frac{1}{1 + e^{k(d-d_0)}}. \tag{3.4}$$

The function $f(d; d_0, k)$ varies smoothly from 1 to 0, reaching $\frac{1}{2}$ at the set midpoint d_0. How fast it varies is tuned by the hyperparameter k. As can be seen from Eq. (3.2), we normalize $f\left(d^{\mathrm{A}}_{m,h}\right)$ for a varying N_{coord}. In three dimensions and in the present framework, N_{coord} is always 4, since we use a simplicial decomposition to determine the landmarks. However, the framework could be changed to include a varying number of coordinating host-lattice atoms, motivating this normalization. The cutoff function in Eq. (3.4) was preferred due to its continuity and simplicity. Because distances are normalized to the equilibrium distance between the Voronoi node and the host atoms, the magnitude of each landmark vector component depends on neither the volume nor shape of the corresponding landmark's polyhedron. This allows landmark analysis to distinguish between sites whose coordination polyhedra have very different volumes, as well as accurately tracking mobile particles through highly distorted sites.

3.2.3 Step 3: Landmark Clustering

The magnitude of each component of the landmark vector indicates the extent to which a mobile atom's position is dominated by that landmark. If, for example, a mobile atom occupies a tetrahedral site, its landmark vector would have one large value at the corresponding landmark's component and some low-magnitude noise for neighboring landmarks. During a transition between sites, there are no dominant contributions, as shown schematically in two dimensions in Fig. 3.4.

If an atom occupies an octahedral site, however, the landmark vector will have four major contributions, corresponding to the four tetrahedrons resulting from the Delaunay triangulation of the octahedron. We show this schematically for two dimensions in Fig. 3.5.

Because we have chosen a smooth function of position for the landmark vector components, the landmark vectors are a continuous function of trajectory time. By definition, landmark vectors are invariant under rigid translations or rotations of the system and as such are ideally suited as descriptors for dominant recurring features. A clustering of the landmark vectors can be used to group similar landmark vectors and therefore discretize our trajectory in landmark space. We use density-based clusters of landmark vectors, where each cluster is described by a high-density region in landmark space, corresponding to a frequent feature in the local environment of the mobile ion. Therefore, we define sites as clusters in landmark space.

We use a custom hierarchical clustering algorithm (described in more detail in Sec. 3.6.1) with a simple cosine similarity metric:

$$S(\vec{l}_A, \vec{l}_B) = \frac{\vec{l}_A \cdot \vec{l}_B}{|\vec{l}_A||\vec{l}_B|}, \tag{3.5}$$

where $\vec{l}_{A/B}$ are landmark vectors. The clustering algorithm scales linearly with the number of

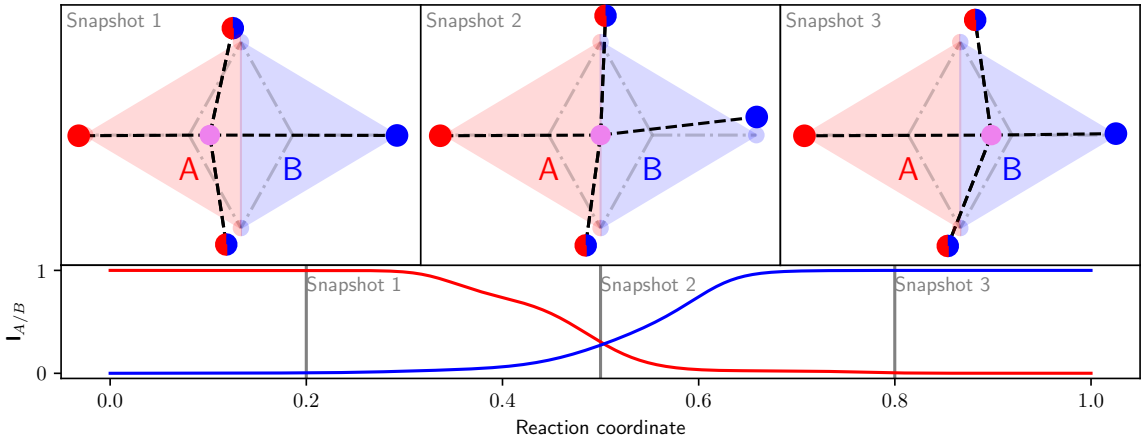

Fig. 3.4: Simplified schematic to illustrate our algorithm: A mobile ion (in violet) is jumping from site A to site B along a straight line. The reaction coordinate of the jump takes a value of 0 when the ion is at the Voronoi node of A and a value of 1 when it is at the Voronoi node of site B. The distance to the neighboring host atoms is marked with a dashed black line. The host-lattice atoms are shown at an instantaneous position (equation of motion of an harmonic oscillator, initialized randomly) and are colored red if they are part of landmark A, blue if part of landmark B, and half red, half blue if they belong to both. We show the Delaunay triangulation based on the equilibrium positions of the host lattice as semi-translucent red and blue triangles. The lower panel shows the landmark vector components of the mobile ion corresponding to A and B in red and blue respectively against the reaction coordinate. The vertical grey lines indicate the three snapshots shown in the top panel. We see that during the transition component A is decreasing while component B is increasing smoothly. At the transition point, the landmark components are approximately equal.

landmark vectors.

The clustering algorithm is run on the landmark vectors computed from the real-space positions of all mobile atoms every n frames, where n is sufficiently small and corresponds to a time span that is below the jump rate. A mobile atom is said to be occupying site i at time t if its corresponding landmark vector at that time is a member of the i-th landmark cluster. If the mobile atom's landmark vector is not a member of any cluster, the atom is said to be unassigned at that time. The time sequence of such site assignments for a given mobile atom is its discretized trajectory; every change of site in that discretized trajectory is defined as a jump event.

The center of each site is defined as the spatial average of all real-space positions of mobile ions assigned to it.

3.2.4 Step 4 (optional): Merge Sites

While one of the main strengths of the landmark analysis is its ability to distinguish between very close sites, that level of resolution often identifies multiple sites where only one should exist. This is mainly due to a lack of data for the clustering. This issue is particularly prominent in host lattices containing sites with greater than four-fold coordination whose coordination polyhedra are highly distorted from the corresponding regular polyhedra. To merge such split sites, a post-processing

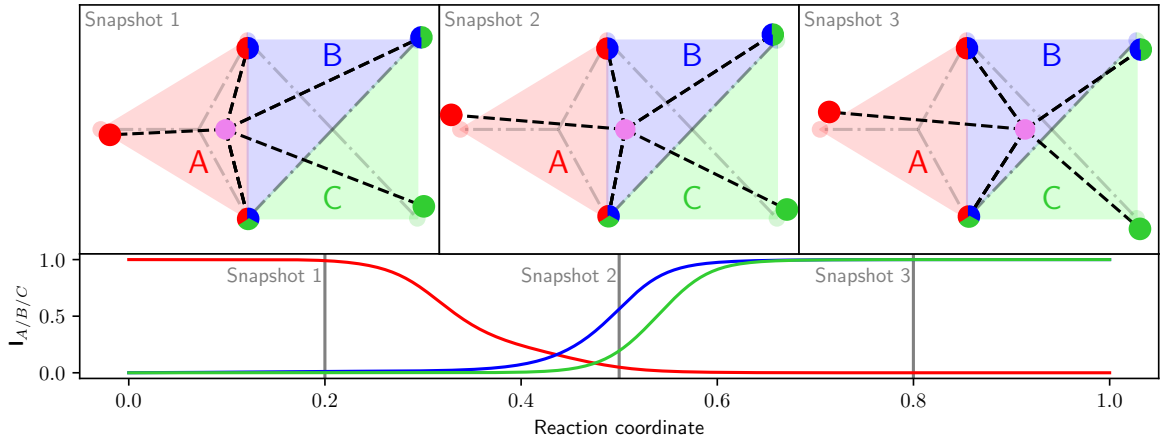

Fig. 3.5: Simplified schematic to illustrate our algorithm for a non-simplicial site, similar to Fig. 3.4. The example contains two sites, one comprising landmark A and the other landmarks B and C. A mobile ion (in violet) is jumping from site A to site B/C along a straight line. The reaction coordinate of the jump takes a value of 0 when the ion is at the Voronoi node of A and a value of 1 when it is at the Voronoi nodes of site B/C. The distance to the neighboring host-lattice atoms is marked with a dashed black line. The host-lattice atoms are shown at an instantaneous position (equation of motion of an harmonic oscillator, initialized randomly), and are colored red if they coordinate landmark A, blue if they coordinate landmark B, and green if they coordinate landmark C. We show the Delaunay triangulation based on the equilibrium positions of the host lattice as semi-translucent red, blue, and green triangles. The lower panel shows the landmark vector components of the mobile ion corresponding to A, B and C in red, blue, and green, respectively, against the reaction coordinate. The vertical grey lines indicate the three snapshots shown in the top panel. We see that during the transition, component A is decreasing, while B and C are increasing similarly. The presence of the mobile ion at site on the right is therefore indicated by high values for both the B and C landmark vector components.

clustering of the sites themselves can be applied, taking into account information from the time domain. We define M as the stochastic matrix observed from the exchanges of ions between sites:

$$[m_{AB}] = \begin{cases} 0 & \text{if } |\vec{r}_A - \vec{r}_B| > \text{cutoff} \\ p_{A\to B} & \text{otherwise} \end{cases}$$

where $\vec{r}_A$ is the center of site A and $p_{A\to B}$ is the probability that an ion occupies site B, conditional on the ion's having occupied site A in the previous frame (for $A \neq B$). For $A = B$ it is the probability that an ion remains at site A until the next frame. We apply Markov Clustering [266] to the weighted graph defined by the stochastic matrix M, resulting in clusters of highly-connected subgraphs. Sites belonging to the same subgraph are merged (additional details are given in Sec. 3.6.2).

3.2.5 Step 5 (optional): Site Type Analysis

Sites are commonly defined by their Wyckoff points, and symmetry-equivalent sites can be interpreted as one site type. Such analysis depends on preexisting crystallographic data and also neglects that the energetics of a site are defined by the local geometry and chemistry. In line with our goal of making unsupervised site analysis possible, we developed a method for determining the type of the sites identified by the steps described from Sec. 3.2.1 to Sec. 3.2.4. Different sites whose environments cannot be distinguished are said to be of the same site type.

We describe local atomic environments using the smooth overlap of atomic positions (SOAP) [124] as implemented in the QUIP molecular dynamics framework [267]. Briefly, a SOAP descriptor is a vector that describes the local geometry around a point in a rotation-, translation-, and permutation-invariant way. The descriptor changes smoothly with the Cartesian coordinates of the structure. For these reasons, SOAP descriptors have become a powerful tool to express local geometry for machine-learning applications [268] and the detection of structural motifs [256, 257].

Multiple SOAP vectors must be computed for each site to provide sufficient data density for subsequent clustering. Computing these vectors for a site requires some procedure for sampling the real-space positions of both the site and its surrounding host-lattice atoms. We implemented two sampling schemes:

(1) Real-space averaging: the real-space positions of all mobile atoms when they occupy the site are collected, and n average real-space positions are computed for the site, where n is a parameter chosen by the user. SOAP is computed on the averaged sites.

(2) SOAP-space averaging: SOAP vectors are computed for all real-space positions with the host-lattice atoms at their corresponding instantaneous positions. Then, n average descriptor vectors are computed in SOAP space.

After reducing the dimensionality of the SOAP vectors with Principal Component Analysis, we cluster them using density-peak clustering [269] with a Euclidean distance metric. A simple parameter estimation scheme is used to determine the number of clusters (see Sec. 3.6.3). Each cluster of descriptor vectors corresponds to a site type. Each site is assigned to the type corresponding to the descriptor cluster to which the majority of its descriptors were assigned. Small majorities (less than 70-80% agreement) typically indicate insufficient data, poorly chosen SOAP parameters, or very similar environments.

3.2.6 Discussion of design choices

The main motivation for a landmark based approach is its ability to significantly reduce noise resulting from thermal vibrations in the system while reducing the dimensionality and discretizing the trajectory of the mobile ions. The design described in this section is driven by physical intuition and trial-and-error. While developing the present approach, we attempted and discarded a number of approaches due to poor performance in trial systems:

(1) Directly clustering the Cartesian coordinates of the mobile ions (the density-based approach

discussed in Sec. 3.1) was found to work poorly in some systems. We show this in more detail in Sec. 3.3.1.

(2) An analysis based on the N nearest neighbors of the mobile atom was tried but discarded, since we could not determine N without relying on the knowledge of the structure under investigation, in particular the expected size of the coordination shell of Li.

(3) We tried various landmark representations, the most simple being the distance to each host-lattice atom, therefore taking the instantaneous positions of host-lattice atoms as landmarks. The results for different systems were not satisfactory.

We conclude this section by pointing out that passing from Cartesian coordinates to landmark vectors can significantly reduce the noise that comes mostly from thermal vibrations in the system. Different formulations of landmarks can be envisioned, and while the present framework performs well for Li-ionic diffusion, a different landmark framework might be needed to describe, for example, Grotthus-like proton diffusion in superprotonic $CsHSO_4$ [263].

3.3 Results and discussion

We apply the algorithms above to ten representative materials, $Li_7La_3Z_2O_{12}$, $LiAlSiO_4$, $Li_{10}GeP_2S_{12}$, $Li_{32}Al_{16}B_{16}O_{64}$, $Li_{24}Sc_8B_{16}O_{48}$, $Li_{24}Ba_{16}Ta_8N_{32}$, $Li_{20}Re_4N_{16}$, $Li_{12}Rb_8B_4P_{16}O_{56}$, $Li_6Zn_6As_6O_{24}$ and $Li_{24}Zn_4O_{16}$. For the subsequent analysis, we also calculate radial distribution functions, mean-square displacements, and ionic densities. The mobile-ion densities $n_{\mathrm{M}}(\boldsymbol{r})$ are calculated from molecular dynamics trajectories as:

$$n_M(\boldsymbol{r}) = \left\langle \sum_m^M \delta(\boldsymbol{r} - \boldsymbol{r}_m(t)) \right\rangle_t , \tag{3.6}$$

where the index m runs over all mobile ions M and the angular brackets $\langle\cdot\rangle_t$ indicate a time average over the trajectory, which is equal to an ensemble average under the assumption of ergodicity. When applying Eq. (3.6) we replace the delta function by a Gaussian with a standard deviation of 0.3Å, and the summation is performed on a grid of ten points per Å in every direction. The tracer diffusion coefficient of the mobile species D_{tr}^M is computed from the mean-square displacement of the mobile ions as a function of time:

$$D_{\mathrm{tr}}^M = \lim_{\tau\to\infty} \frac{1}{6\tau} \frac{1}{N_M} \sum_m^M \left\langle |\boldsymbol{r}_m(\tau + t) - \boldsymbol{r}_m(t)|^2 \right\rangle_t , \tag{3.7}$$

where $\boldsymbol{r}_m(t)$ is the position of the mobile ion at time t. In practice, we fit a line to the mean-square displacement in the diffusive regime. The error of the tracer diffusion coefficients is estimated with a block analysis [270]. The radial distribution function $g(r)_{M-S}$ of the mobile ions M with species S is

calculated as:

$$
\begin{aligned}
g_{M-S}(r) &= \frac{\rho(r)}{f(r)} \\
&= \frac{1}{f(r)} \frac{1}{N_M} \sum_m^M \sum_s^S \langle \delta \left(r - |\boldsymbol{r}_m(t) - \boldsymbol{r}_s(t)| \right) \rangle_t ,
\end{aligned}
\tag{3.8}
$$

where $f(r)$ is the ideal-gas average number density at the same overall density. In addition, we integrate the average number density $\rho(r)$ to give the average coordination number as a function of distance [271].

3.3.1 Analysis of $Li_7La_3Zr_2O_{12}$

Garnet-type structures were proposed as lithium-ionic conductors by Thangadurai *et al.* [229]. The general formula of garnets is $Li_5La_3M_2O_{12}$ (M = Ta, Nb) [272], but aliovalent substitutions of M can change the lithium content. Xie *et al.* [273] studied in more detail the distribution of Li^+ in garnets. Their results indicate that increasing the lithium concentration in garnets leads to an increase in occupation of octahedral sites, which is confirmed by simulations [214] and also in experiments [274]. It has been established [212, 275, 276] for the garnet structure that Li ions can occupy tetragonal 24d sites, octahedral 48g sites and 96h distorted octahedral sites. The latter stem from a site splitting of the 48g sites to increase the Li-Li distances and occur at higher lithium concentrations. In this work, we study the Li-ion distribution of Zr-based cubic garnets with the stochiometric formula $Li_7La_3Zr_2O_{12}$, referred to as LLZO in the remainder.

We sample the dynamics in the cell of 192 atoms in the canonical ensemble via a GLE thermostat [277] at a temperature of 500 K, using a lattice constant of 12.9872 Å, and a polarizable force field. We use LAAMPS [278] to perform the simulation for 10 ns, with the parameters of the force field taken from the work by Mottet *et al.* [279], which accurately reproduces the kinetics of the diffusing process in LLZO.

The estimate of the diffusion coefficient via Eq. (3.7) reveal that Li-ions indeed are diffusive in LLZO, with a tracer diffusion coefficient of $D_{tr}^{Li} = 2.4 \times 10^{-6}\,\mathrm{cm^2\,s^{-1}}$. Application of the Nernst-Einstein equation gives the ionic conductivity σ:

$$
\sigma = \frac{Z^2 e^2 N}{k_B T} \frac{D_{tr}}{H} ,
\tag{3.9}
$$

where (Ze) the carrier's charge, N the carrier density, k_B the Boltzmann constant, T the absolute temperature and H is the ratio between the tracer and charge diffusion coefficient, commonly referred to as Haven ratio: $H = \frac{D_{tr}}{D_\sigma}$. To account for the strong evidence for correlated motion in this material [207, 280], we set the Haven ratio to $H = 0.4$, reported in a study [281] for this Li-ion concentration in LLZO. We find $\sigma = 0.58\,\mathrm{Scm^{-1}}$, which is one order of magnitude larger than the values reported by Murugan *et al.* [282]. This is within the acceptable range, especially for a classical force-field, and not of concern since the focus of this work is the analysis method. The diffusive

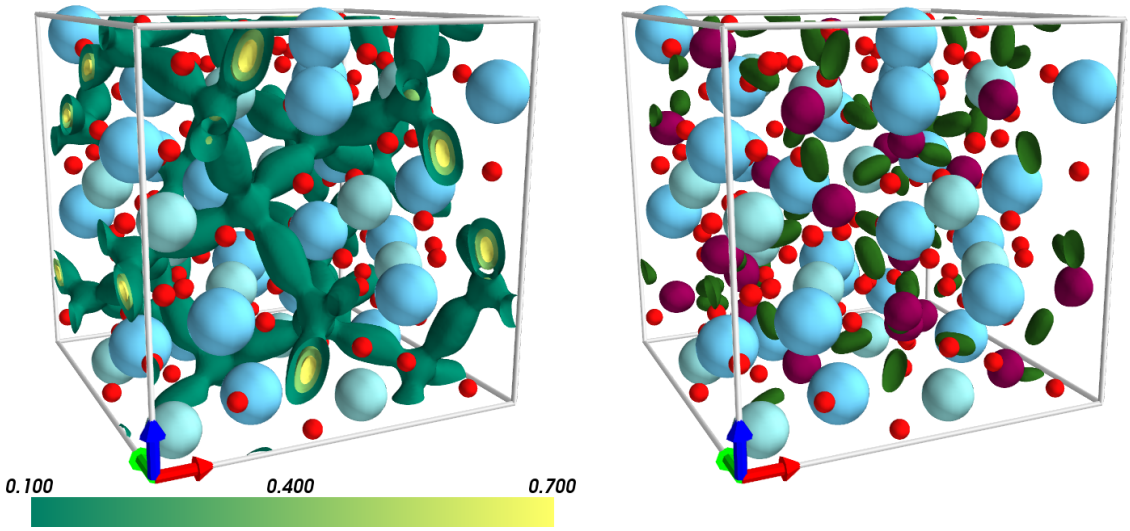

Fig. 3.6: (Left) The Li-ion density in LLZO is shown above as three isosurfaces going from green (low density) to yellow (high density). The equilibrium positions of lanthanum are shown in blue, those of zirconium in turquoise, and those of oxygen in red. The Li-ion densities reveal the three-dimensional percolation pathways in this material. (Right) Li-ion density in LLZO is shown above for the same isovalue (0.1) for Type 0 (octahedral environment) in green and Type 1 (tetrahedral environment) in bordeaux.

pathways can be illustrated by the Li-ion density, shown for three isosurfaces in the left panel of Fig. 3.6. By visual inspection, the densities look similar to those presented by Adams and Rao in their computational study [212]. The splitting of 48g sites into 96h sites [276] cannot be seen from the isosurfaces at any isovalues, which is consistent with the conclusions drawn by Chen *et al.* [251] that density-based clustering of real-space positions cannot resolve the two distinct 96h sites in LLZO from the 48g site. The radial distribution function $g(r)$, shown in the left panel of Fig. 3.7, shows how the Li ions in our simulation are, as expected, coordinated closest by oxygen and then by other Li ions.

We use the site analysis presented to discretize the trajectory of lithium ions into meaningful states, as illustrated for one lithium ion in Fig. 3.8. The subsequent SOAP analysis produces two clearly resolvable clusters, which are detected by the clustering algorithm. We show the first two principal components in the left panel of Fig. 3.9, with a color encoding representing the cluster detected. It is evident that the SOAP descriptor produces data that clusters well in this projection and that the clustering algorithm correctly assigns the clusters. The algorithm detects 24 sites of one kind (type 1) and 83 of another (type 0). We attribute the tetrahedral environment to the former, and the octahedral environment to the latter, since the expected values are 24 sites for the tetrahedral environment and 96 for the octahedral one. The last number is due to the site splitting inside each of the 48 octahedral cavities, leading to two sites inside each octahedral cavity. The under-prediction of the number of octahedral sites is due to the merging, in some cases, of octahedral sites into a

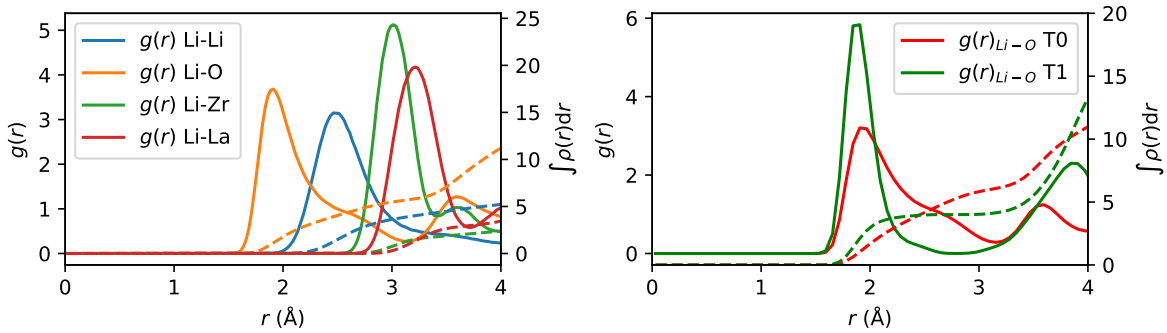

Fig. 3.7: (Left) The Li-Li (blue), Li-O (orange), Li-Zr (green), and Li-La (red) radial distribution functions $g(r)$ are shown as solid lines. The integral, representing the coordination as a function of distance, is plotted against the right axis using dashed lines and the same color encoding. (Right) Radial distribution function for lithium-oxygen pairs for the two distinct site types we found. The red lines correspond to a site of type 0, the green lines to a site type of 1, and the integrals are shown with dashed lines and the same color encoding.

single site. We stress that the numbers of sites presented as final results are after the site-merging step, presented in Sec. 3.2.4. The proximity and fast ion exchange between the octahedral sites in the same cavity explains why our algorithm does not give the correct answer, but it is remarkably close to the correct result, without any encoding of prior information about possible site splitting. Comparing to the study by Chen *et al.* [251], we can conclude that the landmark analysis is able to better distinguish minima in close proximity. We speculate that the main reason is a higher tolerance for thermal vibrations of the host lattice, that can lead to energetic minima being spread in real space.

To ensure that the analysis of LLZO provides reasonable and expected results, we calculate the Li-O radial distribution function $g(r)$ separately for each site type; these are shown in the right panel of Fig. 3.7. Li ions attributed to sites of type 1 have an environment characterized by a distinct nearest-neighbor peak stemming from four-fold coordination of lithium with oxygen, as evidenced

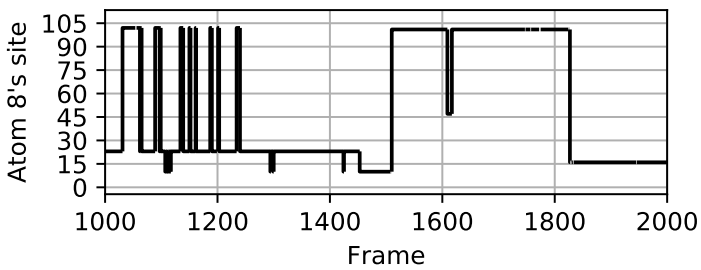

Fig. 3.8: Site trajectory in LLZO at 500 K for a representative mobile lithium ion over 1000 frames. For every frame, we determine the most likely site the ion is occupying. We plot the ion's occupation over time, where discontinuities are interpreted as jumps. The site index on the y axis is arbitrary, and the distances in index space, i.e., the vertical distance in above plot, are not reflective of the actual jump distances.

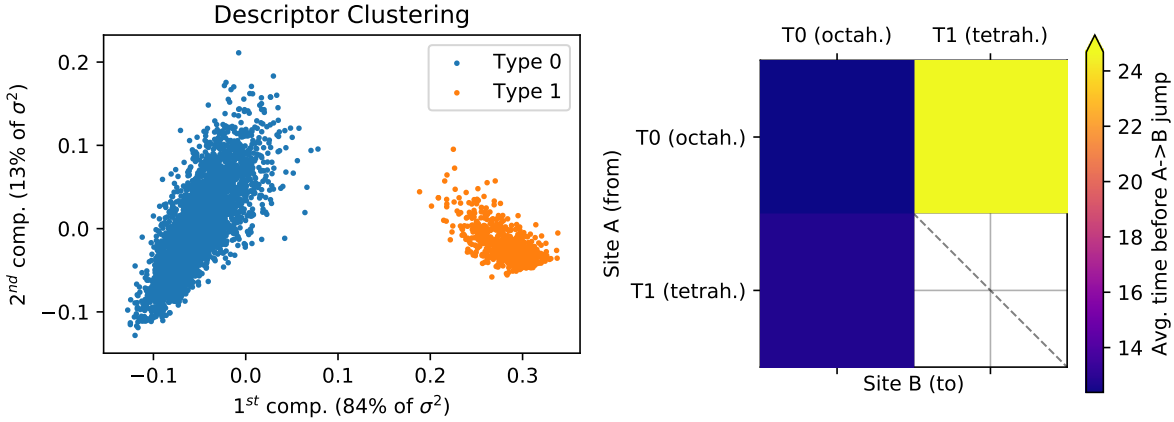

Fig. 3.9: (Left) SOAP descriptor clustering for LLZO. Each point is an average SOAP vector and is colored according to its assigned cluster (site type). The first and second principal components are plotted along the X and Y axes respectively. (Right) We show the jump lag or residence time in LLZO, which is the time an ion spends in site A before jumping to site B, averaged over sites of the same type. The color encodes the residence time, with no color (white) meaning that no jump has been observed. The time is given in multiples of the interval between frames.

by the integral plateauing at a value of four. The first peak for type 0, shown in red, has a shape compatible with a distorted octahedron, due to the appearance of a shoulder, and the weak, but distinguishable, plateau of the integral at a value of approximately 6. This is further evidence that the site types have been correctly attributed to the tetrahedral and octahedral site environments of LLZO, and that the SOAP descriptor can be used to cluster site types correctly. Additionally, we resolve the Li-ion density by site type in the right panel of Fig. 3.6. The isosurfaces are compatible, by visual inspection, with reported work [212]. We also calculate the jump lag, which is the average residence time at a site A before jumping to a site B. If we average over all sites belonging to the same type, as shown in the right panel of Fig. 3.9, we see that jumps between the octahedral sites are fastest. From the site splitting of the 48g into 96h sites follows that two sites are present inside each octahedron, and that there is a free energy barrier between the split sites. Our results are therefore in agreement with *ab initio* calculations [207, 213, 280, 283], that show that the minima in the Li-ion potential energy surface are displaced from the original central site in the octahedral site. The presence of two distinct but very close sites manifests in very high exchange rates between these two. LLZO also displays fast jumps from the tetrahedral into the octahedral environment, whereas the reverse jump takes three to four times longer. No jumps between tetrahedral environments are observed, as expected, since an ion needs to traverse octahedral sites to reach a different tetrahedral site. While the jump probabilities, or lag times, are non-symmetric, the fluxes are symmetric, which is necessary to observe local detailed balance.

The diffusive pathways estimated from the algorithms are shown in Fig. 3.10. The connectivity analysis reveals the existence of a single dominant pathway that allows mobile ions to diffuse through the entire simulation cell. The edge widths in the figure are proportional to the observed flux of

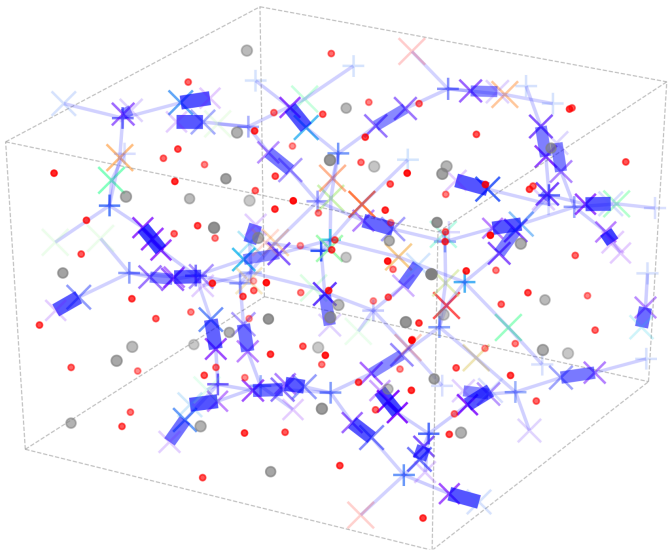

Fig. 3.10: The diffusive pathways in LLZO at 500 K. The centers of sites of type 0 (octahedral environment) and type 1 (tetrahedral environment) are shown as crosses and plusses, respectively. The color of the sites encodes the average residence time. Edges connect sites that have exchanged mobile ions, with the edge width related linearly to the observed flux of particles. The equilibrium host lattice positions of oxygen (red), lanthanum (grey), and zirconium (light grey) are shown as small spheres. The entire network of diffusion has one connected component.

particles, and we see that, where the octahedral site splitting is correctly determined, there is a large flux of ions between split octahedral sites compared to the smaller flux between the tetrahedral and octahedral environments.

Summarizing our results for this material, our site analysis finds the splitting of the 48g to 96h sites, which sets it apart from any density-based analysis. An analysis based on distance criteria to crystallographic sites would have worked as well or better, but obviously requires prior knowledge.

3.3.2 Analysis of $LiAlSiO_4$

The structure of the β-eucryptite $LiAlSiO_4$ [284], referred to as LASO hereafter, is taken from COD [285] entry 9000368. It has been studied for its anisotropic expansion coefficient [286, 287] and its ionic conductivity [288–291]. The structure can be described as an ordered β-quartz solid solution, with alternating aluminum and silicon planes. Location and occupation of the sites for lithium have been contested. In the original reference [284], the difficulties in determining the lithium sites in previous and in the same work are explained very well. For example, earlier work [292] concluded that the Li sites are coplanar with the Al sites, while Pillars and Peacor [284] show that the lithium sites are also present in the Si plane. Later work [289] shows that both sites are available to lithium and establishes the unidimensional chain of these sites as the mechanism for ionic diffusion in this material. There is now a better understanding of this structure and the sites available to lithium, but the original

CIF-file in the COD originating from the experiments by Pillars and Peacor [284] does not list all sites. Any analysis that relies on this knowledge would therefore have failed. Our molecular dynamics simulations and subsequent site analysis yield results that are compatible with the latest literature regarding the ionic transport in this material.

We simulate with first principles $Li_{12}Al_{12}Si_{12}O_{48}$, starting from the reported CIF-file [285]. A full atomic and cell optimization results in a volume increase of 3.6% without changing the cell angles in a significant way. We perform the subsequent dynamical simulations using Born-Oppenheimer molecular dynamics in the canonical ensemble at a temperature of 750 K for 291 ps, with further details given in Sec. 3.6.4.

We show in Fig. 3.11 the Li-ion densities sampled during the dynamics. The unidimensional channels of ionic diffusion are compatible with published results [289, 291]. The diffusion coefficient is hard to converge for the short dynamics we obtained for this system, and so quantifying the diffusion coefficient and its error cannot be done rigorously. We plot the coordinates of Li-ions

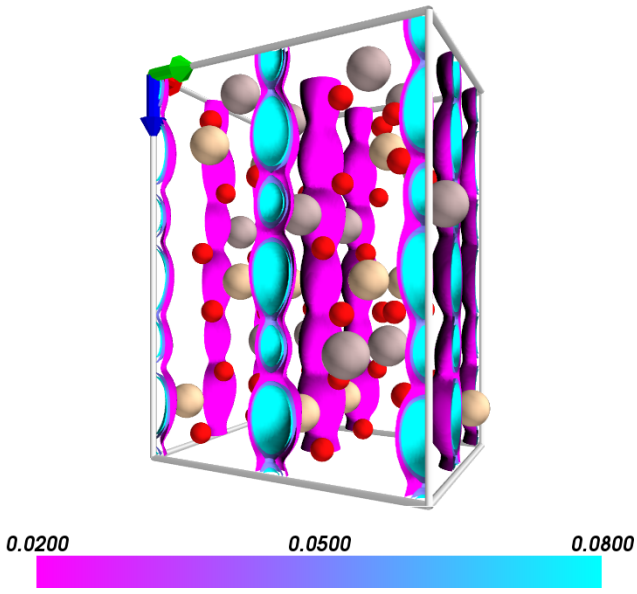

Fig. 3.11: Li-ion density in LASO, shown above as 3 isosurfaces going from violet (low density) to sky blue (high density). The equilibrium positions of oxygen are shown in red, of silicon in grey, and of aluminum in beige. Silicon and aluminum appear in alternating planes perpendicular to the c-axis.

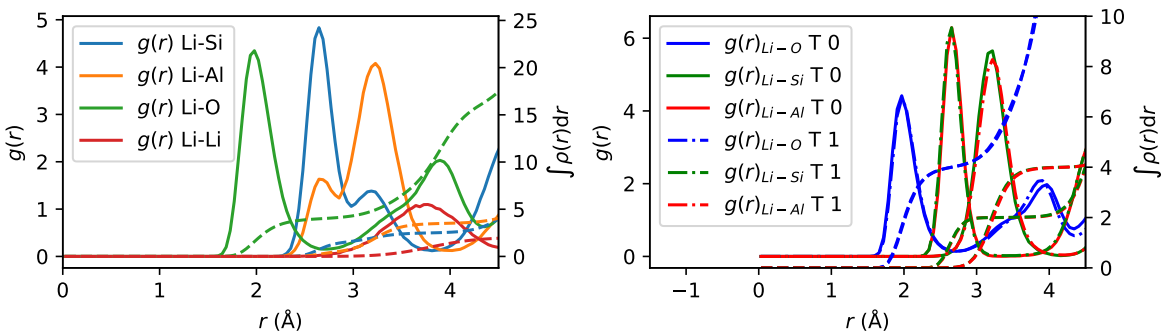

Fig. 3.12: (Left) The Li-Si (blue), Li-Al (orange), Li-O (green), and Li-Li (red) radial distributions $g(r)$ are shown as solid lines. The integral of the average number density is plotted against the right axis as dashed lines in the same color. (Right) Li-O (blue), Li-Si (green), and Li-Al (red) radial distribution functions for the two distinct site types we found. The solid lines correspond to a site of type 0, the dash-dotted lines to a site of type 1.

as a function of time in Fig. 2 of Ref. [293] to show that motion along the z-coordinate is observed during the simulation, compatible with long-range diffusion. The RDFs of Li with all present species, shown in the upper panel of Fig. 3.12, display a first coordination shell composed by four oxygen ions, compatible with literature findings. A second and third shell are composed of silicon and aluminum, with the amplitude of Si being stronger in the second shell, and Al in the third shell. This hints that Li ions prefer sites in the Si plane to those in the Al plane.

When running the site analysis, we find 24 sites of two different types, twelve of type 0 and twelve of type 1, compatible with the latest literature results [289]. The parameters are as given in Sec. 3.6.5, except for a cutoff midpoint of 1.3 instead of 1.5, which is more robust with respect to the total number of sites obtained. The clustering analysis in Fig. 5 of Ref. [293] shows that types can be distinguished easily. An analysis of the RDF for the individual site types, shown in the left panel of Fig. 3.12, reveals that the discriminant is the different coordination of Al and Si, which is detected by the SOAP descriptor. For type 0, the second shell is composed of two aluminum atoms; four silicon atoms are in the third shell. For type 1, the numbers are the same, but silicon is replaced by aluminum and vice versa. The RDF in the left panel of Fig. 3.12 hints at the fact that the Li ions prefer to occupy type 1 sites where the Si ions are closer than the Al ions. From the site analysis of our simulation, we calculate the mean occupation ratio to be 77% for site type 1 and 23% for site type 0. Literature reports give occupancies of 68% and 22% [294], respectively, or a 3:1 ratio [287]. In Fig. 3.13, we show the jump lag between the type sites. Jumps from type 1 to type 0 are about 3.5 times faster, which is necessary to preserve detailed balance. We observe no jumps within the site types, which is expected since the sites' types are alternating along the diffusion channels (see Fig. 3.14).

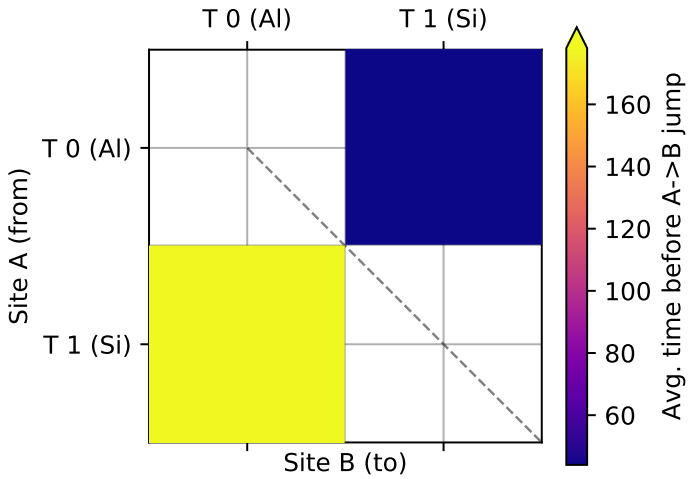

Fig. 3.13: Similarly to the right panel of Fig. 3.9 we show the average residence time before a jump for the two distinct site types in LASO. White corresponds to no jumps occurring.

We can thus show with first-principles molecular dynamics and an unsupervised analysis that the lithium ions occupy two different site types in LASO. This is done without any knowledge of the possible sites, since in the original CIF file only twelve sites (for twelve lithium ions) are given.

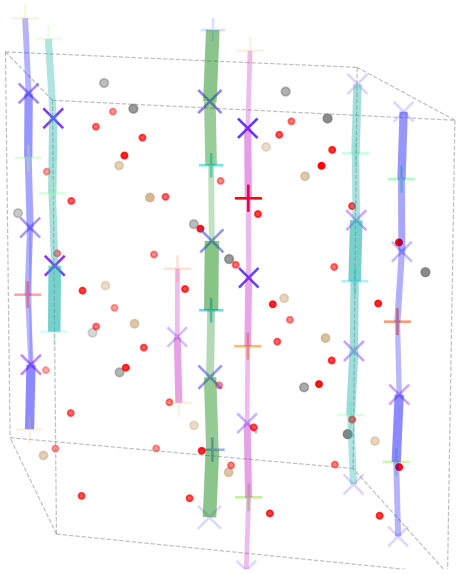

Fig. 3.14: The diffusive pathways in LASO at 750 K: sites of type 0 are shown as crosses and sites of type 1 as pluses. Edges are drawn between sites that exchange ions, similar to Fig. 3.10. Unlike LLZO, the diffusion network has four disconnected components, indicated by differently colored edges; The channels in LASO do not exchange ions in our simulations.

This example highlights the challenges for algorithms that rely on prior knowledge of crystallographic sites. Such information might be missing or wrong, for example, because of the difficulties of resolving low occupancy sites for light elements when using XRD or neutron diffraction, or because of simulation conditions (e.g., temperature) differing from the experimental setup. Relying on all the sites being known can obviously be problematic in some cases. An unsupervised approach requiring minimal knowledge of the structures should be preferred in such cases. Unlike the case of LLZO, a density-based clustering on the lithium-ion positions would very likely also have given the same results, as can be conjectured from the lithium-ion densities in Fig. 3.11, where the highest isovalue clearly shows disconnected regions of high ionic density.

3.3.3 Analysis of tetragonal $Li_{10}GeP_2S_{12}$

The superionic conductor $Li_{10}GeP_2S_{12}$ (LGPS) in its tetragonal phase was first reported by Kamaya *et al.* [239] Its unprecedented ionic conductivity at room temperature motivated studies of its diffusion mechanisms using atomistic simulation techniques [205, 206, 211, 217]. The original paper [239] reports three site types in the unit cell: tetrahedrally coordinated 16h, tetrahedrally coordinated 8f, and octahedrally coordinated 4d sites, all coordinated with sulfur, with only the latter possessing full occupancy. The 16h and 8f sites denote edge-sharing LiS_4 tetrahedra that form one-dimensional channels along the c-axis, the main diffusive pathways [205, 239]. Adams and Rao [217] found evidence for an additional four-fold coordinated site – termed 4c – using classical simulations, which was validated in subsequent experiments by Kuhn *et al.* [295].

We analyze the first-principles molecular dynamics trajectories for LGPS that were produced for a recent work discussing the failure of the Nernst-Einstein relation in this structure [211]. We refer to the reference for computational details, and state only that the trajectories were run with the cp.x code of the Quantum ESPRESSO distribution [181] with a PBE-exchange correlation functional [135]. Using a unit cell of 50 atoms, 428 picoseconds of dynamics were obtained in the microcanonical ensemble, after an equilibration run at a target temperature of 500 K. We find a Li-ion density, shown in Fig. 3.15, that is compatible with literature results on the unidimensional channels [217] that dominate the diffusion in this material. The diffusion in this material, calculated from the mean-square displacement, shown in Fig. 3 of Ref. [293], is $D_{tr}^{Li} = 3.25 \times 10^{-6}\,\mathrm{cm}^2\,\mathrm{s}^{-1}$, compatible with literature results. For example, Kuhn *et al.* [296] report a value of the Li-ion tracer diffusion coefficient of $D_{tr}^{Li} \approx 10^{-6}\,\mathrm{cm}^2\,\mathrm{s}^{-1}$ at 500 K, which is close to our estimate and certainly within the likely error bounds of FPMD that stem from, among other factors, short simulations in small unit cells.

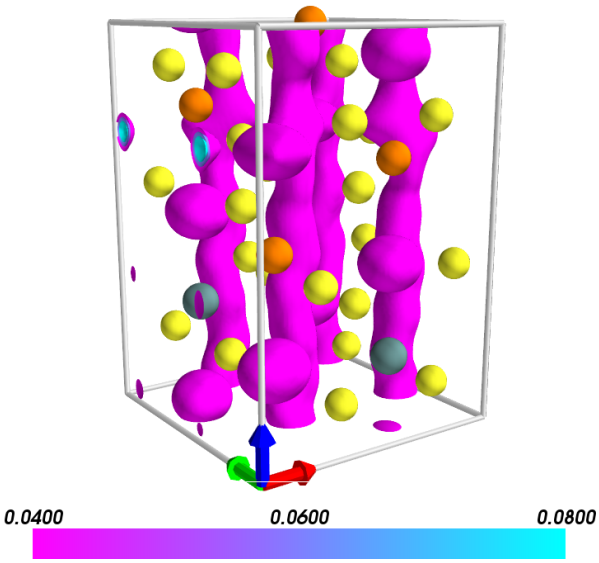

Fig. 3.15: Li-ion density in LGPS is shown above as three isosurfaces from violet (low density) to sky blue (high density). The equilibrium positions of sulfur are shown in yellow, of phosphorus in orange, and of germanium in green. The Li-ion densities reveal the unidimensional ion-conducting channels in this material.

The landmark analysis is applied to the equilibrated trajectory to determine statistics. We treat germanium and phosphorus atoms as one species since the 4d tetrahedral site is occupied by either

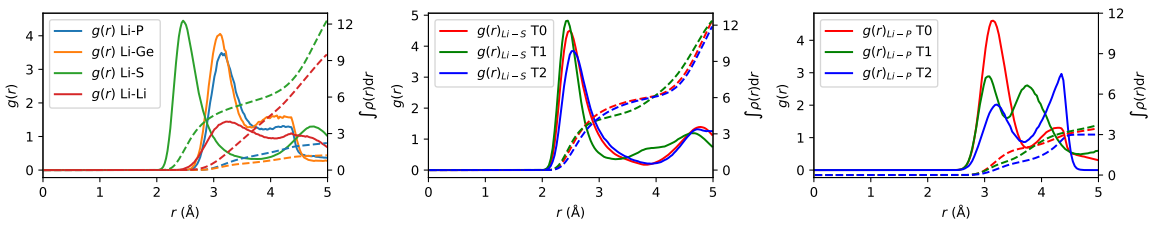

Fig. 3.16: (Left) The Li-P (blue), Li-Ge (orange), Li-S (green) and Li-Li (red) radial distribution functions are shown as solid lines. The Li-Li distribution displays the expected liquid-like lack of structure. Middle and right panels show the RDF of Li-S and Li-P, respectively. In both panels, the RDF is shown for Li occupying sites of type 0 in red, sites of type 1 in green, and and sites of type 2 in blue.

species to avoid identifying extraneous site types due to the arbitrary choice of occupation of these sites. We will refer to both phosphorus and germanium as phosphorus hereafter. After site detection and SOAP clustering, shown in Fig. 4 of Ref. [293], we find 30 sites of type 0, 24 sites of type 1, and four sites of type 2. We see that type 2 corresponds to the octahedral environment of the 4d site. To understand the difference between the different site types, we calculate the RDF for every site type, shown in the middle and bottom panels of Fig. 3.16 for sulfur and phosphorus. A visual depiction of where the sites are located is shown in Fig. 3.17.

In the RDFs between lithium and phosphorus, key differences appear between the different site types. While site type 1 is compatible with four-fold coordination with sulfur, site types 0 and 2 tend to plateau towards a coordination with six sulfur atoms, which is expected only for the latter site type. There is no evidence for a six-fold coordinated site type inside the ion-conducting channel of LGPS. We should note that — to our knowledge — no analysis has yet been done on dynamically short-lived features of the coordination of lithium with sulfur in LGPS, so it is possible that the features we perceive in our analysis are not detected when studying averages. However, we also observe that the algorithm is less robust than for the other studied examples. The number of sites as well as the clustering to types depend in this case more strongly on the parameters chosen for the site analysis. The very similar atomic environment of different site types leads to large overlap of clusters of the SOAP vectors, shown in Fig. 4 of Ref. [293]. The superionic behavior of Li ions in LGPS impedes the precise definition of a site for any single mobile ion in the dynamic potential energy landscape. LGPS, representative of superionic systems, can be seen as a worst-case scenario for the present site analysis.

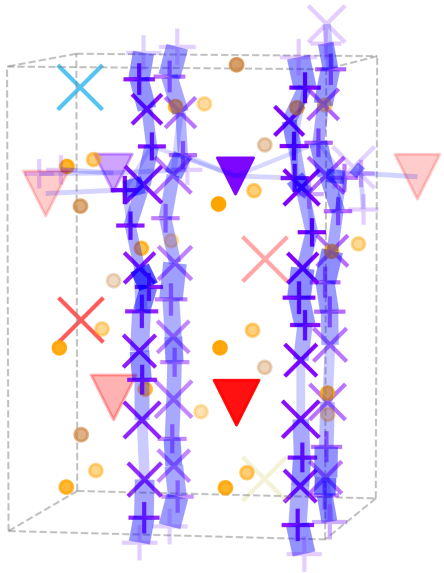

Fig. 3.17: The diffusive pathways in LGPS at 500 K. Sites of type 0 are shown as crosses, sites of type 1 as pluses, and sites of type 2 as triangles. Unlike LASO, the ion-conducting channels do exchange ions, leading to a single connected component, illustrated by one color for the entire network.

When analyzing LGPS it also becomes evident that the classification via SOAP vectors can yield different results than the Wyckoff symbols resulting from symmetry analysis. Different Wyckoff positions can be classified as the same site type if their chemical and geometric environments are too similar to differentiate. Further, as a result of symmetry breaking during molecular dynamics, two sites with the same Wyckoff position can be classified as different types, especially in non-ergodic simulations. This is not necessarily a weakness of the analysis, but something to be aware of. We

note that despite the obvious difficulties in detecting sites and site types reported in the literature, our analysis found four off-channel four-fold coordinated sites, which were termed 4c sites by Adams and Rao [217]. These sites had been missed in earlier FPMD simulations [205], since they were not reported by preceding experiments. Thus an unsupervised and unbiased analysis can help when experimental data is lacking or incomplete.

3.3.4 Non-diffusive structures

To further validate the method, we additionally study seven non-conductive structures. The structures were selected from an ongoing screening effort intended to find new solid-state electrolytes, and chosen from the least conductive systems that had two site types in their CIF file. For every structure, a molecular dynamics simulation is run at a temperature of 1000 K, with simulation lengths long enough to estimate the diffusivity of the material. All other simulation parameters are the same as those presented for LASO in Sec. 3.3.2; details can be found in Sec. 3.6.4. The landmark analysis is run on every second frame of the trajectory (about every 60 fs). We use the same default landmark analysis parameters for all of the materials, with further details given in Sec. 3.6.5.

The results can be seen for each of the seven materials in Table 3.1. For all but two materials, the landmark analysis produces the same number of sites and the same division of those sites into types as given in the corresponding CIF files. For these materials, unlike LGPS, the Wyckoff analysis and the SOAP analysis coincide. In $Li_{20}Re_4N_{16}$ and $Li_{24}Zn_4O_{16}$, however – like in $LiAlSiO_4$ – unsupervised landmark analysis identifies sites that are not present in the CIF files from ICSD (see Fig. 3.18). In $Li_{20}Re_4N_{16}$, these four sites complete the planar connected components in the material; they are transitional sites with low occupancy and residence time. Their existence is confirmed by an analysis of the Li-ion densities observed in the trajectories. In $Li_{24}Zn_4O_{16}$, Li-ions from neighboring sites occasionally and briefly jump to the additional sites and then back. The additional sites again have low occupancy and residence time and are confirmed by a density analysis of the real-space coordinates.

Structure	Sites Wyckoff (CIF)	Sites (Landmark + SOAP)
$Li_{32}Al_{16}B_{16}O_{64}$	16e + 16e	16 + 16 ✓
$Li_{24}Sc_8B_{16}O_{48}$	N/A	8 + 16
$Li_{24}Ba_{16}Ta_8N_{32}$	8e + 16f	8 + 16 ✓
$Li_{20}Re_4N_{16}$	4a + 16g	8 + 16
$Li_{12}Rb_8B_4P_{16}O_{56}$	4d + 8g	4 + 8 ✓
$Li_6Zn_6As_6O_{24}$	3b + 3b	3 + 3 ✓
$Li_{24}Zn_4O_{16}$	16f + 8d	20 + 8

Table 3.1: Comparison between the presented landmark analysis and the sites listed in CIF files taken from structural databases. A checkmark indicates structures where the sites in the CIF file and the results of the unsupervised analysis agree, both in number of site types and number of sites of each type. This is the case in all but two structures, $Li_{20}Re_4N_{16}$ and $Li_{24}Zn_4O_{16}$, which are discussed in the text.

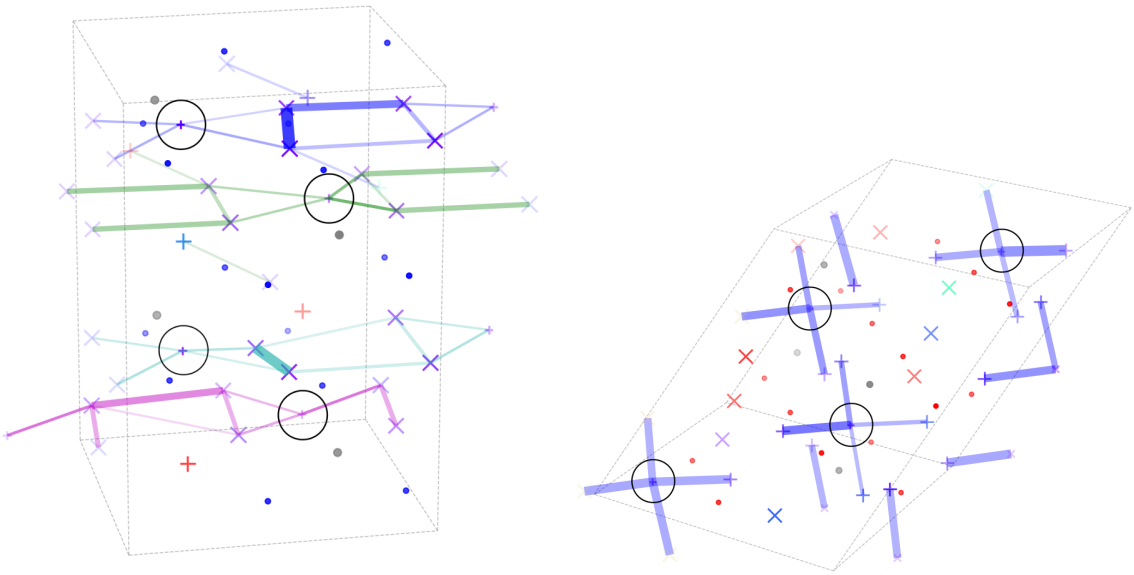

Fig. 3.18: Landmark analysis of $Li_{20}Re_4N_{16}$ (left) and $Li_{24}Zn_4O_{16}$ (right). The sites circled in black are absent in the CIF files.

3.4 Implementation

The landmark analysis presented here is implemented as a component of `SITATOR` [297], a modular, extensible, open-source Python framework for analyzing networks of sites in molecular dynamics simulations of solid-state materials. `SITATOR` provides two fundamental data structures: `SITENETWORK`, which represents possible sites for some mobile atoms in a host lattice and `SITETRAJECTORY`, which stores discretized trajectories for those mobile atoms. A `SITENETWORK` can also store arbitrary site and edge attributes. `SITATOR` includes an optimized implementation of landmark analysis as well as pre-processing utilities for trajectories and tools for analyzing and visualizing the results of site analyses.

3.5 Conclusions

We presented a novel method to perform a site analysis of molecular dynamics trajectories to analyze ionic diffusion in solid-state structures. The method is robust and can run over a large range of materials with a minimal set of parameters and little human intervention. As we have shown, our landmark analysis performs well where other methods fail, whether because of very high exchange rates and/or close proximity between sites (as in LLZO), or because needed prior information is missing (as in LASO, $Li_{20}Re_4N_{16}$, and $Li_{24}Zn_4O_{16}$ where several sites that were occupied during our simulations are not given in the experimental CIF file). As became evident for LGPS, superionic conductors with a liquid-like, highly disordered lithium sublattice are hard to analyze with the tool, and the signals from the analysis need to be studied in further detail in subsequent work. A

suggestion for subsequent work is automatically computing the configurational entropy descriptor $\tilde{S}$ described by Kweon *et al.* [242] While the method presented here will not necessarily outperform carefully chosen analysis tools with parameters specific to the system under investigation, it has advantages when comparing different systems and in high-throughput applications, such as the search for microscopic descriptors for ionic diffusion in the solid state. Another suggestion is to study the collective motion in common superionic conductors from occupation statistics given by the landmark analysis. Concerted motion is important for ionic diffusion in a wide class of systems [227], and an analysis that can be used with the same set of parameters on a wide range of materials can be used to quantify collective effects rigorously.

Acknowledgments

We thank Aris Marcolongo for supplying the LGPS trajectories. We also express our gratitude to Matthieu Mottet who provided force-field parameters for LLZO and advice on running the simulations. We would like to thank Felix Musil, Piero Gasparotto, and Michele Ceriotti for their support with the SOAP descriptor and the `QUIPPY` interface as well as fruitful discussions. We gratefully acknowledge financial support from the Swiss National Science Foundation (SNSF) Project No. 200021-159198. This work was supported by a grant from the Swiss National Supercomputing Centre (CSCS) under project ID mr0.

3.6 Method details

3.6.1 Landmark vector clustering algorithm

When determining the landmarks in a system, we use the efficient implementation of the Voronoi decomposition from `ZEO++` [298, 299], which accounts for periodic boundary conditions. A custom hierarchical agglomerative algorithm is used to cluster the landmark vectors. The algorithm is designed for streaming: no pairwise distance matrix is ever computed or stored, and the landmark vectors can be streamed from disk in the order they were written, avoiding random access. Clusters are represented by their average landmark vectors, called centers. At each iteration clusters whose centers are sufficiently similar are merged. After a small number of iterations, a steady state is reached when no clusters can be merged; this is taken as the final clustering. The original landmark vectors are then each assigned to the cluster whose center they are most similar to.

Two parameters control the characteristics of the landmark clustering: the clustering threshold, which determines how aggressively new clusters (sites) should be added, and the minimum cluster size, which filters out sites whose occupancy is extremely low (such clusters likely represent thermal noise or transitional states). These parameters allow the user to tune spatial and temporal resolution. Specifically:

(1) Set the initial cluster centers $\vec{c}_i$ to the landmark vectors. The order of the landmark vectors does affect the clustering, but in practice we have found the effect to be minimal. We process the landmark vectors in the order they were generated: chronologically and in whatever order

the mobile ions were numbered.

(2) Take the first existing cluster center $\vec{c}_0$ as the first new cluster center $\vec{c}'_0$. Then, for each remaining cluster center $\vec{c}_i$, $i \in [1, N)$:

(a) Find the new cluster center $\vec{c}'_j$ to which the old cluster center $\vec{c}_i$ is most similar:

$$j = \underset{j \in [0, N')}{\arg\max}\, S(\vec{c}_i, \vec{c}'_j),$$

where N' is the current number of new cluster centers and $S(\cdot, \cdot)$ is the normalized cosine metric:

$$S(\vec{c}_i, \vec{c}'_j) = \frac{\vec{c}_i \cdot \vec{c}'_j}{|\vec{c}_i||\vec{c}'_j|}.$$

(b) If $S(\vec{c}_i, \vec{c}'_j) >$ clustering threshold, then merge the old cluster $\vec{c}_i$ into the new cluster $\vec{c}'_j$:

$$\vec{c}'_j = \frac{n\vec{c}'_j + \vec{c}_i}{n+1},$$

where n is the total number of old clusters that have been merged to form $\vec{c}'_j$ so far. Otherwise, keep $\vec{c}_i$ as the center of its own cluster:

$$\vec{c}'_{N'} = \vec{c}_i$$
$$N' = N' + 1$$

(3) Repeat the previous step until no further clusters can be merged; the $\vec{c}_i$, $i \in [0, N)$ are the final clusters.

(4) Assign the landmark vectors to clusters. The assignment threshold controls how dissimilar a landmark vector can be to its cluster's center before it is marked as unassigned. This parameter controls the trade-off between spatial accuracy and the proportion of unassigned mobile atom positions: high values will give greater spatial precision, while lower values will ensure that almost all mobile atoms are assigned to sites at all times. For each landmark vector $\vec{l}$:

(a) If $s >$ assignment threshold, then mark $\vec{l}$ as a member of the corresponding cluster with confidence s. Otherwise, mark $\vec{l}$ as unassigned.

(5) Remove clusters smaller than the minimum cluster size.

(6) Repeat step 4 with the remaining clusters, yielding the final cluster assignments.

3.6.2 Markov clustering

We apply Markov Clustering [266] to the matrix $\boldsymbol{M}$ to simulate biased random walks through a graph, giving preference to high-probability routes. Once the process converges, a set of internally highly

connected subgraphs remains. The sites in each resulting subgraph, if there are more than one, are merged into a single site. Their real-space positions are averaged, and the mobile ions that occupied any of the merged sites now occupy the new site.

We use typical Markov Clustering parameters of 2.0 for both expansion and inflation. We do not add artificial self loops to the graph since $\boldsymbol{M}$ already contains appropriate nonzero values on the diagonal.

3.6.3 Parameter estimation for Density-Peak clustering

Density-peak clustering [269] defines the number of clusters as the number of data points with extreme outlier values of ρ (density) and δ (distance to nearest neighbor with larger ρ), as determined by a user-specified threshold. Rodriguez and Laio [269] suggest a simple heuristic for determining this threshold that we adopt and automate. First, we compute the values $\gamma_i = \rho_i \delta_i$ and sort them into decreasing order. In a well behaved clustering problem, a plot of γ then has a recognizable "elbow," and the points before the elbow – before the curve rapidly flattens out – are the outliers. Thus the problem of determining the thresholds is equivalent to finding the elbow of this curve.

We use a simplified version of the knee-finding algorithm presented by Satopaa *et al.* [300] A straight line is taken between $(0, \gamma_0)$ and (n, γ_n), and the point (i, γ_i) with the maximum distance to that line is taken as the elbow. The ρ and δ values corresponding to that point are then used as the thresholds for the density-peak clustering.

3.6.4 Molecular dynamics parameters

The simulations for LASO and the seven non-diffusive structures are performed with the pw.x module in the Quantum ESPRESSO distribution [181], using pseudopotentials and cutoffs from the SSSP Efficiency library 1.0 [245]. The exchange-correlation used in the DFT is PBE [135]. The materials informatics platform AiiDA [191] is used to ensure full reproducibility of the results and achieve a high degree of automation.

Structure	T_{sim} (ps)	DB	DB-ID
$Li_{32}Al_{16}B_{16}O_{64}$	72	ICSD	50612
$Li_{24}Sc_8B_{16}O_{48}$	218	COD	2218562
$Li_{24}Ba_{16}Ta_8N_{32}$	58	ICSD	75031
$Li_{20}Re_4N_{16}$	159	ICSD	92468
$Li_{12}Rb_8B_4P_{16}O_{56}$	116	ICSD	424352
$Li_6Zn_6As_6O_{24}$	226	ICSD	86184
$Li_{24}Zn_4O_{16}$	407	ICSD	62137

Table 3.2: For every structure analyzed in Sec. 3.3.4, we list the simulation length T_{sim} in picoseconds, the database (DB) from which the structure was retrieved, and the structure's database ID.

We always perform a variable-cell relaxation prior to the molecular dynamics, with a uniform k-point grid of 0.2 $Å^{-1}$ and no electronic smearing since we consider only electronic insulators. The energy and force convergence thresholds are 0.5×10^{-4} and 0.25×10^{-5} in atomic units, respectively. We set the pressure threshold to 0.5 kbar. A meta-convergence threshold on the volume, which specifies the relative volume change between subsequent relaxations, is set to 0.01.

We create supercells with the criterion that the minimal distance between opposite faces is always larger than 6.5 Å. We run the molecular dynamics simulations with a stochastic velocity rescaling thermostat [113] which we implemented into Quantum ESPRESSO, with a characteristic time of the thermostat set to 0.2 ps at constant volume and number of particles (NVT ensemble). The timestep is set to 1.45 fs, and snapshots of the trajectory are taken every 20 time steps.

The origin of the non-diffusive structures is given in Table 3.2, together with the simulation time. The structures are taken from the Inorganic Crystallography Open Database (ICSD) [301] and the Open Crystallography database (COD) [285].

3.6.5 Site analysis parameters

Unless otherwise indicated, the landmark analysis uses a cutoff midpoint of $d_0 = 1.5$ and steepness of $k = 30$, a minimum site occupancy of 1%, and landmark clustering and assignment thresholds of 0.9. For computing SOAP descriptors, unless otherwise specified, we use a Gaussian width of 0.5 Å on the atomic positions, a cutoff transition width of 0.5 Å, and spherical harmonics up to $n_{max} = l_{max} = 6$. The radial cutoff is set to always include the nearest neighbor shell of all other species (excluding the mobile species). We calculate SOAP vectors for mobile ions every tenth frame, and average every 10 SOAP vectors to reduce noise. The principal components of the averaged SOAP vectors are extracted using Principal Component analysis (PCA) to retain at least 95% of the variance, and the clustering is performed in this reduced space.

4 Screening for solid-state electrolytes

If you do not expect the unexpected,
you will not find it.

Ἡράκλειτος ὁ Ἐφέσιος – *Heraclitus of Ephesus*

As explained in Chap. 1, the search for new solid-state Li-ionic conductors is a promising endeavor, since finding new materials that can be used as solid-state electrolytes could result in safer Li-ion batteries of higher energy densities. The pinball model was introduced in Chap. 2, which, due to its computational efficiency, can be used to model the Li-ion diffusion in hundreds or thousands of materials with today's computational power. Therefore, we leveraged the model in a high-throughput computational screening to find, among thousands of solid-state structures, materials that satisfy two key requirements for application as an electrolyte: first, that the materials are electronic insulators, and second, that the materials show high Li-ion diffusion.

As described in Sec. 1.5, running calculations in a high-throughput manner requires a new paradigm, where efficient models are combined with databases to store results, and efficient engines to automate and manage the computations. In the following I show how this computational screening was performed, relying on computational workflows employing the AiiDA materials informatics platform [191]. AiiDA, introduced in Sec. 1.5, embeds data and calculations into a directed acyclic graph, storing therefore the provenance of every result and ensuring reproducibility. An exemplary graph taken from the database used in this work is illustrated in Fig. 4.1.

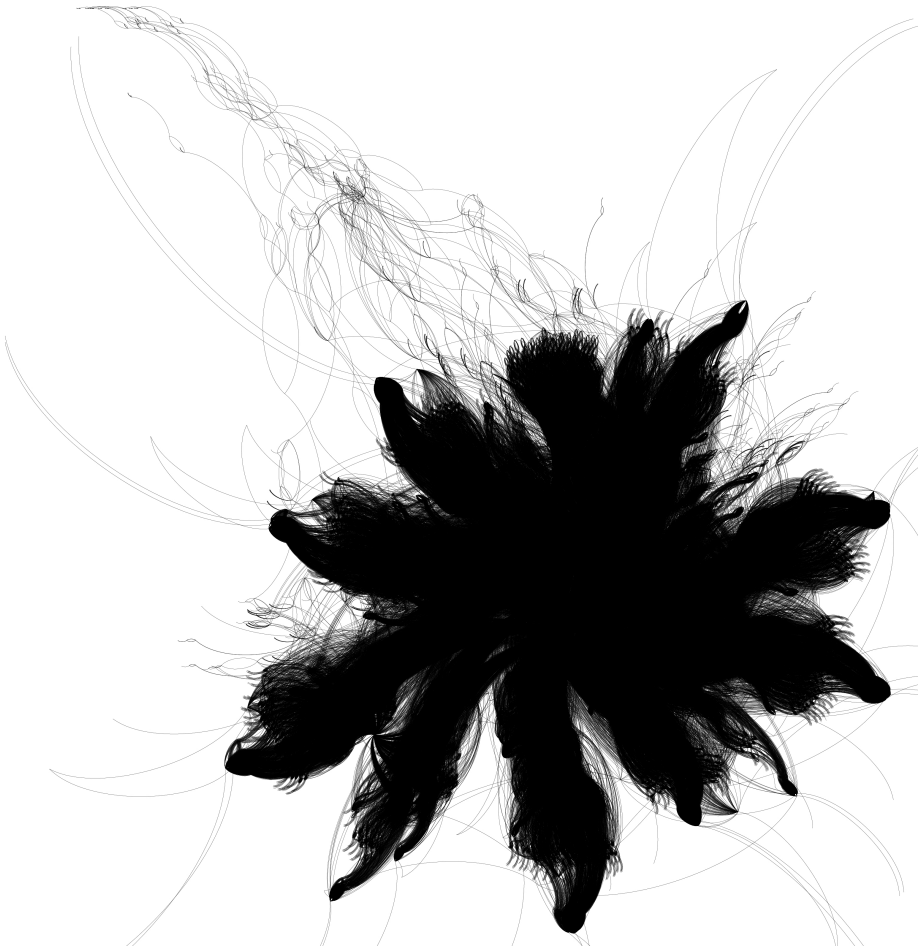

Fig. 4.1: A directed acyclic graph from all calculations performed on ten structures during the screening. Every node is either a calculation or a data instance, connected by an edge if the data is input to or output of a calculation.

The workflows described in the following were implemented by me, and I performed the simulations, analyzed the results, and wrote the following pre-print. The parameter choices were discussed with Aris Marcolongo and Nicola Marzari, and all authors discussed, reviewed, and commented the manuscript.

Authors	Leonid Kahle, Aris Marcolongo, Nicola Marzari
Title	High-throughput computational screening for solid-state Li-ion conductors
Journal reference	*Energy & Environmental Science* (accepted)
arXiv	1909.00623

High-throughput computational screening for solid-state Li-ion conductors

Leonid Kahle,[a] Aris Marcolongo,[a†] and Nicola Marzari[a]

Abstract: We present a computational screening of experimental structural repositories for fast Li-ion conductors, with the goal of finding new candidate materials for application as solid-state electrolytes in next-generation batteries. We start from ~1400 unique Li-containing materials, of which ~900 are insulators at the level of density-functional theory. For those, we calculate the diffusion coefficient in a highly automated fashion, using extensive molecular dynamics simulations on a potential energy surface (the recently published pinball model) fitted on first-principles forces. The ~130 most promising candidates are studied with full first-principles molecular dynamics, first at high temperature and then more extensively for the 78 most promising candidates. The results of the first-principles simulations of the candidate solid-state electrolytes found are discussed in detail.

4.1 Introduction

Application of inorganic solid-state lithium-ionic conductors as electrolytes could mitigate or overcome the severe safety challenges imposed by the use of volatile and flammable liquid or polymer electrolytes in today's Li-ion batteries [25, 46, 73, 78, 87, 197]. Complete replacement of the liquid electrolyte by a solid ceramic would result in an all-solid-state Li-ion battery, highly beneficial due to the higher electrochemical stability of inorganic electrolytes, compared to their organic counterparts [90]. Several structural families of promising solid-state Li-ion conductors have been researched intensely over the last decades [58, 196, 237, 302], but the many necessary criteria for successful deployment, such as fast-ionic/superionic [85, 303, 304] diffusion of Li ions, very low electronic mobility, wide electrochemical stability windows, and high mechanical stability [198, 305–307] motivate the search for novel candidates.

To a large extent, chemical intuition drove in the past the discovery of new solid-state ionic conductors. As a first example, Thangadurai and Weppner [229] found the garnet structure to be a fast-ion conductor. The general formula of the Li-containing garnets is $Li_5La_3M_2O_{12}$ (M=Ta, Nb) [272], but substitution with aliovalent ions can increase or decrease the Li-ion concentration, resulting in a general structural formula [214] of $Li_xB_3C_2O_{12}$ (B=La, Ca, Ba, Sr, Y, ...; C=Zr, Ta, Nb, W, ...), where x can vary from 3 to 7. A second example where chemical intuition lead to a new family of superionic conductors is the recent discovery of Li-argyrodites [308], with the general formula Li_7PS_5X (X=Cl, Br, I) or Li_7PS_6 (sulphur can be replaced with oxygen, but this reduces the ionic conductivity [309]). Third, Li-containing NASICONs (sodium superionic conductors) are phosphates with the structural formula $Li_{1+6x}X_{4+2-x}Y_{3+x}(PO_4)_3$ (X=Ti, Ge, Hf, Zr, ...; Y=Al, Ga, Sc, Y, La, ...) [196,

[a] Theory and Simulation of Materials (THEOS), and National Centre for Computational Design and Discovery of Novel Materials (MARVEL), École Polytechnique Fédérale de Lausanne, CH-1015 Lausanne, Switzerland
† Present address: IBM Research–Zurich, CH-8803 Rüschlikon, Switzerland

310], constituting a family of versatile compounds forming three-dimensional intercalated channels. They originate from work that proposed a structure with suitable channels for Na^+-ion diffusion [311], namely $Na_{1-x}Zr_2P_{3-x}Si_xO_{12}$. Fast Li-ionic diffusion in this family was investigated shortly after for $LiZr_2(PO_4)_3$ [312], $LiIn_2(PO_4)_3$ [313], and doped lithium-titanium phosphates [314, 315].

Chemical substitutions in known ionic conductors have also led to the discovery of new fast-ionic conductors. The family of Li-superionic conductors (LISICON) is a widely studied group of compounds originating from the structural formula $Li_{3+x}(P_{1-x}Si_x)O_4$, where Li_3PO_4 is mixed with Li_4SiO_4, changing the crystal structure from monoclinic ($x < 0.4$) to orthorhombic ($x > 0.5$) [218, 316]. Aliovalent substitutions led to the identification of fast-ionic conductors of the general chemical formula $Li_{4+x-z}X_xY_{1-x-z}Z_zO_4$, (X=B,Al,Zr,..., Y=Si,Ge,Ti,..., Z=P,As,V,...) [232, 317, 318]. Substituting oxygen with sulphur yields the sub-family of thio-LISICONs [231], widely regarded as better conductors than oxygen-based LISICONs due to the higher polarizability of the S^{2-} anions compared to O^{2-} anions [196, 231]. Additional substitutions of the cations with Ge or Sn allow for further compositional variety within this family. As part of the $Li_{4-x}Ge_{1-x}P_xS_4$ system, tetragonal $Li_{10}GeP_2S_{12}$ (LGPS), discovered by Kamaya *et al.* [239] in 2011, is widely considered one of the current best ionic conductors. In summary, major breakthroughs in the discovery of either new families of Li-ionic conductors or via substitutions within known families have been mostly led by chemical intuition, with simulations limited to providing new insight on diffusion mechanism in known materials.

However, the search for new solid-state electrolytes (SSE) with computational methods can be highly effective. Synthesis of ionic compounds and measurement of the ionic conductivity are labor-intensive tasks. In addition, experimental results can be difficult to interpret, as evidenced by the 2011 discovery of superionic tetragonal LGPS [239], even though the same composition was investigated already in 2001 [231] albeit without reporting the tetragonal phase. On the other hand, the calculation of material properties can be highly automated and parallelized [65, 174, 184, 186, 187, 191]. A computational screening for high Li-ionic conductivity, as schematically shown in Fig. 4.2, can probe new structural families for promising Li-ionic conductors that fulfill the requirements to be used as solid-state electrolytes.

In order to ensure low self-discharge of the battery, one key requirement for a SSE is a very low electronic mobility [66], which is determined by the electronic band gap of the material. Various electronic-structure methods can be employed to determine this property of a material, also in a high-throughput manner for computational screening purposes. The computational screening for new SSE by Muy *et al.* [319] and by Sendek *et al.* [320] used the computed electronic band gap, computed with DFT, as a selection criterion, which had to be above 1 eV in both studies.

Electrochemical stability can be calculated from first principles using Kohn-Sham density functional theory [131, 132] and grand-potential phase diagrams [204, 321], which was used in a recent work [322] to screen the garnet family of structures with $x = 3$ for candidates on or close to the convex hull, resulting in 30 new structures in this family. However, many electrolytes are considered for – or already in – application despite narrow electrochemical stability windows, most notably LGPS which is stabilized by interphases [323]. The tuning of interphases and application of protective coatings to

electrolyte or electrode particles [90] allow to extend the electrolyte material's stability window. We therefore view the width of the electrochemical stability of a candidate electrolyte not as a necessary criterion for application as a solid-state electrolyte, and refrain from calculating that property in this study.

The mechanical properties of a solid electrolyte can also be addressed by simulation. The elastic modulus of the electrolyte has been for long a major quantity of interest: it needs to be high enough to prevent dendritic growth of metallic Li and low enough to allow for easy processability and to provide some tolerance for volume changes of the electrodes [94, 198, 324]. The elastic modulus at 0 K can be calculated from first principles by fitting the equation of state, as was done for 23 ionic conductors by Deng *et al.* [325], and finite-temperature effects can be accounted for with the quasiharmonic approximation [326, 327]. Disorder of the Li sublattice, as expected from Li-ion conductors, could also be accounted for in first-principles simulations: Parrinello and Rahman have shown that fluctuations of the strain in the isothermal isobaric (NpT) ensemble, sampled via molecular dynamics simulations at constant stress and temperature, can be used to calculate elastic moduli [328, 329]. However, recent reports suggest that defects, rather than bulk properties, are critical to the suppression of dendrite growth, which explains the poor resistance of the high-modulus garnet structure to Li-metal dendrites [330–332]. Therefore, although the bulk or shear modulus could be easily calculated from first-principles simulations, the application of such criterion to a screening for SSE is not yet properly understood, and we will not employ it.

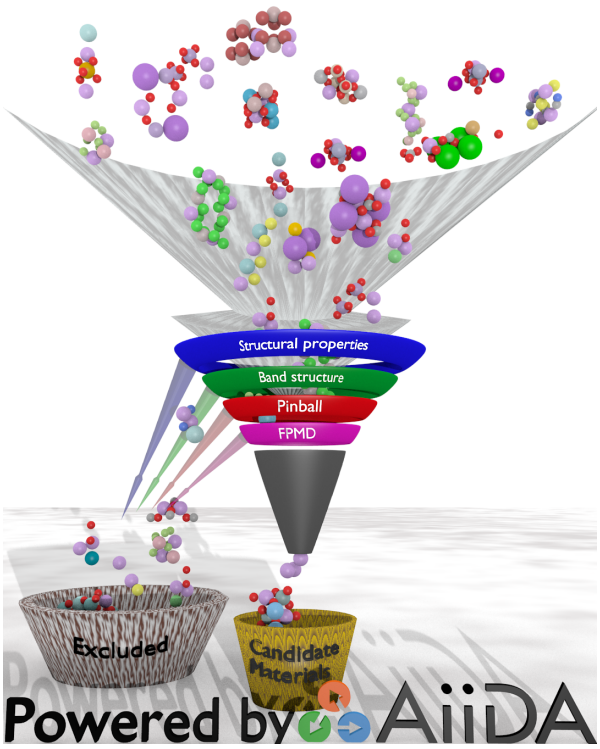

Fig. 4.2: Schematic representation of the screening funnel. Structures downloaded from experimental repositories go sequentially through several computational filters. Each stage of the screening discards structures that are unsuitable as solid-state electrolytes based on ever more complex calculated properties. The final outcome is of a few tens of viable structures, that could be potential candidates for novel solid-state Li-ion conductors.

The diffusion of Li ions and Li-ionic conductivity can also be addressed with atomistic simulations. Computational techniques such as molecular dynamics [116, 117, 333] allow to predict diffusion coefficients and offer insights on the evolution of an atomic system over time in a well-defined thermodynamic ensemble. The dynamics can be driven by classical force fields, with parameters

chosen to reproduce experiments or first-principles calculations, or using first-principles (on-the-fly) approaches based on accurate electronic-structure methods. Historically, the garnet family, due to its large unit cells, was studied extensively using classical force field [212–216]. Force fields were also successfully applied to the LISICON family [218, 232]; as an example, Adams and Rao [217] could show via classical simulations of $Li_{10}GeP_2S_{12}$ that Li ions (partially) occupy an additional site that was not observed in the first synthesis of the material by Kamaya *et al.* [239], with experimental evidence for this site later provided by Kuhn *et al.* [295]. Classical force fields have also been used when studying grain-boundary diffusion, again due to inherently large system sizes, as is the case example in Li-rich antiperovkites [246]. On the other hand, such classical interatomic potentials have to be always carefully fitted for the application in mind. As a consequence, they are often not general enough, and their reliability is questionable for a large-scale screening effort which implies considerable compositional variety. Density-functional theory [132] can provide an accurate and general Hamiltonian for the evolution of atoms, with Car-Parrinello molecular dynamics [128] (CPMD) allowing for a particularly efficient implementation in insulators by propagating electrons and ions together, in contrast to the conventional and more broadly applicable Born-Oppenheimer molecular dynamics (BOMD), that relies on full self-consistency of the electronic degrees of freedom at every step. Superionic conductors were first modelled using CPMD by Cavazzoni *et al.* in 1999 [159], namely superionic H_2O and NH_3 at high pressure and temperature, while in 2006 Wood and Marzari [162] performed CPMD simulations to study the dynamics of the superionic conductor AgI at ambient conditions. Li-ion diffusion was modeled with BOMD only in the last decade, due to its requirement of large system sizes and long time scales [51, 204–211, 280].

Many studies tried to overcome the time limitations of first-principles molecular dynamics (FPMD, to cover both BOMD and CPMD) by calculating migration barriers from static calculations [105, 200–203, 334]. However, the collective nature [211, 214, 227, 281] of Li-ion diffusion in fast conductors makes the estimate of the dominant transitions paths complex. A large-scale screening via estimate of migration barriers would be cumbersome, since the definition of migration pathways remains at this stage human-intensive. Automated calculations of pathways and barriers tackle single-particle migration [222, 335, 336] in the dilute limit, thus neglecting collective effects.

Several descriptors for ionic diffusion have been suggested to circumvent the need for a direct calculation, to avoid unreliable force fields, expensive FPMD, or the identification of complex migration pathways. A first example is the correlation between the diffusion coefficients or Arrhenius barriers of diffusion and the frequencies of specific optical phonons, first presented by Wakamura and Aniya [219, 220, 337] for halides. Evidence for such correlation has also been found in LISICONs, and in the family of olivines [338], and this descriptor constituted the backbone for a very recent screening for solid-state Li-ion conductors [319]. As a second example, the importance of accessible volume for diffusion [221, 222] led to the development of the bond-valence method by Adams and Swenson [223], and several efforts [224, 225] employed this inexpensive method for screening purposes. An approach that tackles the collective nature of diffusion is proposed via an entropy descriptor by Kweon *et al.* [242] to account for site frustration. Together with local bond frustration [226, 242] and dynamical

frustration given by the interaction of Li ions with a dynamically changing landscape, a picture emerges that explains fast-ionic diffusion in the class of *closo*-borates. In addition, machine-learning tools have been applied to predict ionic diffusion from a manifold of possible descriptors [320], but with limited data available, training machine-learning models to the required accuracy is ambitious. We conclude this cursory overview of computational methods with the comment that screening for fast-ion conductors with existing methods remains challenging, either due to the limited accuracy of descriptors or force-fields, or the complexity and computational cost of first-principles approaches.

Calculating the diffusion of Li ions in a screening scenario accurately, with molecular dynamics, calls for a different approach, that combines the computational efficiency of force fields with the generality and accuracy of density-functional theory. We recently proposed the pinball model [248] as an accurate framework for the dynamics of Li ions in the solid state. Details and derivation are in the original paper, but we iterate here the key assumptions behind the model. First, since Li ions negligibly perturb the valence electronic charge density of an ionic system, the charge density is assumed to no longer depend on the instantaneous positions of Li ions. Second, since freezing the host lattice (i.e. everything other than lithium) has a minor effect on the resulting dynamics (especially for stiff systems), we consider the Li ions moving in a frozen host lattice with a frozen charge density. We use this pinball model as the backbone for a high-throughput screening effort to find fast ionic conductors, to be followed by extensive first-principles simulations for the most promising candidates. We present details of the methods in Sec. 4.2, also laying out the automatization efforts undertaken. This is followed by presentation and discussion of the results in Sec. 4.3. We summarize and give our conclusions and outlook in Sec. 4.4.

4.2 Methods

4.2.1 Automation and provenance

Any high-throughput effort requires a highly automated framework for launching, monitoring, parsing, and storing a large number of calculations on many structures. Recording explicitly, ideally in an easily queryable format, the provenance of the resulting data allows for fully reproducible results [17, 165, 173–175]. To achieve automation and explicit storage of the provenance, we leverage the Automated Interactive Infrastructure and Database for Computational Science (AiiDA) materials informatics platform, developed by Pizzi *et al.* [191]. The novelty of AiiDA in the field of materials informatics is that every calculation is stored as a node in a graph, with input data forming incoming nodes, and output data stored as outcoming nodes, that can again be input to a different calculation. To illustrate the principle, we show such a graph (from the database created in this work) for a single structure in Fig. 4.3. The resulting directed acyclic graph stores the full provenance of every result. In addition, AiiDA allows for a high degree of automation and parallelization via its daemon. Every calculation presented in this work is run with AiiDA.

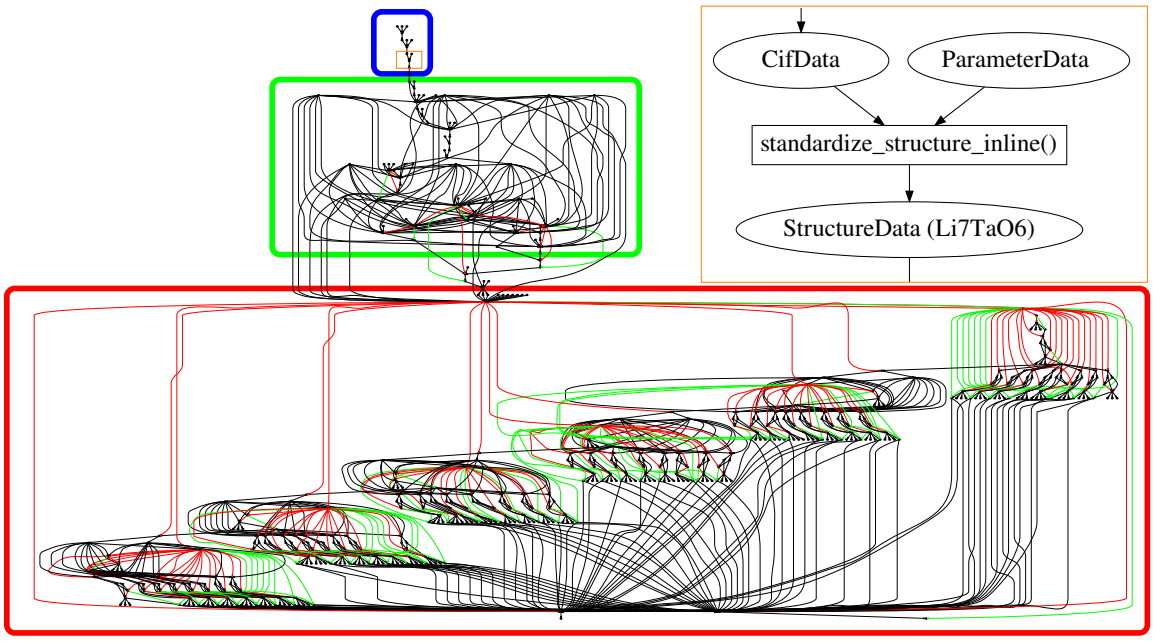

Fig. 4.3: We show above how every calculation and data-instance is stored in a directly acyclic graph in AiiDA for one specific material (Li_7TaO_6). Every node in the graph is either a calculation instance or a data instance. We enlarge, as an example, the orange inset, which shows how a CIF file (represented as a *CifData* instance) and a dictionary containing parameters (represented by a *ParameterData* instance) are input to calculation that extracts the structure and standardize it. A data being input to or output of a a calculation is shown by black connecting edges [191]. In addition, green lines denote logical provenance (a workflow returning a data instance) and red lines refer to operational provenance (a workflow calling a workflow or calculation). The subgraph corresponding to the structure ingestion is given inside the blue rectangle; the subsequent calculations of band structures, variable-cell relaxations, and fitting of the pinball model are inside the green rectangle, while the calculation of the diffusion coefficient with the pinball model at one temperature is shown in the red rectangle.

4.2.2 Structure ingestion

CIF files of all Li-containing structures are retrieved from two structural repositories, namely the Inorganic Crystal Structure Database (ICSD) [301] and the Crystallography Open Database (COD) [285], using tools that are provided by AiiDA. Here, we disregard structures that have partial occupancies or attached hydrogen. This is mainly due to the complexity of creating different derivative configurations, that usually require sampling strategies [339, 340]. The additional refinement of CIF-files is described in the work by Mounet *et al.* [187]. We employ the same protocol, using COD-tools [341] to standardize the CIF-files, and the structure-matcher of pymatgen [342] to compare crystal structures using the CMPZ-algorithm [343] in order to remove duplicates and work with unique structures. Parameters used and additional details are given in Sec. 4.5.1.

4.2.3 Structural properties

Additional filters are applied to exclude certain elements: hydrogen-containing compounds (because the effect of light hydrogen on Li motion in the pinball model has not been studied), and elements that are very rare, or dangerous (details given in Sec. 4.5.2). An additional filter is applied on atomic distances to exclude common organic compounds and structures where atomic distances are so small that we have to assume a corrupted or incorrect representation (additional details given in Sec. 4.5.3).

4.2.4 Electronic structure

In order to estimate whether a structure is electronically insulating, we perform a single SCF calculation at the experimental geometry using density-functional theory (DFT). While DFT generally underestimates the electronic band gap of a material, one observes qualitative agreement with experimental measurements. This allows us to employ such an inexpensive single-point calculation as an estimate [344–346]. We perform all DFT simulations in this work with the pw.x code, part of the Quantum ESPRESSO distribution [181], and use PBE [135] as the exchange-correlation functional. We always take pseudopotentials and cutoffs from the Standard Solid-State Pseudopotential (SSSP) Efficiency 1.0 library [245], that verifies pseudopotentials from different methods and libraries [347–352]. For this initial estimate of the electronic structure we use Marzari-Vanderbilt cold smearing [353] (additional details given in Sec. 4.5.4). A system is judged as insulating if the lowest state of the conduction band shows negligible electronic occupation (see Sec. 4.5.4), which is a function of the band gap. This is generally underestimated by PBE, but the criterion we chose is not too strict. For all insulating structures, we proceed with a variable-cell relaxation to the ground-state geometry, as explained in Sec. 4.5.5.

4.2.5 Diffusion in the pinball model

Supercells for molecular dynamics simulations are created from every relaxed structure as specified in Sec. 4.5.6, with a minimum distance criterion d_{inner} = 8 Å between opposite faces. The Hamiltonian of the pinball model [248] is:

$$\begin{aligned}\mathscr{H}_P =& \frac{1}{2}\sum_{p}^{P} M_p \dot{\boldsymbol{R}}_p^2 + \alpha_1 E_N^{P-P} + \alpha_2 E_N^{H-P} \\ &+ \beta_1 \sum_{p}^{P} \int n_{R_{H_0}}(\boldsymbol{r}) V_p^{LOC}(\boldsymbol{r}) d\boldsymbol{r},\end{aligned} \tag{4.1}$$

where $\boldsymbol{R}_p$ are the positions of pinballs (i.e. the Li ions) and $\dot{\boldsymbol{R}}_p$ their velocities; E_N^{P-P} is the electrostatic interaction between the pseudopotentials cores of the pinballs, E_N^{H-P} the interaction between the pinballs and the host lattice, V_p^{LOC} the local pseudopotential of a Li core and its 1s electrons, and $n_{R_{H_0}}(\boldsymbol{r})$ is the frozen charge density of the system that parametrically depends only on the ground state positions of the host lattice $\boldsymbol{R}_{H_0}$. With respect to the original formulation [248], we neglect

the non-local interactions of the pinball pseudopotential core with the frozen wavefunctions of the system. As discussed in the same reference, this term adds some accuracy, but comes at a higher computational cost. The local pinball of Eq. (4.1) used in this work has only quadratic scaling with system size, compared to cubic scaling when including non-local interactions. For all supercells with up to 500 atoms we fit the parameters α_1, α_2 and β_1 for the pinball Hamiltonian, with details for the fitting given in Sec. 4.5.7. Larger supercells are discarded from the screening, due to the computational costs.

All structures that are successfully fitted are passed to the diffusion workflow, that converges the diffusion coefficient at a given temperature to a desired threshold. The target temperature is 1000 K, and independent blocks sampling the canonical ensemble (constant number of particles, volume and temperature) are obtained as specified in Sec. 4.5.8. For each block, the tracer diffusion coefficient of Li D_{tr}^{Li} is calculated from the mean-square displacement as [270, 271]:

$$\begin{aligned} D_{tr}^{\mathrm{Li}} &= \lim_{t\to\infty} \frac{1}{6t} \langle \mathrm{MSD}(t) \rangle_{NVT} \\ &= \lim_{t\to\infty} \frac{1}{6t} \frac{1}{N_{\mathrm{Li}}} \sum_{l}^{\mathrm{Li}} \left\langle |\boldsymbol{R}_l(t+\tau) - \boldsymbol{R}_l(\tau)|^2 \right\rangle_\tau , \end{aligned} \tag{4.2}$$

where $\langle \cdots \rangle_{NVT}$ indicates the average over the canonical ensemble sampled ergodically by the molecular dynamics simulation, replacing thus the ensemble average with a time average $\langle \cdots \rangle_\tau$. We perform a linear regression of MSD(t) between 8 ps and 10 ps in order to extract the diffusion coefficient from the slope the MSD in the diffusive regime. The regime between 8 ps and 10 ps offers high statistical accuracy and lies in the diffusive regime for fast ionic conductors [354]. The uncertainty of the diffusion is estimated from the variance of this quantity in the independent blocks. For all analysis of the trajectories, we use tools of our open-source Suite for Analysis of Molecular Simulations (SAMOS) [355].

4.2.6 First-principles molecular dynamics

For structures showing significant diffusion in the pinball model at 1000 K, we calculate the diffusion coefficient at the same temperature with FPMD. However, we exclude structures that are referred to as unstable in the experimental reference entered into the databases, or that are already well-known ionic conductors, in order to focus the computational time on systems that are not being studied actively in the literature, since the main purpose of this work is screening for novel ionic conductors. We perform Born-Oppenheimer molecular dynamics, with details given in Sec. 4.5.9, and estimate the diffusion coefficient also using Eq. (4.2).

For structures that show significant diffusion in the FPMD simulations at 1000 K, we calculate the diffusion coefficient at three lower temperatures, namely 750 K, 600 K, and 500 K, which are equidistant on the inverse temperature scale of the Arrhenius plot. We fit the slope of the MSD, given by Eq. (4.2), in custom intervals and perform block analysis for an estimate of the statistical error of the diffusion [270, 354]. For the structures that show significant diffusion also at the lowest

temperature, we estimate the activation energy of diffusion from a linear fit to the Arrhenius behavior. We use Bayesian error propagation to report the statistical error of the activation energy.

For several structures, we calculate the Li-ion (probability) density $n_{Li}(\boldsymbol{r})$ to visualize connected diffusive components in the system:

$$n_{Li}(\boldsymbol{r}) = \left\langle \sum_{l}^{Li} \delta(\boldsymbol{r} - \boldsymbol{R}_l(t)) \right\rangle_t , \tag{4.3}$$

where l runs over the Li ions in the system, whose positions at time t are given by $\boldsymbol{R}_l(t)$, and the angular brackets $\langle \cdots \rangle_t$ indicate a time/trajectory average. In practice, we replace the delta function by a Gaussian with a standard deviation of 0.3 Å, and perform the summation on a grid (of 10 points per Å in every direction), as implemented in SAMOS [355]. To show Li-ion densities, we plot isosurfaces at values of 0.1, 0.01, and 0.001 Å^{-3} in cyan, blue, and purple, respectively.

4.3 Results and discussion

Downloading all Li-containing compounds in the ICSD [301] and COD [285] structural repositories results in 8627 and 7228 entries, respectively. The first filter ensures that structures have no attached hydrogens and no partial occupancies, and leads to 3956 and 3777 structures from the ICSD and COD, respectively. We extract a total of 7472 valid structures (261 CIF-files could not be interpreted by the pymatgen [342] CIF-reader) from the CIF-files, of which we find 4963 to be unique using the pymatgen structure matcher. 1362 of these unique structures pass also the filters on elements and bond distances (see Secs. 4.5.2 and 4.5.3), and of these 1016 are insulators at the PBE-DFT level, according to the criterion explained in Sec. 4.5.4. 971 of the 1016 insulators could be successfully relaxed, the remainder failing due problems with the iterative self-consistency. A histogram of the volumes after relaxation divided by the volume before relaxation (i.e. the experimental volume from the database), as shown in Fig. 4.4, reveals that a structure is more likely to expand than contract, as expected for the PBE functional. While the volume changes are rather small (peaked at 4%, i.e. 1.3% per direction for isotropic expansion) for almost all cases, there are outliers that expand or contract substantially, likely due to van der Waals interactions.

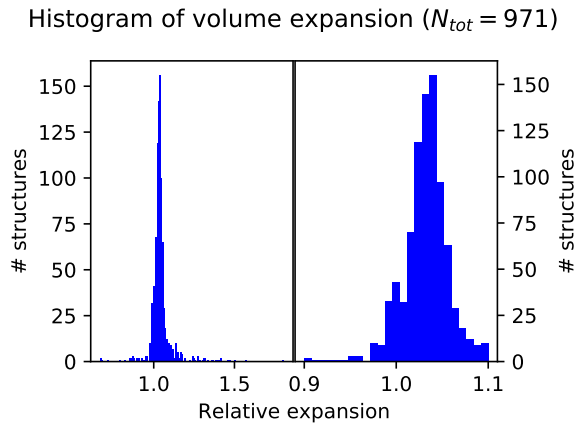

Fig. 4.4: Histogram of the relative volume expansion between the experimental and the calculated ground-state volumes (at the PBE level) for 971 structures studied. In the left panel, we show the entire histogram, on the right we zoom on the region between 0.9 and 1.1.

We were able to obtain the coefficients α_1, α_2, and β_1 of Eq. (4.1) in 916 cases, of which 903 are judged to be sufficiently good based on the r^2 correlation between DFT and pinball forces. Failure to fit in the remaining cases is mainly due to failures of the iterative self-consistent convergence for training configurations. The diffusion workflows in the pinball model completed successfully in 796 cases, summing up to a simulation time of 7.6 μs. Reasons for this 12% failure rate are drifts in the constant of motion and the inability to converge the diffusion coefficient. We take the 200 systems with the highest diffusion in the pinball model at 1000 K, and exclude from this set systems that either have been reported as good ionic conductors in the literature and have been studied independently by several groups, or that are referred to as unstable at room temperature in the experimental reference.

Before discussing the results of FPMD, we give an overview of the structures that we exclude because they have been already studied substantially in the literature. The classification of all know ionic conductors found at this stage of the screening allows for an assessment whether the screening can be considered holistic, meaning that the entire compositional variety is captured. Known LISICON structures that we find are $Li_7P_3S_{11}$ [209], Li_4GeS_4 [356], and Li_4SnS_4 [357] from the LISICON family, and $Li_5La_3Ta_2O_{12}$ and $Li_5La_3Nb_2O_{12}$ [213, 229, 358, 359] from the garnet family. The cubic garnets are generally reported with partial occupancies on the Li sites, which is the reason we do not have the prototypical cubic garnet structure $Li_7La_3Zr_2O_{12}$ among our candidates. However, $Li_5La_3Ta_2O_{12}$ (ICSD entry 68252) contains no partial occupancies and was therefore found in the screening. We find also many NASICONs such as $Li_3Sc_2P_3O_{12}$ [360], $Li_3In_2P_3O_{12}$ [313], $LiZr_2P_3O_{12}$ [312], $LiTi_2P_3O_{12}$ [361], and $Li_4ZnP_2O_8$ [362]. We find in the screening both oxide and sulphide argyrodytes, namely Li_6PS_5I [363], Li_6PClO_5 and Li_6PBrO_5 [309], and $Li_5PS_4Cl_2$ [210].

In the remainder, we focus on the remaining 132 materials that were studied with accurate FPMD, summing up to a simulation time of 45 ns. Due to the computational cost of FPMD, obtaining more simulation time per compound, or treatment of more candidates at an *ab initio* level of theory was not feasible. We divide the analysis of candidates into four categories, based on the observed diffusion in FPMD:

(A) Structures that show diffusion at high (1000 K) and at low (500 K) temperature are classified as fast-ion conductors.

(B) Structures that show diffusion at high temperature, but either show slow diffusion at lower temperatures, or could not have their diffusion resolved at lower temperature, are classified as potential ionic conductors.

(C) Structures that show negligible diffusion at high temperature are classified as not being ionically conducting.

(D) Structures where, due to computational difficulties, we can make no precise statements, but that could be good candidates based on the results of the simulations of the pinball model alone.

Unitcell	DB	DB-id	Supercell	Volume change	T^{sim}_{500}	T^{sim}_{600}	T^{sim}_{750}	T^{sim}_{1000}
$Li_1Ga_1I_4$	ICSD	60850	$Li_4Ga_4I_{16}$	19.5%	726.4	726.4	552.1	218.1
$Li_1Ga_1Br_3$	ICSD	61338	$Li_8Ga_8Br_{24}$	14.2%	406.8	435.8	232.4	58.2
$Li_2Cs_1I_3$	ICSD	245988	$Li_8Cs_4I_{12}$	-13.1%	726.4	726.4	348.7	160.0
$Li_{10}Ge_1P_2S_{12}$	-	-	$Li_{20}Ge_2P_4S_{24}$	4.8%	726.4	493.9	174.3	218.1
$Li_5Cl_3O_1$	ICSD	419852	$Li_{40}Cl_{24}O_8$	0.0%	726.4	726.4	232.4	261.8
$Li_5Cl_3O_1$	ICSD	419852	$Li_{20}Cl_{12}O_4$	0.0%	726.4	726.4	726.4	218.1
$Li_7Ta_1O_6$	ICSD	74950	$Li_{56}Ta_8O_{48}$	4.0%	552.1	639.2	203.4	72.7

Table 4.1: For all structures that we classify as fast-ionic conductors, we report the stoichiometric formula, the database and identifier of the repository this structure originates from, the formula of the supercell used, the relative volume change during the variable-cell relaxation, and the simulation times at 500 K, 600 K, 750 K, and 1000 K (in ps).

4.3.1 Fast-ionic conductors

This first group includes ionic conductors that could be of significant interest for application as solid-state electrolytes. Due to their fast conduction, we are able to resolve the diffusion also at lower temperatures and extract the activation barriers, which are shown in Fig. 4.5. To our knowledge, they have not been studied extensively or at all by experiments, apart from LGPS. The provenance (ICSD/-COD entries), volume change during cell relaxation, and simulations times of the candidates in this group are given in Table 4.1.

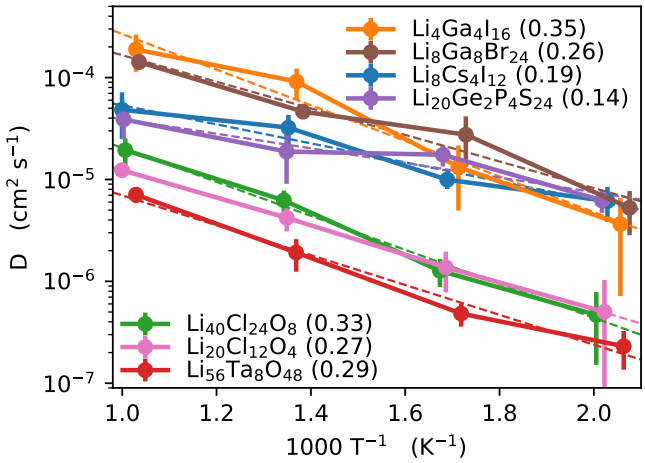

Fig. 4.5: Diffusion from FPMD for $Li_4Ga_4I_{16}$, $Li_7Ga_8Br_{24}$, $Li_8Cs_4I_{12}$, $Li_{20}Ge_2P_4S_{24}$, $Li_{40}Cl_{24}O_8$, $Li_{20}Cl_{12}O_4$, and $Li_{56}Ta_8O_{48}$ as solid lines in orange, brown, blue, violet, green, pink, and red, respectively (we refer to the composition of the actual supercell studied). The line of best fit is shown as a dashed line of the same color. The activation barriers, extracted from the slope of the fit, are in the legend (in brackets) in eV.

$Li_{20}Ge_2P_4S_{24}$: The well-known superionic conductor $Li_{20}Ge_2P_4S_{24}$ [204–206, 211, 239] (LGPS) is included by us in the set of candidates as a reference, since it constitutes one of the best Li-ion conductors. The MSDs (shown in Fig. D.1) are compatible with fast-ion diffusion at every temperature studied. We show the MSDs extracted at 750 K in the top left panel of Fig. 4.6. We find an activation barrier of 0.14 eV, which is slightly lower than previous computational studies, but certainly within the error due to finite statistics in FPMD: Marcolongo and Marzari [211] estimate a value of 0.18 eV, Ong *et al.* [204] of 0.21 eV.

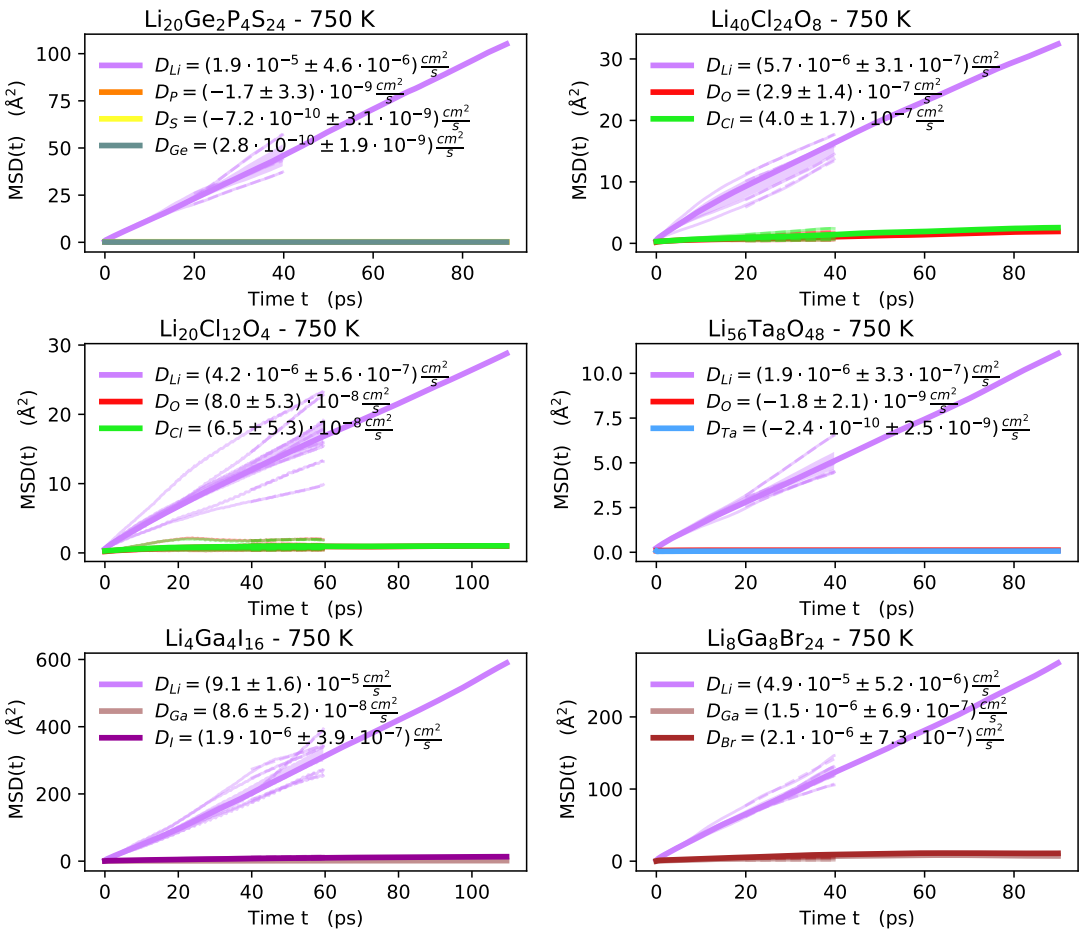

Fig. 4.6: We show the MSD of all species at 750 K from FPMD in $Li_{20}Ge_2P_4S_{24}$, $Li_{40}Cl_{24}O_8$, $Li_{20}Cl_{12}O_4$, $Li_{56}Ta_8O_{48}$, $Li_4Ga_4I_{16}$, and $Li_8Ga_8Br_{24}$ (left to right and top to bottom). The MSD of the entire trajectory is shown as a solid line for each species, calculated using Eq. (4.2). The thin lines show the tracer diffusion calculated for different blocks of the trajectory; from each such line, we calculate the mean and error of the diffusion coefficient from the slope of the linear fit between 20 ps and 30 ps (dashed lines).

LGPS has been classified via simulation as a three-dimensional ionic conductor, however with a predominant diffusion along the *c*-axis within characteristic channels [205, 364]. We reproduce this diffusion behavior, as shown by the Li-ion density in Fig. 4.7.

Li_5Cl_3O: We study this material at two different supercell sizes to control for finite size effects, namely $Li_{40}Cl_{24}O_8$ and $Li_{20}Cl_{12}O_4$. The structure was first reported by Reckeweg *et al.* [365], and its usage as a SSE is speculated in the reference, but we found no evidence that this was ever tested. $Li_{20}Cl_{12}O_4$/$Li_{40}Cl_{24}O_8$ are simulated with FPMD at 500 K for 726 ps/581 ps, at 600 K for 726 ps/523 ps, at 750 K for 726 ps/232 ps, and for 218 ps/262 ps at 1000 K. A certain degree of host-lattice diffusion is observed, which could indicate an instability of the lattice at the increased temperatures of simulation. The MSD of every species at 750 K are shown in the top right and center left panels of

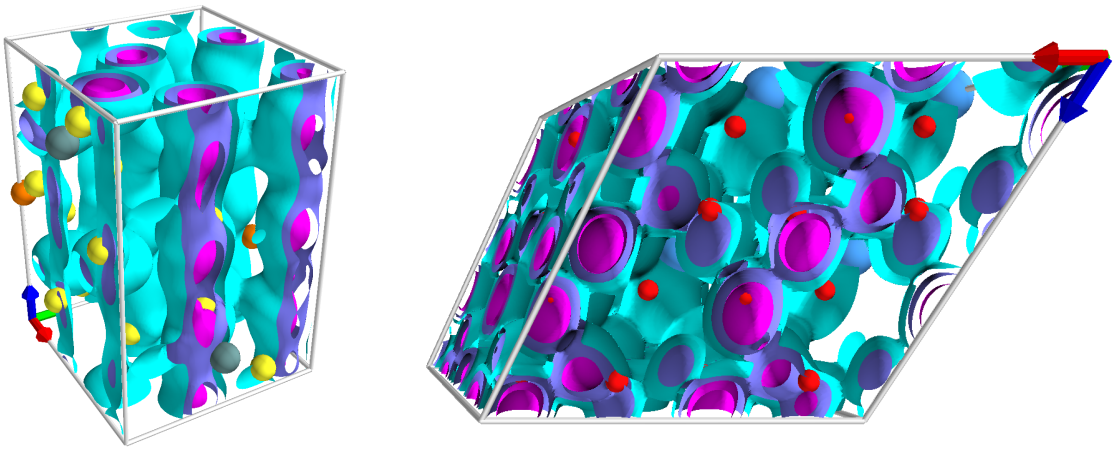

Fig. 4.7: (Left) Li-ionic density of $Li_{20}Ge_2P_4S_{24}$ at 500 K from FPMD. The unidimensional channels along the *c*-axis (along blue arrow) are clearly visible; see text for detail on how we calculate the density and the isosurface levels. (Right) Li-ionic density of $Li_{56}Ta_8O_{48}$ at 500 K from FPMD.

Fig. 4.6, while the other temperatures can be found in Figs. D.4 and D.5. The Arrhenius behavior is plotted in Fig. 4.5 with the other candidates of this group. We estimate the barriers as 0.29 eV and 0.27 eV for the larger and smaller supercell, respectively. The diffusion coefficients are compatible for the two supercells, indicating that our results are not subject to large finite-size effects. The barrier is certainly low enough to classify this material as a candidate solid-state electrolyte. However, the synthesis of the material involves elemental lithium, which means that producing a purely ionic sample without mtextitet al.lic side phases could be challenging for experimental validation.

Li_7TaO_6: This Li-tantalate is studied in its supercell $Li_{56}Ta_8O_{48}$. Its ionic conductivity was studied experimentally by Delmas *et al.* [366], Nomura and Greenblatt [367], and by Mühle *et al.* [368], showing a high activation barrier of 0.66 eV – 0.67 eV. The latter two references also observe a regime of low energy barrier, at low temperatures (< 50 °C) for Nomura and Greenblatt, and at high temperatures (< 400 °C) for Mühle *et al.* Our simulations of 73 ps, 203 ps, 640 ps and 552 ps at 1000 K, 750 K, 600 K and 500 K, respectively, show fast-ionic diffusion within a stable host lattice and result in an activation barrier of 0.29 eV. The MSDs for all species extracted from the simulation at 750 K are shown in the center right panel of Fig. 4.6 (all temperatures plotted in Fig. D.7). We plot three isosurfaces of the Li-ion densities, calculated from the lowest temperature (500 K) simulation, in the right panel of Fig. 4.7, giving evidence for three-dimensional diffusion and a single connected component of diffusion. Although the material has been studied experimentally, the high ionic diffusion from FPMD calls for additional studies for its application as a solid-state electrolyte. The substitution of Ta with aliovalent dopants could change the Li-ion concentration and improve the Li-ionic conductivity, as shown in the garnet structure [214].

$LiGaI_4$ and $LiGaBr_3$: We also find that the Ga-doped halides $LiGaI_4$ and $LiGaBr_3$ could show very promising Li-ion diffusion. $LiGaBr_3$ was first synthesized by Hönle and Simon [369], together with

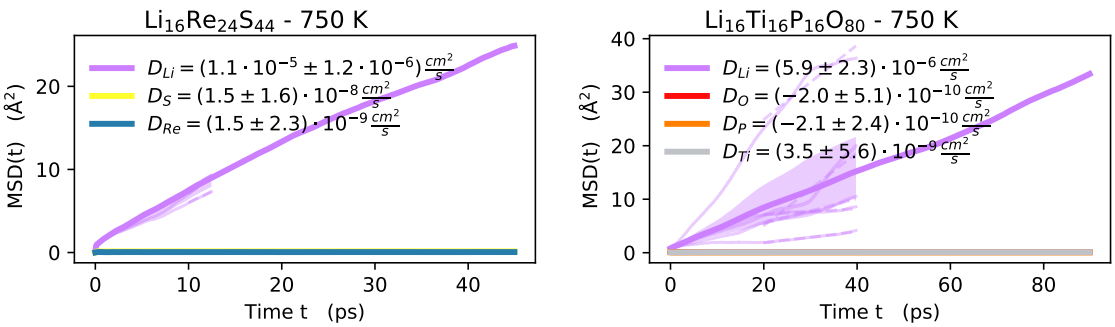

Fig. 4.8: MSD of all species in $Li_{16}Re_{24}S_{44}$ (top) and $Li_{16}Ti_{16}P_{16}O_{80}$ (bottom) at 750 K from FPMD. As explained in the caption of Fig. 4.6, the MSD of the entire trajectory is plotted as a solid line for each species, while thin lines show the tracer diffusion calculated for different blocks of the trajectory, allowing for an estimate of the error for the MSD, which is given by the shaded area.

$LiGaBr_4$, evidence that Ga can change oxidation states in the structure. The same reference reports this material as a layered structure $Li_2^+[Ga_2Br_6]^{2-}$. $LiGaI_4$ was synthesized by Hönle *et al.* [370] The volume expansion of 19.5% and 14.2% during the variable-cell relaxation hints at an instability of the structure, likely due to the lack of van-der-Waals dispersion corrections, and imply that our results from the FPMD should be interpreted with care, and that such interactions should be included in future screenings. For example, we find that $LiGaI_4$ contracts by 1.03% during a variable-cell relaxation using the same parameters as in Sec. 4.2.4 and adding the Grimme dispersion correction [371]. We plot the MSD for the supercells $Li_4Ga_4I_{16}$ and $Li_8Ga_8Br_{24}$ at 750 K in the bottom panels of Fig. 4.6 (other temperatures are in Figs. D.3 and D.2). We observe high ionic diffusion of Li ions, but also non-negligible diffusion of the sublattice, further signs of instabilities in this material. Since indium-doped LiBr, Li_3InBr_6 is a known ionic conductor [226], our results suggest studying in greater detail also the Ga-doped Li bromide and Li iodide. The same compounds were also proposed as SSE candidates in the high-throughput study by Muy *et al.* [319]

Li_2CsI_3: The Cs-doped Li-iodide Li_2CsI_3 was first synthesized in 1983 [372] in monoclinic phase studied by us. In this structure, we observe a volume contraction by 13.1%. Our simulations of 160 ps at 1000 K, 349 ps at 750 K and 726 ps at 500 K and 600 K reveal a high diffusion for Li ions, but also significant diffusion of the host lattice (see Fig. D.6). It remains to be studied with different methods whether the host lattice is stable at room temperature and whether the host-lattice instability is an artifact of our simulations. Nevertheless, the high Li-ion diffusion from FPMD make this material another candidate solid-state electrolyte.

4.3.2 Potential fast-ionic conductors

We portray in the following all materials where we observe ionic diffusion at high temperature, but where our FPMD simulations either do not show significant diffusion at low temperature or where we cannot resolve the low-temperature diffusion, either because we cannot reach the necessary time scales with FPMD or because we did not attempt to simulate the low-temperature regime. We order

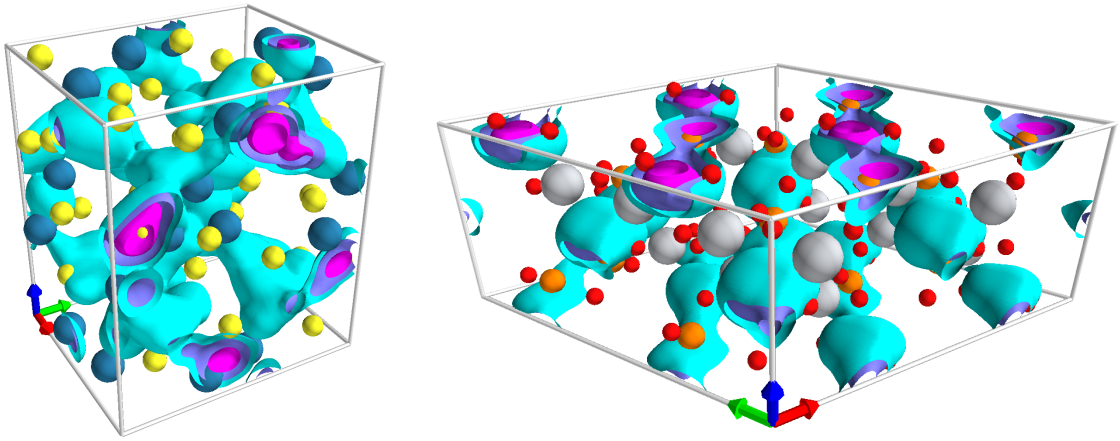

Fig. 4.9: Li-ionic density of $Li_{16}Re_{24}S_{44}$ (left) and $Li_{16}Ti_{16}P_{16}O_{80}$ (right) at 500 K from FPMD.

the results by the likelihood that these materials show fast-ionic diffusion at all temperatures. We stress that many of the materials might show significant ionic conductivity in experiments also at low temperatures. The inability of our simulations to resolve the diffusion at lower temperature is due to the fact that structures with a lower diffusion coefficient require longer simulation times, which often cannot be afforded with FPMD. For example, Murugan and Weppner [282] report an ionic conductivity of 0.02 S cm^{-1} for cubic LLZO at 500 K, which results in a tracer diffusion 2×10^{-7} cm^2 s^{-1}, assuming a Haven ratio of 1 [211]. Given this diffusion coefficient, an ion travels in 100 ps on average a mean-squared distance of $6D_{tr}\,t \approx 1$ Å^2. It is obvious that a simulation of ~100 ps cannot resolve the diffusive behavior of Li ions in the garnet at 500 K. Therefore the following materials could be ionic conductors also at ambient temperatures.

$Li_4Re_6S_{11}$: We study $Li_4Re_6S_{11}$, first synthesized by Bronger *et al.* [373] in its supercell $Li_{16}Re_{24}S_{44}$. We observed a volume expansion of 2.61% during the cell relaxation. Our simulations at 500 K (for 87.1 ps), 600 K (174 ps), 750 K (87.2 ps) and 1000 K (290.8 ps) give evidence for high ionic diffusion. We show this at 750 K in Fig. 4.8, and for the other temperatures in Fig. D.8. The short simulations do not allow to resolve the diffusion at low temperature, which forbids us to classify this material into the group fast-ionic conductors. Nevertheless, the molecular dynamics dynamics are compatible with diffusive behavior also at low temperature. In addition, we find the host lattice to be stable during the dynamics. We show the Li-ion density, calculated from the simulation at 500 K, in the left panel of Fig. 4.9, which classifies this material as a three-dimensional ion conductor.

$LiTiPO_5$: The oxyorthophosphate α-$LiTiPO_5$ [374] is studied in its supercell $Li_{16}Ti_{16}P_{16}O_{80}$. We observed a volume expansion of 5.76% during the cell relaxation. The host lattice is dynamically stable and shows no diffusion. Our simulations of at least 232.4 ps show highly diffusive behavior for the Li ions at high temperature, and significant diffusion diffusion at low temperature, but are not accurate enough to allow for a quantitative results at low temperature. The MSD obtained from our simulations is shown in the right panel of Fig. 4.8 for 750 K (other temperatures in Fig. D.9). The

Li-ion density at 500 K, illustrated in the right panel of Fig. 4.9, gives evidence for uni-dimensional conductive pathways in this material.

Li_6PS_5I: The lithium argyrodite Li_6PS_5I is simulated in the supercell of $Li_{48}P_8S_{40}I_8$. We are not able to resolve the diffusion in the diffusive regime precisely, and classify also this material as a potential ionic conductor. We became aware afterwards that its ionic conductivity is known from experiments and simulation [375].

Others: We report in the following the materials that show significant diffusion at high (1000 K) and intermediate (600 K and 750 K) temperatures, but no diffusion at low (500 K) temperature. (1) The first is $Li_5BS_4O_{16}$ [376], studied in its supercell $Li_{20}B_4S_{16}O_{64}$. Our simulations of 218 ps at 1000 K and 610 ps at the lower temperatures give evidence (see Fig. D.11) for fast-ionic diffusion at high and intermediate temperatures, within a stable host lattice. The diffusion is three-dimensional, as illustrated by the Li-ion density at 600 K, given in Fig. 4.10. At 500 K, there is no or negligible diffusion observed in the simulation. (2) We simulate $LiTaGeO_5$ [377] in the supercell $Li_4Ta_4Ge_4O_{20}$ for at least 145 ps at the four different temperatures. The reference reports a phase transition at 231 K to a disordered phase. Our conclusions only adhere to the ordered phase. The structure shows high ionic diffusion at high and intermediate temperatures, but our 500 K simulation show no diffusive behavior. The respective MSDs computed from the trajectories are shown in Fig. D.12. (3) For $LiIO_3$, which we study in its supercell $Li_8I_8O_{24}$, we observe a large volume expansion of 15%, and significant host-lattice diffusion. The diffusion of Li ions is considerable at high temperatures, but drops to negligible diffusion at low temperature (see Fig. D.15). This compound is suggested by Muy *et al.* [319] as a candidate SSE.

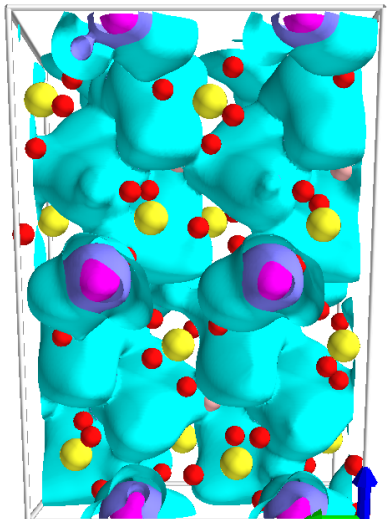

Fig. 4.10: Li-ionic density of $Li_{20}B_4S_{16}O_{64}$ at 600 K.

In the following, we report the candidate materials that show significant diffusion at high temperature, but where the diffusion becomes very small or negligible at intermediate temperatures (600 K or 750 K). (1) The β-eucryptite $LiAlSiO_4$ was first referenced by Pillars *et al.* [284], and its ionic conductivity was studied experimentally in 1980 [294], where a uni-dimensional transport mechanism was observed. A more recent computational and experimental study [378] confirmed this behavior. We also observe the uni-dimensional transport along the c-axis of this material with our simulation in the supercell $Li_{12}Al_{12}Si_{12}O_{48}$. The host-lattice remains stable during the dynamics, whereas Li ions show significant diffusion at high temperature. At 600 K the diffusion is negligible (see Fig. D.13). (2) $Li_2Mg_2S_3O_{12}$ [379], that we studied in its supercell $Li_8Mg_8S_{12}O_{48}$ also shows significant diffusion at high temperature, that however drops significantly when lowering the temperature,

and becomes very low around 600 K. A derived structure (doped with Fe and V) was studied as a cathode material [380]. (3) We study the perthioborate [381] $Li_2B_2S_5$ in its supercell, $Li_8B_8S_{20}$. In this structure, Li-ions are intercalated between layers of $Be_2S_5{}^{2-}$. The diffusion at high temperature is substantial (see Fig. D.16). Despite the low diffusion at low temperatures, promising results at high temperature for $Li_2B_2S_5$ suggest that the family of perthioborates could be studied more extensively. The high-throughput screening by Sendek *et al.* [320] suggests this compound as a candidate SSE. (4) $Li_6Y(BO_3)_3$ was researched for potential application in solid-state lasers [382]. We simulate its supercell $Li_{24}Y_4B_{12}O_{36}$ with FPMD, and observe fast-ionic diffusion at 1000 K and 750 K, which is shown in Fig. D.16. At lower temperature (600 K and below), the diffusion becomes too small detect with FPMD. From the Li-ion densities (shown in Fig. 4.11) it is evident that in-plane diffusive pathway in this material is no longer active at lower temperatures. This is consistent with recent work on the same compound by Lopez-Bermudez *et al.* [383], who estimated the barriers to Li-ion diffusion using DFT climbing nudged elastic band calculations. (5) We simulate Li_3CsCl_4 [384] in its supercell, $Li_{24}Cs_8Cl_{32}$. The two-dimensional ionic diffusion at elevated temperatures (see Fig. 4.12) drops substantially at 600 K, as shown in Fig. D.18. (6) Also the orthodiphosphate $Li_9Ga_3(P_2O_7)_3(PO_4)_2$ [385], studied as $Li_{18}Ga_6P_{16}O_{58}$, displays significant diffusion at high temperatures, but negligible diffusion at 600 K (see Fig. D.19). A Va-analogue of this structure was researched [386] as a cathode material.

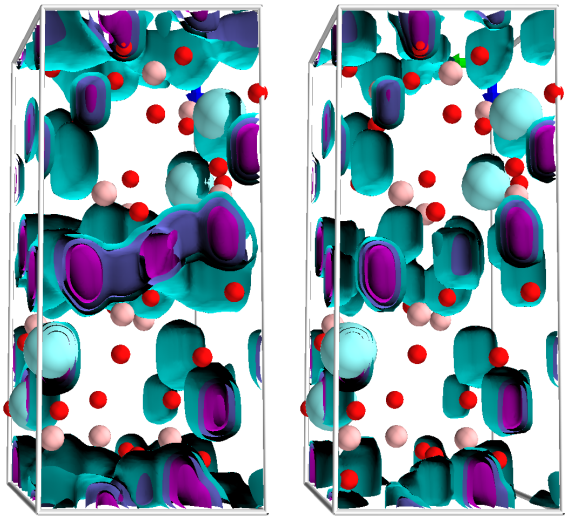

Fig. 4.11: Li-ionic density of $Li_{24}Y_4B_{12}O_{36}$ at 750 K in the left panel and 500 K on the right panel.

In the following, we describe structures that show only diffusion at high temperature (1000 K), but no diffusion at lower temperatures (750 K, 600 K, and 500 K). (1) As a first example, $Li_7RbSi_2O_8$ was synthetized accidentally by Bernet and Hoppe [387] as a new type of orthosilicate. We simulate the supercell
$Rb_8Li_{12}B_4P_{16}O_{56}$ and observe diffusion only at high temperature. (2) The lithium disulfate $Li_2S_2O_7$ [388], studied as $Li_{16}S_{16}O_{56}$, also shows diffusion only at 1000 K and none at the lower temperatures. (3) $Li_2In_2GeS_6$ and (4) $Li_2ZnSnSe_4$ were researched independently [389, 390] for the nonlinear optical properties in the infrared spectrum. We simulated the respective supercells $Li_{16}In_{16}Ge_8S_{48}$ and $Li_{16}Zn_8Sn_8Se_{32}$, and both structures show diffusion at 1000 K and no diffusion at lower temperatures, as can be seen in Fig. D.24 and Fig. D.22. Also (6) Li_3GaF_6, studied as $Li_{18}Ga_6F_{36}$, (7) $Li_2T_3O_7$, studied as $Li_8Ti_{12}O_{28}$, and (8) $LiMoAsO_6$, studied as $Li_8Mo_8As_8O_{48}$ show diffusion only at high temperature. The MSD are shown in Figs. D.23, D.25, and D.26, respectively.

We also study an additional 21 structures at 1000 K alone, without simulating the diffusion also at lower temperatures. We find them to show non-negligible diffusion, but the diffusion is not high enough to warrant a costly estimate of the diffusion at lower temperature and extraction of the barrier, or because very similar compounds have their activation barrier computed. We find diffusion in the doped halides $LiGaCl_3$ [391], $LiGaBr_4$ [369], Li_6MgBr_8 [392], and $LiAuF_4$ [393]. We also calculate the diffusion of Li ions in the phosphides Li_3P_7 [394] and LiP_7 [395], the sulfides Li_3AsS_3 [396] and $LiRb_2TaS_4$ [397], and the selenides $LiAlSe_2$ [398] and $Li_2In_2SiSe_6$ [389]. The same applies to the borate $LiBS_4Cl_4O_{12}$ [399] and the NASICON-type phosphate $LiSn_2P_3O_{12}$ [400], the germanates $Li_4G_9O_{20}$ [401] $Li_2Ge_4O_9$ [402], the metaperiodate $LiIO_4$ [403], the phosphates Li_4P_{207} [404] and $LiInP_2O_7$ [405], the phenakyte Li_2SeO_4 [406], the titanate Li_4TiO_4 [407], the silicate $Li_6Si_2O_7$ [408], and the borosulfonate $LiBS_2O_8$ [409]. The materials are listed, with the supercell employed, the originating database entry, the volume expansion, and the simulation length at 1000 K in Table D.2.

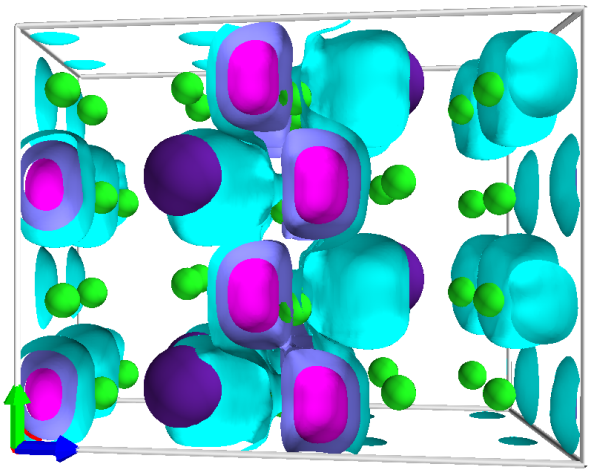

Fig. 4.12: Li-ionic density of $Li_{24}Cs_8Cl_{32}$ at 750 K.

4.3.3 Non-diffusive structures

We also find 70 materials to be not diffusive at 1000 K in our FPMD simulations. These are structures where our simulations give evidence that this structure will also not conduct in experiment, unless doped significantly. The materials are listed in Table D.3, together with the respective ICSD/COD entry, the volume change, and the simulation time. In the following, we only give a brief summary of the materials.

We observe no diffusion in the doped nitrides Li_2CeN_2, Li_5ReN_4 [410], Li_7PN_4, Li_3ScN_2 [411], Li_7NbN_4 [412], Li_3AlN_2 [413], Li_6WN_4 [414], or Li_4TaN_3 [415], nor in the niobium-doped oxynitride $Li_{16}Nb_2N_8O_1$ [416]. The doped halides $LiAuF_4$ [417] and $LiInNb_3Cl_9$ [418] also show no diffusive behavior. The borates $Li_2AlB_5O_{10}$ [419], $Li_3Sc(BO_3)_2$ [420], $Li_3GaB_2O_6$ [421], Li_2AlBO_4 [422], $Li_3GaB_2O_6$, and $Li_8Be_5B_6O_{18}$ [423] are poorly diffusing in FPMD simulations, as is also the borophosphate $Li_2NaBP_2O_8$ [424]. We also consider the phosphates $Li_2Cd(PO_3)_4$ [425], $LiPO_3$ [426], $Li_4ZnP_2O_8$ [427], and $Li_9Mg_3F_3P_4O_{16}$ [428] as poor ionic conductors at full Li-ion occupation. For the last case, this is in contradiction to the reported ionic conductivity from experiment [428]. The phosphide Li_4SrP_2 [429] is a poor ionic conductor, based on our simulations. The same applies to the silicates $LiBSi_2O_6$ [430], $L_2Si_3O_7$ [431], $LiYSiO_4$, Li_3AlSiO_5 [432], and $Li_2Si_2O_5$ [433], and the tellurates

Li_3TeO_3 [434], Li_4TeO_5 [435], and Li_6TeO_6 [436], Also the tantalate $Li_6Sr_3Ta_2O_{11}$ [437], studied for its photoluminescence, is a poor ionic conductor, as is the La-doped carbonate $LiLaC_2O_3$ [438], or the K-doped aluminate Li_4KAlO_4 [439]. The zincates, molybdates and arsenates we classify as non-diffusive are: Li_2MoO_4 [440], $LiZnAsO_4$ [441], $Li_3AlMo_2As_2O_{14}$ [442], $LiKZnO_2$ [443], Li_6ZnO_4 [444]. The last structure was confirmed to not be an ionic conductor unless doped with Nb [445]. Additional oxides that are poor ionic conductors are the germanate $Li_4Ge_5O_{12}$ [446] and the phenakite Li_2WO_4 [424]. We also find Li_3AuO_3 [447] to not be diffusive. Interestingly, a study by Filsø*et al.* [448] found this materials to be a threedimensional ionic conductor using an approximate electron-density descriptor. At full occupation with lithium, we do not see any diffusion. This is also the case for the niobate Li_4KNbO_5 [449], as well as Li_2PdO_2 [450] and Li_8PtO_6 [451].

4.3.4 Structures diffusive in the pinball model

We have 14 structure where we can not make a statement from FPMD, mostly due to frequent failures during the dynamics, especially during the self-consistent minimization of the electronic charge density. The materials are given in Table D.4 and summarized in the following.

Materials that show ionic diffusion in the pinball model are the molybdate $Li_4Mo_3O_8$, the silicate $LiTaSiO_5$ [452], the ortho-diphosphate,$Li_2P_2PdO_7$ the nalipoite Li_2NaPO_4 the layered borate $Li_3BaNaB_6O_{12}$ [453], the borates $LiNaB_4O_7$ [454] and Li_2NaBO_3 [455], and the boracite-type $Li_{10}B_{14}Cl_2O_{25}$ [456], where a transport mechanism is observed in the experiment. We also cannot study he doped halides $LiAuI_4$ [457], Li_3ScF_6 [458], and $LiNb_3Cl_8$ [459] with FPMD. The same applies to $LiAuS_4O_{14}$ [460], the NASICON $LiZr_2As_3O_{12}$ [461], and $LiAlGeO_5$ [462]. For the latter, a study employing CPMD shows no Li-ion diffusion [463].

4.3.5 Context of this screening

As described in Sec. 4.2, we screen all the Li-containing materials in the ICSD and COD experimental structure databases without partial occupancies on any site and at full Li stoichiometry for solid-state ionic conductors. This work is therefore not a complete screening of these databases. For example, another 645 (not necessarily unique) structures in ICSD & COD show partial occupancy only on Li sites and full occupancy on sites occupied by other species.

A structure with full occupancy on all Li sites should not be ionically conducting if we neglect Li diffusion via interstitial sites. Only upon the introduction of Li vacancies could the vacancy-assisted Li-ionic diffusion be unlocked. However, the fact that we find several ionic conductors can be explained. First, we conduct our computational experiments at elevated temperature, for which the Li occupations reported in CIF files, usually measured at room temperature, are merely indicative. Second, due to inherent difficulties in determining the Li-ion positions in XRD, many low-occupancy sites might have been discarded when reporting the structure. Therefore, the class of Li-ionic system at full stoichiometry and without partial occupancies contains Li-ionic conductors, as we show. Of course, screening for solid-state ionic conductors within another class of materials (systems reported with partial occupancies) should result in more candidates for solid-state electrolytes. However,

screening of structures with partial occupancies requires additional work to assess methods to find the ground-state volume for the specific potential method employed, since variable-cell relaxation can only be done at integer occupations. However, screening of structures with partial occupancies requires additional work to assess methods to find the ground-state volume for the specific potential method employed, since variable-cell relaxation can only be done at integer occupations. The strong dependence of the diffusion coefficient [196, 204, 283, 316, 318, 464] on the cell volume demands a high accuracy.

Furthermore, the creation of Li vacancies in all materials should result in new candidates, since a high diffusion upon the introduction of vacancies indicates that the structure could be doped into high ionic conductivity in experiment. This can be done for structures with or without partial occupancies. In short, the tools and methodology presented here can be used to study materials with partial occupancy at varying Li-ion concentration, for a complete screening of structural repositories for novel solid-state ionic conductors.

This first screening also allows us also to estimate how well the pinball performs in a screening scenario, since we have plenty of data to compare FPMD and pinball simulations for the same structures. In Fig. 4.13 we show the diffusion at 1000 K for 95 structures computed with FPMD (D_{FPMD} on x-axis) and the pinball model (D_{PB} on y-axis). The diffusion coefficient from FPMD is not well reproduced by the pinball model, which can have several causes. First, the local pinball could be inaccurate, compared to the non-local pinball [248]. Second, fitting the pinball model with snapshots from random displacements could result in parameters $\alpha_{1,2}$ and β_1 that do not reproduce the forces on Li ions accurately during the dynamics. Third, freezing the charge density could have a larger effect on the Li-ion dynamics than in the prototypical ionic conductors studied beforehand [248]. Last, freezing the host lattice could also have a larger effect on the Li-ion dynamics than anticipated. For another screening with the pinball model, especially at varying stoichiometry, the accuracy of the pinball model should be improved by studying these effects individually. Nevertheless, while we see many false positives in our screening, it is critical to state that so far no false negatives have emerged. A ~50% ratio of false positives is very much tolerable for screening application, and outweighed by the low computational cost of the pinball, for which we give additional details in Sec. 4.6. To assess further the quality of the pinball model as a screening criterion, we take all

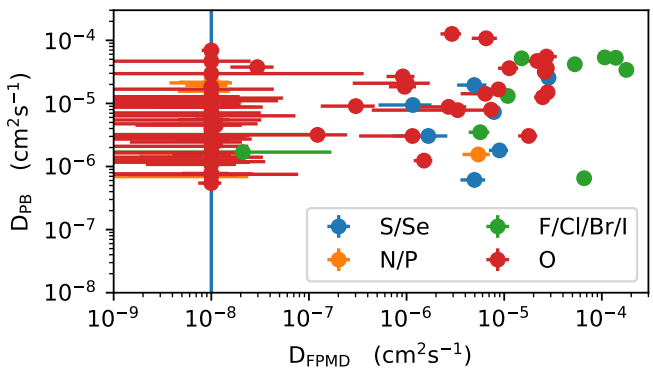

Fig. 4.13: Diffusion FPMD vs pinball model used in the screening at 1000 K for 95 materials, color-coded by the predominant anion. The vertical line at 10^{-8} gives the limit below which we cannot converge the slope of the MSD with FPMD, therefore we set this as the lower boundary for diffusion.

candidates that were studied with FPMD and split the set into four quartiles, sorted by the diffusion in the pinball model (also at 1000 K). For each quartile we calculate the success rate, which is the percentage of candidates that show diffusion above 10^{-7} cm^2 s^{-1} in FPMD (at 1000 K). For the top quartile, the success rate is 71%, which drops to 36%, 33%, and 21% for the second, third, and forth quartile, respectively. This is strong evidence that the diffusion coefficient measured with the pinball model can be used effectively to find fast-ionic conductors: the higher the diffusion in the pinball model, the higher the probability that the same structure will conduct in FPMD.

The same procedure, namely splitting the set of candidates into quartiles based on the diffusion coefficient in the pinball model, allows to find an upper bound for the presence of false negatives. In the bottom quartile, the success rate was 21%, which means that the success rate for less diffusing structures will be lower, if we assume that the success rate is monotonically declining as a function of the diffusion coefficient in the pinball model. We can therefore define an upper bound of 21% of false negatives in our screening, that is structures that are diffusive but were not discovered as fast-ion diffusors in our screening. Such high value, although being an upper bound, motivates further screening studies using different methods.

4.4 Conclusions & outlook

We presented a computational screening of two large repositories of experimental structures, the ICSD [301] and COD [285], totalling ~1'400 unique crystal structures. We used the Kohn-Sham band gap from density-functional theory at the PBE level to find electronically insulating systems and filtered for systems that are likely to display fast-ionic diffusion by harnessing the computational efficiency of the pinball model [248] with molecular dynamics, which captures the collective effects of Li-ion migration, totalling 7.6 μs of simulation time. About 130 structures that showed high Li-ion diffusion in the pinball model were simulated with accurate first-principles molecular dynamics for a total of 45 ns at high and intermediate temperatures, enabling also the extraction of the activation energy from first principles. We found five materials with fast ionic diffusion, some in the range of the well-known superionic conductor $Li_{10}GeP_2S_{12}$, as for example the Li-oxide chloride Li_5Cl_3O, the doped halides Li_2CsI_3, $LiGaI_4$, and $LiGaBr_3$, or the Li-tantalate Li_7TaO_6. We also found 40 materials that show significant diffusion at 1000 K, but where we cannot rigorously extract the barrier due to the short time scales accessible to FPMD, such as $Li_4Re_6S_{11}$ and $LiTiPO_5$. These potential fast-ionic conductors could be studied further, in more detail, by experiments and simulations, and could result in new fast-ionic conductors or even electrolytes for next-generation solid-state Li-ion batteries.

Our data could also serve to search for descriptors of fast-ionic conduction, which would be of significant interest to the community. We unfortunately do not find any general trends from structural features or symmetries, which indicates that a more thorough analysis should be performed. To facilitate this goal, we uploaded the first-principles simulations performed in this work to an open-source archive on the MaterialsCloud [465]. Coupled with new methods and analysis

techniques [242, 320, 335, 336], the data should be useful in the ongoing search for novel descriptors of fast Li-ion diffusion in the solid state [196, 338].

Acknowledgements

We gratefully acknowledge support from the Swiss National Science Foundation (MARVEL NCCR and project 200021-159198) and the Swiss National Supercomputing Centre CSCS (project s836). We gratefully acknowledge support from the Swiss National Science Foundation (MARVEL NCCR and project 200021-159198) and the Swiss National Supercomputing Centre CSCS (project s836). We thank Sokseiha Muy, Loris Ercole, Giuliana Materzanini, Amber Mace, and Berend Smit for fruitful discussions.

4.5 Method details

4.5.1 Duplicate filter parameters

All structures that have the same stoichiometric formula are compared. Structures are marked as equal if one of the structures can be mapped into the other by the pymatgen structure matcher [342], using an angle tolerance of 5°, a relative lattice tolerance of 20%, and a site tolerance of 30%. For all structures found to be equal, one representative is chosen randomly, while all other structures are marked as duplicates and are not processed further in the screening.

4.5.2 Composition filters

Additional filters are applied to remove structures that do not meet the the following criteria: First, we include only structures that contain the anions N, O, F, P, S, Cl, Se, Br, and I. Second, we only keep structures that do not contain hydrogen, since the pinball model has never been tested for hydrogen-containing Li-ionic conductors. Physical intuitions suggests that hydrogen – being lighter than lithium – should yield to lithium motion, which is not compatible with he frozen framework of the model. Third, we remove structures that contain noble gas atoms (He, Ne, Ar, Kr, Xe, or Rn), 3d-transition metals (V, Cr, Mn, Fe, Co, Ni, or Cu) due to their capability to change oxidation states, or elements that are radioactive (Tc, Po, Rn, Ac, Th, Pa, U). Fourth, we remove structures that have elements above mercury in the periodic table, since the applications as SSE would be very unlikely. Last, we apply a filter checking whether there are enough anions that can accept the valence electron of lithium. For each structure, we add the number of Li ions to the number of anions multiplied by their most common oxidation states (-1 for halogens, -2 for chalcogens, -3 for pnictogens). If the final number is above 0, we reject the structure because we assume not all Li atoms will not find electron acceptors for charge transfer.

4.5.3 Bond distance filters

For every structure, we calculate all bond distances $\{A-B\}$ between species A and B, so we can select only compositions that show bond distances that are compatible with inorganic materials.

We remove structures with C – N < 1.6 Å (cyanide group); F – F < 1.5 Å, Cl – Cl < 2.1 Å, Br – Br < 1.6 Å, I – I < 2.8 Å (halide molecules); C – C < 1.6 Å (carbon double/triple bonds); O – O < 1.6 Å (peroxide group); $X_i - X_j < 0.8$ Å, where $X_{i/j}$ can be any element, to remove structures with any bonds being shorter than the H – H bond.

4.5.4 Electronic structure

The Marzari-Vanderbilt cold smearing [353] is set for all calculations to $\sigma = 0.02$ Ry ≈ 0.27 eV, and we augment the number of valence bands by 20%. The Brillouin-zone is sampled with a Monkhorst-Pack grid with a density of 0.2 Å^{-1}. If the lowest-energy state above the Fermi-level is occupied by more than 10^{-3} of an electron we classify that structure as not electronically insulating and reject it from the candidates.

4.5.5 Variable-cell relaxation

After applying an initial random distortion, with distortions taken from the normal distribution with $\sigma = 0.1$Å to break crystal symmetries, we apply the BFGS algorithm as implemented in Quantum ESPRESSO to converge the crystal structure until all following criteria have been met. First, the forces on the atoms need to be converged to below 5×10^{-5} Ry bohr^{-1}; Second, the total energy difference between consecutive iterations needs to be below 1×10^{-4} Ry; Third, the pressure has to be less than 0.5 kbar. Kpoint-grids are chosen as explained in Sec. 4.5.4. No valence bands are added, and no smearing is applied, since only electronic insulators are relaxed. Van-der-Waals contributions are not considered.

4.5.6 Supercell creation

All possible supercells are built by expanding the unit cell vectors of the primitive cell $\boldsymbol{a}_{p_1}$, $\boldsymbol{a}_{p_2}$ and $\boldsymbol{a}_{p_3}$ to the supercell vectors $\boldsymbol{a}_{s_1}$, $\boldsymbol{a}_{s_2}$ and $\boldsymbol{a}_{s_3}$ via an expansion by a 3×3 matrix $\bar{R}$ of integers [340]:

$$\left(\boldsymbol{a}_{s_1}, \boldsymbol{a}_{s_2}, \boldsymbol{a}_{s_3}\right) = \begin{pmatrix} R_{11} & R_{12} & R_{13} \\ R_{21} & R_{22} & R_{23} \\ R_{31} & R_{32} & R_{33} \end{pmatrix} \left(\boldsymbol{a}_{p_1}, \boldsymbol{a}_{p_2}, \boldsymbol{a}_{p_3}\right). \tag{4.4}$$

We apply the criterion that the supercell needs to enclose a sphere of a diameter d_{inner} (distance criterion) that defines a minimal distance of interaction of a particle with periodic images. We find the coefficients $R_{ij} \in \mathbb{Z}$ of $\bar{R}$ that minimize the volume of the cell under this constraint, using our implementation of SUPERCELLOR [466].

4.5.7 Fitting

After preliminary tests, it was determined that 5000 force components are needed for accurate fitting. As an example, $Li_{20}Ge_2P_4S_{24}$ has 20 Li ions, which results in $\lceil 5000/(3 \cdot 20) \rceil = 84$ uncorrelated snapshots being needed for the fitting ($y = \lceil x \rceil$ refers to the ceiling function: the output $y \in \mathbb{Z}$ of this function is the smallest integer larger or equal to its input $x \in \mathbb{R}$). Since the generation of these

snapshots with BOMD defeats the purpose of an efficient screening, we create the snapshots by displacements of the Li ions from equilibrium taken from a normal distribution with $\sigma = 0.1$ Å. For each such configuration, one calculation in the pinball model and one calculation with DFT is performed. Only the forces are used to regress the parameters α_1, α_2, and β_1 of Eq. (4.1).

4.5.8 Temperature control

We need to control the temperature of the system we are simulating in the pinball model with minimal effects on the dynamics. However, the number of particles that can move in pinball model is quite small, making thermalization difficult to achieve. We also observed that systems of small Li-ion density show very slow equilibration of the energy. Such a system resembles a system of weakly coupled harmonic oscillators, for which well-known thermostats like the Nosé-Hoover tend to fail. Local thermostats, such as the Andersen (stochastic collision) thermostat [106] can handle such cases well, but have two major disadvantages. First, they have system-dependent parameters, such as the collision frequency, determining the strength of interaction between the modes of the system and the external bath [271], and system-dependent parameters are problematic in any high-throughput scenario. Second, the thermostat could suppress diffusion [107], depending on the collision frequency. To prevent the dynamics being affected by a thermostat, we branch microcanonical simulations from uncorrelated snapshots of a canonical trajectory at the target temperature, a technique that has been explored for path-integral molecular dynamics [467].

We use a timestep of dt = 0.96 fs, with snapshots being stored every 20 dt. The collision frequency of the thermostat for the canonical simulations is set to 1000 dt, and snapshots for the start of the microcanonical branches are taken every 3000 dt, which means that every particle's velocities are reset on average three times between consecutive snapshots. In practice, eight snapshots are generated in one canonical run (in 24'000 timesteps) to allow for a certain degree of parallelization over microcanonical trajectories. Therefore, eight microcanonical simulations (each for 50'000 dt) can be performed in parallel after the completion of the canonical simulation. This operation is done at least four times (setting the minimum simulation time to $4 \cdot 8 \cdot 50000 \cdot 0.96$ fs = 1.5 ns), and maximally 48 times, setting the maximum simulation time to $48 \cdot 8 \cdot 50000 \cdot 0.96$ fs = 18.4 ns. In between, after completion of each canonical trajectory with eight microcanonical branches, the workflow checks whether the error of the mean of the diffusion coefficients, estimated from all microcanonical simulations, is either converged below 1×10^{-8} cm^2 s^{-1} or 5% of the mean of the diffusion.

4.5.9 FPMD

The supercells are created from a unit cell with the distance criterion set to $d_{inner} = 6.5$ Å to allow for smaller cells than for the pinball simulations, due to the computational cost and scaling of FPMD.

We perform Born-Oppenheimer molecular dynamics with a timestep of dt = 1.45 fs, simulating the canonical ensemble with the stochastic velocity rescaling [113] thermostat, implemented by us into Quantum ESPRESSO, using a characteristic decay time $\tau = 100$ dt to achieve efficient thermalization.

A continuous trajectory is created using a custom AiiDA workflow that converges the error of the mean of the diffusion to below 1×10^{-8} cm^2 s^{-1} or to below 5% of the mean of the diffusion. The workflow terminates the molecular dynamics simulations when this criterion is reached, therefore the trajectories have different lengths. The Brillouin-zone is sampled at the Γ-point only.

4.6 Computational cost of the screening

For the results reported in this work, we ran 2'503 SCF-calculations, 5'214 variable-cell relaxations, 171'370 molecular dynamics simulations in the pinball model, and 11'525 FPMD calculations, also counting restarts. The calculations were performed on four different clusters: The Bellatrix cluster of EPFL, having computing nodes of two Intel® Sandy Bridge processors running at 2.2 GHz, with eight cores each; The Fidis cluster of EPFL, with two Intel® Broadwell processors running at 2.6 GHz, with 14 cores each; The XC40 partition of the Piz Daint cluster at the Swiss National Supercomputing Centre (CSCS), with compute nodes of two Intel® Xeon E5-2695 v4 with 18 cores each, running at 2.1 GHz; The XC50 partition of the Piz Daint cluster at CSCS, with nodes of 12 Intel® Xeon E5-2690 v3 at 2.60 GHz processors. We give the computational cost of the simulations in Fig. 4.14, discerning by computer and calculation type. The dominant calculations are the pinball simulations and the FPMD. In Fig. 4.15 we show a histogram of the average node-time per ionic step for all the structures that were successfully fitted, revealing that the computational cost of the pinball model is about four orders of magnitude lower. The computational efficiency was utilized to get converged statistics for all structures that were simulated with the pinball model, resulting in a larger total simulation time, which explains why the total computational cost is en par with FPMD. It is evident that screening the same number of structures just with FPMD would not have been possible with today's computer performance.

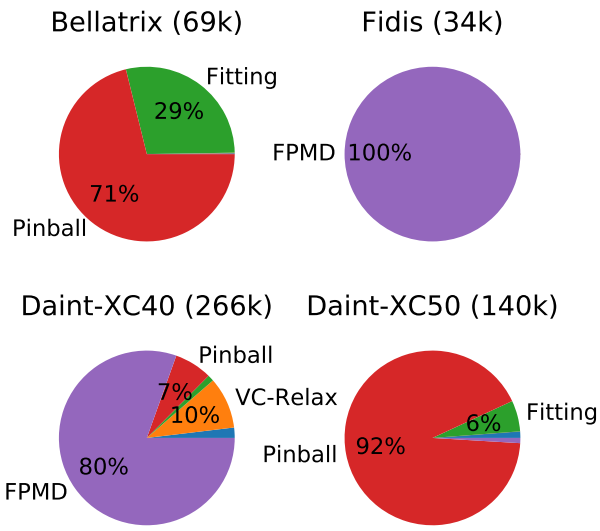

Fig. 4.14: The total node hours used in each cluster is above every pie chart, which gives the relative usage for each type of calculation in this cluster. The pinball simulations are in red, all simulations that were done for the fitting of the model in green, variable-cell relaxations are shown in orange, and single point SCF-calculations in blue.

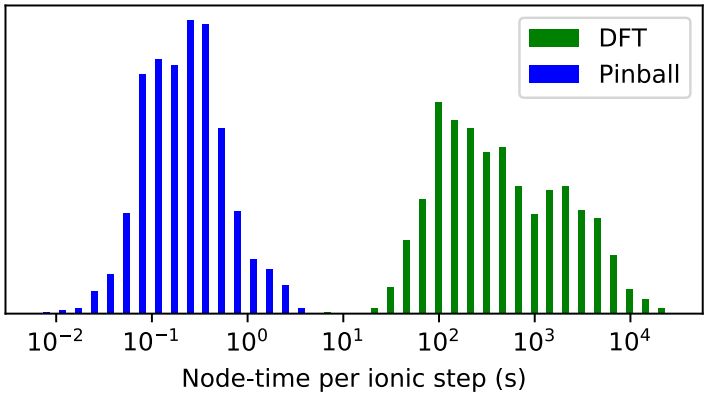

Fig. 4.15: Histogram of the average node-time per ionic step for each structure, in the pinball model in blue and with DFT in green.

5 The solid-state Li-ion conductor Li_7TaO_6

You may write me down in history,
with your bitter, twisted lies.
You may tread me in the very dirt,
but still, like dust, I'll rise.

Does my sassiness upset you?
Why are you beset with gloom?
'Cause I walk like I've got oil wells
Pumping in my living room.

Maya Angelou

The previous Chap. 4 described a high-throughput computational screening to find new Li-ion conductors. The best oxide we find in the screening, in terms of its Li-ionic diffusion, is the Li-hexa-oxometallate Li_7TaO_6, with an activation barrier of ~0.3 eV, which attracted the attention of experimental collaborators at the Paul Scherrer Institute, resulting in a common work on the characterization of Li_7TaO_6 from experiment and simulation.

Our simulations on Li_7TaO_6 include accurate first-principles molecular dynamics calculations, combined with long classical simulations employing a polarizable force field. The diffusion obtained with the two different methods, introduced in Secs. 1.3 and 1.4, agrees very well, allowing for a calculation of the diffusion properties also at room temperature with the classical force field. We analyzed the resulting trajectories (see Fig. 5.1) with the methods presented in the preceding Chap. 3 to characterize the diffusion in this material, which has not yet been studied by atomistic simulation.

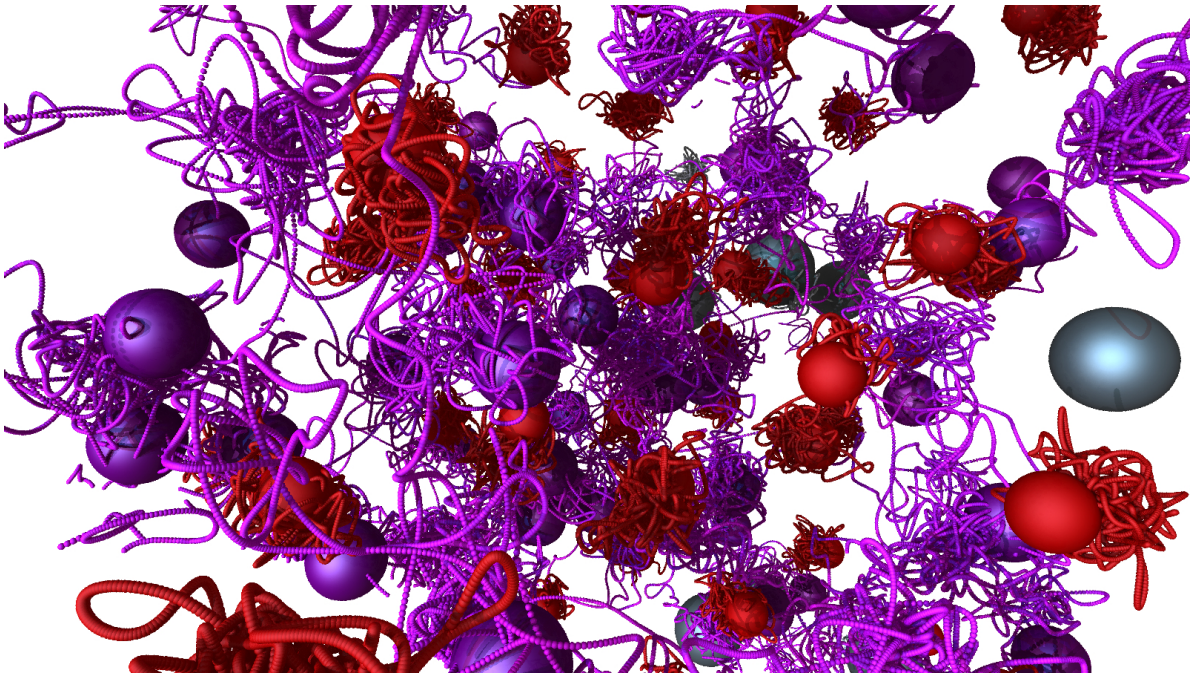

Fig. 5.1: Lithium-ion diffusion in Li_7TaO_6: Lithium positions are presented by purple spheres for a snapshot of a molecular dynamics trajectory, while the positions of oxygen and tantalum atoms are marked by red and grey spheres, respectively. Small dots in the same color denote past positions, highlighting the fast-ionic diffusion of Li ions in this material.

I conducted first-principles molecular dynamics simulations and analyzed the resulting trajectories. Our collaborators at IBM fitted an an interatomic potential for Li_7TaO_6 and we jointly analyzed the resulting simulations. The following article is adapted from a preprint, written collaboratively by several authors; however, I only report the sections where I had a direct contribution, which include mainly the calculation and interpretation of diffusion coefficients and analysis of diffusive pathways in Li_7TaO_6.

Authors	Leonid Kahle, Xi Cheng, Tobias Binninger, Steven D. Lacey, Aris Marcolongo, Federico Zipoli, Elisa Gilardi, Claire Villevieille, Mario El Kazzi, Nicola Marzari, Daniele Pergolesi
Title	The solid-state Li-ion conductor Li_7TaO_6: A combined computational and experimental study
Journal reference	*Solid State Ionics* (under review)

The solid-state Li-ion conductor Li_7TaO_6: A combined computational and experimental study

Leonid Kahle,[a‡] Xi Cheng,[c‡] Tobias Binninger,[b‡] Steven David Lacey,[d] Aris Marcolongo,[b] Federico Zipoli,[b] Elisa Gilardi,[c] Claire Villevieille,[d] Mario El Kazzi,[d] Nicola Marzari,[a] and Daniele Pergolesi*[cd]

Abstract: We study the oxo-hexametallate Li_7TaO_6 with first-principles Born-Oppenheimer molecular dynamics at high temperature, obtaining an activation barrier of 0.27 eV, indicating that this material is a fast ionic conductor, contrary to previous experimental findings. To confirm our results, we simulate the material using classical polarizable force-field molecular dynamics, resulting in excellent agreement with the first-principles simulations. This allows to simulate Li_7TaO_6 using larger supercell sizes and longer simulation times. We calculate the ionic conductivity at room temperature (300 K) and obtain a high ionic conductivity of 5.7×10^{-4} S cm^{-1}. Furthermore, we elucidate the diffusive pathways in this material, finding a weak anisotropy of the diffusion matrix.

5.1 Introduction

Li-ion batteries power a critical set of portable technologies [16] and are key to the deployment of electric vehicles, necessary to mitigate the carbon footprint of the vehicle fleet. It is important to overcome the constraints on safety [58, 73] and power/energy density [78] of today's Li-ion batteries, largely due to the use of liquid and organic electrolytes. Solid-state electrolytes (SSE) are a promising alternative for next-generation batteries [89, 197, 198] and are being intensely researched using experiments and simulations [196, 272, 468]. Low electronic mobility, a large electrochemical stability window, good mechanical stability, and high Li-ionic conductivity are key properties that must be satisfied by any solid-state ionic conductor to qualify for potential applications as a SSE [66, 198].

Several structural families have been and are being investigated as candidates for SSE application. The Li-conducting garnets, with the well-known representatives $Li_5La_3Ta_2O_{12}$ and $Li_7La_3Zr_2O_{12}$ [229, 282, 469], are one example of a thoroughly studied family of Li-ionic conductors. Aliovalent substitutions on the Li, La, and Zr/Ta sites have led to a large variety of related structures [276, 470], aiding in the stabilization of the ionically faster conducting cubic phase, and introducing vacancies to facilitate Li-ion diffusion. Recent work focuses on characterizing dendritic growth through the garnet-based SSE [471], and the interface between the electrolyte and electrode [472, 473]. Li-superionic conductors (LISICON) comprise another family of compounds explored for high ionic conductivity. One

[a] *Theory and Simulation of Materials (THEOS), and National Centre for Computational Design and Discovery of Novel Materials (MARVEL), École Polytechnique Fédérale de Lausanne, CH-1015 Lausanne, Switzerland.*
[b] *IBM Research–Zurich, CH-8803 Rüschlikon, Switzerland*
[c] *Laboratory for Multiscale Materials Experiments, Paul Scherrer Institut, CH-5232 Villigen PSI, Switzerland*
[d] *Electrochemistry Laboratory, Paul Scherrer Institut, CH-5232 Villigen PSI, Switzerland.*
‡ These authors contributed equally to this work

such compound is $Li_{3+x}(P_{1-x}Si_x)O_4$, a solid solution of Li_3PO_4 and Li_4SiO_4 [218, 316]; Substitutions of P and Si with B, Al, Zr, Ge, Ti, or As led to the discovery of several fast conductors [232, 317, 318], and the substitution of sulfur with oxygen resulted in the sub-family of thio-LISICONs [231, 356, 474–477]. The increased ionic conductivity of these compounds compared to the respective oxygen-based LISICONs is attributed to a higher polarizability of the anion [196, 231]. One of the best ionic conductors, tetragonal $Li_{10}GeP_2S_{12}$ (LGPS) [239], with an ionic conductivity of 12 mS cm^{-1} at room temperature, is found in this family. However, sulfur substitution has a deleterious effects on the electrochemical stability [323] of the SSE, compared to their oxygen counterparts. In addition, oxides have higher bulk and shear moduli than sulfides, and this increased mechanical stability could benefit the suppression of Li-metal dendrite growth [306].

Switching to thin-film batteries could also lead to technological breakthroughs due to beneficial mechanical properties (lower susceptibility to volume changes) and low resistance due to reduced dimensions [58, 90, 478]. Lithium phosphorus oxynitrides (LiPON) $Li_xPO_yN_z$ ($x = 2y + 3z - 5$) can be grown into amorphous thin films, but its activation barriers at ~0.55 eV, and ionic conductivity at room temperature of 2.3×10^{-6} S cm^{-1} are significantly worse than LGPS [479]. Still, these shortcomings are compensated by reductions in the electrolyte thickness for use in thin-film batteries. Growing thio-LISICONs or garnets as thin films has also been investigated recently [480–482]. Still, the search for more candidate SSE for Li-ion batteries is of major importance [224, 319, 320], and novel discoveries could lead to rapid advances in the field.

In this work, we highlight the oxo-hexametallate Li_7TaO_6 and study its ionic conductivity. This material has been characterized experimentally, first by Scholder and Gläser [483, 484], and later by Wehrum and Hoppe [485], and its structure is shown in Fig. 5.2. Synthesis of a single-crystalline sample is mentioned in the latter reference, where the authors mixed Li_2O and Ta_2O_5 in a 7.7:1 molar ratio and annealed the mixture for 156 days at 1000 °C. While the aforementioned studies only refer to synthesis and structural properties, a few studies also report measurements of the Li-ionic conductivity in Li_7TaO_6. Delmas *et al.* [366] studied the phases Li_8MO_6 (M = Zr, Sn) and Li_7LO_6 (L = Nb, Ta) in 1979, finding the Li-tantalate to have the highest ionic conductivity among the four structures, namely 4.3×10^{-8} S cm^{-1} at 300 K, and an activation barrier of 0.66 eV, measured with impedance spectroscopy on multicrystalline samples of 80% density with respect to the theoretical density. The authors suggested for this structure a two-dimensional diffusive pathway within the Ta layers. In 1984, Nomura and Greenblatt [367] studied Li_7TaO_6, measuring ionic conductivities as low as of 3.7×10^{-8} S cm^{-1} for at room temperature, and an activation barrier of 0.46 eV in a low temperature regime, and 0.67 eV in a high temperature regime, with the transition occurring at approximately 50 °C. The authors managed to increase the ionic conductivity of Li_7TaO_6 by doping it with Nb, Bi, Zr, or Ca on the Ta site, with the highest ionic conductivity (3.4×10^{-7} S cm^{-1}) reached for $Li_{7.4}Ta_{0.6}Zr_{0.4}O_6$. In the most recent work on Li_7TaO_6, Mühle *et al.* [368] determined in 2004 its ionic conductivity using impedance spectroscopy, reporting a value of 1.53×10^{-7} S cm^{-1} at 50 °C and an activation barrier of 0.29 eV at 400–700 °C, and 0.68 eV at 50–400 °C.

In summary, we note that only three studies have – to our knowledge – investigated ionic diffusion in Li_7TaO_6 in the last four decades, with reasonable agreement in the Arrhenius behavior of the ionic conductivity, with all studies reporting values between 0.66 eV and 0.68 eV. However, a more diffusive regime with a lower barrier is found above 400 °C degrees by Mühle *et al.* [368], with no other work having studied this regime. Nomura and Greenblatt report a lower barrier at lower temperature [367]. Interestingly, this is not confirmed by the other studies, even though this regime was probed by Delmas *et al.* [366] and Mühle *et al.* [368] In addition, no prior work reports the electrochemical stability window of Li_7TaO_6, and no atomistic simulation were performed on this material to elucidate the ionic transport mechanism.

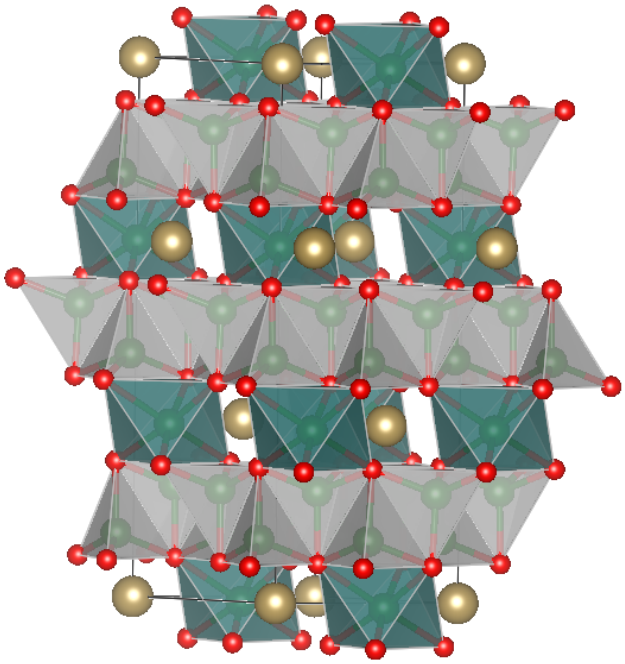

Fig. 5.2: The structure of Li_7TaO_6: Tantalum, lithium, and oxygen atoms are shown as gold, green, and orange spheres, respectively. The coordination of Li sites is highlighted by polyhedra. Octahedrally coordinated sites (green polyhedra) are within the plane of Ta atoms, and tetrahedrally-coordinated sites (grey polyhedra) are in between planes of Ta atoms.

The structure, deposited into the Inorganic Crystal Structure Database [301], was identified by us as a fast ionic conductor during an ongoing computational screening employing the pinball model [248], motivating additional research on the material and its applicability as a SSE. As we will show in this work, the ionic conductivity predicted both via accurate, if short, first-principles molecular dynamics as well as extensive classical molecular dynamics is of high value, marking this structure as a promising candidate SSE.

Details of the methods employed are given in Sec. 5.2, followed by the illustration and discussion of the results in Sec. 5.3. We summarize our work and present the conclusions in Sec. 5.4.

5.2 Methods

5.2.1 Molecular dynamics simulations

First-principles molecular dynamics (FPMD) are a powerful tool to study the diffusion mechanisms of solid-state Li-ionic conductors, calculating forces on the fly and accurately from the ground-state electronic structure at every step during the atomic dynamics. In this work we performed Born-Oppenheimer FPMD simulations in the framework of density-functional theory (DFT) [132],

using the implementation of the plane-wave pseudopotential method in the PWscf module of the Quantum ESPRESSO distribution [181]. We used the Perdew-Burke-Enzerhof (PBE) [135] exchange-correlation functional, and pseudopotentials and cutoffs suggested by the Standard Solid-State Pseudopotential (SSSP) Efficiency library 1.0 [245, 348, 349, 486].

We took the primitive cell of Li_7TaO_6 from ICSD [301] entry 74950 and performed a variable-cell relaxation of the primitive cell with a dense $8 \times 8 \times 7$ k-point mesh (further details are given Sec. D.5.1). One calculation of the electronic density of states (shown in Fig. 5.3) using DFT+U_{sc}, where the Hubbard U was calculated self-consistently from linear response [138, 487] to account for possible strong localization of electrons in the d states of Ta, gave evidence that Li_7TaO_6 is an electronic insulator, with a calculated band gap of 4.5 eV at DFT-PBE+U_{sc} level. For the FPMD simulations we created a $2 \times 2 \times 2$ supercell of La_7TaO_6 (112 atoms) to minimize spurious periodic image interactions and to allow for finite-temperature sampling. The resulting supercell will be referred to as $Li_{56}Ta_8O_{48}$ in the remainder, for clarity. Due to the presence of a large band gap, the Brillouin zone was sampled at the Γ point only, with no electronic smearing, using a threshold for the electronic charge density minimization of 1.12×10^{-10} Ry. We performed molecular dynamics simulations using the standard Verlet integrator [115], with 1.45 fs timesteps, sampling the canonical (NVT) ensemble, i.e. fixing the number of particles, the volume, and the temperature of the system. The latter was controlled with a stochastic velocity rescaling thermostat [113], implemented by us into PWscf, with a characteristic time for the thermostat set to 0.2 ps, which was found to result in efficient thermalization, but does not affect on the dynamics of the system. We simulated Li_7TaO_6 at 500 K, 600 K, 750 K, and 1000 K,

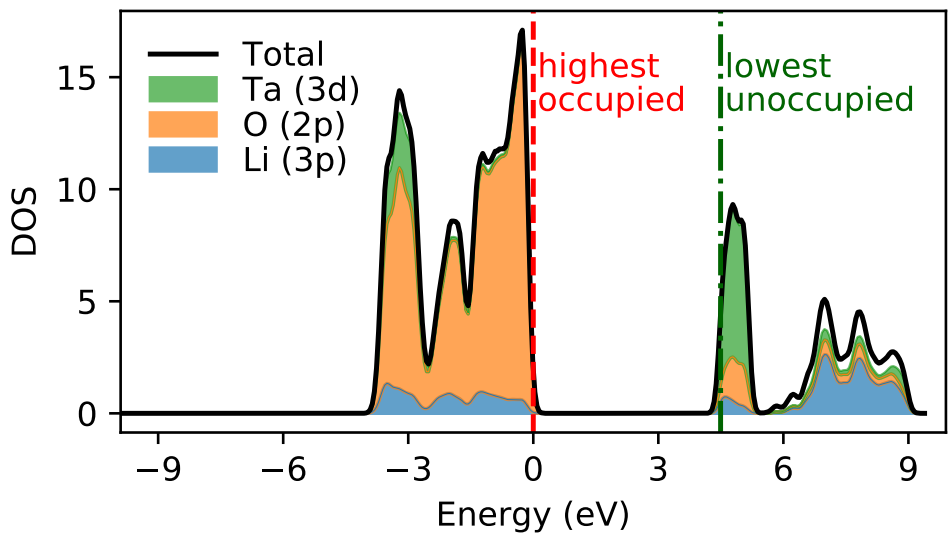

Fig. 5.3: The electronic density of states from DFT+U_{sc} as a black solid line at ±10 eV from the highest occupied state, marked with a red dashed line at 0 eV (green dash-dotted line for loweest valence state). We also project the density of states onto the atomic orbitals, shown in green for Ta (3d), orange for O (2p), and blue for Li (3s). We applied a Gaussian broadening ($\sigma = 0.01$ eV) to smoothen the spectrum.

for simulation times of 552 ps, 639 ps, 203 ps, and 73 ps, respectively. The criterion for stopping the simulations was given by the relative standard error of the diffusion coefficient becoming 10% or less. We managed all the dynamics with workflows of the AiiDA materials informatics [191] platform, to ensure automation and fully reproducible results.

Force-field molecular dynamics: FPMD simulations have accurate interatomic forces but are restricted to short time and length scales. In order to support the statistical relevance of our results we developed a classical core-shell potential [488] which is suitable to describe solid-state electrolyte materials [279]. The inter-atomic potential energy is given by the sum of the electrostatic energy between ions, a Buckingham term describing the short range repulsion, and van-der-Waals interactions between particles i and j at a distance r_{ij}:

$$U(r_{ij}) = \frac{q_i q_j e^2}{r_{ij}} + Ae^{-\frac{r_{ij}}{\rho}} - \frac{C}{r_{ij}^6}, \tag{5.1}$$

where q, A, C, and ρ are species-dependent model parameters. In addition to the interactions given in Eq. (5.1), selected types of atoms can be refined considering them as two particles, referred to as core and shell, modeling the ionic core and electronic shell respectively. In these cases the total atomic charge is split between the core and the the shell, allowing for a finite dipole contribution which models polarization effects; we will therefore refer to this classical potential as a polarizable force field (PFF). The core and the shell interact via harmonic springs, and the mass of the shell must be chosen small enough to ensure adiabatic separation (i.e. no mutual thermalization) between the slow ionic motion and the fast relaxation of the electrons, as is done in the Born-Oppenheimer approximation, and a condition which was always respected in our simulations.

We optimized the parameters of the force-field following the approach described by Zipoli and Curioni [489] via a simultaneous minimization of the force and energy mismatches on selected configurations, which were selected from short molecular dynamics runs at the PBE level [135] including van-der-Waals correction within the Grimme-D2 parametrization [371] as implemented in the CP2K code [182]. In the present parametrization of Li_7TaO_6 only the more polarizable oxygen atoms were treated with a core and a shell; in Sec. D.5.2 we report in detail the fitting procedure and its quality. With the optimized parameters we performed PFF simulations using the LAMMPS code for large scale molecular dynamics simulations [490], for a supercell of 90720 atoms. access to such long length and time scales permitted to follow a three-step protocol to ensure the reliability of the resulting trajectories: First, we equilibrated the simulation cell by coupling the entire system (ions and shells) to a barostat, setting the pressure to $p = 1$ bar, and coupling the ions to a Berendsen thermostat. This setup reproduces closely an NPT ensemble in which the light cold shells follow adiabatically the ions, which are coupled to a thermostat. We performed ten simulations at different target temperatures between 300 K and 900 K. In a second step we fixed, for each temperature, the equilibrium volume, and the simulations continued in the canonical ensemble (NVT), using a Nosé-Hoover integrator with a coupling time of 0.5 ps applied to the ions (no thermostat on the shells). We

note that the temperature of the O shells, about 1 K, presented a negligible drift of 1.5×10^{-2} K ns^{-1}, confirming the adiabatic decoupling between the motion of ions and shells. Finally, the thermostat was removed to sample at constant volume and energy in the microcanonical (NVE) ensemble. This way we ruled out the possibility that the thermostat or barostat influenced the dynamics, and we used the NVE trajectories to calculate diffusion coefficients. The length of the NVE simulations depended on the target temperature, and both are reported in the Sec. D.6.1.

Analysis of trajectories: The mean-square displacements (MSD) of the diffusing species is the microscopic property that links to the (macroscopic) tracer diffusion coefficient [104]. We calculated the MSD of species S, with N_S atoms in the simulation cell, from the molecular dynamics trajectory:

$$\mathrm{MSD}^S(\tau) = \frac{1}{N_S}\sum_i^S \langle |\boldsymbol{r}_i(\tau+t) - \boldsymbol{r}_i(t))|^2\rangle_t, \tag{5.2}$$

where $\boldsymbol{r}_i(t)$ is the position of the i-atom at time t. Averaging over all trajectory timesteps is denoted as a time average by the angular brackets $\langle\cdots\rangle_t$; assuming ergodicity, this is equivalent to an ensemble average under the relevant thermodynamic conditions. The tracer diffusion coefficient of species S, D^S_{tr}, was calculated from the long time limit of the MSD:

$$D^S_{tr} = \lim_{\tau\to\infty}\frac{1}{6\tau}\mathrm{MSD}^S(\tau). \tag{5.3}$$

We performed a least-squares regression to find the line of best fit to the MSD in the diffusive regime, while block analysis [270] was used to estimate the error of the tracer diffusion coefficient. Via the Nernst-Einstein equation, and assuming a Haven ratio of one, we estimated the ionic conductivity σ:

$$\sigma = \frac{e^2 C}{k_B T} D^{\mathrm{Li}}_{tr}, \tag{5.4}$$

where C is the average Li-ion density in the system. We also estimated the tracer diffusion matrix $\boldsymbol{D}^S$ of species S as follows:

$$D^S_{ab} = \lim_{\tau\to\infty}\frac{1}{2\tau}\frac{1}{N_S}\sum_i^S \left\langle \left(r_i^a(\tau+t) - r_i^a(t)\right)\cdot\left(r_i^b(\tau+t) - r_i^b(t)\right)\right\rangle_t, \tag{5.5}$$

where $r_i^a(t)$ is the position of the i-th atom along the Cartesian coordinate a at time t. The tracer diffusion coefficient defined in Eq. (5.3) can also be calculated from the diffusion coefficient matrix of Eq. (5.5) as: $D^S_{tr} = 1/3\cdot\mathrm{Tr}(\boldsymbol{D}^S)$. $\boldsymbol{D}^S$ contains additional information on the anisotropy of the diffusion. The normalized variance of the eigenvalues of the diffusion matrix is referred to as the fractional anisotropy (FA) [491].

The Li-ion probability density $n_{\mathrm{Li}}(\boldsymbol{r})$ was calculated from trajectories via an average over all the

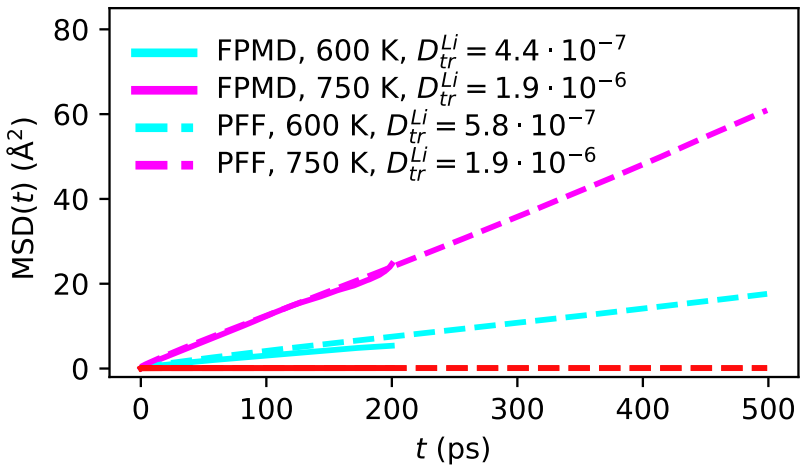

Fig. 5.4: The MSD(t) of Li and O, calculated in the small $Li_{56}Ta_8O_{48}$ supercell, at 600 K and 750 K for the pFF and FPMD in dashes and solid lines, respectively. Oxygen, in red, shows no diffusion in any simulation, evidenced by a flat MSD. The diffusion of Li ions, estimated from the slope of the MSD, is given in the legend (in $cm^2\,s^{-1}$).

frames of the trajectory:

$$n_{\mathrm{Li}}(\boldsymbol{r}) = \left\langle \sum_i^{\mathrm{Li}} \delta(\boldsymbol{r} - \boldsymbol{r}_i(t)) \right\rangle_t , \tag{5.6}$$

where the Li-ions are indexed by i. Due to finite statistics, we replaced the delta function in Eq. (5.6) by a Gaussian with a standard deviation of 0.3 Å.

We also calculated the radial distribution function (RDF) $g(r)_{S-S'}$ of species S with species S' as:

$$g_{S-S'}(r) = \frac{\rho(r)}{f(r)} = \frac{1}{f(r)} \frac{1}{N_S} \sum_i^S \sum_j^{S'} \left\langle \delta\left(r - \left|\boldsymbol{r}_i(t) - \boldsymbol{r}_j(t)\right|\right) \right\rangle_t , \tag{5.7}$$

where $f(r)$ is the ideal-gas average number density at the same mean density. We obtained the coordination number at r by integrating the average number density $\rho(r')$ from 0 to r.

In addition, we analyzed the trajectories using the SITATOR package, allowing for an unsupervised analysis [336] of the resulting sites and diffusive pathways. The analysis returns states and transitions of the diffusion pathway by projecting the Li-ion coordinates into a finite-dimensional vector space describing the position relative to the host lattice, in this case the tantalum and oxygen sublattice of Li_7TaO_6. A subsequent clustering permits to identify crystallographic sites. The parameters used in this work are given in Sec. D.5.3.

5.3 Results and discussion

First, the compatibility between FPMD and PFF simulations with respect to the Li-ionic diffusion is assessed for the same $Li_{56}Ta_8O_{48}$ supercell, each relaxed at 0 K prior to the simulation. In Fig. 5.4 we

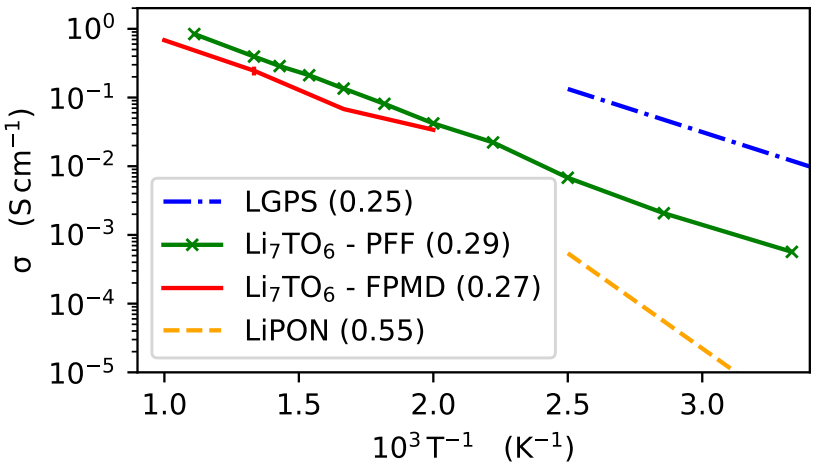

Fig. 5.5: Arrhenius behavior of the ionic conductivities of Li_7TaO_6 simulated with FPMD (red solid line) and PFF (green solid line). We compare to the experimental ionic conductivities of LGPS [239] (blue dashed-dotted line) and LiPON [479] (orange dashed line). The activation energies are given in the legend within brackets (in eV).

plot the MSD of Li and O, calculated using Eq. (5.2) from the FPMD and PFF simulations at 600 K and 750 K. A diffusive regime can be clearly discerned, evidence that the FPMD simulations performed are sufficiently long to get converged results. The MSD calculated from the FPMD (solid lines) and PFF (dashed lines) simulations give compatible slopes. The MSD of the oxygen atoms gives evidence for the stability of the rigid framework formed by the non-diffusive atoms and for the absence of lattice drift. Possible size effects, discussed in greater detail in section Sec. D.6.1, are not expected to change significantly the conductivity in the simulations. The excellent agreement between FPMD and PFF allows us to use the PFF to calculate the ionic conductivity also at lower temperatures,

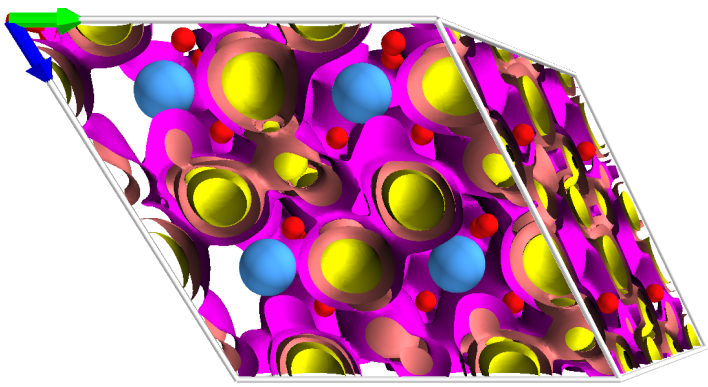

Fig. 5.6: The Li-ion density of Li_7TaO_6 at 600 K. We show the isosurfaces at 0.001, 0.01, and 0.1 Å^{-3} in violet, orange, and yellow, respectively. The average positions of the oxygens are shown as red spheres, and of tantalum as blue spheres. We chose a different orientation compared to Figs. 5.2 and 5.8, to showcase more clearly the diffusion in the plane of Ta ions and out of plane.

for a more rigorous prediction at ambient temperature, which requires longer simulation times. We use the PFF in NPT simulations to equilbrate the lattice parameters at the target temperature, and we control for size effects by using a larger supercell. In Fig. 5.5 we report the computed ionic conductivities from the PFF and FPMD simulations together with the conductivities of LGPS [239] and LiPON [479] for comparison. We estimate the activation energy for Li_7TaO_6 at 0.27 eV from the FPMD simulations and 0.29 eV from the PFF simulations, in good agreement with each other. The activation energies for Li_7TaO_6 are slightly higher than the experimental activation barrier for LGPS, which ranges from 0.22 to 0.25 eV [239, 296] and much lower than the activation barrier of 0.55 eV found in LIPON [479]. Overall the results of our simulations indicate that Li_7TaO_6 could be a very promising Li-ionic conductor, suitable for application as solid-state electrolyte.

The Li-ion probability density $n(\boldsymbol{r})$ from the FPMD simulation at 600 K (our longest FPMD trajectory), is reported in Fig. 5.6, where we show three different isosurfaces. The lower isovalue of 0.001 $Å^{-3}$ allows to discern a connected network of Li-ion diffusion pathways, additional evidence that the material is a good ionic conductor. The high-density isovalue displays disconnected regions of high probability density, showing that crystallographic sites can be indeed clearly identified.

From the FPMD trajectories we calculated the RDF of Li with all other species between 0 and 4 Å, using Eq. (5.7). The resulting RDFs, shown in Fig. 5.7, reveal that Li ions are, as expected, closest coordinated by oxygen, but the coordination number cannot be rigorously extracted due to the fact that this type of analysis is not able to distinguish between different types of sites for Li in different coordination. To understand further the geometry of the Li sites we see in simulation, we analyzed the Li-ion dynamics with the SITATOR package [336], to characterize the distinct sites ions visit during the simulation. By computing chemical and geometrical fingerprints for each site, we classify sites by their type. We find two sites that we label type 0 and six sites that we label type 1, per formula unit of Li_7TaO_6, for both the FPMD trajectory and the PFF trajectory at 600 K. The clustering of the descriptor vectors for each site (see Fig. D.50) results in distinct clusters, evidence of a clear difference in the geometric and chemical environment of the sites. Calculating the $g(r)_{Li-O}$ for each

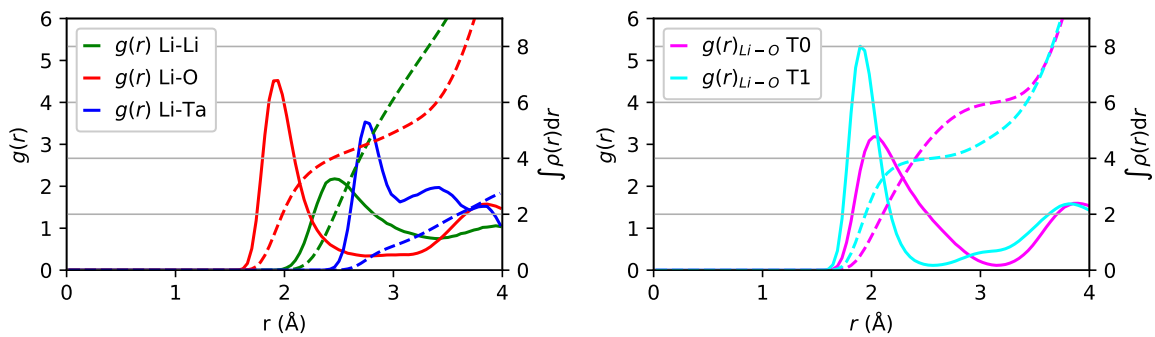

Fig. 5.7: (Left) The Li-Li, Li-O, and Li-Ta RDF from FPMD trajectories at 600 K are shown as green, red, and blue solid lines, respectively. We show the integral of average number density as dashed lines, using the same color encoding. (Right) The Li-O RDF for site type 0 in violet and site type 1 in cyan.

site type separately, we observe a different coordination number, which is estimated from the plateau of the Li-O RDF shown in the right panel of Fig. 5.7. Site type 0 is coordinated by six oxygen atoms and is an octahedral site, compared to four oxygen atoms for the tetrahedral site type 1, in excellent agreement with published results [366, 485] on the Li-ion sites in this structure. Fig. 5.8 shows the connectivity of the sites for a PFF trajectory at 600 K. From this analysis we see one connected component, i.e. starting from every site, a Li-ion can reach every other site in the system via a sequence of jumps, but we observe that the material has a more strongly connected plane of diffusion between the octahedral sites of type 0. There is however also significant diffusion perpendicular to the plane, where the tetrahedral sites are located. This behavior is reflected in the value of the FA, which is stable with respect to the temperature at a value of ~ 0.3, signature of an anisotropic type of diffusion. Ideal FA values are 0.0, 0.7, and 1.0 for isotropic, two-dimensional, and uni-dimensional diffusion. Analyzing further the diffusion matrix, we find two equal eigenvalues, with the respective diffusion direction lying in plane, whereas the perpendicular diffusion is a factor of ~2 lower. We therefore classify the material as a three-dimensional conductor, but with a preference for in-plane diffusion.

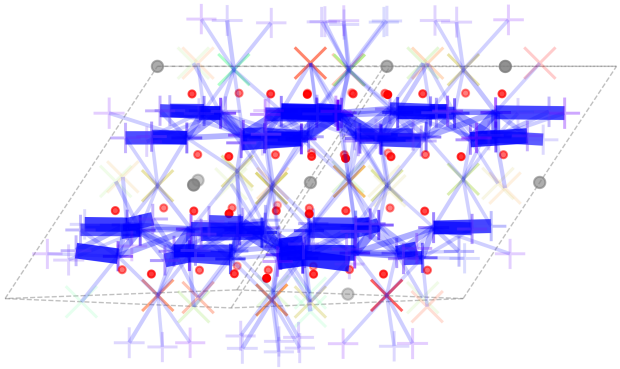

Fig. 5.8: We show the results of the site analysis for a $2 \times 2 \times 2$ cell of Li_7TaO_6. The lines connecting the sites are drawn if these sites have exchanged Li-ions, with the thickness depending linearly on the observed flux.

5.4 Conclusions

We studied the hexa-oxometallate Li_7TaO_6 using accurate first-principles as well as polarizable force-field molecular dynamics simulations, finding excellent agreement between the two methods. From our simulations we conclude that the compound investigated is a fast-ionic conductor also at room temperature. The activation barriers of 0.27 eV and 0.29 eV, estimated from the FPMD and PFF simulations, respectively, are of sufficiently low value to highlight this material as a potential candidate material for SSE application.

6 Conclusions

For every complex problem there is an answer that is clear, simple and wrong.

Henry Louis Mencken

6.1 Summary

The need for novel Li-ionic conductors was outlined in the introductory Chap. 1, where I also describe how atomistic simulations can be exploited to search for new materials that could be applied as solid-state electrolytes in Li-ion batteries. However, for a computational screening based on molecular dynamics, existing methods were either very expensive, or not accurate enough. The pinball model, presented in Chap. 2, was derived from the first-principles Hamiltonian of density-functional theory, using physical observations of how the charge density depends on Li-ion motion, resulting in a model that is about three orders of magnitude cheaper than state-of-the-art first-principles molecular dynamics, while the losses in accuracy are tolerable for screening applications. The computational efficiency of the pinball model was leveraged in a high-throughput computational screening, presented in Chap. 4, resulting in several candidates which were characterized with accurate first-principles molecular dynamics. One candidate, namely Li_7TaO_6, was characterized in more detail and presented in Chap. 5. In addition to modeling of, and screening for, solid-state Li-ion conductors, I worked on a framework to help understand the atomistic origin of fast-ion conduction in these materials. As presented in Chap. 3, we developed a new method to analyze molecular dynamics trajectories in an automated fashion, relying on the unsupervised clustering of atomic neighborhood descriptors to detect jumps of Li ions during the molecular dynamics. Existing methods in the literature either relied on pre-existing knowledge of the diffusive pathways, or were less accurate due to use of the real-space density as a clustering target.

6.2 Future work

The largest item that is left unfinished is the implementation, testing, and validation of the “flexible” pinball model (see Chap. C), where the host lattice is allowed to vibrate harmonically around its

equilibrium configuration, with the charge density being updated from linear response. Such a model would be invaluable for more accurate description of the Li-ion diffusion, especially for large systems where first-principles molecular dynamics are not feasible. For screening purposes, it remains doubtful whether the flexible pinball model could be used, given a larger computational cost and additional complexity. Also the frozen-host pinball, as presented in Chap. 2, can be improved. First, the importance of the non-local interactions is not fully understood. We find these interactions to generally increase the accuracy of the model, but the degree of improvement heavily depends on the system investigated. Second, the strategies for fitting the parameters for the pinball model need to be more rigorously assessed and compared.

Regarding the screening, the work presented here should only be seen as a first exploratory work, as the screening only included structures reported without partial occupancies, and calculated the Li-ionic diffusion at full Li-ion occupation, neglecting possible effects of dopants. Several regions of composition space remained uncharted, and it needs to be left to future work to also find robust protocols to find fast Li-ion conductors among structures with partial occupancies, and to study the effect of doping.

Finally, plenty of data has been generated in the form of molecular dynamics trajectories of ionic conductors, and we also developed a model to automatically detect diffusive pathways inside a Li-ion conductor and jumps during the simulation. An attempt to harvest this data in a search for descriptors for fast-ion diffusion would be challenging, due to the large amount of data and inherent complexity of this problem. But finding descriptors for ionic conductivity would be very valuable to drive the search for new solid-state electrolytes forward, and to increase our understanding of the driving forces of fast-ionic or superionic diffusion in the solid state.

A Diffusion

A.1 Derivation of Einstein relation

The following proof was originally published by Einstein in 1905 [104], in German, who derived that diffusion is proportional to the mean-square displacement of a particle in one dimension (extension to three dimensions is straightforward). We have N particles and are looking at a small time interval τ of their motion. First, we assume that particles move by small steps Δ with a probability $\phi(\Delta)$, normalized to integrate to 1 for all possible moves:

$$\int_{-\infty}^{\infty} \phi(\Delta)\mathrm{d}\Delta = 1. \tag{A.1}$$

Second, we assume the function $\phi(\Delta)$ to be symmetric, which means that $\phi(\Delta) = \phi(-\Delta)$ and $\int_{-\infty}^{\infty} \Delta\phi(\Delta)d\Delta = 0$. The next function to introduce is the particle probability density $f = f(x,t)$, a function of space and time. Knowing the function f at time t, how can we calculate $f(x,t+\tau)$? First, we can exploit the fact the τ is small. A Taylor expansion in time around $f(x,t)$, discarding all second- and higher-order terms, results in:

$$f(x,t+\tau) = f(x,t) + \tau\frac{\partial f}{\partial t}. \tag{A.2}$$

It is equally possible to exploit the fact that we know where particles are at t and the distance they need to travel to get the location x at time $t+\tau$:

$$f(x,t+\tau) = \int_{-\infty}^{\infty} f(x-\Delta,t)\phi(\Delta)d\Delta, \tag{A.3}$$

assuming the probability $\phi(\Delta)$ does not depend on time. Also here, we can use the fact that Δ is small, and express $f(x-\Delta,t)$ as a Taylor series around $f(x,t)$:

$$f(x,t+\tau) = f(x,t)\int_{-\infty}^{\infty} \phi(\Delta)d\Delta - \frac{\partial f}{\partial x}\int_{-\infty}^{\infty} \Delta\phi(\Delta)d\Delta + \frac{\partial^2 f}{\partial x^2}\int_{-\infty}^{\infty} \frac{\Delta^2}{2}\phi(\Delta)d\Delta + \mathcal{O}(\Delta^3). \tag{A.4}$$

Since ϕ is normalized and symmetric, Eq. (A.4) simplifies to:

$$f(x,t+\tau) = f(x,t) + \frac{\partial^2 f}{\partial x^2}\int_{-\infty}^{\infty}\frac{\Delta^2}{2}\phi(\Delta)d\Delta, \tag{A.5}$$

where we also discard $\mathcal{O}(\Delta^3)$. We set the right hand of Eq. (A.2) and Eq. (A.5) equal and obtain:

$$\begin{aligned} f(x,t) + \tau\frac{\partial f}{\partial t} &= f(x,t) + \frac{\partial^2 f}{\partial x^2}\int_{-\infty}^{\infty}\frac{\Delta^2}{2}\phi(\Delta)d\Delta \\ \tau\frac{\partial f}{\partial t} &= \frac{\partial^2 f}{\partial x^2}\int_{-\infty}^{\infty}\frac{\Delta^2}{2}\phi(\Delta)d\Delta. \end{aligned} \tag{A.6}$$

We remember Fick's second law of diffusion for one dimension $\frac{\partial C}{\partial t} = D\frac{\partial^2 C}{\partial x^2}$. When comparing to Eq. (A.6), we recognize that $f = C$ and that the diffusion coefficient of such system is:

$$D = \frac{1}{2\tau}\int_{-\infty}^{\infty}\Delta^2\phi(\Delta)d\Delta = \frac{1}{2\tau}\left\langle\Delta^2\right\rangle. \tag{A.7}$$

Therefore, the diffusion is proportional to the square of a displacement Δ, that occurs with a probability $\phi(\Delta)$ in a short time interval τ. Not knowing the probability, one can sample $\langle\Delta^2\rangle_t$ as a time average from a trajectory: $\langle\Delta^2\rangle = \langle\left(R_x(t+\tau) - R_x(t)\right)^2\rangle$. Inserting this information in above Eq. (A.7), we obtain:

$$D = \lim_{\tau\to\infty}\frac{1}{2\tau}\left\langle\left(R_x(t+\tau) - R_x(t)\right)^2\right\rangle, \tag{A.8}$$

where we take the long-time limit of τ in order to consider all possible processes that constitute Δ^2. It should be noted that Smoluchowski gave a different proof for this relationship, but with the same result, and this equation above is therefore often called Einstein–Smoluchowski diffusion equation [492].

A.2 Green-Kubo relation for diffusion

The previous Sec. A.1 shows how the diffusion is related to the MSD, namely as given by Eq. (A.8). I will now show that the diffusion can be calculated as an integral over an auto-correlation function, a so-called Green-Kubo integral [493, 494]. Since we are looking at a process linear in time, I can rewrite that equation as

$$D = \frac{1}{6}\lim_{\tau\to\infty}\frac{\partial}{\partial\tau}\left\langle\left(\boldsymbol{R}(t+\tau) - \boldsymbol{R}(t)\right)^2\right\rangle_t. \tag{A.9}$$

I first differentiate by parts, taking into account that the difference in positions between t and $t+\tau$ can be obtained by integrating over the particle velocities:

$$\begin{aligned} D =& \frac{1}{6}\lim_{\tau\to\infty}\left\langle 2\frac{\partial\big(\boldsymbol{R}(t+\tau)-\boldsymbol{R}(t)\big)}{\partial\tau}\big(\boldsymbol{R}(t+\tau)-\boldsymbol{R}(t)\big)\right\rangle_t. \\ =& \frac{1}{3}\lim_{\tau\to\infty}\left\langle \boldsymbol{V}(t+\tau)\int_t^{t+\tau}\boldsymbol{V}(t')\mathrm{d}t'\right\rangle_t. \end{aligned} \tag{A.10}$$

Having a Gaussian random process $\boldsymbol{V}(t)$, the absolute value over which one integrates does not matter, but only differences [271].

$$D = \frac{1}{3}\lim_{\tau\to\infty}\left\langle \int_t^{t+\tau}\boldsymbol{V}(t+\tau)\boldsymbol{V}(t')\mathrm{d}t'\right\rangle_t. \tag{A.11}$$

$$= \frac{1}{3}\lim_{\tau\to\infty}\left\langle \int_t^{t+\tau}\boldsymbol{V}(t)\boldsymbol{V}(t')\mathrm{d}t'\right\rangle_t = \frac{1}{3}\int_{t'=0}^{\infty}\left\langle \boldsymbol{V}(t)\boldsymbol{V}(t'+t)\right\rangle_t \mathrm{d}t'. \tag{A.12}$$

$$\tag{A.13}$$

Therefore, the diffusion coefficient D can be calculated either via the Einstein relation or by employing the velocity auto-correlation function. They give equivalent results in the limit of infinite statistics and dense sampling, but approach these limits differently [495, 496]

A.3 Ionic conductivity

We can use another Green-Kubo relation to calculation the conductivity of a material, namely [493, 497]:

$$\sigma = \frac{\Omega}{3k_BT}\int_0^{\infty}\left\langle \boldsymbol{J}(t)\boldsymbol{J}(t'+t)\right\rangle_t \mathrm{d}t', \tag{A.14}$$

where Ω is the system volume, T the temperature, and $\boldsymbol{J}$ the flux of charge. In an ionic system, in the absence of any electronic charge flux, $\boldsymbol{J}$ is given by the flux of particles, determined by velocity and particle charge: $\boldsymbol{J}(t) = \Omega^{-1}\sum_I \boldsymbol{V}_I(t)q_i$. Therefore, we obtain for the ionic conductivity the following expression:

$$\sigma = \frac{(Ze)^2}{3\Omega k_BT}\int_0^{\infty}\left\langle \sum_{I,J}\boldsymbol{V}_I(t)\boldsymbol{V}_J(t'+t)\right\rangle_t \mathrm{d}t', \tag{A.15}$$

where I assumed that all particles carry the same charge, an integer multiple of the elementary charge $q_i = Ze$. Comparing to Eq. (A.13) we notice similarities, which allows to define two different diffusion coefficients for a system of N particles, the tracer diffusion coefficient D_{tr} and the charge

diffusion coefficient D_σ:

$$D_{tr} = \frac{1}{N}\sum_I^N \lim_{\tau\to\infty}\frac{1}{6\tau}\left\langle \left(\boldsymbol{R}_I(t+\tau)-\boldsymbol{R}_I(t)\right)^2\right\rangle_t \tag{A.16}$$

$$= \frac{1}{3N}\sum_I^N \int_{t'=0}^{\infty}\left\langle \boldsymbol{V}_I(t)\boldsymbol{V}_I(t'+t)\right\rangle_t \mathrm{d}t' \tag{A.17}$$

$$D_\sigma = \lim_{\tau\to\infty}\frac{N}{6\tau}\left\langle \left(\boldsymbol{R}_{COM}(t+\tau)-\boldsymbol{R}_{COM}(t)\right)^2\right\rangle_t \tag{A.18}$$

$$= \frac{N}{3}\int_{t'=0}^{\infty}\left\langle \boldsymbol{V}_{COM}(t)\boldsymbol{V}_{COM}(t'+t)\right\rangle_t \mathrm{d}t', \tag{A.19}$$

where $\boldsymbol{V}_{COM} = \frac{1}{N}\sum_I^N \boldsymbol{V}_I$ and $\boldsymbol{R}_{COM} = \frac{1}{N}\sum_I^N \boldsymbol{R}_I$ stand for the center of mass velocity and position, respectively. While the tracer diffusion describes how fast a single particles moves, the collective or charge diffusion describes how fast particles diffuse collectively [211, 498]. From the difference, one understands where the distinction is:

$$D_\sigma - D_{tr} = \frac{1}{3N}\int_{t'=0}^{\infty}\left\langle \sum_{I,J}\boldsymbol{V}_I(t)\boldsymbol{V}_J(t'+t)\right\rangle_t \mathrm{d}t' - \frac{1}{3N}\int_{t'=0}^{\infty}\sum_I^N\left\langle \boldsymbol{V}_I(t)\boldsymbol{V}_I(t'+t)\right\rangle_t \mathrm{d}t' \tag{A.20}$$

$$= \frac{1}{3N}\sum_I^N\int_{t'=0}^{\infty}\left\langle \sum_{J\neq I}\boldsymbol{V}_I(t)\boldsymbol{V}_J(t'+t)\right\rangle_t \mathrm{d}t'. \tag{A.21}$$

Therefore, the difference is given by the correlation in the motion between the different particles I and J. Positively correlated motion between particles (of the same charge) leads to enhanced charge diffusion [211, 281]. The ratio between tracer and charge diffusion is called the Haven ratio $H = \frac{D_{tr}}{D_\sigma}$. In the absence of correlation, e.g. the dilute limit, the Haven ratio is 1. By comparing Eq. (A.19) to Eq. (A.15), we obtain the Nernst-Einstein equation:

$$\sigma = \frac{N(Ze)^2}{\Omega k_B T}D_\sigma = \frac{N(Ze)^2}{\Omega k_B T}\frac{D_{tr}}{H} \tag{A.22}$$

B Storing and querying in AiiDA

As outlined in Sec. 1.5, computational screening requires a framework that is highly automatized, enables the storage of data with its provenance, provides an environment for a scientist to interact with her data, and facilitates the sharing of data and workflows. In the following, I will explain how the storage and querying in AiiDA permit these requirements.

B.1 Storing in AiiDA

In the original implementation of AiiDA introduced by Pizzi *et al.* [191], every data, calculation, or code instance is a subclass of Node, that can be connected via directional links. Node is a Python-class, subclassed from the Object Relational Mapper (ORM) in the Django framework, which maps to a table in an SQL database: Every time a user creates a new Node instance, a new row is inserted into this table, and every time a user loads or manipulates a Node instance, a row is read or updated in this specific table, respectively. Code, Calculation, and Data are subclasses of Node, and therefore stored in the same table (as are also all subclasses of Data, Calculation, or Code). Every node can have attributes, that store the content specific to a Node instance. As an example, StructureData, a subclass of Data, stores species and positions of the atoms as attributes. Attributes are key-value pairs that have strings as keys; values can be strings, integers, floats, date-times, booleans, lists, or dictionaries. These attributes were stored as explicit rows in separate table, as explained in Ref. [191]. Due to recent efforts, it is possible to store attributes as JavaScript object notation (JSON) entries in the same table containing the Node instances. Since Django did not provide the JSON functionality, and in order to be more independent of a specific ORM implementation such as Django, we undertook the effort to create an abstract implementation, that can be used with different frameworks and database schemata, or even database management systems. A second implementation relies on SQLAlchemy instead of Django, for example, and allows to store attributes of nodes more efficiently in JSON entries.

B.2 Querying in AiiDA

The abstraction of the ORM means that an abstract querying functionality needs to exist as well, in order to allow for a query to be independent of the implementation. We implemented this

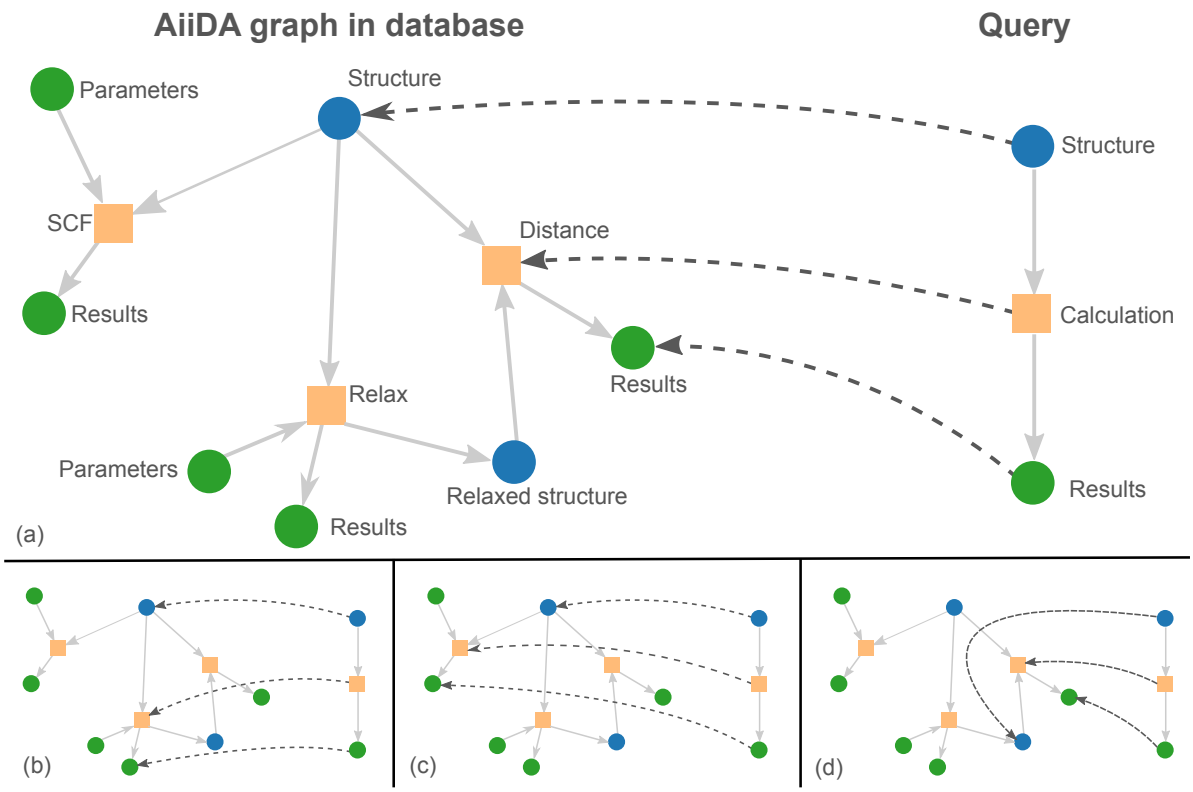

Fig. B.1: An schematic AiiDA graph (large) and a possible embedding of a graph query, shown on the right. Squares represent calculations and circles represent data instances (structures in blue and dictionaries/parameters in green). The query specifies a search for any calculation that has a structure as an input and that created results stored as a dictionary. The subfigures (b, c, d) show other possible embeddings of the query.

functionality within the *QueryBuilder* class of AiiDA, which allows to define queries that are translated or built upon execution into the specific query for the database schema used. Therefore, only one query needs to be written, independent of how the nodes created by a user are stored. An additional advantage is that most scientific users of AiiDA might not be able to express a query in the native database language such as PostgreSQL. The API of the QueryBuilder is designed for common queries, and with a syntax that Python users should be accustomed to. The standard operations of relational algebra, namely joins, selections, and projections, are implemented in the QueryBuilder and allow also for very complex queries within AiiDA.

We understand a graph query as a projection of a subgraph (the entities queried for) onto the graph stored in a database. This is shown in Fig. B.1: on the top left, we give the schematic for a realistic graph in an AiiDA database: one structure has been input to a single-point self-consistent field (SCF) calculation, and a geometric relaxation. The effect of the relaxation on the structure has been computed with a Distance calculation. A possible query is given on the top right; a user might ask for possible graphs that consist of: a structure, input to a calculation, with a result (a

dictionary-data node) as output. The query has four different possible embeddings for this specific AiiDA graph, that are shown in the separate panels. Therefore, four results are solutions to this query.

As an additional functionality, queries typically require filters on the attributes of each node (or link), that can be specified using the QueryBuilder API. For instance, the user might want to filter only for those results containing a *total_energy* key, and whose value is within a given range. This, for instance, would exclude embeddings (a) and (d) of Fig. B.1 from the solutions, if we assume that the results of distance calculations do not contain such a key. Additional filters, for example on the volume of the input structure, can help to further specify the query.

Finally, the user can define possible projections, i.e., which (subset of) information should be returned for each matching result. These can for instance be the calculation node itself, the value of the *total_energy* attribute of the result, or the chemical elements of the input structure. An example code is given below, where the query would return all MD calculations executed with Quantum ESPRESSO's PWscf code running currently on the remote machine(s), and the input structures used for those calculations.

```
from aiida.orm import QueryBuilder, DataFactory, CalculationFactory
from aiida.common.datastructures import calc_states

StructureData = DataFactory("structure")
ParameterData = DataFactory("parameter")
PwCalculation = CalculationFactory("quantumespresso.pw")

# Creating instance of QueryBuilder
qb = QueryBuilder()

# Tell the instance to query for all PW-calculations in the specific state
# WITHSCHEDULER (which means it is running on a remote machine):
qb.append(PwCalculation, project='*',
  filters={'state':calc_states.WITHSCHEDULER})

# and join the calculations with structures that are input to these
# calculations:
qb.append(StructureData, project='*', input_of=PwCalculation)

# and also join them with the input parameters, filtering by the parameters
# specifying its an MD simulation:
qb.append(ParameterData, input_of=PwCalculation,
  filters={'attributes.CONTROL.calculation':{'==':'md'}})
```

```
# retrieve all results:
results = qb.all()
```

The QueryBuilder will translate this query, via SQLAlchemy's query language, into an SQL expression that depends on the underlying database schema. After execution of the query, the QueryBuilder translates the results into AiiDA instances that the user can interact with.

C The flexible pinball model

C.1 Introduction

The derivation of the pinball model in Chap. 2 is physically motivated, and is easy to derive. In the following I go into more detail, and show how the pinball model can be expressed as a Taylor expansion around the host-lattice ground-state geometry. The pinball model of Chap. 2, referred to as *pinball 1* or *rigid pinball* in the following (due to the fact that the host lattice is fixed to equilibrium positions) is a direct first result, since it is the zeroth term of the Taylor expansion. Considering first- and second-order terms allows to formulate a *pinball 2*, where the host lattice is allowed to move and the charge density updated using density-functional perturbation theory. The derivation shown here was done together with Aris Marcolongo.

We start with a splitting of the Hamiltonian into two sublattices: the host lattice H with ion positions $\boldsymbol{R}_H$ and a sublattice P of pinball ions at positions $\boldsymbol{R}_P$. The Hamiltonian of such a system is:

$$\mathscr{H} = \frac{1}{2}\sum_h^H M_h \dot{\boldsymbol{R}}_h^2 + \frac{1}{2}\sum_p^P M_p \dot{\boldsymbol{R}}_p^2 + U_{DFT}(\boldsymbol{R}_H, \boldsymbol{R}_P) \tag{C.1}$$

The potential energy surface in DFT, U_{DFT}, is given by:

$$\begin{aligned} U_{DFT}(\boldsymbol{R}^P, \boldsymbol{R}^H) =& E_N^{P-P} + E_N^{H-H} + E_N^{H-P} \\ &+ \int n(\boldsymbol{r}) V_{ext}^{H,P}(\boldsymbol{r}) \mathrm{d}\boldsymbol{r} + F[n]; \quad \text{with} \quad n = n[\boldsymbol{R}^H, \boldsymbol{R}^P], \end{aligned} \tag{C.2}$$

where $F[n]$ is the universal functional of the density, given by the sum over the kinetic energy, the Hartree-energy, and the exchange-correlation energy: $F[n] = T_0[n] + E_H[n] + E_{xc}[n]$. The electrostatic interaction between the nuclei of species A with species B is given by $E_N^{A-B} = \sum_I^A \sum_J^B \frac{Z_I Z_J}{|R_I - R_J|}$ and $V_{ext}^A(r)$ is the external potential from all ions of species A.

We generalize the assumptions of the pinball model:

(1) The pinballs are ionized, and instead of calculating the charge density of the system self-consistently, we calculate it from the external potential from the host ions and a Jellium. We spread the charges of the pinball ions homogeneously across the unit cell: $n^{H,P} = n^{H,J}$ We

approximate U_{DFT} with U by taking $n = n^{H,J}$ in Eq. (C.2).

(2) The host-lattice ions vibrate in wells around their equilibrium positions $\boldsymbol{R}_0^H$ in the presence of a Jellium. With respect to the *rigid* pinball, we allow for movement of the host lattice.

Applying the assumption (2) to Eq. (C.1) allows us to express the Hamiltonian as a Taylor series around the ground-state host-lattice geometry $\boldsymbol{R}_0^H$. For any potential energy U, we obtain:

$$\begin{aligned}\mathscr{H} =& \frac{1}{2}\sum_h^H M_h \dot{\boldsymbol{R}}_h^2 + \frac{1}{2}\sum_p^P M_p \dot{\boldsymbol{R}}_p^2 + U(\boldsymbol{R}^H = \boldsymbol{R}_0^H, R^P) + \sum_h^H \frac{\partial U}{\partial \boldsymbol{R}_h}(\boldsymbol{R}^H = \boldsymbol{R}_0^H, \boldsymbol{R}^P)\Delta \boldsymbol{R}_h \\ &+ \frac{1}{2}\sum_{h,h'}^H \frac{\partial^2 U}{\partial \boldsymbol{R}_h \partial \boldsymbol{R}_{h'}}(\boldsymbol{R}^H = \boldsymbol{R}_0^H, \boldsymbol{R}^P)\Delta \boldsymbol{R}_h \Delta \boldsymbol{R}_{h'},\end{aligned} \tag{C.3}$$

where we neglect higher-order terms.

C.2 Equations & identities

Some equations and identities that we will exploit later are given here. The first concerns the derivative of the DFT energy. We apply Eq. (6.3) in [499] to the potential of a system of host ions and the Jellium. At the ground state charge density the potential is 0:

$$V_{ext}^{H,J}(\boldsymbol{r}) + \frac{\delta F}{\delta n}\left[n^{H,J}\right] - \mu = 0$$

We split the term into terms that depend on $\boldsymbol{r}$ and those that do not:

$$V_{ext}^{H}(\boldsymbol{r}) + \frac{\delta F}{\delta n}\left[n^{H,J}\right] = \mu - V_{ext}^{J} = \text{const} \tag{C.4}$$

Another important identity that will be exploited later comes from the Hellman-Feynman forces, that have to be 0 at equilibrium. For the system of host ions at $R^H = R_0^H$ and the Jellium we obtain:

$$-\frac{\partial E_N^{H_0-H_0}}{\partial \boldsymbol{R}_h} - \int \frac{\partial V_{ext}^{H_0}}{\partial \boldsymbol{R}_h} n^{H_0,J}(\boldsymbol{r})\mathrm{d}\boldsymbol{r} = 0 \tag{C.5}$$

We take the expression for the Born–von Karman force constant matrix $\overline{C}$ for the host ions alone from the Eq. (22) in [500]:

$$C_{hh'} = \frac{\partial^2 E_N^{H_0-H_0}}{\partial \boldsymbol{R}_{h'} \partial \boldsymbol{R}_h} + \int \frac{\partial n^{H_0,J}}{\partial \boldsymbol{R}_{h'}} \frac{\partial V_{ext}^{H_0}}{\partial \boldsymbol{R}_h}\mathrm{d}\boldsymbol{r} + \int n^{H_0} \frac{\partial V_{ext}^{H_0}}{\partial \boldsymbol{R}_h \partial \boldsymbol{R}_{h'}}\mathrm{d}\boldsymbol{r} \tag{C.6}$$

C.3 Detailed derivation

C.3.1 First term of the expansion

The first term in the expansion of Eq. (C.3) becomes:

$$U(\boldsymbol{R}^H = \boldsymbol{R}_0^H, \boldsymbol{R}^P) = E_N^{P-P} + E_N^{H_0-H_0} + E_N^{H_0-P} + \int n^{H_0,J}(\boldsymbol{r}) V_{ext}^{H_0,P}(\boldsymbol{r}) \mathrm{d}\boldsymbol{r} + F[n^{H_0,J}] \tag{C.7}$$

We recognize that this is equivalent to the formulation of the rigid pinball given in Eq. (2.4).

C.3.2 Second term

First we derive U with respect to the position of a host ion. We cannot apply the Hellman-Feynman theorem since $n^{H,J}$ is not the ground state charge density of the system of $H+P$.

$$\begin{aligned}
\frac{\partial U}{\partial \boldsymbol{R}_h} =& \frac{\partial}{\partial \boldsymbol{R}_h}(E_N^{H-H} + E_N^{H-P}) + \frac{\partial}{\partial \boldsymbol{R}_h}\int V_{ext}^{P,H}(\boldsymbol{r}) n^{H,J}(\boldsymbol{r}) \mathrm{d}\boldsymbol{r} + \frac{\partial}{\partial \boldsymbol{R}_h} F[n^{H,J}] \\
=& \frac{\partial}{\partial \boldsymbol{R}_h}(E_N^{H-H} + E_N^{H-P}) + \int \frac{\partial V_{ext}^{H}(\boldsymbol{r})}{\partial \boldsymbol{R}_h} n^{H,J}(\boldsymbol{r}) \mathrm{d}\boldsymbol{r} + \int V_{ext}^{P,H}(\boldsymbol{r}) \frac{\partial n^{H,J}(\boldsymbol{r})}{\partial \boldsymbol{R}_h} \mathrm{d}\boldsymbol{r} + \frac{\partial}{\partial \boldsymbol{R}_h} F[n^{H,J}] \\
=& \frac{\partial}{\partial \boldsymbol{R}_h}(E_N^{H-H} + E_N^{H-P}) + \int \frac{\partial V_{ext}^{H}(\boldsymbol{r})}{\partial \boldsymbol{R}_h} n^{H,J}(\boldsymbol{r}) \mathrm{d}\boldsymbol{r} + \int \frac{\partial n^{H,J}(\boldsymbol{r})}{\partial \boldsymbol{R}_h} V_{ext}^{P}(\boldsymbol{r}) \\
&+ \int \frac{\partial n^{H,J}(\boldsymbol{r})}{\partial \boldsymbol{R}_h} \left(V_{ext}^{H}(\boldsymbol{r}) + \frac{\delta F}{\delta n}[n^{H,J}] \right) \mathrm{d}\boldsymbol{r}
\end{aligned} \tag{C.8}$$

We recognize the term in brackets of the last line in Eq. (C.8) as being the constant derived in Eq. (C.4). Exploiting that gives us for the last term:

$$\begin{aligned}
\int \frac{\partial n^{H,J}(\boldsymbol{r})}{\partial \boldsymbol{R}_h} \left(V_{ext}^{H}(\boldsymbol{r}) + \frac{\delta F}{\delta n}[n^{H,J}] \right) \mathrm{d}\boldsymbol{r} &= \int \frac{\partial n^{H,J}(\boldsymbol{r})}{\partial \boldsymbol{R}_h} \left(\mu - V_{ext}^{J} \right) \mathrm{d}\boldsymbol{r} \\
&= \left(\mu - V_{ext}^{J} \right) \frac{\partial}{\partial \boldsymbol{R}_h} \int n^{H,J} \mathrm{d}\boldsymbol{r} \\
&= 0
\end{aligned} \tag{C.9}$$

Using the result of Eq. (C.9) simplifies Eq. (C.8) to:

$$\frac{\partial U}{\partial \boldsymbol{R}_h} = \frac{\partial}{\partial \boldsymbol{R}_h}(E_N^{H-H} + E_N^{H-P}) + \int \frac{\partial V_{ext}^{H}(\boldsymbol{r})}{\partial \boldsymbol{R}_h} n^{H,J}(\boldsymbol{r}) \mathrm{d}\boldsymbol{r} + \int V_{ext}^{P}(\boldsymbol{r}) \frac{\partial n^{H,J}(\boldsymbol{r})}{\partial \boldsymbol{R}_h} \mathrm{d}\boldsymbol{r} \tag{C.10}$$

Taking the result of Eq. (C.10) at $R^H = R_0^H$ gives us:

$$\begin{aligned}
\frac{\partial U}{\partial \boldsymbol{R}_h}(\boldsymbol{R}^H = \boldsymbol{R}_0^H, \boldsymbol{R}^P) =& \frac{\partial}{\partial \boldsymbol{R}_h}(E_N^{H_0-H_0} + E_N^{H_0-P}) + \int \frac{\partial V_{ext}^{H_0}(\boldsymbol{r})}{\partial \boldsymbol{R}_h} n^{H_0,J}(\boldsymbol{r}) \mathrm{d}\boldsymbol{r} \\
&+ \int V_{ext}^{P}(\boldsymbol{r}) \frac{\partial n^{H_0,J}(\boldsymbol{r})}{\partial \boldsymbol{R}_h} \mathrm{d}\boldsymbol{r}
\end{aligned} \tag{C.11}$$

We exploit the identity given in Eq. (C.5) to get the final result for the second term in the expansion:

$$\frac{\partial U}{\partial \boldsymbol{R}_h}(\boldsymbol{R}^H = \boldsymbol{R}_0^H, \boldsymbol{R}^P) = \frac{\partial}{\partial \boldsymbol{R}_h} E_N^{H_0-P} + \int V_{ext}^P(\boldsymbol{r}) \frac{\partial n^{H_0,J}(\boldsymbol{r})}{\partial \boldsymbol{R}_h} \mathrm{d}\boldsymbol{r} \tag{C.12}$$

C.3.3 Third term

We derive Eq. (C.10) by the position of a host ion:

$$\begin{aligned}\frac{\partial^2 U}{\partial \boldsymbol{R}_h \partial \boldsymbol{R}_{h'}} =& \frac{\partial^2}{\partial \boldsymbol{R}_h \partial \boldsymbol{R}_{h'}}(E_N^{H-H} + E_N^{H-P}) + \int \frac{\partial^2 V_{ext}^H(\boldsymbol{r})}{\partial \boldsymbol{R}_h \partial \boldsymbol{R}_{h'}} n^{H,J}(\boldsymbol{r}) \mathrm{d}\boldsymbol{r} \\ &+ \int \frac{\partial V_{ext}^H(\boldsymbol{r})}{\partial \boldsymbol{R}_h} \frac{\partial n^{H,J}(\boldsymbol{r})}{\partial \boldsymbol{R}_{h'}} \mathrm{d}\boldsymbol{r} + \int V_{ext}^P(\boldsymbol{r}) \frac{\partial^2 n^{H,J}(\boldsymbol{r})}{\partial \boldsymbol{R}_h \partial \boldsymbol{R}_{h'}} \mathrm{d}\boldsymbol{r}.\end{aligned} \tag{C.13}$$

The last term in the expansion becomes:

$$\begin{aligned}\frac{\partial^2}{\partial \boldsymbol{R}_h \partial \boldsymbol{R}_{h'}} U(\boldsymbol{R}^H = \boldsymbol{R}_0^H, \boldsymbol{R}^P) =& \frac{\partial^2}{\partial \boldsymbol{R}_h \partial \boldsymbol{R}_{h'}}(E_N^{H_0-H_0} + E_N^{H_0-P}) + \int \frac{\partial V_{ext}^{H_0}(\boldsymbol{r})}{\partial \boldsymbol{R}_h} \frac{\partial n^{H_0,J}(\boldsymbol{r})}{\partial \boldsymbol{R}_{h'}} \mathrm{d}\boldsymbol{r} \\ &+ \int \frac{\partial^2 V_{ext}^{H_0}(\boldsymbol{r})}{\partial \boldsymbol{R}_h \partial \boldsymbol{R}_{h'}} n^{H_0,J}(\boldsymbol{r}) \mathrm{d}\boldsymbol{r} + \int V_{ext}^P(\boldsymbol{r}) \frac{\partial^2 n_0^H(\boldsymbol{r})}{\partial \boldsymbol{R}_h \partial \boldsymbol{R}_{h'}} \mathrm{d}\boldsymbol{r}\end{aligned} \tag{C.14}$$

We can substitute a few terms in Eq. (C.14) with the constant as defined in Eq. (C.6) and get:

$$\frac{\partial^2}{\partial \boldsymbol{R}_h \partial \boldsymbol{R}_{h'}} U(\boldsymbol{R}^H = \boldsymbol{R}_0^H, \boldsymbol{R}^P) = \frac{\partial^2}{\partial \boldsymbol{R}_h \partial \boldsymbol{R}_{h'}} E_N^{H_0-P} + \int V_{ext}^P(\boldsymbol{r}) \frac{\partial^2 n_0^H(\boldsymbol{r})}{\partial \boldsymbol{R}_h \partial \boldsymbol{R}_{h'}} \mathrm{d}\boldsymbol{r} + C_{hh'}$$

C.3.4 Final Hamiltonian

We insert Eqs. (C.7), (C.12), and (C.15) into Eq. (C.3). After removing all constant terms we obtain:

$$\begin{aligned}\mathscr{H} =& \frac{1}{2}\sum_h^H M_h \dot{R}_h^2 + \frac{1}{2}\sum_p^P M_p \dot{R}_p^2 + E_N^{P-P} + E_N^{H_0-P} + \int n^{H_0,J}(\boldsymbol{r}) V_{ext}^P(\boldsymbol{r}) \mathrm{d}\boldsymbol{r} \\ &+ \sum_h^H \left(\frac{\partial E_N^{H_0-P}}{\partial \boldsymbol{R}_h} + \int \frac{\partial n^{H_0,J}(\boldsymbol{r})}{\partial \boldsymbol{R}_h} V_{ext}^P \mathrm{d}\boldsymbol{r} \right) \Delta \boldsymbol{R}_h \\ &+ \frac{1}{2}\sum_{hh'}^H \left(\frac{\partial^2}{\partial \boldsymbol{R}_h \partial \boldsymbol{R}_{h'}} E_N^{H_0-P} + \int V_{ext}^P(\boldsymbol{r}) \frac{\partial^2 n^{H_0,J}(\boldsymbol{r})}{\partial \boldsymbol{R}_h \partial \boldsymbol{R}_{h'}} \mathrm{d}\boldsymbol{r} + C_{hh'} \right) \Delta \boldsymbol{R}_h \Delta \boldsymbol{R}_{h'}.\end{aligned} \tag{C.15}$$

We can simplify the last equation further (though this is not necessary) by exploiting the expansion of the Ewald term to second order:

$$E_N^{H-P} = E_N^{H_0-P} + \sum_h^H \frac{\partial E_N^{H_0-P}}{\partial \boldsymbol{R}_h} \Delta \boldsymbol{R}_h + \frac{1}{2}\sum_{hh'}^H \frac{\partial^2 E_N^{H_0-P}}{\partial \boldsymbol{R}_h R_h h'} \Delta \boldsymbol{R}_h \Delta \boldsymbol{R}_{h'} + \mathscr{O}(\Delta^3),$$

resulting in:

$$\begin{aligned}\mathscr{H} =& \frac{1}{2}\sum_{h}^{H} M_h \dot{R}_h^2 + \frac{1}{2}\sum_{p}^{P} M_p \dot{R}_p^2 + E_N^{P-P} + E_N^{H-P} \\ &+ \int V_{ext}^{P}\left(n^{H_0,J}(\boldsymbol{r}) + \sum_{h}^{H}\frac{\partial n^{H_0,J}(\boldsymbol{r})}{\partial \boldsymbol{R}_h}\Delta\boldsymbol{R}_h + \frac{1}{2}\sum_{hh'}^{H}\frac{\partial^2 n^{H_0,J}(\boldsymbol{r})}{\partial \boldsymbol{R}_h \partial \boldsymbol{R}_{h'}}\Delta\boldsymbol{R}_h\Delta\boldsymbol{R}_{h'}\right)\mathrm{d}\boldsymbol{r} \\ &+ \frac{1}{2}\sum_{hh'}^{H} C_{hh'}\Delta\boldsymbol{R}_h\Delta\boldsymbol{R}_{h'}. \end{aligned} \tag{C.16}$$

C.3.5 Forces

We get the forces acting on a pinball p by deriving Eq. (C.16) with respect to the pinball position:

$$\begin{aligned}\boldsymbol{F}_p =& -\frac{\partial}{\partial \boldsymbol{R}_p}\left(E_N^{H-P} + E_N^{P-P}\right) \\ &- \int \frac{\partial V_{ext}^{P}}{\partial \boldsymbol{R}_p}\left(n^{H_0,J} + \sum_{h}^{H}\frac{\partial n^{H_0,J}(\boldsymbol{r})}{\partial \boldsymbol{R}_h}\Delta\boldsymbol{R}_h + \frac{1}{2}\sum_{hh'}^{H}\frac{\partial^2 n^{H_0,J}(\boldsymbol{r})}{\partial \boldsymbol{R}_h \partial \boldsymbol{R}_{h'}}\Delta\boldsymbol{R}_h\Delta\boldsymbol{R}_{h'}\right)\mathrm{d}\boldsymbol{r}, \end{aligned} \tag{C.17}$$

and the forces on the host ions are, equivalently:

$$\boldsymbol{F}_h = -\frac{\partial E_N^{H-P}}{\partial \boldsymbol{R}_h} - \int \frac{\partial n^{H_0,J}(\boldsymbol{r})}{\partial \boldsymbol{R}_h} V_{ext}^{P}(\boldsymbol{r})\mathrm{d}\boldsymbol{r} - \sum_{h'}^{H}\Delta\boldsymbol{R}_{h'}\left(\int \frac{\partial^2 n^{H_0,J}}{\partial \boldsymbol{R}_h \partial \boldsymbol{R}_{h'}} V_{ext}^{P}\mathrm{d}\boldsymbol{r} + C_{hh'}\right). \tag{C.18}$$

C.4 Conclusion

The derivation of the pinball 2 generalizes the *frozen* pinball, presented in Chap. 2. We have implemented the model, given by Eqs. (C.16), (C.17), and (C.18) into the PWscf code of the Quantum ESPRESSO distribution. The conservation of the total energy during the dynamics points to a correct implementation, but the dynamics are not stable due to the occurrence of very large forces when the host ions are displaced further away due to incomplete cancellation of the divergent nuclei-electron and nuclei-nuclei terms. More work will be required to correct for this.

D Supplemental information

D.1 Fast-ionic conductors

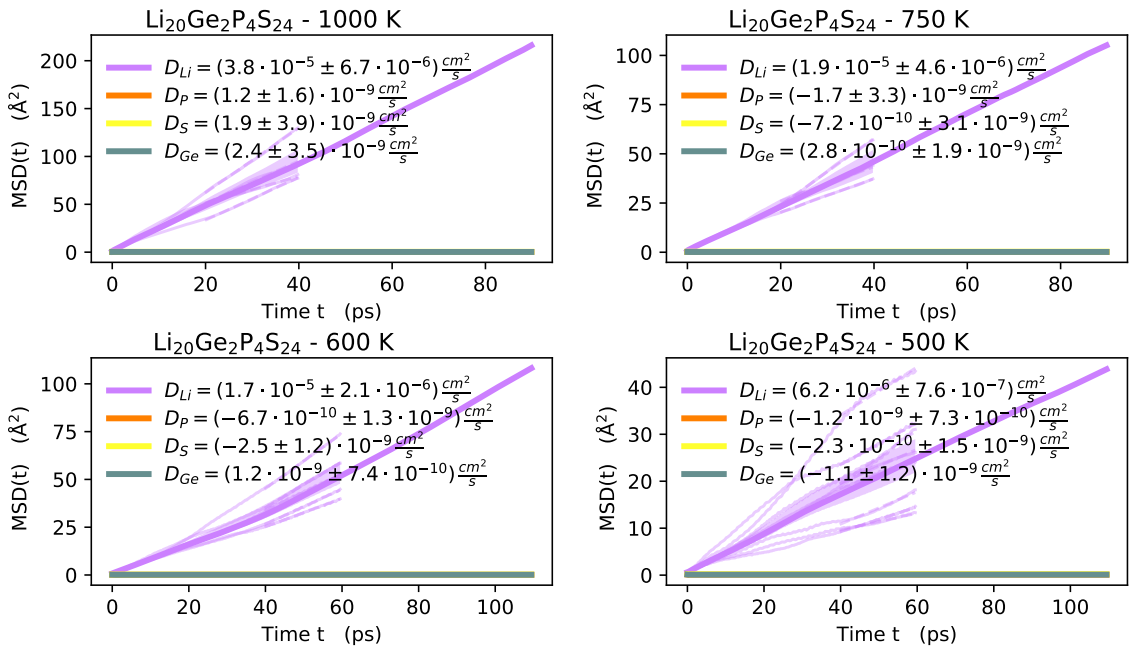

Fig. D.1: MSD(t) for $Li_{20}Ge_2P_4S_{24}$ from FPMD for all temperatures studied.

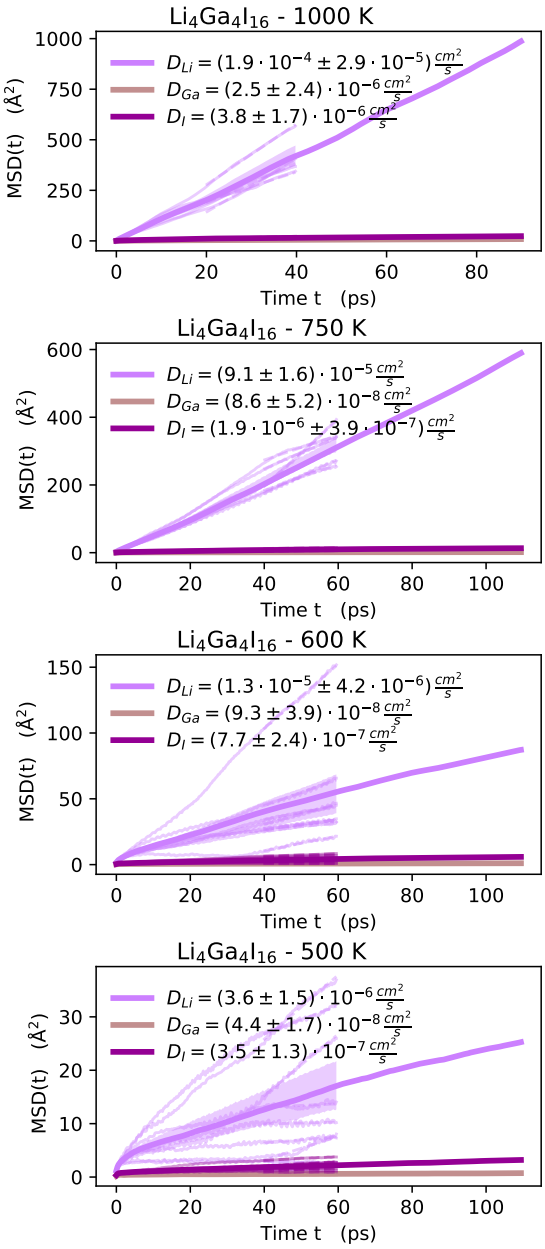

Fig. D.2: MSD(t) for $Li_4Ga_4I_{16}$ from FPMD for all temperatures studied.

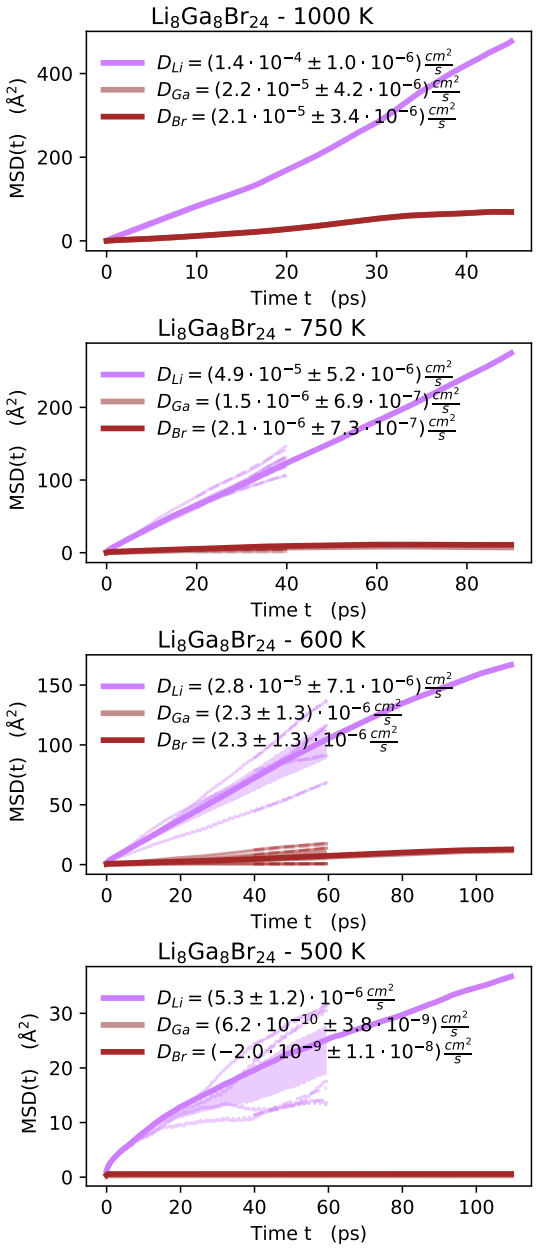

Fig. D.3: MSD(t) for $Li_8Ga_8Br_{24}$ from FPMD for all temperatures studied.

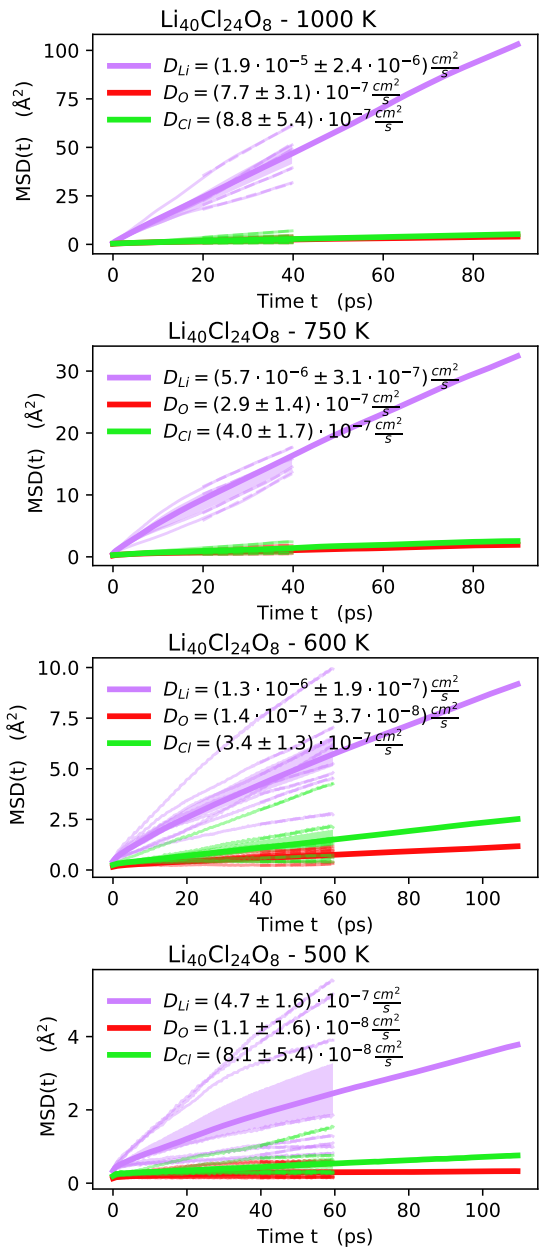

Fig. D.4: MSD(t) for $Li_{40}Cl_{24}O_8$ from FPMD for all temperatures studied.

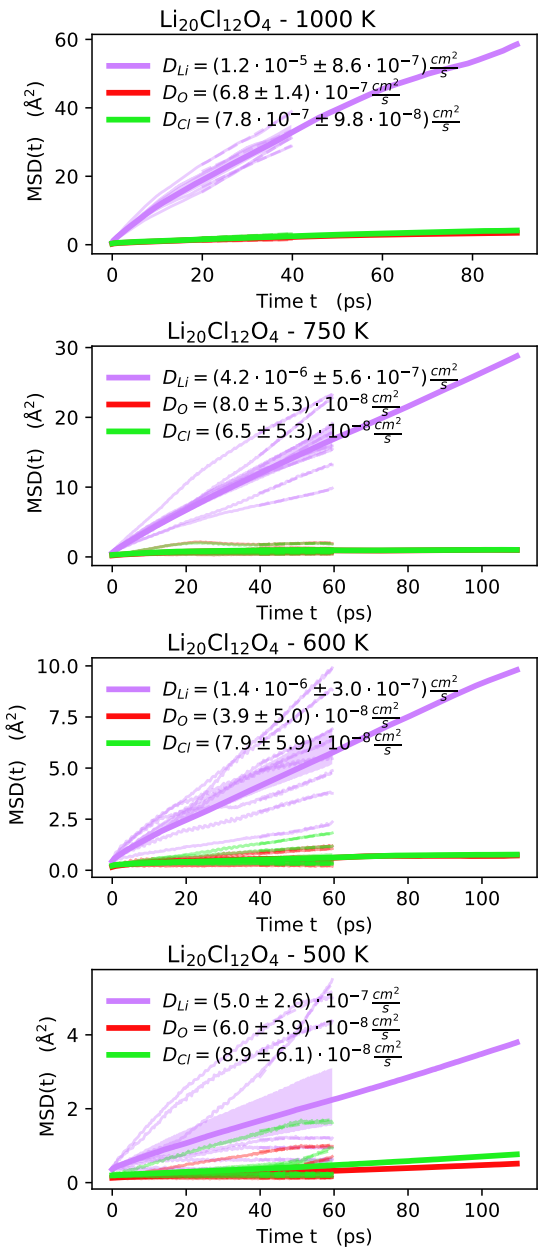

Fig. D.5: MSD(t) for $Li_{20}Cl_{12}O_4$ from FPMD for all temperatures studied.

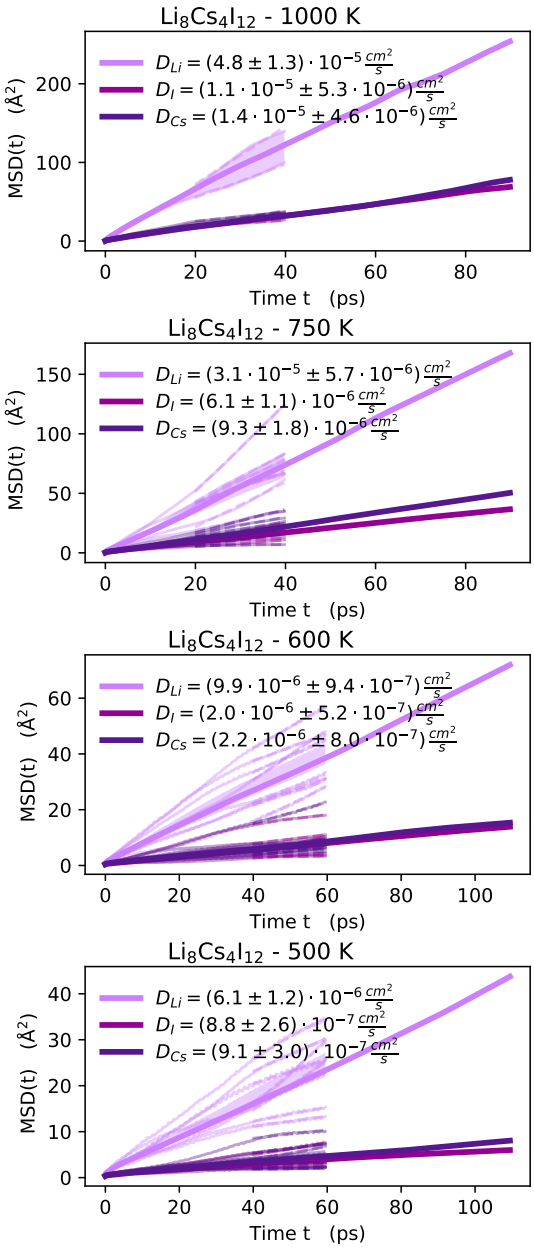

Fig. D.6: MSD(t) for $Li_8Cs_4I_{12}$ from FPMD for all temperatures studied.

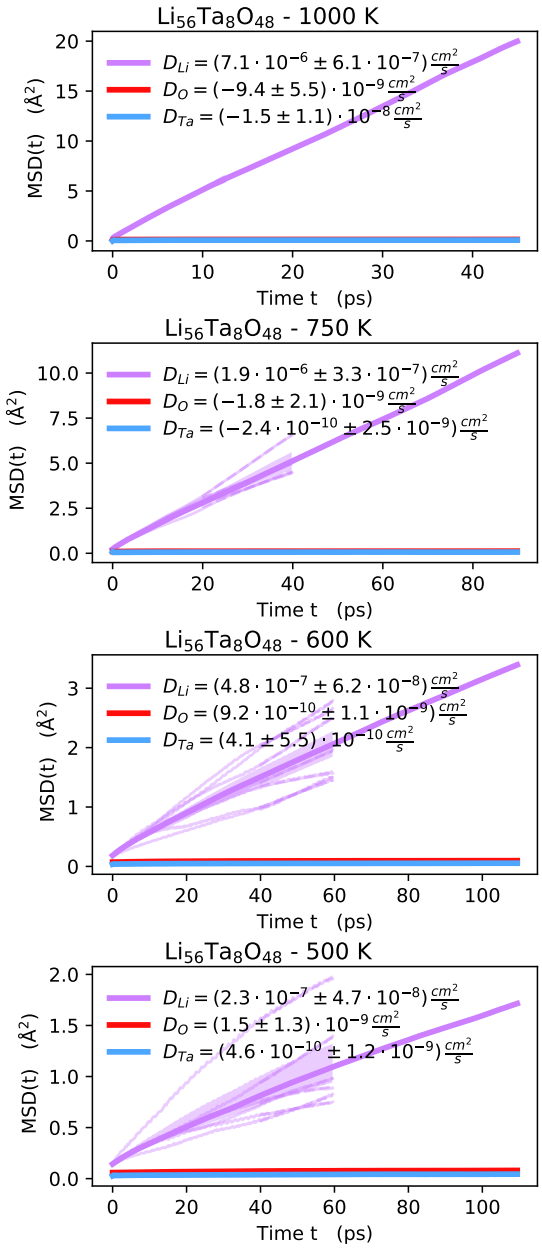

Fig. D.7: MSD(t) for $Li_{56}Ta_8O_{48}$ from FPMD for all temperatures studied.

D.2 Potential fast-ionic conductors

Structure	DB	DB-id	Supercell	Figure	Δ_{vol}	T^{sim}_{500}	T^{sim}_{600}	T^{sim}_{750}	T^{sim}_{1000}
$Li_4Re_6S_{11}$	COD	1008693	$Li_{16}Re_{24}S_{44}$	D.8	2.6%	87.1	174.3	87.2	290.8
$Li_6P_1S_5I_1$	ICSD	421083	$Li_{48}P_8S_{40}I_8$	D.10	2.9%	87.2	87.2	87.2	72.7
$Li_2B_2S_5$	COD	1510745	$Li_8B_8S_{20}$	D.16	5.4%	203.4	203.4	348.7	145.4
$Li_1Ta_1Ge_1O_5$	ICSD	280992	$Li_4Ta_4Ge_4O_{20}$	D.12	3.5%	145.3	523.0	319.6	218.1
$Li_2S_2O_7$	ICSD	188009	$Li_{16}S_{16}O_{56}$	D.21	5.4%	232.4	145.3	174.3	203.6
$Li_1I_1O_3$	ICSD	20032	$Li_{16}I_{16}O_{48}$	D.15	15.3%	145.3	726.4	523.0	72.7
$Li_1Al_1Si_1O_4$	COD	9000368	$Li_{12}Al_{12}Si_{12}O_{48}$	D.13	3.6%	145.3	697.3	290.6	218.1
$Li_5B_1S_4O_{16}$	ICSD	428002	$Li_{20}B_4S_{16}O_{64}$	D.11	6.3%	610.2	610.2	610.2	218.1
$Li_2Mg_2S_3O_{12}$	COD	2020217	$Li_8Mg_8S_{12}O_{48}$	D.14	4.1%	145.3	726.4	406.8	218.1
$Li_1Ti_1P_1O_5$	ICSD	39761	$Li_{16}Ti_{16}P_{16}O_{80}$	D.9	5.8%	232.4	232.4	261.5	218.1
$Li_3Cs_1Cl_4$	ICSD	245975	$Li_{24}Cs_8Cl_{32}$	D.18	1.6%	726.4	726.4	726.4	218.1
$Li_6Y(BO_3)_3$	COD	1510933	$Li_{24}Y_4B_{12}O_{36}$	D.17					
$Li_2Zn_1Sn_1Se_4$	COD	7035178	$Li_{16}Zn_8Sn_8Se_{32}$	D.22	4.2%	145.3	145.3	145.3	218.1
$Li_2Ti_3O_7$	ICSD	193803	$Li_8Ti_{12}O_{28}$	D.25	2.6%	145.3	145.3	145.3	218.1
$Rb_1Li_7Si_2O_8$	ICSD	33864	$Rb_4Li_{28}Si_8O_{32}$	D.20	2.8%	145.3	145.3	726.4	218.1
$Li_3Ga_1F_6$	COD	8101456	$Li_{18}Ga_6F_{36}$	D.23	4.8%	145.3	145.3	145.3	218.1
$Li_2In_2Ge_1S_6$	COD	4329224	$Li_{16}In_{16}Ge_8S_{48}$	D.24	5.6%	145.3	261.5	145.3	218.1
$Li_1Mo_1As_1O_6$	COD	2014117	$Li_8Mo_8As_8O_{48}$	D.26	8.2%	610.2	145.3	174.3	218.1
$Li_9Ga_3P_8O_{29}$	COD	2208797	$Li_{18}Ga_6P_{16}O_{58}$	D.19	2.1%	145.3	145.3	261.5	218.1

Table D.1: The structures that are found as potential ionic conductors and studied at different temperatures (500 K – 1000 K). We give the stoichiometric formula, the database and identifier of the repository this structure originates from, the formula of the supercell used, the figure where the mean-square displacement is shown in this supplemental information, and the simulation times at 500 K, 600 K, 750 K, and 1000 K (in ps).

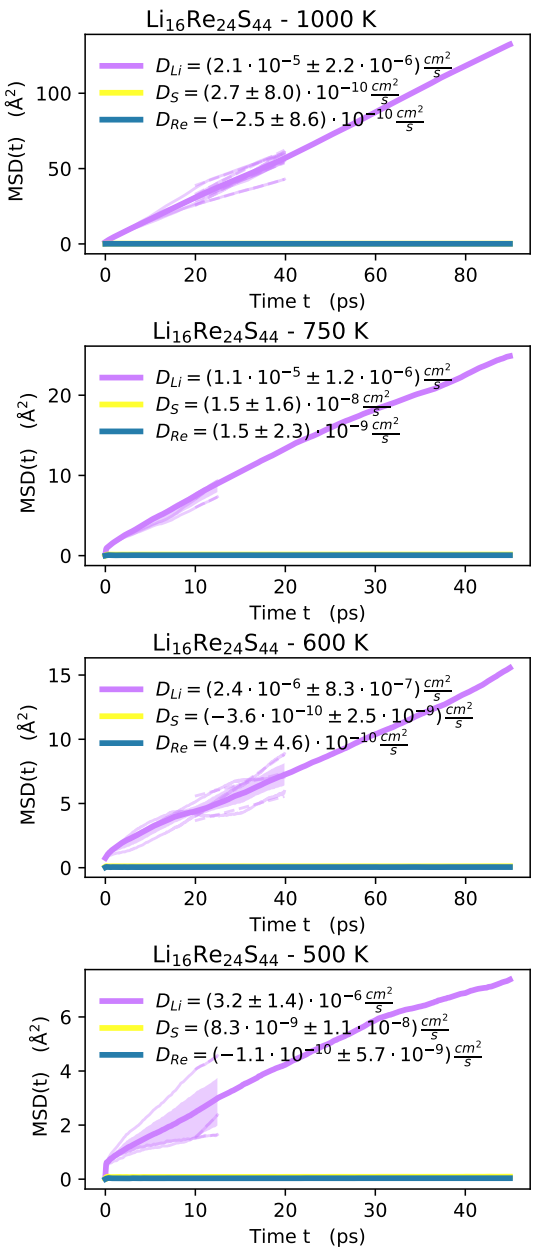

Fig. D.8: MSD(t) for $Li_{16}Re_{24}S_{44}$ from FPMD for all temperatures studied.

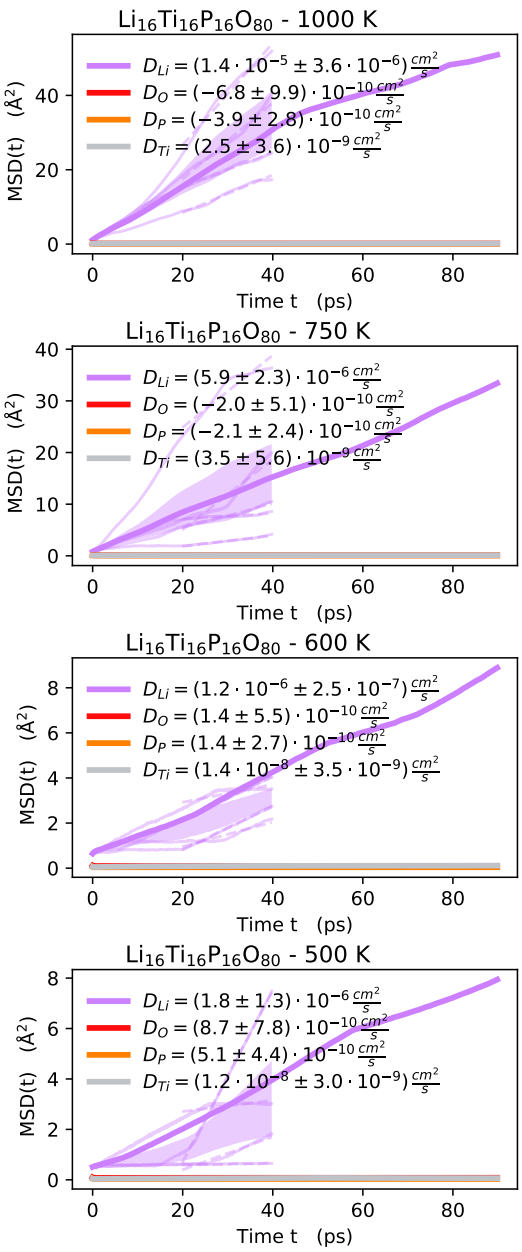

Fig. D.9: MSD(t) for $Li_{16}Ti_{16}P_{16}O_{80}$ from FPMD for all temperatures studied.

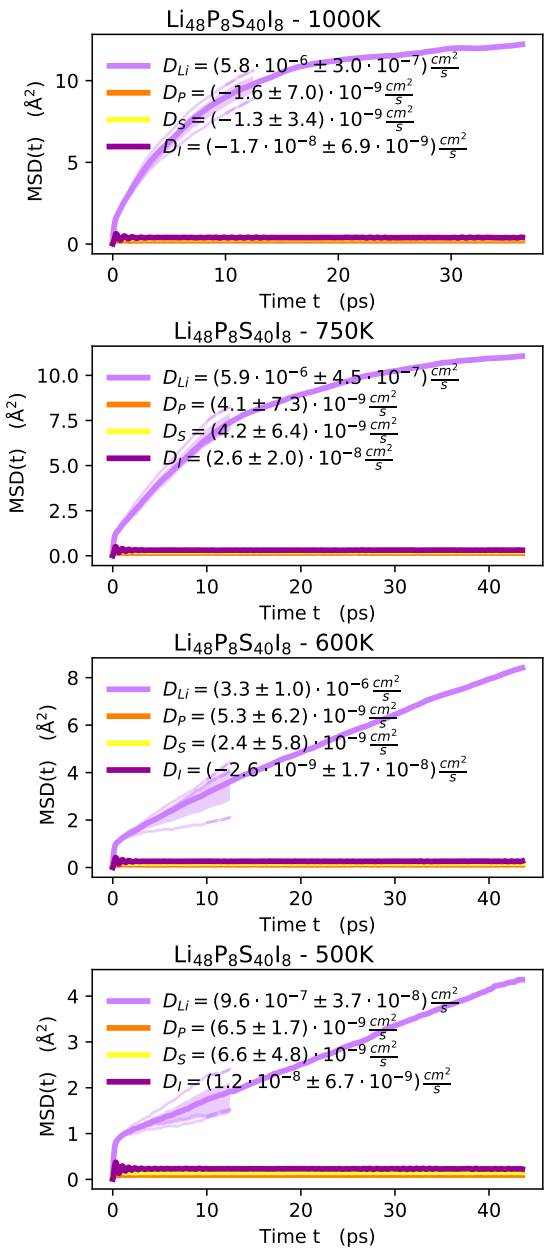

Fig. D.10: MSD(t) for $Li_{48}P_8S_{40}I_8$ from FPMD for all temperatures studied.

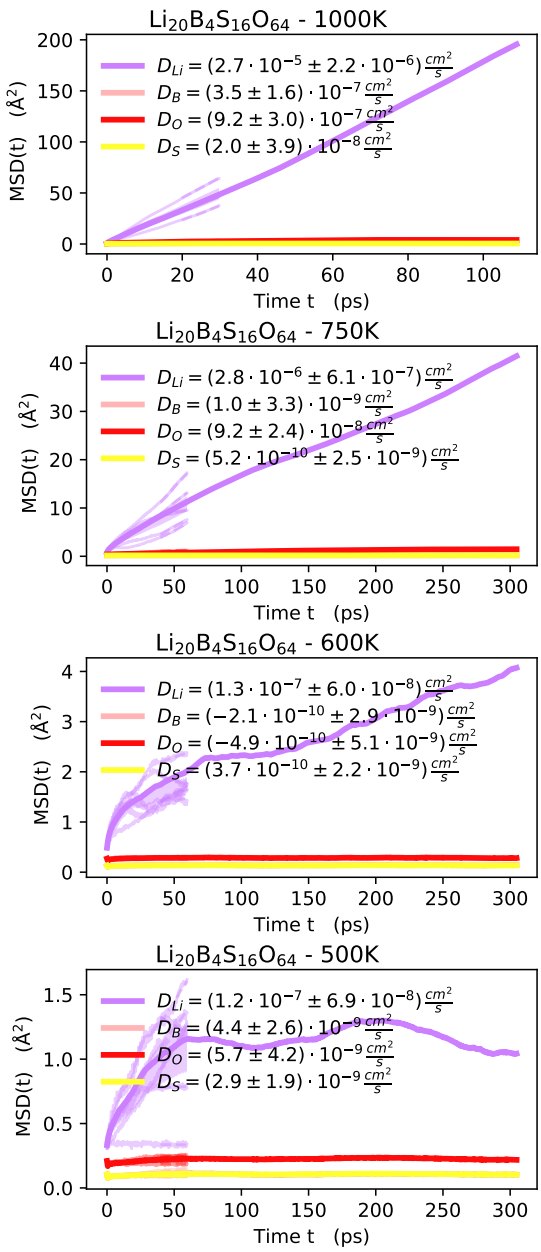

Fig. D.11: MSD(t) for $Li_{20}B_4S_{16}O_{64}$ from FPMD for all temperatures studied.

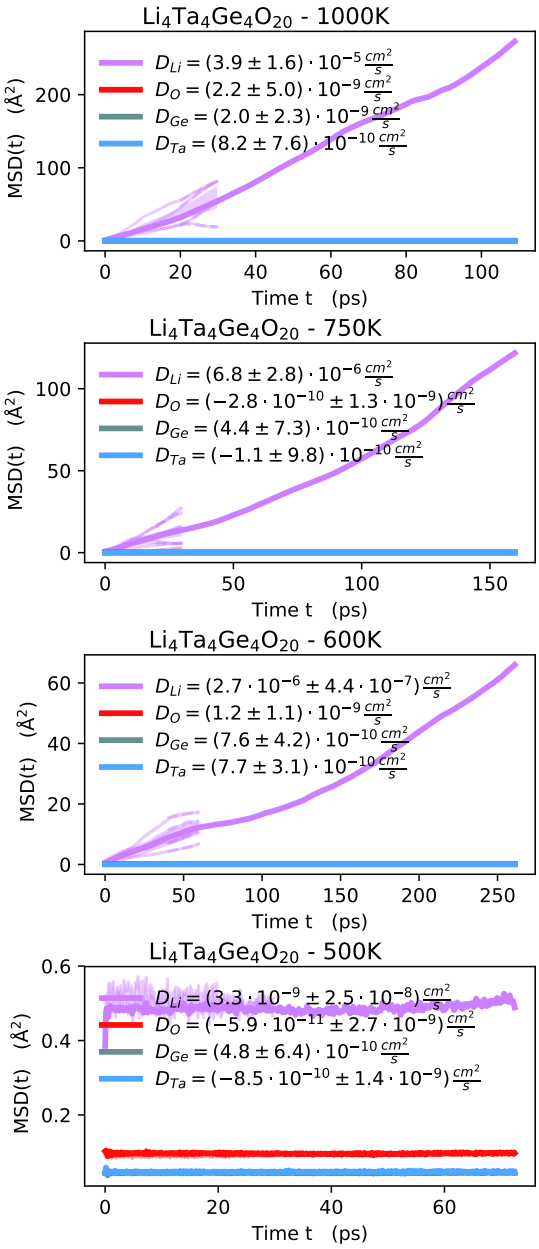

Fig. D.12: MSD(t) for $Li_4Ta_4Ge_4O_{20}$ from FPMD for all temperatures studied.

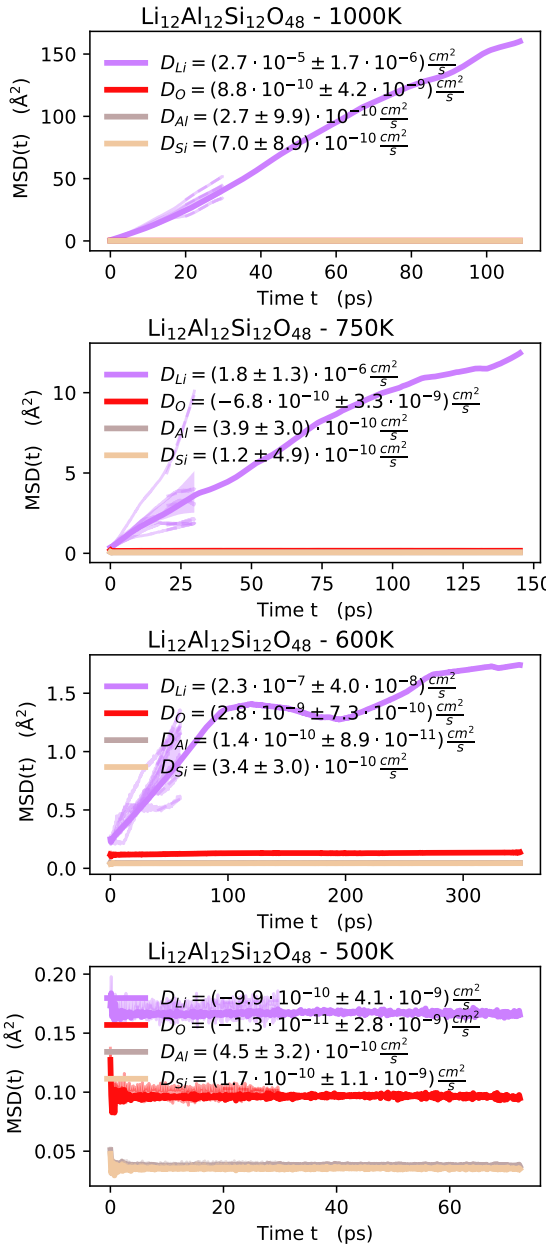

Fig. D.13: MSD(t) for $Li_{12}Al_{12}Si_{12}O_{48}$ from FPMD for all temperatures studied.

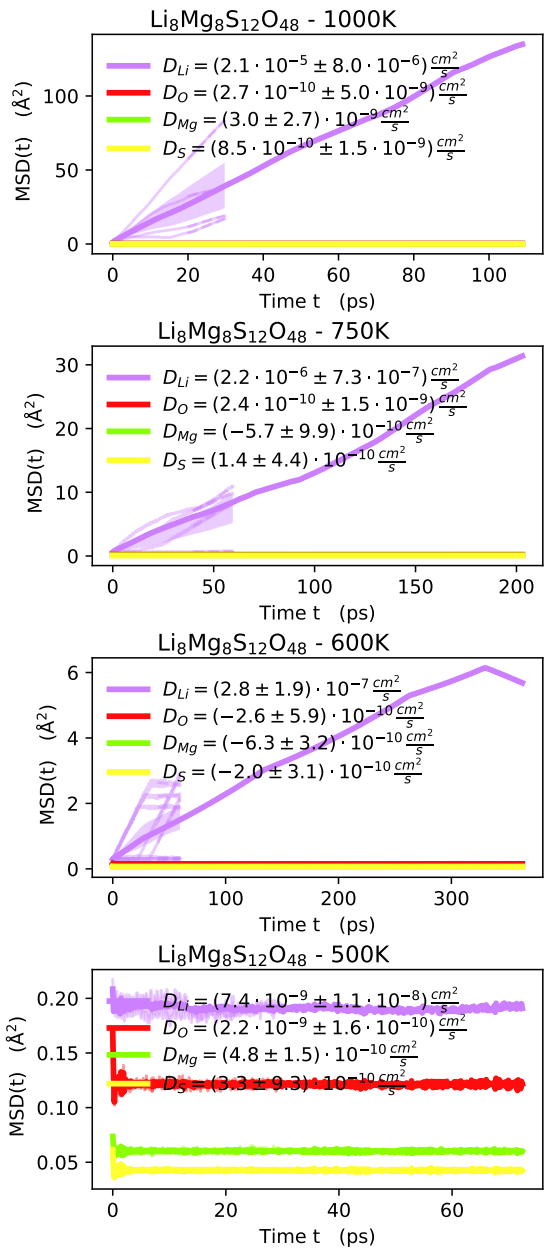

Fig. D.14: MSD(t) for $Li_8Mg_8S_{12}O_{48}$ from FPMD for all temperatures studied.

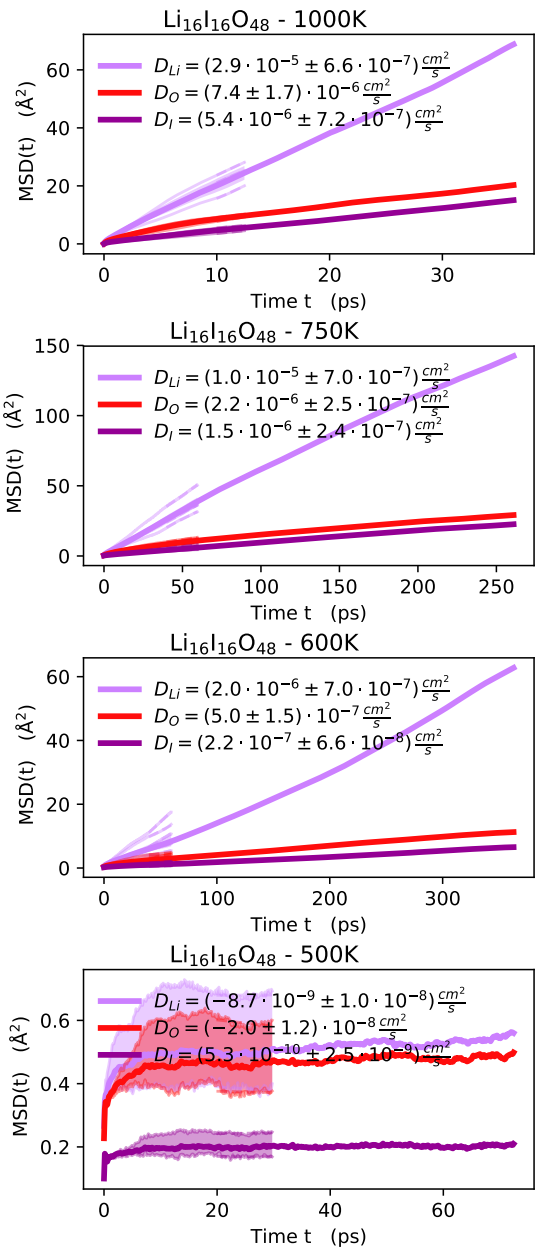

Fig. D.15: MSD(t) for $Li_{16}I_{16}O_{48}$ from FPMD for all temperatures studied.

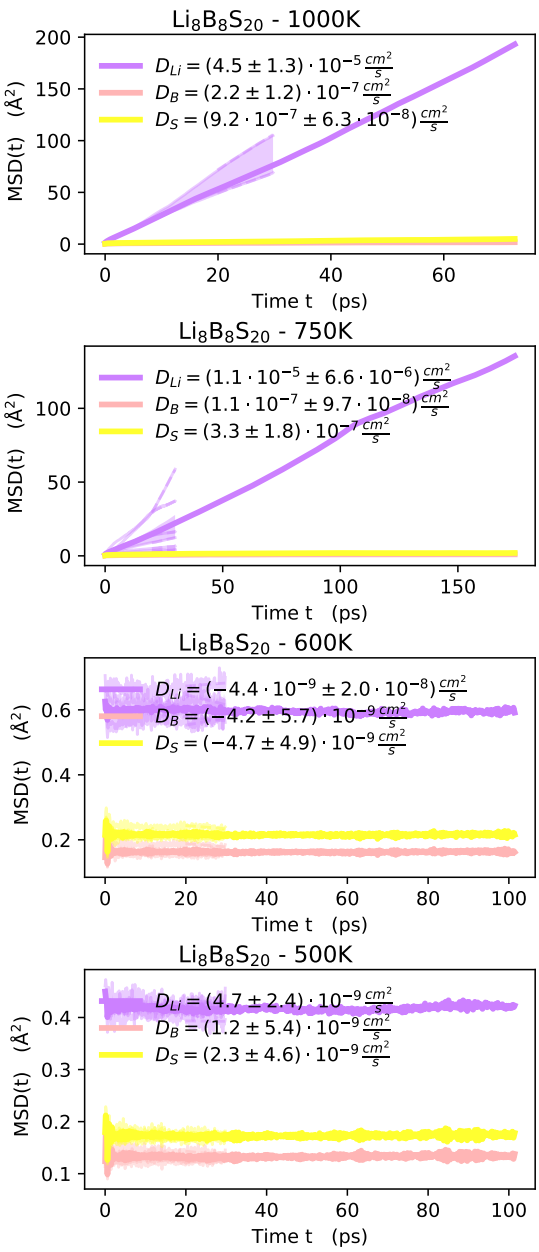

Fig. D.16: MSD(t) for $Li_8B_8S_{20}$ from FPMD for all temperatures studied.

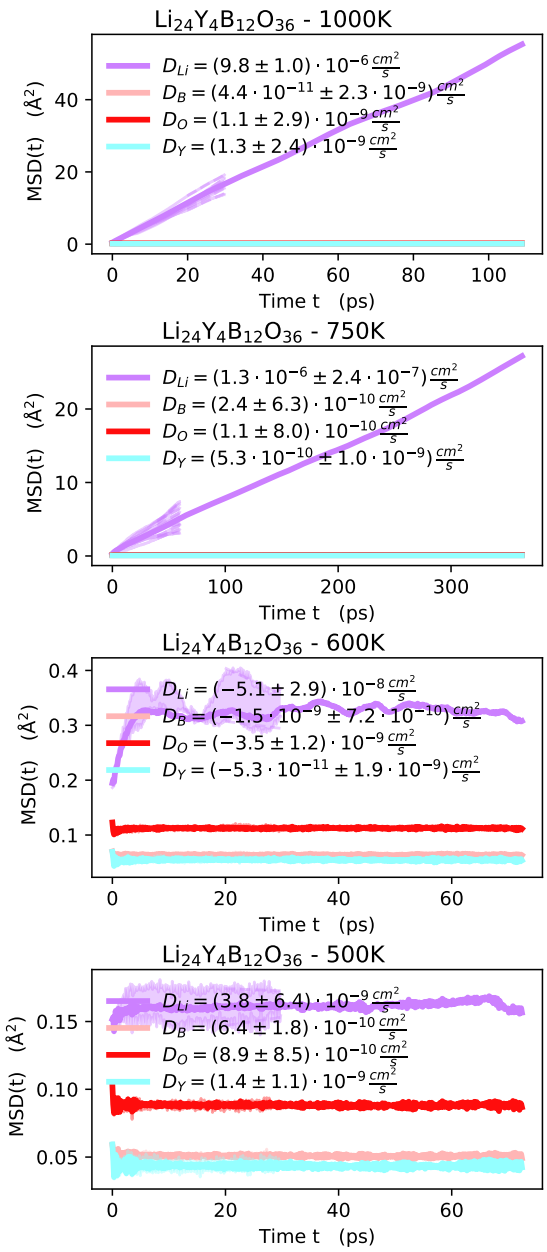

Fig. D.17: MSD(t) for $Li_{24}Y_4B_{12}O_{36}$ from FPMD for all temperatures studied.

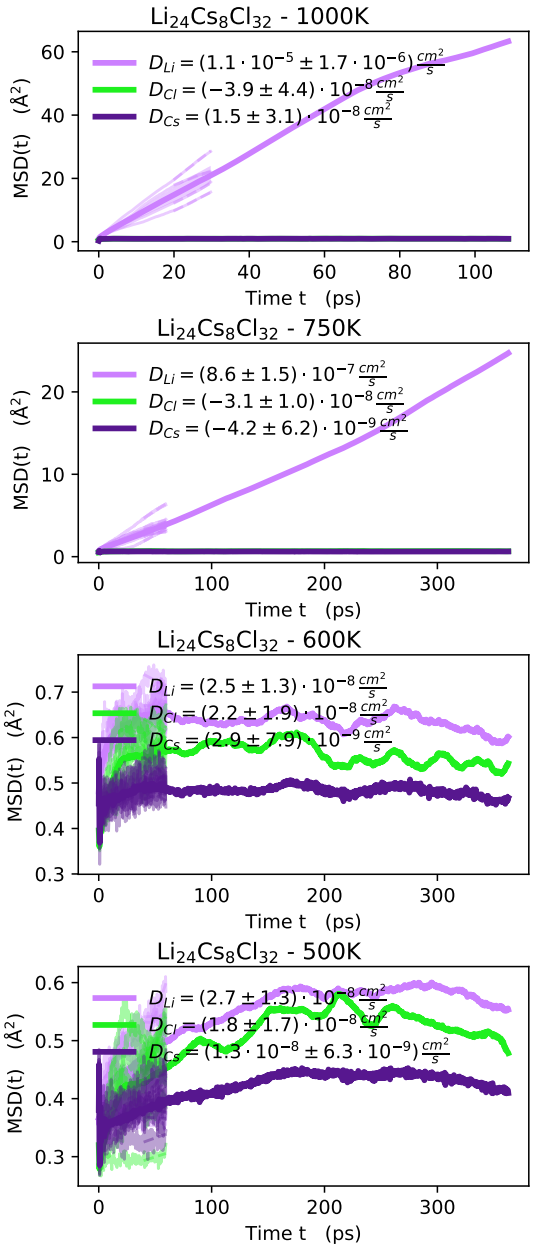

Fig. D.18: MSD(t) for $Li_{24}Cs_8Cl_{32}$ from FPMD for all temperatures studied.

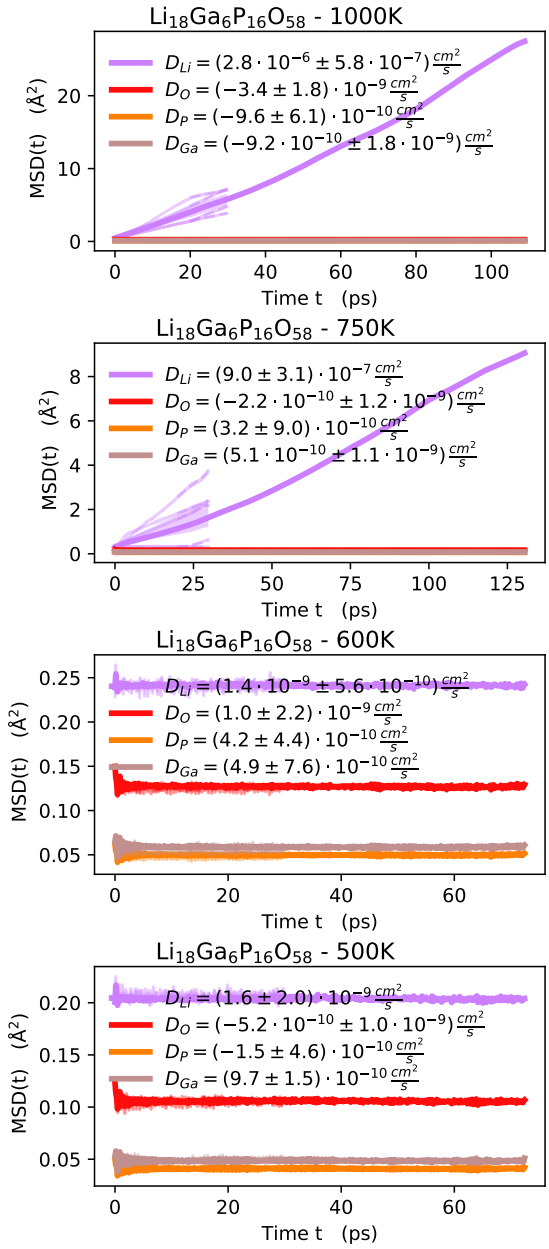

Fig. D.19: MSD(t) for $Li_{18}Ga_6P_{16}O_{58}$ from FPMD for all temperatures studied.

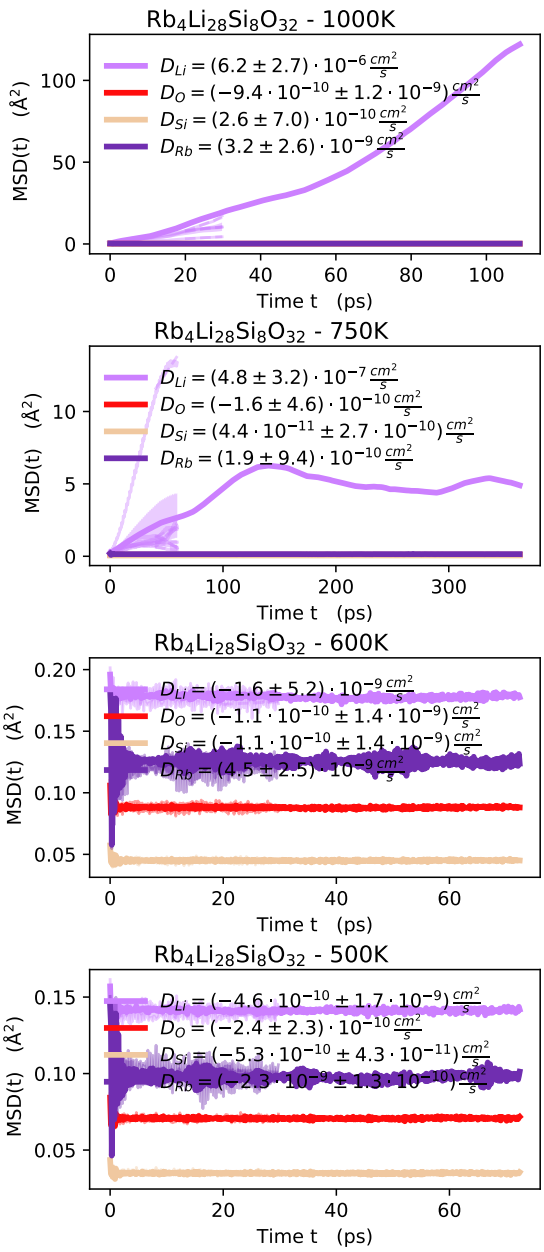

Fig. D.20: MSD(t) for $Rb_4Li_{28}Si_8O_{32}$ from FPMD for all temperatures studied.

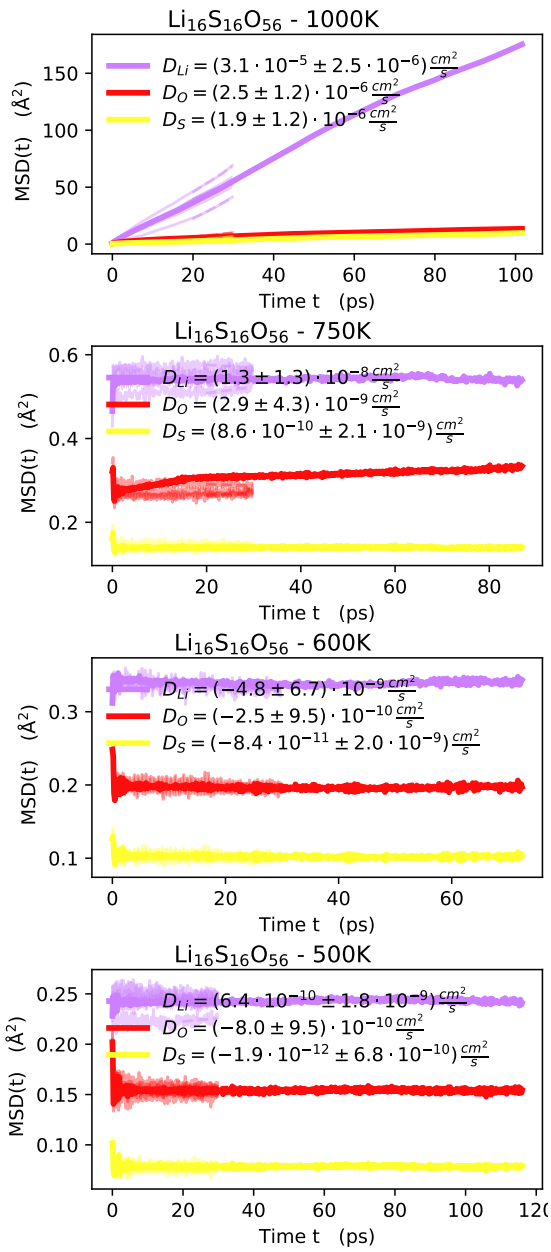

Fig. D.21: MSD(t) for $Li_{16}S_{16}O_{56}$ from FPMD for all temperatures studied.

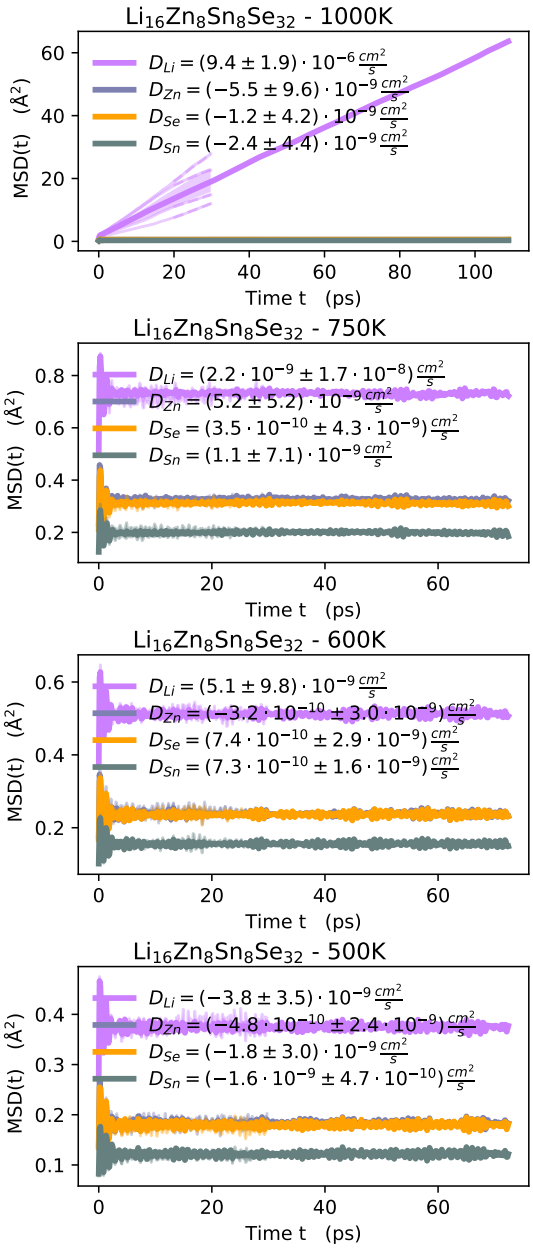

Fig. D.22: MSD(t) for $Li_{16}Zn_8Sn_8Se_{32}$ from FPMD for all temperatures studied.

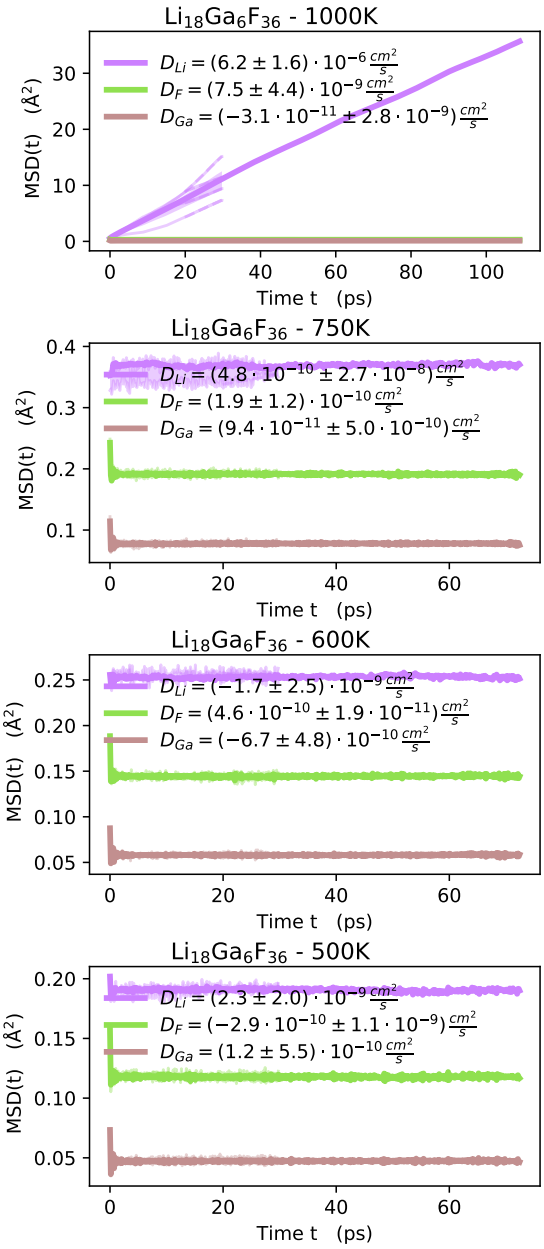

Fig. D.23: MSD(t) for $Li_{18}Ga_6F_{36}$ from FPMD for all temperatures studied.

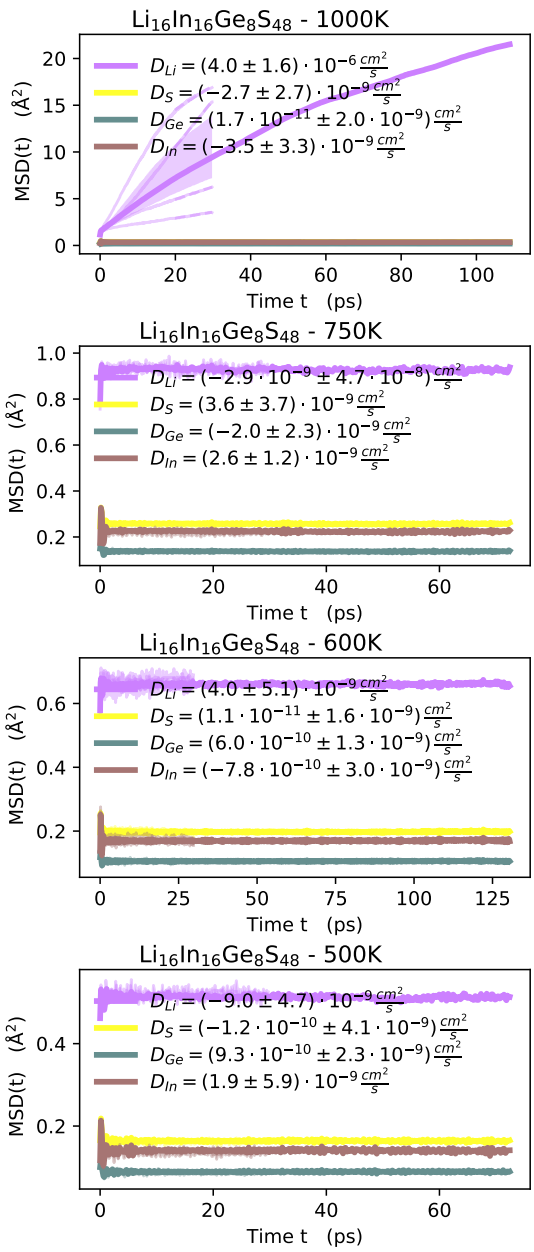

Fig. D.24: MSD(t) for $Li_{16}In_{16}Ge_8S_{48}$ from FPMD for all temperatures studied.

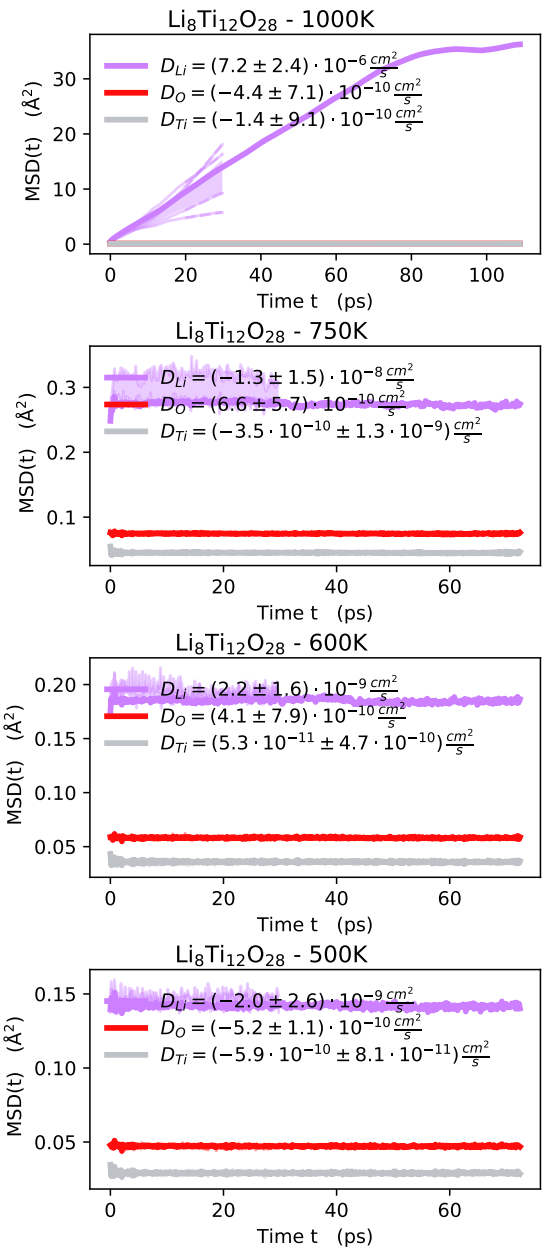

Fig. D.25: MSD(t) for $Li_8Ti_{12}O_{28}$ from FPMD for all temperatures studied.

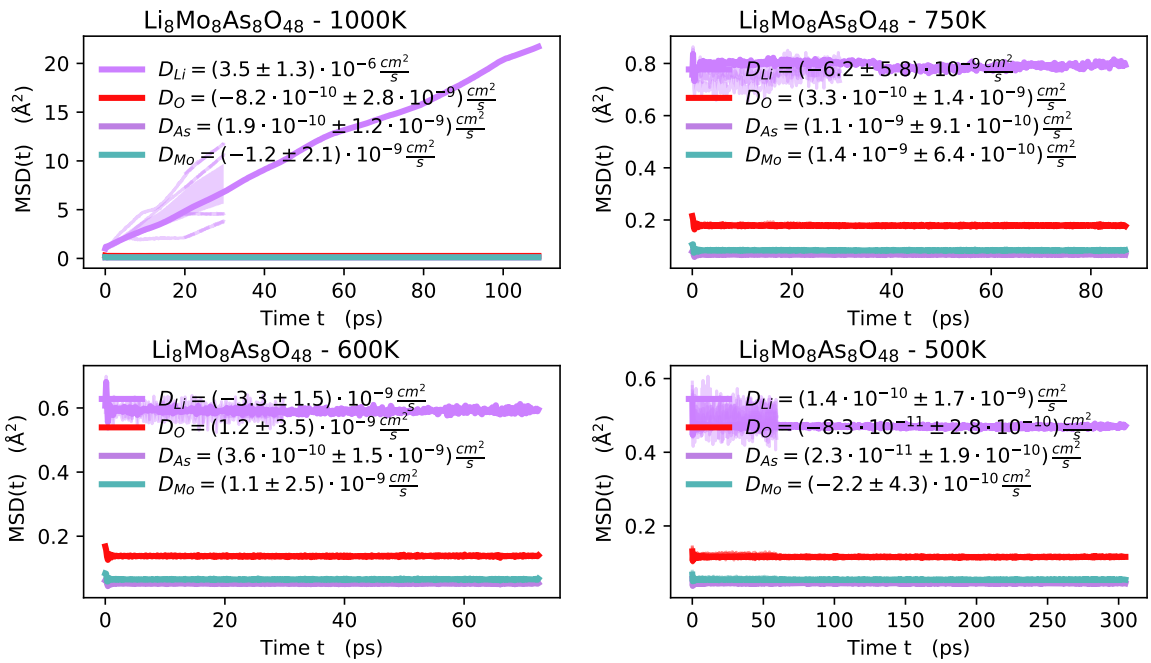

Fig. D.26: MSD(t) for $Li_8Mo_8As_8O_{48}$ from FPMD for all temperatures studied.

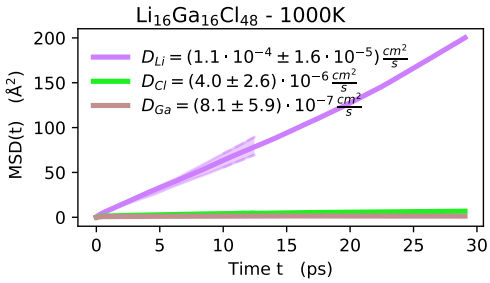

Fig. D.27: MSD(t) for $Li_{16}Ga_{16}Cl_{48}$.

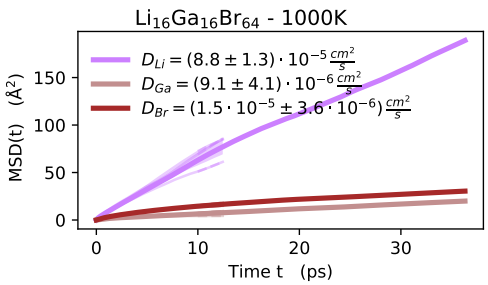

Fig. D.28: MSD(t) for $Li_{16}Ga_{16}Br_{64}$.

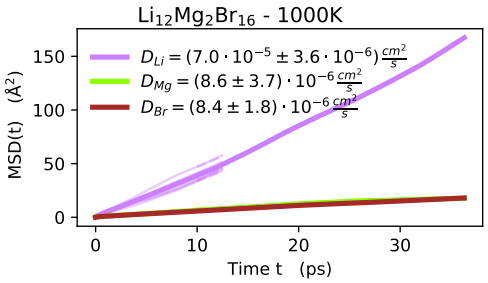

Fig. D.29: MSD(t) for $Li_{12}Mg_2Br_{16}$.

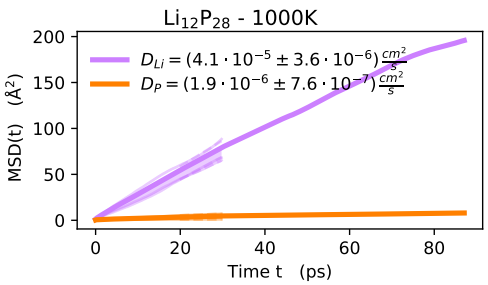

Fig. D.30: MSD(t) for $Li_{12}P_{28}$.

Structure	DB	DB-id	Supercell	Fig.	Δ_{vol}	T^{sim}_{1000}
$Li_1Ga_1Cl_3$	COD	1530096	$Li_{16}Ga_{16}Cl_{48}$	D.27	17.0%	58.2
$Li_1Ga_1Br_4$	ICSD	61337	$Li_{16}Ga_{16}Br_{64}$	D.28	30.8%	72.7
$Li_6Mg_1Br_8$	ICSD	73275	$Li_{12}Mg_2Br_{16}$	D.29	2.0%	72.7
Li_3P_7	ICSD	60774	$Li_{12}P_{28}$	D.30	2.1%	174.5
$Li_3As_1S_3$	COD	2007413	$Li_{12}As_4S_{12}$	D.31	2.9%	189.1
$Li_1B_1S_4Cl_4O_{12}$	COD	1004054	$Li_4B_4S_{16}Cl_{16}O_{48}$	D.32	11.7%	218.1
$Li_1Sn_2P_3O_{12}$	ICSD	83831	$Li_2Sn_4P_6O_{24}$	D.33	4.1%	87.3
$Li_4Ge_9O_{20}$	ICSD	34361	$Li_4Ge_9O_{20}$	D.34	5.4%	58.2
$Li_1I_1O_4$	COD	1536985	$Li_8I_8O_{32}$	D.35	10.4%	58.1
$Rb_2Li_1Ta_1S_4$	COD	1535645	$Rb_8Li_4Ta_4S_{16}$	D.36	6.4%	436.3
Li_1P_7	ICSD	23621	Li_8P_{56}	D.37	5.2%	436.3
$Li_4P_2O_7$	COD	2005920	$Li_{16}P_8O_{28}$	D.38	4.0%	43.6
$Li_2Ge_4O_9$	COD	2019177	$Li_{16}Ge_{32}O_{72}$	D.39	4.7%	189.1
$Li_1Au_1F_4$	ICSD	33953	$Li_8Au_8F_{32}$	D.40	11.9%	58.2
$Li_2Se_1O_4$	ICSD	67234	$Li_{12}Se_6O_{24}$	D.41	5.3%	116.3
$Li_1Al_1Se_2$	COD	4321118	$Li_{16}Al_{16}Se_{32}$	D.42	3.1%	218.1
$Li_1In_1P_2O_7$	ICSD	60935	$Li_4In_4P_8O_{28}$	D.43	6.3%	436.3
$Li_4Ti_1O_4$	ICSD	75164	$Li_{24}Ti_6O_{24}$	D.44	1.4%	436.3
$Li_6Si_2O_7$	COD	1539516	$Li_{24}Si_8O_{28}$	D.45	1.9%	445.2
$Li_2In_2Si_1Se_6$	COD	4329225	$Li_{16}In_{16}Si_8Se_{48}$	D.46	5.5%	218.1
$Li_1B_1S_2O_8$	ICSD	425174	$Li_8B_8S_{16}O_{64}$	D.47	6.9%	218.1

Table D.2: We list all the structures that have been calculated only at 1000 K, and where we find diffusion of Li ions, although not high enough to warrant a calculation also at lower temperatures.

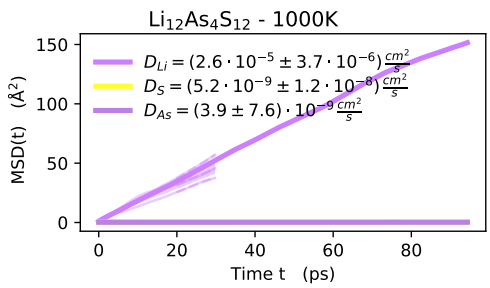

Fig. D.31: MSD(t) for $Li_{12}As_4S_{12}$.

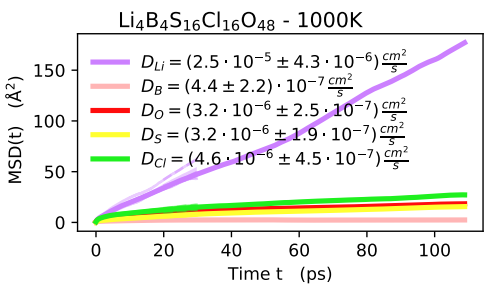

Fig. D.32: MSD(t) for $Li_4B_4S_{16}Cl_{16}O_{48}$.

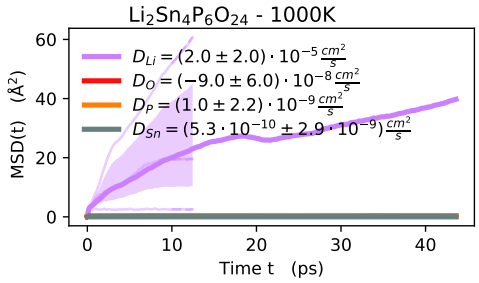

Fig. D.33: MSD(t) for $Li_2Sn_4P_6O_{24}$.

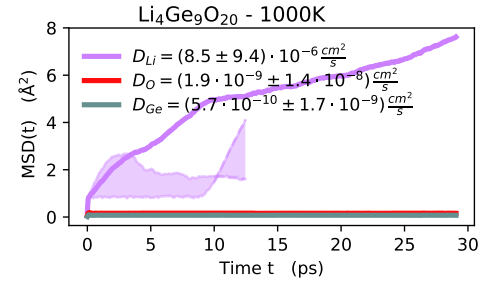

Fig. D.34: MSD(t) for $Li_4Ge_9O_{20}$.

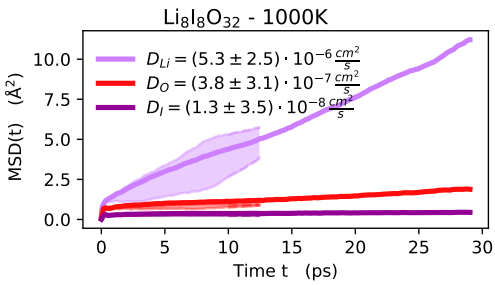

Fig. D.35: MSD(t) for $Li_8I_8O_{32}$.

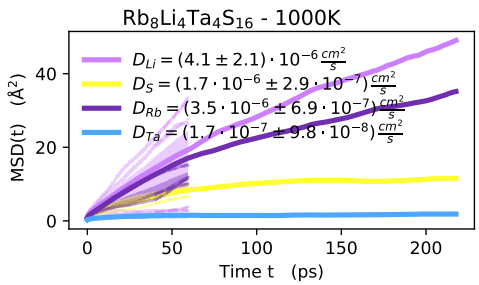

Fig. D.36: MSD(t) for $Rb_8Li_4Ta_4S_{16}$.

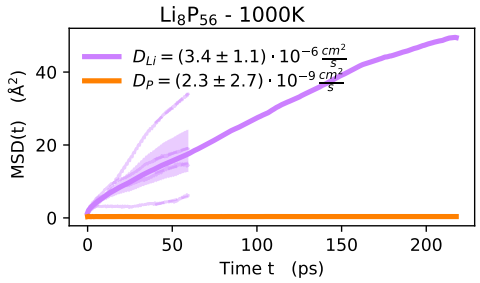

Fig. D.37: MSD(t) for Li_8P_{56}.

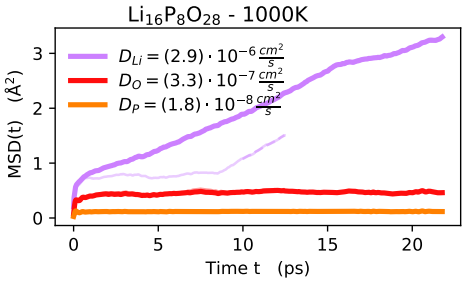

Fig. D.38: MSD(t) for $Li_{16}P_8O_{28}$.

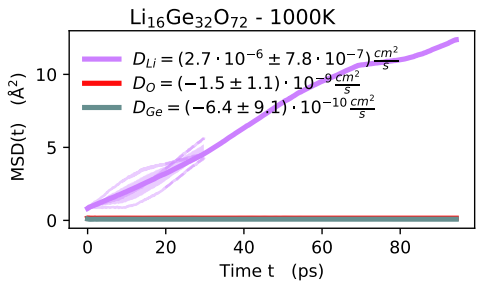

Fig. D.39: MSD(t) for $Li_{16}Ge_{32}O_{72}$.

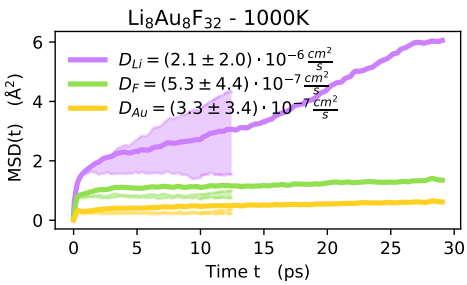

Fig. D.40: MSD(t) for $Li_8Au_8F_{32}$.

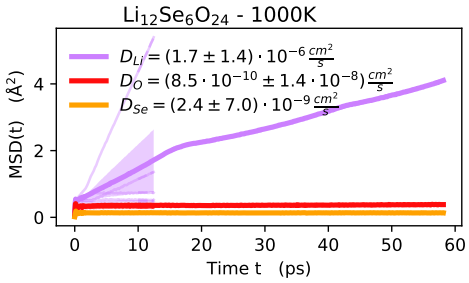

Fig. D.41: MSD(t) for $Li_{12}Se_6O_{24}$.

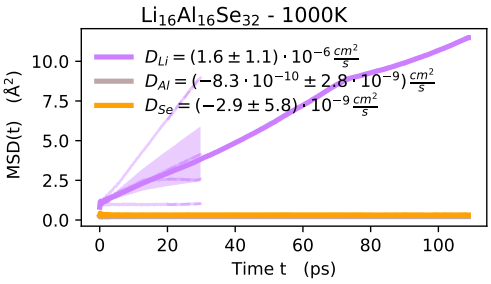

Fig. D.42: MSD(t) for $Li_{16}Al_{16}Se_{32}$.

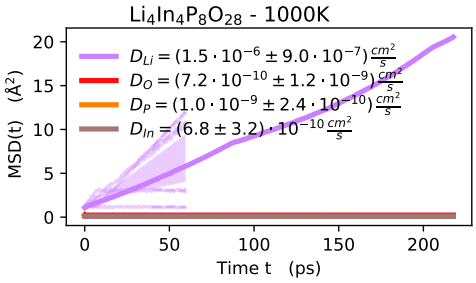

Fig. D.43: MSD(t) for $Li_4In_4P_8O_{28}$.

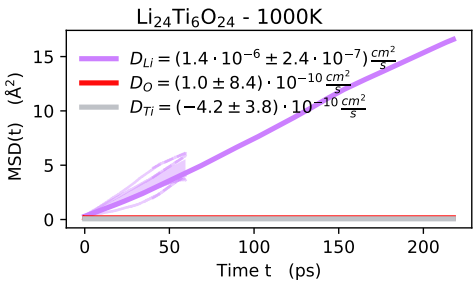

Fig. D.44: MSD(t) for $Li_{24}Ti_6O_{24}$.

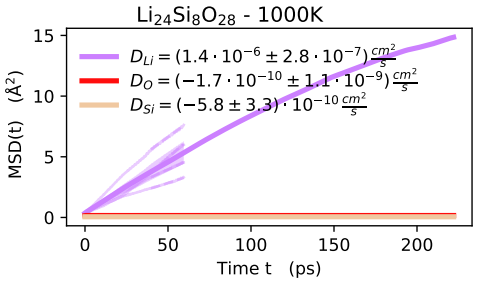

Fig. D.45: MSD(t) for $Li_{24}Si_8O_{28}$.

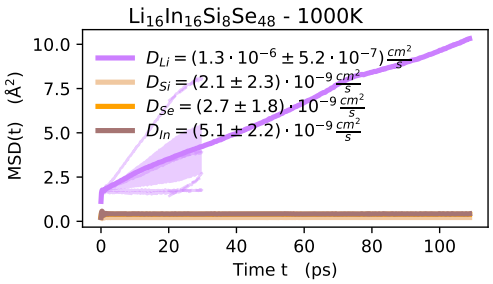

Fig. D.46: MSD(t) for $Li_{16}In_{16}Si_8Se_{48}$.

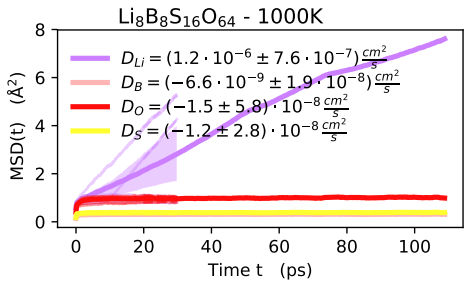

Fig. D.47: MSD(t) for $Li_8B_8S_{16}O_{64}$.

D.3 Non-diffusive structures

Structure	DB	DB-id	Supercell	Volume change	T^{sim}_{1000}
$Li_2Ce_1N_2$	ICSD	34003	$Li_{16}Ce_8N_{16}$	1.1%	334.5
$Li_6Sr_3Ta_2O_{11}$	COD	4306193	$Li_{24}Sr_{12}Ta_8O_{44}$	2.0%	218.1
$Li_5Re_1N_4$	ICSD	92468	$Li_{20}Re_4N_{16}$	0.2%	160.0
$Li_6Zn_1O_4$	ICSD	62137	$Li_{24}Zn_4O_{16}$	1.6%	407.2
$Li_4K_1Al_1O_4$	ICSD	65260	$Li_{64}K_{16}Al_{16}O_{64}$	1.9%	87.3
$Li_2Al_1B_5O_{10}$	COD	2012178	$Li_8Al_4B_{20}O_{40}$	4.9%	72.7
$Li_2Cs_3Br_5$	ICSD	245978	$Li_8Cs_{12}Br_{20}$	-12.5%	72.7
$Na_1Li_2B_1P_2O_8$	ICSD	291512	$Na_4Li_8B_4P_8O_{32}$	4.7%	101.8
$Li_1La_1C_2O_6$	ICSD	174533	$Li_4La_4C_8O_{24}$	3.2%	72.7
$Li_1Au_1F_4$	COD	1510140	$Li_{16}Au_{16}F_{64}$	14.8%	43.6
$Li_1Si_2B_1O_6$	COD	1511474	$Li_{16}Si_{32}B_{16}O_{96}$	2.7%	101.8
$Li_2Cd_1P_4O_{12}$	COD	1008009	$Li_8Cd_4P_{16}O_{48}$	5.3%	116.3
$Li_2Si_3O_7$	COD	1501470	$Li_{16}Si_{24}O_{56}$	3.5%	72.7
$Li_2Te_1O_3$	ICSD	4317	$Li_{32}Te_{16}O_{48}$	10.3%	72.7
$Li_3Au_1O_3$	COD	1510224	$Li_{36}Au_{12}O_{36}$	2.9%	58.2
$Sr_1Li_2Si_2N_4$	COD	4002768	$Sr_{12}Li_{24}Si_{24}N_{48}$	-0.4%	72.7
$Li_1Y_1Mo_3O_8$	ICSD	28526	$Li_3Y_3Mo_9O_{24}$	2.5%	72.7
$Li_2Mo_1O_4$	COD	7024042	$Li_{12}Mo_6O_{24}$	3.8%	48.5
$Li_2Pd_1O_2$	ICSD	61199	$Li_{24}Pd_{12}O_{24}$	2.0%	72.7
$Li_3Sc_1B_2O_6$	COD	2218562	$Li_{24}Sc_8B_{16}O_{48}$	1.7%	218.1
$Li_1Nb_3In_1Cl_9$	ICSD	75071	$Li_2Nb_6In_2Cl_{18}$	7.3%	334.5
$Li_6W_1N_4$	ICSD	153620	$Li_{24}W_4N_{16}$	0.1%	72.7
$Li_1Zn_1As_1O_4$	ICSD	86184	$Li_6Zn_6As_6O_{24}$	6.4%	226.5
$Li_4Ta_1N_3$	COD	1535987	$Li_{32}Ta_8N_{24}$	0.1%	72.7
$Li_3Sc_1N_2$	COD	1532734	$Li_{24}Sc_8N_{16}$	-0.5%	43.6
$Li_3Al_1Mo_2As_2O_{14}$	COD	2220995	$Li_9Al_3Mo_6As_6O_{42}$	3.2%	174.5
$Li_1P_1O_3$	COD	9014879	$Li_{24}P_{24}O_{72}$	5.3%	130.9
$Li_7P_1N_4$	ICSD	642182	$Li_{56}P_8N_{32}$	0.2%	72.7
$Li_1Y_1Si_1O_4$	ICSD	34079	$Li_8Y_8Si_8O_{32}$	3.0%	101.8
$Li_2Si_2O_5$	COD	2003027	$Li_{16}Si_{16}O_{40}$	4.1%	72.7
$Li_{16}Nb_2N_8O_1$	ICSD	174443	$Li_{64}Nb_8N_{32}O_4$	-1.7%	58.2
$Li_9Mg_3P_4O_{16}F_3$	ICSD	426103	$Li_{36}Mg_{12}P_{16}O_{64}F_{12}$	3.4%	72.7
$Li_8Pt_1O_6$	ICSD	61218	$Li_{32}Pt_4O_{24}$	2.2%	87.3
$Li_3Ga_1B_2O_6$	COD	1511740	$Li_{24}Ga_8B_{16}O_{48}$	7.1%	58.2
$Li_3Al_1Si_1O_5$	COD	7224138	$Li_{48}Al_{16}Si_{16}O_{80}$	3.1%	58.2
$Li_8Be_5B_6O_{18}$	COD	4337787	$Li_{32}Be_{20}B_{24}O_{72}$	2.2%	145.4

Structure	DB	DB-id	Supercell	Volume change	T_{1000}^{sim}
$Li_4K_1Nb_1O_5$	ICSD	73124	$Li_{32}K_8Nb_8O_{40}$	3.3%	58.2
$Li_4Te_1O_5$	COD	1530934	$Li_{16}Te_4O_{20}$	7.2%	72.7
$Li_4Ge_5O_{12}$	COD	9007843	$Li_{16}Ge_{20}O_{48}$	5.1%	72.7
$Li_7Nb_1N_4$	COD	2000944	$Li_{56}Nb_8N_{32}$	-0.7%	58.2
$Li_3Al_1N_2$	COD	1537475	$Li_{24}Al_8N_{16}$	0.4%	72.7
$Li_3Ga_1B_2O_6$	COD	2242045	$Li_{24}Ga_8B_{16}O_{48}$	2.2%	58.2
$Li_2Al_1B_1O_4$	ICSD	50612	$Li_{32}Al_{16}B_{16}O_{64}$	3.5%	72.7
$Li_4Zn_1P_2O_8$	COD	1544389	$Li_{16}Zn_4P_8O_{32}$	3.7%	72.7
$K_1Li_1Zn_1O_2$	ICSD	49022	$K_6Li_6Zn_6O_{12}$	3.1%	72.7
$Li_6Te_1O_6$	ICSD	40247	$Li_{48}Te_8O_{48}$	13.8%	58.2
$Li_2W_1O_4$	ICSD	67236	$Li_{12}W_6O_{24}$	3.6%	87.3
$Sr_1Li_4P_2$	ICSD	416888	$Sr_4Li_{16}P_8$	0.5%	72.7
$Li_3B_7O_{12}$	COD	9007831	$Li_{12}B_{28}O_{48}$	4.1%	145.4
$Sr_1Li_2Ta_2O_7$	ICSD	246277	$Sr_4Li_8Ta_8O_{28}$	2.4%	72.7
$Cs_2Li_3B_5O_{10}$	COD	7213712	$Cs_8Li_{12}B_{20}O_{40}$	0.0%	218.1
$Li_3Ba_2Ta_1N_4$	ICSD	75031	$Li_{24}Ba_{16}Ta_8N_{32}$	0.8%	58.2
$Li_2Si_2O_5$	ICSD	69300	$Li_{32}Si_{32}O_{80}$	3.5%	72.7
$Li_6Be_3B_4O_{12}$	COD	4337786	$Li_{24}Be_{12}B_{16}O_{48}$	2.2%	72.7
$Li_1In_1Ge_1O_4$	ICSD	167518	$Li_{16}In_{16}Ge_{16}O_{64}$	-0.1%	58.2
$Cs_2Li_2B_2P_4O_{15}$	ICSD	424281	$Cs_8Li_8B_8P_{16}O_{60}$	5.9%	58.2
$Li_2Te_1W_1O_6$	COD	4330276	$Li_{16}Te_8W_8O_{48}$	3.0%	72.7
$Li_4Al_3Ge_3Br_1O_{12}$	ICSD	87991	$Li_8Al_6Ge_6Br_2O_{24}$	2.5%	72.7
$Li_2Mo_4O_{13}$	ICSD	4155	$Li_6Mo_{12}O_{39}$	5.9%	72.7
$Li_2Ta_2O_3F_6$	ICSD	405777	$Li_{24}Ta_{24}O_{36}F_{72}$	4.5%	101.8
$Li_2Mg_1Si_1O_4$	COD	7222190	$Li_{16}Mg_8Si_8O_{32}$	2.7%	72.7
$Li_3Ba_2Nb_1N_4$	ICSD	75516	$Li_{24}Ba_{16}Nb_8N_{32}$	0.4%	58.2
$Rb_2Li_3B_1P_4O_{14}$	ICSD	424352	$Rb_8Li_{12}B_4P_{16}O_{56}$	5.8%	116.3
$Li_6Zr_1Be_1F_{12}$	COD	1528861	$Li_{24}Zr_4Be_4F_{48}$	0.0%	58.2
$Li_1B_1O_2$	COD	2310701	$Li_{32}B_{32}O_{64}$	6.4%	72.7
$Li_2B_3P_1O_8$	COD	7031897	$Li_{16}B_{24}P_8O_{64}$	7.3%	218.1
$Li_3Al_1B_2O_6$	COD	1100060	$Li_{24}Al_8B_{16}O_{48}$	3.7%	87.3
$Li_1Re_1O_4$	COD	1535227	$Li_{12}Re_{12}O_{48}$	8.2%	145.4
$K_1Li_1Y_1F_5$	ICSD	187751	$K_{16}Li_{16}Y_{16}F_{80}$	1.8%	105.3
$Li_1Nb_1O_3$	ICSD	182033	$Li_{16}Nb_{16}O_{48}$	2.5%	58.2

Table D.3: Structures that show negligible Li-ion diffusion at 1000 K in FPMD are listed below

D.4 Structures diffusive in pinball model

Structure	DB	DB-id	Supercell	Volume change
$Li_4Mo_3O_8$	ICSD	84602	$Li_{24}Mo_{18}O_{48}$	5.8%
$Li_1Ta_1Si_1O_5$	COD	1534486	$Li_4Ta_4Si_4O_{20}$	3.1%
$Li_2P_2Pd_1O_7$	COD	1000333	$Li_8P_8Pd_4O_{28}$	14.9%
$Na_1Li_2P_1O_4$	COD	9004248	$Na_8Li_{16}P_8O_{32}$	3.9%
$Ba_1Na_1Li_3B_6O_{12}$	ICSD	423774	$Ba_2Na_2Li_6B_{12}O_{24}$	2.9%
$Na_1Li_1B_4O_7$	ICSD	416956	$Na_4Li_4B_{16}O_{28}$	4.2%
$Na_1Li_2B_1O_3$	COD	1511223	$Na_{16}Li_{32}B_{16}O_{48}$	2.8%
$Li_1Au_1S_4O_{14}$	COD	4326716	$Li_4Au_4S_{16}O_{56}$	22.1%
$Li_{10}B_{14}Cl_2O_{25}$	COD	1530960	$Li_{10}B_{14}Cl_2O_{25}$	1.8%
$Li_1Au_1I_4$	COD	1510187	$Li_8Au_8I_{32}$	8.4%
$Li_5La_3Nb_2O_{12}$	ICSD	68251	$Li_{20}La_{12}Nb_8O_{48}$	2.4%
$Li_1Zr_2As_3O_{12}$	ICSD	190656	$Li_2Zr_4As_6O_{24}$	4.0%
$Li_1Al_1Ge_1O_5$	COD	1526845	$Li_8Al_8Ge_8O_{40}$	-6.3%
$Li_3Sc_1F_6$	COD	1535801	$Li_{18}Sc_6F_{36}$	4.0%
$Li_1Nb_3Cl_8$	ICSD	50232	$Li_4Nb_{12}Cl_{32}$	5.8%

Table D.4: We list all structures that are diffusive in the pinball model, but where we could not estimate the diffusion from FPMD

D.5 Supplementary methods to study Li_7TaO_6

D.5.1 Variable cell relaxation

For the variable-cell relaxation, we use the pw.x module of the Quantum ESPRESSO distribution. The unit cell of Li_7TaO_6 is relaxed to its ground state at an external pressure of 0. Sampling of the Brillouin zone is achieved using a Γ-centred Monkhorst-Pack grid, with a k-point density of 0.2 $Å^{-1}$. For the primitive cell, this results in a $8 \times 8 \times 7$ grid. No electronic smearing is used, since this material is an electronic insulator. The converge on the SCF-cycle is set to 10^{-10} Ry. The energy convergence threshold is set to 0.5×10^{-4} atomic units (Hartree), the force convergence threshold to 0.25×10^{-5} atomic units (Hartree bohr^{-1}), and the pressure convergence to 0.5 kbar. We also apply a convergence threshold on the relative volume change between subsequent vc-relaxations, which

has to reach below 0.01.

D.5.2 PFF

Only twelve parameters are necessary to model the three-species Li_7TaO_6 system. We optimized the charges of Li, Ta and O ions, keeping fixed the charge ratio Ta/Li and O/Li to 5 and -2, respectively. With this constraint there is only one parameter to be optimized. Two additional parameters are needed to define the value of the harmonic spring connecting each O_{core}-O_{shell} pair and the partition of the oxygen charge between core and shell, O_{core} and O_{shell}, and three parameters A, b, and C of the Buckingham potential for the three pairs Li-O_{shell}, Ta-O_{shell} and O_{shell}-O_{shell}.
The mass of the O_{shell} was chosen as 0.1 a.m.u., to ensure adiabatic separation between the slow ionic motion and the fast relaxation of the electrons, as in the Born-Oppenheimer approximation. We used a spring constant $\frac{1}{2}$k = 40.0 eV Å^{-2} and a timestep of 0.2 fs, which allows to correctly integrate the fast motion of the light shells, and conserve the total energy. The ionic temperature is computed among all atoms including the O-cores, and excluding the O-shells. The A [eV], ρ [Å], C [eV Å^6] parameters in LAMMPS metal units are:
pair_coeff Ta O-shell 1425.13678818149 0.310874507606626 0.492934959089643
pair_coeff Li O-shell 5289.70042451377 0.192533324764572 0.881644692566042
pair_coeff O-shell O-shell 10 26822.4383457393 0.216525934819903 19.1837810833034
The A and C values of all the remaining pairs are set equal to zero. The electrostatic contribution is active among all pairs. The Li, O, and Ta charges are 0.731, -1.462, and 3.655, respectively. The charge of the core and the shell oxygen are +1.17903 and -2.64103, respectively.

The relaxed theoretical lattice parameters of the equivalent unit cell are a=5.389 Å and c=14.634 Å which are very close to the experimental values a=5.3869 Å and c=15.1367 Å given in the record 74949 of ICSD database.

Constant temperature simulations at both the experimental and theoretical volumes have been carried out at 300 K and 600 K via DFT-PBE with vdW Grimme-D2. The temperature was maintained constant via an Adaptive-Langevin thermostat, and the total duration of the simulations was 5.2 ps.

Comparing the classical PFF to the DFT as in [489], we compute the following errors: the RSMD of the energy is 1.27 meV/atom, the RSMD of the forces 0.39 eV Å^{-1}, and the correlation is 0.95 (a measure of how parallel the two vectors are, defined by Eq. 15 of [489]). The RSMD energy and forces are defined by Eq. 12 and 13 of the same reference.

D.5.3 Parameters for sitator

For the landmark analysis, we use a midpoint and steepness of the cutoff function of 1.4 and 30, respectively. The minimum site occupancy is 0.01, a site that is occupied less is discarded. Clustering and assignment threshold are both set to 0.9. The SOAP parameters used are: a standard deviation for the Gaussian on the atomic position of 0.5 Å, a cutoff of 4 Å, and $n_{max} = l_{max} = 6$. For the dimensionality reduction with PCA, 95% of the variance needs to be retained.

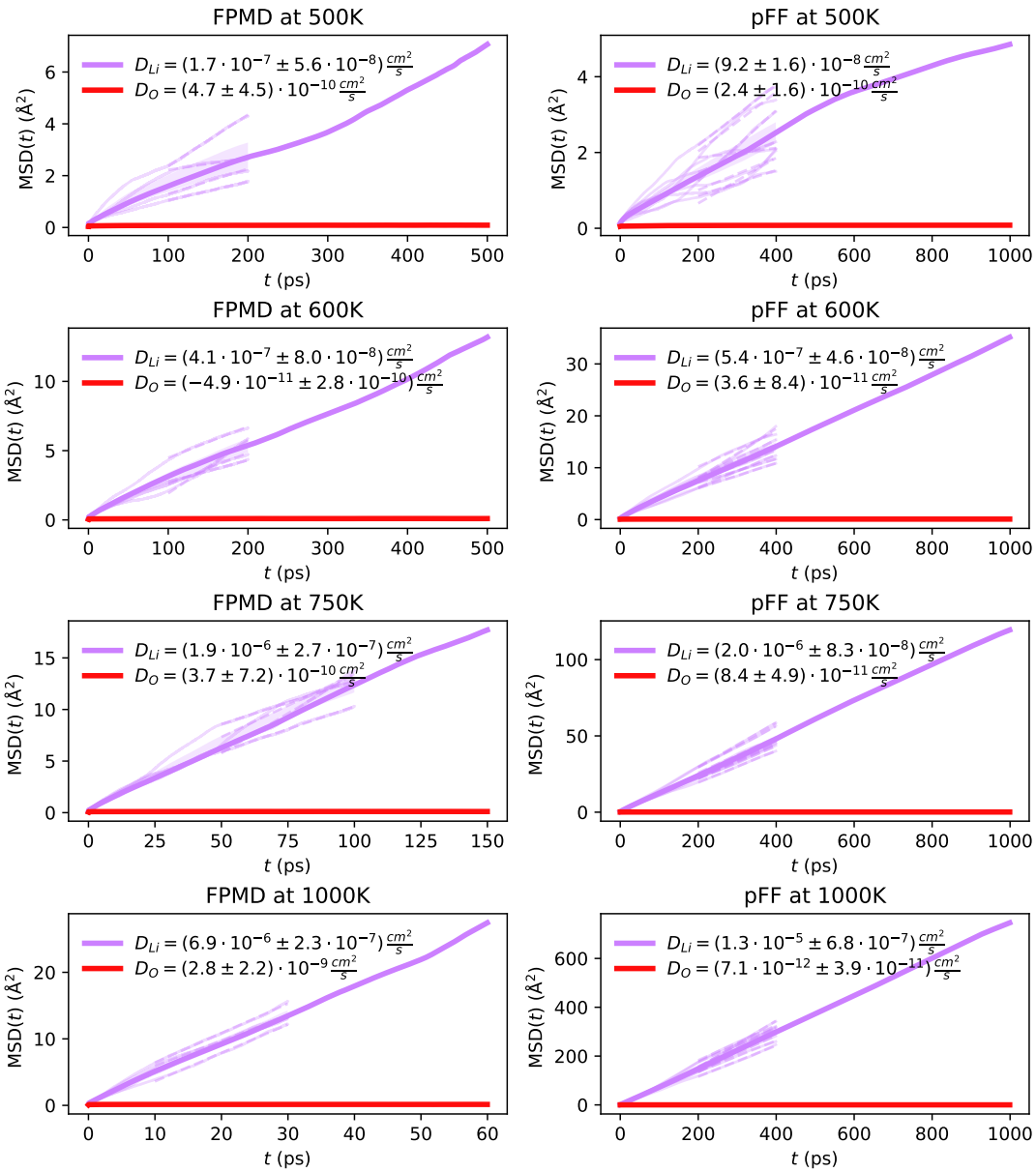

Fig. D.48: We show the MSD for Li and O at 500, 600, 750, and 1000 K (top to bottom), computed from the FPMD trajectories (left) and the PFF trajectories (right).

D.6 Supplementary results on Li_7TaO_6

D.6.1 Molecular dynamics

Comparison between PFF and FPMD.

In Fig. D.48 we report the Li-ion and O-ion MSD in the FPMD and pFF simulations. Overall, we observe very good agreement between the two different computational methods. We note that the pFF-simulations are performed also in a $Li_{56}Ta_8O_{48}$ supercell for this specific comparison. However, each cell is relaxed prior to the dynamics, at 0 K, for a good comparison. This is important for the

simulations of Li_7TaO_6, as will be discussed in the following.

In Fig. D.49, we compare the effect of supercell size for the pFF simulations in a $Li_{56}Ta_8O_{48}$ supercell. Overall, our results indicate that we get good agreement between pFF and FPMD if the simulations are performed at the ground-state cell geometry for the respective simulation technique. That is to say, if we allow to relax the cell using the pFF, we also get compatible results with FPMD in a cell relaxed with DFT. Further, if the cell is not allowed to relax, the order magnitude of the conductivity and the activation energy are not largely affected. Thanks to these tests, we could conclude that the fitted force-fields is really able to reproduce the same microscopic dynamics of the FPMD, and are therefore suited for extrapolating results at lower temperatures and larger volumes.

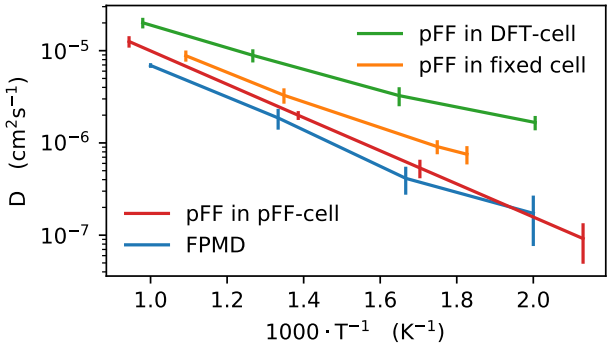

Fig. D.49: Arrhenius behavior of diffusion of Li in Li_7TaO_6, estimated with FPMD (blue lines) or pFF at different cell sizes: The green line shows the diffusion with pFF with the cell relaxed with DFT. The orange line shows the diffusion with pFF with the cell fixed at the experimental lattice constants. The red line shows the diffusion when the cell is allowed to relax to its ground state with the pFF.

Additional site analysis results

We show some additional results of the site analysis, that are not needed for comprehension of our article, but give additional details. In Fig. D.50 we show the descriptor clustering of the site analysis of the FPMD-simulation at 600 K. In Fig. D.51, we give the RDF for the simulation using the polarizable force field (simulating the $Li_{56}Ta_8O_{48}$ supercell).

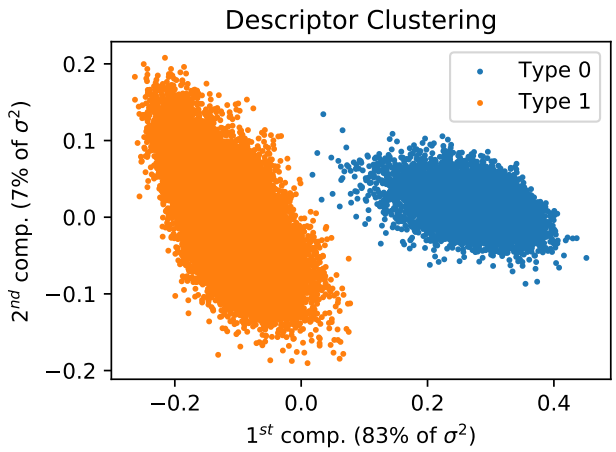

Fig. D.50: We show the descriptor clustering of Li_7TaO_6 at 600 K (FPMD). Each descriptor is computed from the environment of a Li ion, and the color indicates gives the clusters associated by the automated density peak clustering. We only show the first two dominant components, nevertheless, the clusters are distinguishable, evidence for a robust clustering due to chemical and geometric difference between the site types.

Additional results from PFF simulations

We equilibrate the cell via constant pressure MD simulations at the following temperatures: 300, 350, 400, 450, 500, 550, 600, 650, 700, 750 and 900 K. The cell parameters at each temperature are

T	a (Å)	b (Å)	c (Å)	D ($cm^2\,s^{-1}$)	σ ($S\,cm^{-1}$)	t (ns)
300	95.1923	91.5653	88.6421	1.55×10^{-9}	5.67×10^{-4}	4.6
350	95.2953	91.6768	88.6959	6.60×10^{-9}	2.07×10^{-3}	2.4
400	95.4067	91.7912	88.7550	2.49×10^{-8}	6.80×10^{-3}	2.4
450	95.5397	91.9092	88.8127	9.17×10^{-8}	2.22×10^{-2}	0.35
500	95.6589	92.0405	88.8746	1.94×10^{-7}	4.20×10^{-2}	2.4
550	95.7874	92.1736	88.9349	4.12×10^{-7}	8.09×10^{-2}	2.4
600	95.9270	92.3034	88.9972	7.50×10^{-7}	1.35×10^{-1}	0.35
650	96.0658	92.4357	89.0620	1.28×10^{-6}	2.11×10^{-1}	2.4
700	96.2004	92.5777	89.1275	1.88×10^{-6}	2.87×10^{-1}	2.4
750	96.3512	92.7138	89.1935	2.78×10^{-6}	3.95×10^{-1}	0.35
900	96.8101	93.1541	89.4011	7.19×10^{-6}	8.40×10^{-1}	0.1

Table D.5: We report temperature T, equilibrium lattice parameters a, b, and c, diffusion coefficient D, conductivity σ, and duration of the NVE simulation t for the supercell of 90720 atoms.

reported in Table D.5.

DFT+U forces

We investigate whether the localization of the electrons of the d states in transition metal oxides affects the results of the dynamics. We take 10 snapshots from our FPMD trajectory at 600 K and calculate forces on that atoms using DFT+U_{sc}. The U is calculated self-consistently for every single snapshot. The value of the Hubbard U ranges from 2.05±0.1 eV to 2.09±0.1 eV, giving good compatibility. In Fig. D.52 we plot the forces on the atoms for different species, showing perfect agreement. We conclude that DFT+U is not needed to describe the dynamics of Li_7TaO_6.

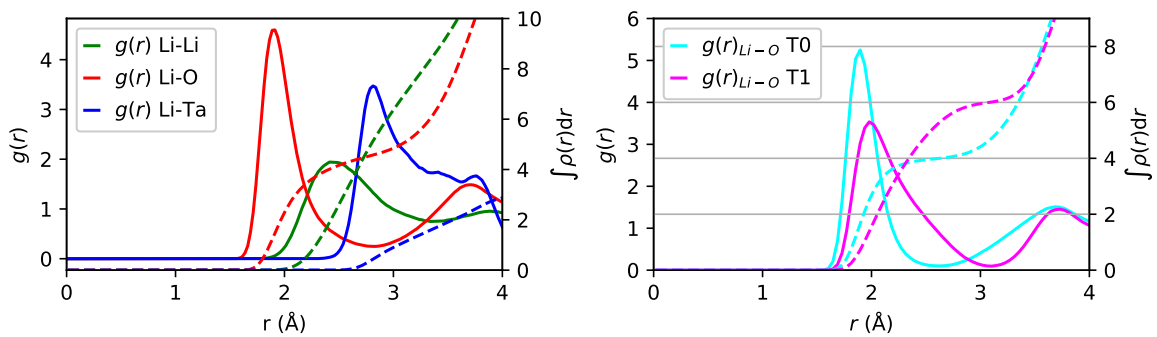

Fig. D.51: We calculate the RDF for the trajectory obtained from classical molecular dynamics at 600 K, giving results in good agreement with the FPMD simulations. We show the Li-Li, Li-O, and Li-Ta RDF in the left panel, and the Li-O RDF by site type in the right panel.

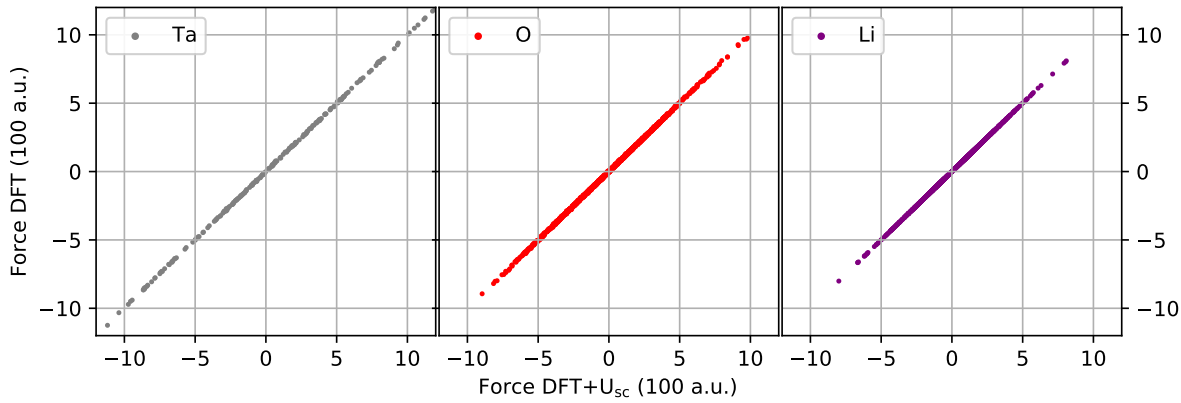

Fig. D.52: We compare the forces (in atomic units) calculated from DFT on the y-axis against forces for the same configurations from DFT+U_{sc} on the x-axis for Ta (left), O (center), and Li (right).

Bibliography

[1] J.-M. Tarascon and M. Armand, Issues and challenges facing rechargeable lithium batteries, *Nature* **414**, 359–367, 2001.

[2] M. M. Thackeray, C. Wolverton and E. D. Isaacs, Electrical energy storage for transportation–approaching the limits of, and going beyond, lithium-ion batteries, *Energy & Environmental Science* **5**, 7854–7863, 2012.

[3] M. S. Whittingham, Electrical Energy Storage and Intercalation Chemistry, *Science* **192**, 1126–1127, 1976.

[4] J. Broadhead and A. Butherus, Patent US3791867A, 1974.

[5] J. O. Besenhard and G. Eichinger, High energy density lithium cells: Part I. Electrolytes and anodes, *Journal of Electroanalytical Chemistry and Interfacial Electrochemistry* **68**, 1–18, 1976.

[6] B. M. L. Rao, R. W. Francis and H. A. Christopher, Lithium-Aluminum Electrode, *Journal of The Electrochemical Society* **124**, 1490–1492, 1977.

[7] P. V. Braun, J. Cho, J. H. Pikul, W. P. King and H. Zhang, High power rechargeable batteries, *Current Opinion in Solid State and Materials Science* **16**, 186–198, 2012.

[8] J. Vetter *et al.*, Ageing mechanisms in lithium-ion batteries, *Journal of Power Sources* **147**, 269–281, 2005.

[9] D. W. Murphy and P. A. Christian, Solid State Electrodes for High Energy Batteries, *Science* **205**, 651–656, 1979.

[10] N. A. Godshall, I. D. Raistrick and R. A. Huggins, Thermodynamic investigations of ternary lithium-transition metal-oxygen cathode materials, *Materials Research Bulletin* **15**, 561–570, 1980.

[11] K. Mizushima, P. C. Jones, P. J. Wiseman and J. B. Goodenough, Li_xCoO_2 ($0 < x \leq 1$): A new cathode material for batteries of high energy density, *Materials Research Bulletin* **15**, 783–789, 1980.

[12] J. B. Goodenough, K. Mizushima and T. Takeda, Solid-Solution Oxides for Storage-Battery Electrodes, *Japanese Journal of Applied Physics* **19**, 305, 1980.

[13] J. B. Goodenough, Oxide-Ion Electrolytes, *Annual Review of Materials Research* **33**, 91–128, 2003.

[14] A. Yoshino, The Birth of the Lithium-Ion Battery, *Angewandte Chemie International Edition* **51**, 5798–5800, 2012.

[15] K. Ozawa, Lithium-ion rechargeable batteries with $LiCoO_2$ and carbon electrodes: the

$LiCoO_2$/C system, *Solid State Ionics* **69**, 212–221, 1994.

[16] M. Armand and J.-M. Tarascon, Building better batteries, *Nature* **451**, 652–657, 2008.

[17] G. Ceder, Opportunities and challenges for first-principles materials design and applications to Li battery materials, *MRS Bulletin* **35**, 693–701, 2010.

[18] G. E. Blomgren, The Development and Future of Lithium Ion Batteries, *Journal of The Electrochemical Society* **164**, A5019–A5025, 2017.

[19] M. Li, J. Lu, Z. Chen and K. Amine, 30 Years of Lithium-Ion Batteries, *Advanced Materials* **30**, 1800561, 2018.

[20] B. Scrosati and J. Garche, Lithium batteries: Status, prospects and future, *Journal of Power Sources* **195**, 2419–2430, 2010.

[21] K. Sheikh, B. X. Chen and I. Penn, Lithium-Ion Batteries Work Earns Nobel Prize in Chemistry for 3 Scientists, *The New York Times* , 2019.

[22] E. Karden, S. Ploumen, B. Fricke, T. Miller and K. Snyder, Energy storage devices for future hybrid electric vehicles, *Journal of Power Sources* **168**, 2–11, 2007.

[23] V. Etacheri, R. Marom, R. Elazari, G. Salitra and D. Aurbach, Challenges in the development of advanced Li-ion batteries: a review, *Energy & Environmental Science* **4**, 3243, 2011.

[24] D. Larcher and J.-M. Tarascon, Towards greener and more sustainable batteries for electrical energy storage, *Nature Chemistry* **7**, 19–29, 2015.

[25] A. Kwade, W. Haselrieder, R. Leithoff, A. Modlinger, F. Dietrich and K. Droeder, Current status and challenges for automotive battery production technologies, *Nature Energy* **3**, 290–300, 2018.

[26] H. Oman, Hydrogen-fueled pollution-free transportation, *IEEE Aerospace and Electronic Systems Magazine* **17**, 34–40, 2002.

[27] L. Chapman, Transport and climate change: a review, *Journal of Transport Geography* **15**, 354–367, 2007.

[28] D. J. Wuebbles and A. K. Jain, Concerns about climate change and the role of fossil fuel use, *Fuel Processing Technology* **71**, 99–119, 2001.

[29] R. C. Duncan and W. Youngquist, Encircling the Peak of World Oil Production, *Natural Resources Research* **8**, 219–232, 1999.

[30] IEA (Paris), *Global EV Outlook 2019*, 2019, https://www.iea.org/publications/reports/globalevoutlook2019/.

[31] S. Castle, Britain to Ban New Diesel and Gas Cars by 2040, *The New York Times* , 2017.

[32] J. B. Goodenough and K.-S. Park, The Li-Ion Rechargeable Battery: A Perspective, *Journal of the American Chemical Society* **135**, 1167–1176, 2013.

[33] J. B. Goodenough, Evolution of Strategies for Modern Rechargeable Batteries, *Accounts of Chemical Research* **46**, 1053–1061, 2013.

[34] D. W. Sang-hun, Choe and V. Goel, Samsung Halts Galaxy Note 7 Production as Battery Problems Linger, *The New York Times* , 2016.

[35] J. Mouawad, Report on Boeing 787 Dreamliner Battery Flaws Finds Lapses at Multiple Points,

The New York Times , 2014.

[36] R. Marom, S. F. Amalraj, N. Leifer, D. Jacob and D. Aurbach, A review of advanced and practical lithium battery materials, *Journal of Materials Chemistry* **21**, 9938–9954, 2011.

[37] J. O. Besenhard and H. P. Fritz, Cathodic reduction of graphite in organic solutions of alkali and $NR4^+$ salts, *Journal of Electroanalytical Chemistry and Interfacial Electrochemistry* **53**, 329–333, 1974.

[38] S. Goriparti, E. Miele, F. De Angelis, E. Di Fabrizio, P. R. Zaccaria and C. Capiglia, Review on recent progress of nanostructured anode materials for Li-ion batteries, *Journal of Power Sources* **257**, 421–443, 2014.

[39] M. S. Whittingham, History, Evolution, and Future Status of Energy Storage, *Proceedings of the IEEE* **100**, 1518–1534, 2012.

[40] J. R. Szczech and S. Jin, Nanostructured silicon for high capacity lithium battery anodes, *Energy & Environmental Science* **4**, 56–72, 2010.

[41] M. Ge, J. Rong, X. Fang and C. Zhou, Porous Doped Silicon Nanowires for Lithium Ion Battery Anode with Long Cycle Life, *Nano Letters* **12**, 2318–2323, 2012.

[42] M. M. Thackeray, W. I. F. David, P. G. Bruce and J. B. Goodenough, Lithium insertion into manganese spinels, *Materials Research Bulletin* **18**, 461–472, 1983.

[43] M. M. Thackeray, P. J. Johnson, L. A. de Picciotto, P. G. Bruce and J. B. Goodenough, Electrochemical extraction of lithium from $LiMn_2O_4$, *Materials Research Bulletin* **19**, 179–187, 1984.

[44] A. K. Padhi, K. S. Nanjundaswamy and J. B. Goodenough, Phospho-olivines as Positive-Electrode Materials for Rechargeable Lithium Batteries, *Journal of The Electrochemical Society* **144**, 1188–1194, 1997.

[45] M. S. Whittingham, Lithium Batteries and Cathode Materials, *Chemical Reviews* **104**, 4271–4302, 2004.

[46] J. B. Goodenough and Y. Kim, Challenges for Rechargeable Li Batteries, *Chemistry of Materials* **22**, 587–603, 2010.

[47] R. Malik, F. Zhou and G. Ceder, Kinetics of non-equilibrium lithium incorporation in $LiFePO_4$, *Nature Materials* **10**, 587–590, 2011.

[48] G. Hautier *et al.*, Phosphates as Lithium-Ion Battery Cathodes: An Evaluation Based on High-Throughput ab Initio Calculations, *Chemistry of Materials* **23**, 3495–3508, 2011.

[49] B. Xu, D. Qian, Z. Wang and Y. S. Meng, Recent progress in cathode materials research for advanced lithium ion batteries, *Materials Science and Engineering: R: Reports* **73**, 51–65, 2012.

[50] B. C. Melot and J.-M. Tarascon, Design and Preparation of Materials for Advanced Electrochemical Storage, *Accounts of Chemical Research* **46**, 1226–1238, 2013.

[51] Y. Mo, S. P. Ong and G. Ceder, Insights into Diffusion Mechanisms in P2 Layered Oxide Materials by First-Principles Calculations, *Chemistry of Materials* **26**, 5208–5214, 2014.

[52] D. Liu *et al.*, Spinel materials for high-voltage cathodes in Li-ion batteries, *RSC Adv.* **4**, 154–167, 2014.

[53] P. Rozier and J. M. Tarascon, Review–Li-Rich Layered Oxide Cathodes for Next-Generation

Li-Ion Batteries: Chances and Challenges, *Journal of The Electrochemical Society* **162**, A2490–A2499, 2015.

[54] F. Hao *et al.*, Taming Active Material-Solid Electrolyte Interfaces with Organic Cathode for All-Solid-State Batteries, *Joule* **3**, 1349–1359, 2019.

[55] A. Manthiram, Materials Challenges and Opportunities of Lithium Ion Batteries, *The Journal of Physical Chemistry Letters* **2**, 176–184, 2011.

[56] M. Winter and R. J. Brodd, What Are Batteries, Fuel Cells, and Supercapacitors?, *Chemical Reviews* **104**, 4245–4270, 2004.

[57] G. Girishkumar, B. McCloskey, A. C. Luntz, S. Swanson and W. Wilcke, Lithium–Air Battery: Promise and Challenges, *The Journal of Physical Chemistry Letters* **1**, 2193–2203, 2010.

[58] E. Quartarone and P. Mustarelli, Electrolytes for solid-state lithium rechargeable batteries, *Chemical Society Reviews* **40**, 2525, 2011.

[59] K. M. Abraham and Z. Jiang, A Polymer Electrolyte-Based Rechargeable Lithium/Oxygen Battery, *Journal of The Electrochemical Society* **143**, 1–5, 1996.

[60] T. Ogasawara, A. Débart, M. Holzapfel, P. Novák and P. G. Bruce, Rechargeable Li_2O_2 Electrode for Lithium Batteries, *Journal of the American Chemical Society* **128**, 1390–1393, 2006.

[61] J. S. Hummelshøj *et al.*, Communications: Elementary oxygen electrode reactions in the aprotic Li-air battery, *The Journal of Chemical Physics* **132**, 071101, 2010.

[62] Y.-C. Lu *et al.*, Lithium–oxygen batteries: bridging mechanistic understanding and battery performance, *Energy & Environmental Science* **6**, 750–768, 2013.

[63] R. Younesi, G. M. Veith, P. Johansson, K. Edström and T. Vegge, Lithium salts for advanced lithium batteries: Li–metal, Li–O_2, and Li–S, *Energy & Environmental Science* **8**, 1905–1922, 2015.

[64] T. Vegge, J. M. Garcia-Lastra and D. J. Siegel, Lithium–oxygen batteries: At a crossroads?, *Current Opinion in Electrochemistry* **6**, 100–107, 2017.

[65] G. Ceder, G. Hautier, A. Jain and S. P. Ong, Recharging lithium battery research with first-principles methods, *MRS Bulletin* **36**, 185–191, 2011.

[66] V. Thangadurai and W. Weppner, Recent progress in solid oxide and lithium ion conducting electrolytes research, *Ionics* **12**, 81–92, 2006.

[67] C. A. Vincent, Lithium batteries: a 50-year perspective, 1959–2009, *Solid State Ionics* **134**, 159–167, 2000.

[68] Q. Zhong, A. Bonakdarpour, M. Zhang, Y. Gao and J. R. Dahn, Synthesis and Electrochemistry of $LiNi_xMn_{2-x}O_4$, *Journal of The Electrochemical Society* **144**, 205–213, 1997.

[69] G. T.-K. Fey, W. Li and J. R. Dahn, $LiNiVO_4$: A 4.8 Volt Electrode Material for Lithium Cells, *Journal of The Electrochemical Society* **141**, 2279–2282, 1994.

[70] K. Amine, H. Yasuda and M. Yamachi, Olivine $LiCoPO_4$ as 4.8 V Electrode Material for Lithium Batteries, *Electrochemical and Solid-State Letters* **3**, 178–179, 2000.

[71] A. M. Haregewoin, A. S. Wotango and B.-J. Hwang, Electrolyte additives for lithium ion battery electrodes: progress and perspectives, *Energy & Environmental Science* **9**, 1955–1988, 2016.

[72] M. H. Braga, N. S. Grundish, A. J. Murchison and J. B. Goodenough, Alternative strategy for a

safe rechargeable battery, *Energy & Environmental Science* **10**, 331–336, 2017.

[73] P. G. Balakrishnan, R. Ramesh and T. Prem Kumar, Safety mechanisms in lithium-ion batteries, *Journal of Power Sources* **155**, 401–414, 2006.

[74] P. Arora and Z. J. Zhang, Battery Separators, *Chemical Reviews* **104**, 4419–4462, 2004.

[75] G. Jeong *et al.*, Nanotechnology enabled rechargeable Li–SO_2 batteries: another approach towards post-lithium-ion battery systems, *Energy & Environmental Science* **8**, 3173–3180, 2015.

[76] I. Stassen and G. Hambitzer, Metallic lithium batteries for high power applications, *Journal of Power Sources* **105**, 145–150, 2002.

[77] L. Zinck, M. Borck, C. Ripp and G. Hambitzer, Purification process for an inorganic rechargeable lithium battery and new safety concepts, *Journal of Applied Electrochemistry* **36**, 1291–1295, 2006.

[78] J. L. Schaefer, Y. Lu, S. S. Moganty, P. Agarwal, N. Jayaprakash and L. A. Archer, Electrolytes for high-energy lithium batteries, *Applied Nanoscience* **2**, 91–109, 2012.

[79] E. Markevich, V. Baranchugov and D. Aurbach, On the possibility of using ionic liquids as electrolyte solutions for rechargeable 5 V Li ion batteries, *Electrochemistry Communications* **8**, 1331–1334, 2006.

[80] V. Baranchugov, E. Markevich, E. Pollak, G. Salitra and D. Aurbach, Amorphous silicon thin films as a high capacity anodes for Li-ion batteries in ionic liquid electrolytes, *Electrochemistry Communications* **9**, 796–800, 2007.

[81] J. Fuller, R. T. Carlin and R. A. Osteryoung, The Room Temperature Ionic Liquid 1-Ethyl-3-methylimidazolium Tetrafluoroborate: Electrochemical Couples and Physical Properties, *Journal of The Electrochemical Society* **144**, 3881–3886, 1997.

[82] A. Nishimoto, M. Watanabe, Y. Ikeda and S. Kohjiya, High ionic conductivity of new polymer electrolytes based on high molecular weight polyether comb polymers, *Electrochimica Acta* **43**, 1177–1184, 1998.

[83] C. Capiglia, J. Yang, N. Imanishi, A. Hirano, Y. Takeda and O. Yamamoto, DSC study on the thermal stability of solid polymer electrolyte cells, *Journal of Power Sources* **119-121**, 826–832, 2003.

[84] G. Feuillade and P. Perche, Ion-conductive macromolecular gels and membranes for solid lithium cells, *Journal of Applied Electrochemistry* **5**, 63–69, 1975.

[85] P. Knauth and H. L. Tuller, Solid-State Ionics: Roots, Status, and Future Prospects, *Journal of the American Ceramic Society* **85**, 1654–1680, 2002.

[86] K. Takada, Progress and prospective of solid-state lithium batteries, *Acta Materialia* **61**, 759–770, 2013.

[87] J. Janek and W. G. Zeier, A solid future for battery development, *Nature Energy* **1**, 16141, 2016.

[88] J. B. Goodenough and P. Singh, Review—Solid Electrolytes in Rechargeable Electrochemical Cells, *Journal of The Electrochemical Society* **162**, A2387–A2392, 2015.

[89] J. Li, C. Ma, M. Chi, C. Liang and N. J. Dudney, Solid Electrolyte: the Key for High-Voltage Lithium Batteries, *Advanced Energy Materials* **5**, 1401408, 2015.

[90] J. G. Kim *et al.*, A review of lithium and non-lithium based solid state batteries, *Journal of*

Power Sources **282**, 299–322, 2015.

[91] A. B. Yaroslavtsev, Solid electrolytes: main prospects of research and development*, *Russian Chemical Reviews* **85**, 1255, 2016.

[92] J. B. Bates, N. J. Dudney, B. Neudecker, A. Ueda and C. D. Evans, Thin-film lithium and lithium-ion batteries, *Solid State Ionics* **135**, 33–45, 2000.

[93] W. Weppner, *Encyclopedia of Electrochemical Power Sources*, Elsevier, Amsterdam, 2009, pp. 162–168.

[94] C. Monroe and J. Newman, The Impact of Elastic Deformation on Deposition Kinetics at Lithium/Polymer Interfaces, *Journal of The Electrochemical Society* **152**, A396–A404, 2005.

[95] J. Cho and M. Liu, Preparation and electrochemical properties of glass-polymer composite electrolytes for lithium batteries, *Electrochimica Acta* **42**, 1481–1488, 1997.

[96] M. Diaw, A. Chagnes, B. Carré, P. Willmann and D. Lemordant, Mixed ionic liquid as electrolyte for lithium batteries, *Journal of Power Sources* **146**, 682–684, 2005.

[97] G. B. Appetecchi, G. T. Kim, M. Montanino, F. Alessandrini and S. Passerini, Room temperature lithium polymer batteries based on ionic liquids, *Journal of Power Sources* **196**, 6703–6709, 2011.

[98] J. Fuller, A. C. Breda and R. T. Carlin, Ionic Liquid-Polymer Gel Electrolytes, *Journal of The Electrochemical Society* **144**, L67–L70, 1997.

[99] A. Hayashi *et al.*, Preparation and Characterization of Lithium Ion Conducting Glass–Polymer Composites, *Chemistry Letters* **30**, 814–815, 2001.

[100] Y. Inda, T. Katoh and M. Baba, Development of all-solid lithium-ion battery using Li-ion conducting glass-ceramics, *Journal of Power Sources* **174**, 741–744, 2007.

[101] Y.-S. Hu, Batteries: Getting solid, *Nature Energy* **1**, 16042, 2016.

[102] H. Mehrer, *Diffusion in Solids*, Springer Berlin Heidelberg, Berlin, Heidelberg, 2007, vol. 155.

[103] J. Crank and E. P. J. Crank, *The Mathematics of Diffusion*, Clarendon Press, 1979.

[104] A. Einstein, Über die von der molekularkinetischen Theorie der Wärme geforderte Bewegung von in ruhenden Flüssigkeiten suspendierten Teilchen, *Annalen der Physik* **322**, 549–560, 1905.

[105] A. Van der Ven, G. Ceder, M. Asta and P. D. Tepesch, First-principles theory of ionic diffusion with nondilute carriers, *Physical Review B* **64**, 184307, 2001.

[106] Hans C. Andersen, Molecular dynamics simulations at constant pressure and/or temperature, *The Journal of Chemical Physics* **72**, 2384–2393, 1980.

[107] H. Tanaka, K. Nakanishi and N. Watanabe, Constant temperature molecular dynamics calculation on Lennard-Jones fluid and its application to water, *The Journal of Chemical Physics* **78**, 2626–2634, 1983.

[108] H. J. C. Berendsen, J. P. M. Postma, W. F. van Gunsteren, A. DiNola and J. R. Haak, Molecular dynamics with coupling to an external bath, *The Journal of Chemical Physics* **81**, 3684–3690, 1984.

[109] S. Nosé, A unified formulation of the constant temperature molecular dynamics methods, *The Journal of Chemical Physics* **81**, 511–519, 1984.

[110] W. G. Hoover, Canonical dynamics: Equilibrium phase-space distributions, *Physical Review A* **31**, 1695–1697, 1985.

[111] P. H. Hünenberger, *Advanced Computer Simulation*, Springer Berlin Heidelberg, 2005, pp. 105–149.

[112] E. A. Koopman and C. P. Lowe, Advantages of a Lowe-Andersen thermostat in molecular dynamics simulations, *The Journal of Chemical Physics* **124**, 204103, 2006.

[113] G. Bussi, D. Donadio and M. Parrinello, Canonical sampling through velocity rescaling, *The Journal of Chemical Physics* **126**, 014101, 2007.

[114] W. G. Hoover, Constant-pressure equations of motion, *Physical Review A* **34**, 2499–2500, 1986.

[115] L. Verlet, Computer "Experiments" on Classical Fluids. I. Thermodynamical Properties of Lennard-Jones Molecules, *Physical Review* **159**, 98–103, 1967.

[116] B. J. Alder and T. E. Wainwright, Phase Transition for a Hard Sphere System, *The Journal of Chemical Physics* **27**, 1208–1209, 1957.

[117] A. Rahman, Correlations in the Motion of Atoms in Liquid Argon, *Physical Review* **136**, A405–A411, 1964.

[118] H. Heinz, R. A. Vaia, B. L. Farmer and R. R. Naik, Accurate Simulation of Surfaces and Interfaces of Face-Centered Cubic Metals Using 12–6 and 9–6 Lennard-Jones Potentials, *The Journal of Physical Chemistry C* **112**, 17281–17290, 2008.

[119] M. A. González, Force fields and molecular dynamics simulations, *École thématique de la Société Française de la Neutronique* **12**, 169–200, 2011.

[120] J. Behler and M. Parrinello, Generalized Neural-Network Representation of High-Dimensional Potential-Energy Surfaces, *Physical Review Letters* **98**, 146401, 2007.

[121] J. Behler, Atom-centered symmetry functions for constructing high-dimensional neural network potentials, *The Journal of Chemical Physics* **134**, 074106, 2011.

[122] N. Artrith, T. Morawietz and J. Behler, High-dimensional neural-network potentials for multicomponent systems: Applications to zinc oxide, *Physical Review B* **83**, 153101, 2011.

[123] K. Hansen *et al.*, Assessment and Validation of Machine Learning Methods for Predicting Molecular Atomization Energies, *Journal of Chemical Theory and Computation* **9**, 3404–3419, 2013.

[124] A. P. Bartók, R. Kondor and G. Csányi, On representing chemical environments, *Physical Review B* **87**, 184115, 2013.

[125] A. P. Bartók, M. C. Payne, R. Kondor and G. Csányi, Gaussian Approximation Potentials: The Accuracy of Quantum Mechanics, without the Electrons, *Physical Review Letters* **104**, 136403, 2010.

[126] M. A. Wood and A. P. Thompson, Extending the accuracy of the SNAP interatomic potential form, *The Journal of Chemical Physics* **148**, 241721, 2018.

[127] R. Drautz, Atomic cluster expansion for accurate and transferable interatomic potentials, *Physical Review B* **99**, 014104, 2019.

[128] R. Car and M. Parrinello, Unified Approach for Molecular Dynamics and Density-Functional Theory, *Physical Review Letters* **55**, 2471–2474, 1985.

[129] M. Born and R. Oppenheimer, Zur Quantentheorie der Molekeln, *Annalen der Physik* **389**, 457–484, 1927.

[130] W. M. C. Foulkes, L. Mitas, R. J. Needs and G. Rajagopal, Quantum Monte Carlo simulations of solids, *Reviews of Modern Physics* **73**, 33–83, 2001.

[131] P. Hohenberg and W. Kohn, Inhomogeneous Electron Gas, *Physical Review* **136**, B864–B871, 1964.

[132] W. Kohn and L. J. Sham, Self-Consistent Equations Including Exchange and Correlation Effects, *Physical Review* **140**, A1133–A1138, 1965.

[133] P.-F. Loos and P. M. W. Gill, A tale of two electrons: Correlation at high density, *Chemical Physics Letters* **500**, 1–8, 2010.

[134] J. P. Perdew and A. Zunger, Self-interaction correction to density-functional approximations for many-electron systems, *Physical Review B* **23**, 5048–5079, 1981.

[135] J. P. Perdew, K. Burke and M. Ernzerhof, Generalized Gradient Approximation Made Simple, *Physical Review Letters* **77**, 3865–3868, 1996.

[136] K. Lejaeghere *et al.*, Reproducibility in density functional theory calculations of solids, *Science* **351**, aad3000, 2016.

[137] V. I. Anisimov, J. Zaanen and O. K. Andersen, Band theory and Mott insulators: Hubbard U instead of Stoner I, *Physical Review B* **44**, 943–954, 1991.

[138] M. Cococcioni and S. de Gironcoli, Linear response approach to the calculation of the effective interaction parameters in the LDA+U method, *Physical Review B* **71**, 035105, 2005.

[139] S. Curtarolo, D. Morgan and G. Ceder, Accuracy of ab initio methods in predicting the crystal structures of metals: A review of 80 binary alloys, *Calphad* **29**, 163–211, 2005.

[140] A. D. Becke, A new mixing of Hartree–Fock and local density-functional theories, *The Journal of Chemical Physics* **98**, 1372–1377, 1993.

[141] R. G. Parr and W. Yang, Density-Functional Theory of the Electronic Structure of Molecules, *Annual Review of Physical Chemistry* **46**, 701–728, 1995.

[142] K. Raghavachari, Perspective on "Density functional thermochemistry. III. The role of exact exchange", *Theoretical Chemistry Accounts* **103**, 361–363, 2000.

[143] J.-D. Chai and M. Head-Gordon, Systematic optimization of long-range corrected hybrid density functionals, *The Journal of Chemical Physics* **128**, 084106, 2008.

[144] K. Burke, Perspective on density functional theory, *The Journal of Chemical Physics* **136**, 150901, 2012.

[145] V. Milman *et al.*, Electronic structure, properties, and phase stability of inorganic crystals: A pseudopotential plane-wave study, *International Journal of Quantum Chemistry* **77**, 895–910, 2000.

[146] D. A. Bardwell *et al.*, Towards crystal structure prediction of complex organic compounds – a report on the fifth blind test, *Acta Crystallographica Section B: Structural Science* **67**, 535–551, 2011.

[147] L. Zhu, H. Liu, C. J. Pickard, G. Zou and Y. Ma, Reactions of xenon with iron and nickel are predicted in the Earth's inner core, *Nature Chemistry* **6**, 644–648, 2014.

[148] I. Errea *et al.*, High-Pressure Hydrogen Sulfide from First Principles: A Strongly Anharmonic Phonon-Mediated Superconductor, *Physical Review Letters* **114**, 157004, 2015.

[149] C. Liu *et al.*, Multiple superionic states in helium-water compounds, *Nature Physics* , 1, 2019.

[150] C. J. Pickard and F. Mauri, All-electron magnetic response with pseudopotentials: NMR chemical shifts, *Physical Review B* **63**, 245101, 2001.

[151] M. Profeta, M. Benoit, F. Mauri and C. J. Pickard, First-Principles Calculation of the ^{17}O NMR Parameters in Ca Oxide and Ca Aluminosilicates: the Partially Covalent Nature of the Ca–O Bond, a Challenge for Density Functional Theory, *Journal of the American Chemical Society* **126**, 12628–12635, 2004.

[152] D. Porezag and M. R. Pederson, Infrared intensities and Raman-scattering activities within density-functional theory, *Physical Review B* **54**, 7830–7836, 1996.

[153] M. Lazzeri and F. Mauri, First-Principles Calculation of Vibrational Raman Spectra in Large Systems: Signature of Small Rings in Crystalline SiO_2, *Physical Review Letters* **90**, 036401, 2003.

[154] R. J. Heaton and P. A. Madden, Fluctuating ionic polarizabilities in the condensed phase: first-principles calculations of the Raman spectra of ionic melts, *Molecular Physics* **106**, 1703–1719, 2008.

[155] P. Umari, Raman spectra of disordered oxides from first principles, *Thesis*, École Polytechnique Fédérale de Lausanne, 2003.

[156] Q. Wan, L. Spanu, G. A. Galli and F. Gygi, Raman Spectra of Liquid Water from Ab Initio Molecular Dynamics: Vibrational Signatures of Charge Fluctuations in the Hydrogen Bond Network, *Journal of Chemical Theory and Computation* **9**, 4124–4130, 2013.

[157] G. Galli, R. M. Martin, R. Car and M. Parrinello, Melting of Diamond at High Pressure, *Science* **250**, 1547–1549, 1990.

[158] M. P. Grumbach and R. M. Martin, Phase diagram of carbon at high pressures and temperatures, *Physical Review B* **54**, 15730–15741, 1996.

[159] C. Cavazzoni, G. L. Chiarotti, S. Scandolo, E. Tosatti, M. Bernasconi and M. Parrinello, Superionic and Metallic States of Water and Ammonia at Giant Planet Conditions, *Science* **283**, 44–46, 1999.

[160] C. J. Wu, J. N. Glosli, G. Galli and F. H. Ree, Liquid-Liquid Phase Transition in Elemental Carbon: A First-Principles Investigation, *Physical Review Letters* **89**, 135701, 2002.

[161] X. Wang, S. Scandolo and R. Car, Carbon Phase Diagram from Ab Initio Molecular Dynamics, *Physical Review Letters* **95**, 185701, 2005.

[162] B. C. Wood and N. Marzari, Dynamical Structure, Bonding, and Thermodynamics of the Superionic Sublattice in α–AgI, *Physical Review Letters* **97**, 166401, 2006.

[163] R. P. Feynman, Forces in Molecules, *Physical Review* **56**, 340–343, 1939.

[164] *Edison Museum in Beaumont Texas – About Thomas Alva Edison Inventions*, http://edisonmuseum.org/content3399.html.

[165] G. Hautier, Finding the needle in the haystack: Materials discovery and design through computational ab initio high-throughput screening, *Computational Materials Science* **163**, 108–116, 2019.

[166] G. Hautier, High-throughput data mined prediction of inorganic compounds and computational discovery of new lithium-ion battery cathode materials, *Thesis*, Massachusetts Institute of Technology, 2011.

[167] M. Lebl, Parallel Personal Comments on "Classical" Papers in Combinatorial Chemistry, *Journal of Combinatorial Chemistry* **1**, 3–24, 1999.

[168] K. H. Bleicher, H.-J. Böhm, K. Müller and A. I. Alanine, Hit and lead generation: beyond high-throughput screening, *Nature Reviews Drug Discovery* **2**, 369, 2003.

[169] X.-D. Xiang *et al.*, A Combinatorial Approach to Materials Discovery, *Science* **268**, 1738–1740, 1995.

[170] H. Koinuma and I. Takeuchi, Combinatorial solid-state chemistry of inorganic materials, *Nature Materials* **3**, 429, 2004.

[171] R. A. Potyrailo and V. M. Mirsky, Combinatorial and High-Throughput Development of Sensing Materials: The First 10 Years, *Chemical Reviews* **108**, 770–813, 2008.

[172] G. H. Jóhannesson, T. Bligaard, A. V. Ruban, H. L. Skriver, K. W. Jacobsen and J. K. Nørskov, Combined Electronic Structure and Evolutionary Search Approach to Materials Design, *Physical Review Letters* **88**, 255506, 2002.

[173] G. Hautier, A. Jain and S. P. Ong, From the computer to the laboratory: materials discovery and design using first-principles calculations, *Journal of Materials Science* **47**, 7317–7340, 2012.

[174] S. Curtarolo, G. L. W. Hart, M. B. Nardelli, N. Mingo, S. Sanvito and O. Levy, The high-throughput highway to computational materials design, *Nature Materials* **12**, 191–201, 2013.

[175] K. Alberi *et al.*, The 2019 materials by design roadmap, *Journal of Physics D: Applied Physics* **52**, 013001, 2018.

[176] R. R. Schaller, Moore's law: past, present and future, *IEEE Spectrum* **34**, 52–59, 1997.

[177] T. N. Theis and H.-S. P. Wong, The End of Moore's Law: A New Beginning for Information Technology, *Computing in Science & Engineering* **19**, 41–50, 2017.

[178] M. M. Waldrop, The chips are down for Moore's law, *Nature News* **530**, 144, 2016.

[179] G. Kresse and J. Furthmüller, Efficient iterative schemes for *ab initio* total-energy calculations using a plane-wave basis set, *Physical Review B* **54**, 11169–11186, 1996.

[180] M. D. Segall *et al.*, First-principles simulation: ideas, illustrations and the CASTEP code, *Journal of Physics: Condensed Matter* **14**, 2717–2744, 2002.

[181] P. Giannozzi *et al.*, QUANTUM ESPRESSO: a modular and open-source software project for quantum simulations of materials, *Journal of Physics: Condensed Matter* **21**, 395502, 2009.

[182] J. Hutter, M. Iannuzzi, F. Schiffmann and J. VandeVondele, CP2K: atomistic simulations of condensed matter systems, *Wiley Interdisciplinary Reviews: Computational Molecular Science* **4**, 15–25, 2014.

[183] C. J. Pickard and R. J. Needs, High-Pressure Phases of Silane, *Physical Review Letters* **97**, 045504, 2006.

[184] I. E. Castelli *et al.*, Computational screening of perovskite metal oxides for optimal solar light capture, *Energy & Environmental Science* **5**, 5814–5819, 2012.

[185] G. Hautier, C. Fischer, V. Ehrlacher, A. Jain and G. Ceder, Data Mined Ionic Substitutions for

the Discovery of New Compounds, *Inorganic Chemistry* **50**, 656–663, 2011.

[186] G. Hautier, A. Jain, H. Chen, C. Moore, S. Ping Ong and G. Ceder, Novel mixed polyanions lithium-ion battery cathode materials predicted by high-throughput *ab initio* computations, *Journal of Materials Chemistry* **21**, 17147–17153, 2011.

[187] N. Mounet *et al.*, Two-dimensional materials from high-throughput computational exfoliation of experimentally known compounds, *Nature Nanotechnology* **13**, 246, 2018.

[188] A. H. Larsen *et al.*, The atomic simulation environment–a Python library for working with atoms, *Journal of Physics: Condensed Matter* **29**, 273002, 2017.

[189] S. Curtarolo *et al.*, AFLOW: An automatic framework for high-throughput materials discovery, *Computational Materials Science* **58**, 218–226, 2012.

[190] A. Jain *et al.*, FireWorks: a dynamic workflow system designed for high-throughput applications, *Concurrency and Computation: Practice and Experience* **27**, 5037–5059, 2015.

[191] G. Pizzi, A. Cepellotti, R. Sabatini, N. Marzari and B. Kozinsky, AiiDA: Automated Interactive Infrastructure and Database for Computational Science, *Computational Materials Science* **111**, 218–230, 2016.

[192] L. Moreau *et al.*, The Open Provenance Model core specification (v1.1), *Future Generation Computer Systems* **27**, 743–756, 2011.

[193] M. Baker, 1,500 scientists lift the lid on reproducibility, *Nature News* **533**, 452, 2016.

[194] D. Fanelli, Opinion: Is science really facing a reproducibility crisis, and do we need it to?, *Proceedings of the National Academy of Sciences* **115**, 2628–2631, 2018.

[195] G. Pacchioni, *The Overproduction of Truth: Passion, Competition, and Integrity in Modern Science*, Oxford University Press, 2018.

[196] J. C. Bachman *et al.*, Inorganic Solid-State Electrolytes for Lithium Batteries: Mechanisms and Properties Governing Ion Conduction, *Chemical Reviews* **116**, 140–162, 2016.

[197] Y. Kato *et al.*, High-power all-solid-state batteries using sulfide superionic conductors, *Nature Energy* **1**, 16030, 2016.

[198] A. Manthiram, X. Yu and S. Wang, Lithium battery chemistries enabled by solid-state electrolytes, *Nature Reviews Materials* **2**, 16103, 2017.

[199] Y. A. Du and N. A. W. Holzwarth, Li Ion Diffusion Mechanisms in the Crystalline Electrolyte γ-Li_3PO_4, *J. Electrochem. Soc.* **154**, A999–A1004, 2007.

[200] N. Holzwarth, N. Lepley and Y. A. Du, Computer modeling of lithium phosphate and thiophosphate electrolyte materials, *Journal of Power Sources* **196**, 6870–6876, 2011.

[201] N. D. Lepley, N. A. W. Holzwarth and Y. A. Du, Structures, Li^+ mobilities, and interfacial properties of solid electrolytes Li_3PS_4 and Li_3PO_4 from first principles, *Phys. Rev. B* **88**, 104103, 2013.

[202] F. Du, X. Ren, J. Yang, J. Liu and W. Zhang, Structures, Thermodynamics, and Li^+ Mobility of $Li_{10}GeP_2S_{12}$, *The Journal of Physical Chemistry C* **118**, 10590–10595, 2014.

[203] B. Lang, B. Ziebarth and C. Elssser, Lithium Ion Conduction in $LiTi_2(PO_4)_3$ and Related Compounds Based on the NASICON Structure, *Chem. Mater.* **27**, 5040–5048, 2015.

[204] S. P. Ong, Y. Mo, W. D. Richards, L. Miara, H. S. Lee and G. Ceder, Phase stability, electrochemical

stability and ionic conductivity of the $Li_{10\pm1}MP_2X_{12}$ (M = Ge, Si, Sn, Al or P, and X = O, S or Se) family of superionic conductors, *Energy Environ. Sci.* **6**, 148–156, 2013.

[205] Y. Mo, S. P. Ong and G. Ceder, First Principles Study of the $Li_{10}GeP_2S_{12}$ Lithium Super Ionic Conductor Material, *Chemistry of Materials* **24**, 15–17, 2012.

[206] M. Xu, J. Ding and E. Ma, One-dimensional stringlike cooperative migration of lithium ions in an ultrafast ionic conductor, *Applied Physics Letters* **101**, 031901, 2012.

[207] K. Meier, T. Laino and A. Curioni, Solid-State Electrolytes: Revealing the Mechanisms of Li-Ion Conduction in Tetragonal and Cubic LLZO by First-Principles Calculations, *The Journal of Physical Chemistry C* **118**, 6668–6679, 2014.

[208] Y. Wang *et al.*, Design principles for solid-state lithium superionic conductors, *Nature Materials* **14**, 1026–1031, 2015.

[209] I.-H. Chu *et al.*, Insights into the Performance Limits of the $Li_7P_3S_{11}$ Superionic Conductor: A Combined First-Principles and Experimental Study, *ACS Applied Materials & Interfaces* **8**, 7843–7853, 2016.

[210] Z. Zhu, I.-H. Chu and S. P. Ong, $Li_3Y(PS_4)_2$ and $Li_5PS_4Cl_2$: New Lithium Superionic Conductors Predicted from Silver Thiophosphates using Efficiently Tiered Ab Initio Molecular Dynamics Simulations, *Chemistry of Materials* **29**, 2474–2484, 2017.

[211] A. Marcolongo and N. Marzari, Ionic correlations and failure of Nernst-Einstein relation in solid-state electrolytes, *Physical Review Materials* **1**, 025402, 2017.

[212] S. Adams and R. P. Rao, Ion transport and phase transition in $Li_{7-x}La_3(Zr_{2-x}M_x)O_{12}$ (M = Ta^{5+}, Nb^{5+} , x = 0, 0.25), *J. Mater. Chem.* **22**, 1426–1434, 2012.

[213] M. Xu, M. S. Park, J. M. Lee, T. Y. Kim, Y. S. Park and E. Ma, Mechanisms of Li^+ transport in garnet-type cubic $Li_{3+x}La_3M_2O_{12}$ (M = Te, Nb, Zr), *Physical Review B* **85**, 052301, 2012.

[214] B. Kozinsky *et al.*, Effects of Sublattice Symmetry and Frustration on Ionic Transport in Garnet Solid Electrolytes, *Physical Review Letters* **116**, 055901, 2016.

[215] M. J. Klenk and W. Lai, Finite-size effects on the molecular dynamics simulation of fast-ion conductors: A case study of lithium garnet oxide $Li_7La_3Zr_2O_{12}$, *Solid State Ionics* **289**, 143–149, 2016.

[216] M. Burbano, D. Carlier, F. Boucher, B. J. Morgan and M. Salanne, Sparse Cyclic Excitations Explain the Low Ionic Conductivity of Stoichiometric $Li_7La_3Zr_2O_{12}$, *Physical Review Letters* **116**, 135901, 2016.

[217] S. Adams and R. P. Rao, Structural requirements for fast lithium ion migration in $Li_{10}GeP_2S_{12}$, *Journal of Materials Chemistry* **22**, 7687–7691, 2012.

[218] Y. Deng *et al.*, Structural and Mechanistic Insights into Fast Lithium-Ion Conduction in Li_4SiO_4-Li_3PO_4 Solid Electrolytes, *Journal of the American Chemical Society* **137**, 9136–9145, 2015.

[219] K. Wakamura, Roles of phonon amplitude and low-energy optical phonons on superionic conduction, *Phys. Rev. B* **56**, 11593–11599, 1997.

[220] K. Wakamura, Effects of electronic band on activation energy and of effective charge on lattice distortion in superionic conductors, *Journal of Physics and Chemistry of Solids* **59**, 591–598, 1998.

[221] J. T. Kummer, β-Alumina electrolytes, *Progress in Solid State Chemistry* **7**, 141–175, 1972.

[222] S. Adams and J. Swenson, Bond valence analysis of transport pathways in RMC models of fast ion conducting glasses, *Phys. Chem. Chem. Phys.* **4**, 3179–3184, 2002.

[223] S. Adams and J. Swenson, Determining Ionic Conductivity from Structural Models of Fast Ionic Conductors, *Phys. Rev. Lett.* **84**, 4144–4147, 2000.

[224] M. Avdeev, M. Sale, S. Adams and R. P. Rao, Screening of the alkali-metal ion containing materials from the Inorganic Crystal Structure Database (ICSD) for high ionic conductivity pathways using the bond valence method, *Solid State Ionics* **225**, 43–46, 2012.

[225] R. Xiao, H. Li and L. Chen, Candidate structures for inorganic lithium solid-state electrolytes identified by high-throughput bond-valence calculations, *Journal of Materiomics* **1**, 325–332, 2015.

[226] N. Adelstein and B. C. Wood, Role of Dynamically Frustrated Bond Disorder in a Li^+ Superionic Solid Electrolyte, *Chem. Mater.* **28**, 7218–7231, 2016.

[227] X. He, Y. Zhu and Y. Mo, Origin of fast ion diffusion in super-ionic conductors, *Nature Communications* **8**, 15893, 2017.

[228] A. D. Sendek, Q. Yang, E. D. Cubuk, K.-A. N. Duerloo, Y. Cui and E. J. Reed, Holistic computational structure screening of more than 12000 candidates for solid lithium-ion conductor materials, *Energy & Environmental Science* **10**, 306–320, 2017.

[229] V. Thangadurai, H. Kaack and W. J. F. Weppner, Novel Fast Lithium Ion Conduction in Garnet-Type $Li_5La_3M_2O_{12}$ (M = Nb, Ta), *Journal of the American Ceramic Society* **86**, 437–440, 2003.

[230] H.-J. Deiseroth *et al.*, Li_6PS_5X: A Class of Crystalline Li-Rich Solids With an Unusually High Li^+ Mobility, *Angewandte Chemie International Edition* **47**, 755–758, 2008.

[231] R. Kanno and M. Murayama, Lithium Ionic Conductor Thio-LISICON: The Li_2S-GeS_2-P_2S_5 System, *J. Electrochem. Soc.* **148**, A742–A746, 2001.

[232] Y. Deng *et al.*, Enhancing the Lithium Ion Conductivity in Lithium Superionic Conductor (LISICON) Solid Electrolytes through a Mixed Polyanion Effect, *ACS Applied Materials & Interfaces* **9**, 7050–7058, 2017.

[233] S. G. Louie, S. Froyen and M. L. Cohen, Nonlinear ionic pseudopotentials in spin-density-functional calculations, *Physical Review B* **26**, 1738–1742, 1982.

[234] F. Ercolessi and J. B. Adams, Interatomic Potentials from First-Principles Calculations: The Force-Matching Method, *EPL (Europhysics Letters)* **26**, 583, 1994.

[235] A. Huq, J. W. Richardson, E. R. Maxey, D. Chandra and W.-M. Chien, Structural studies of Li_3N using neutron powder diffraction, *Journal of Alloys and Compounds* **436**, 256–260, 2007.

[236] T. Lapp, S. Skaarup and A. Hooper, Ionic conductivity of pure and doped Li_3N, *Solid State Ionics* **11**, 97–103, 1983.

[237] U. v. Alpen, A. Rabenau and G. H. Talat, Ionic conductivity in Li_3N single crystals, *Applied Physics Letters* **30**, 621–623, 1977.

[238] V. L. McLaren, C. A. Kirk, M. Poisot, M. Castellanos and A. R. West, Li^+ ion conductivity in rock salt-structured nickel-doped Li_3NbO_4, *Dalton Transactions* **0**, 3042–3047, 2004.

[239] N. Kamaya *et al.*, A lithium superionic conductor, *Nature Materials* **10**, 682–686, 2011.

[240] L. C. Grenier and G. Bassi, Affinement de la structure de Li_3NbO_4, *Bull. Soc. Franc. Crist.* **88**, 345–346, 1965.

[241] K. Ukei, H. Suzuki, T. Shishido and T. Fukuda, Li_3NbO_4, *Acta Crystallographica Section C: Crystal Structure Communications* **50**, 655–656, 1994.

[242] K. E. Kweon *et al.*, Structural, Chemical, and Dynamical Frustration: Origins of Superionic Conductivity in *closo*-Borate Solid Electrolytes, *Chemistry of Materials* **29**, 9142–9153, 2017.

[243] A. Jain *et al.*, Commentary: The Materials Project: A materials genome approach to accelerating materials innovation, *APL Materials* **1**, 011002, 2013.

[244] L. V. Woodcock, Isothermal molecular dynamics calculations for liquid salts, *Chemical Physics Letters* **10**, 257–261, 1971.

[245] G. Prandini, A. Marrazzo, I. E. Castelli, N. Mounet and N. Marzari, Precision and efficiency in solid-state pseudopotential calculations, *npj Computational Materials* **4**, 72, 2018.

[246] J. A. Dawson, P. Canepa, T. Famprikis, C. Masquelier and M. S. Islam, Atomic-Scale Influence of Grain Boundaries on Li-Ion Conduction in Solid Electrolytes for All-Solid-State Batteries, *Journal of the American Chemical Society* **140**, 362–368, 2018.

[247] A. K. Sagotra, D. Chu and C. Cazorla, Influence of lattice dynamics on lithium-ion conductivity: A first-principles study, *Physical Review Materials* **3**, 035405, 2019.

[248] L. Kahle, A. Marcolongo and N. Marzari, Modeling lithium-ion solid-state electrolytes with a pinball model, *Physical Review Materials* **2**, 065405, 2018.

[249] L. Ercole, A. Marcolongo and S. Baroni, Accurate thermal conductivities from optimally short molecular dynamics simulations, *Scientific Reports* **7**, 15835, 2017.

[250] N. J. de Klerk, E. van der Maas and M. Wagemaker, Analysis of Diffusion in Solid-State Electrolytes through MD Simulations, Improvement of the Li-Ion Conductivity in β-Li_3PS_4 as an Example, *ACS Applied Energy Materials* **1**, 3230–3242, 2018.

[251] C. Chen, Z. Lu and F. Ciucci, Data mining of molecular dynamics data reveals Li diffusion characteristics in garnet $Li_7La_3Zr_2O_{12}$, *Scientific Reports* **7**, 40769, 2017.

[252] J. B. Varley *et al.*, Understanding Ionic Conductivity Trends in Polyborane Solid Electrolytes from Ab Initio Molecular Dynamics, *ACS Energy Letters* **2**, 250–255, 2017.

[253] Y. Deng *et al.*, Crystal Structures, Local Atomic Environments, and Ion Diffusion Mechanisms of Scandium-Substituted Sodium Superionic Conductor (NASICON) Solid Electrolytes, *Chemistry of Materials* **30**, 2618–2630, 2018.

[254] B. Kozinsky, *Handbook of Materials Modeling: Applications: Current and Emerging Materials*, Springer International Publishing, Cham, 2018, pp. 1–20.

[255] W. D. Richards *et al.*, Design and synthesis of the superionic conductor $Na_{10}SnP_2S_{12}$, *Nature Communications* **7**, 11009, 2016.

[256] P. Gasparotto and M. Ceriotti, Recognizing molecular patterns by machine learning: An agnostic structural definition of the hydrogen bond, *The Journal of Chemical Physics* **141**, 174110, 2014.

[257] P. Gasparotto, R. H. Meissner and M. Ceriotti, Recognizing Local and Global Structural Motifs at the Atomic Scale, *Journal of Chemical Theory and Computation* **14**, 486–498, 2018.

[258] R. Wehner, B. Michel and P. Antonsen, Visual navigation in insects: coupling of egocentric and geocentric information, *Journal of Experimental Biology* **199**, 129–140, 1996.

[259] R. Möller, Insect visual homing strategies in a robot with analog processing, *Biological Cybernetics* **83**, 231–243, 2000.

[260] E. Prodan and W. Kohn, Nearsightedness of electronic matter, *Proceedings of the National Academy of Sciences of the United States of America* **102**, 11635–11638, 2005.

[261] L. Pauling, THE PRINCIPLES DETERMINING THE STRUCTURE OF COMPLEX IONIC CRYSTALS, *Journal of the American Chemical Society* **51**, 1010–1026, 1929.

[262] N. Molinari, J. Mailoa and B. Kozinsky, Effect of Salt Concentration on Ion Clustering and Transport in Polymer Solid Electrolytes: A Molecular Dynamics Study of PEO-LiTFSI, *Chem. Mater.* **30**, 6298–6306, 2018.

[263] B. C. Wood and N. Marzari, Proton dynamics in superprotonic $CsHSO_4$, *Physical Review B* **76**, 134301, 2007.

[264] B. J. Morgan and P. A. Madden, Relationships between Atomic Diffusion Mechanisms and Ensemble Transport Coefficients in Crystalline Polymorphs, *Physical Review Letters* **112**, 145901, 2014.

[265] A. Okabe, B. Boots, K. Sugihara and S. N. Chiu, *Spatial Tessellations: Concepts and Applications of Voronoi Diagrams*, John Wiley & Sons, Chichester, UK, 2009.

[266] S. Van Dongen, Graph Clustering Via a Discrete Uncoupling Process, *SIAM Journal on Matrix Analysis and Applications* **30**, 121–141, 2008.

[267] *libAtoms/QUIP molecular dynamics framework: http://www.libatoms.org: libAtoms/QUIP*, 2018, https://github.com/libAtoms/QUIP.

[268] S. De, A. P. Bartók, G. Csányi and M. Ceriotti, Comparing molecules and solids across structural and alchemical space, *Physical Chemistry Chemical Physics* **18**, 13754–13769, 2016.

[269] A. Rodriguez and A. Laio, Clustering by fast search and find of density peaks, *Science* **344**, 1492–1496, 2014.

[270] M. P. Allen and D. J. Tildesley, *Computer simulation of liquids*, Clarendon Press, Oxford, 1987.

[271] D. Frenkel and B. Smit, *Understanding Molecular Simulation: From Algorithms to Applications*, Academic Press, San Diego, 1996.

[272] P. Knauth, Inorganic solid Li ion conductors: An overview, *Solid State Ionics* **180**, 911–916, 2009.

[273] H. Xie, J. A. Alonso, Y. Li, M. T. Fernández-Díaz and J. B. Goodenough, Lithium Distribution in Aluminum-Free Cubic $Li_7La_3Zr_2O_{12}$, *Chemistry of Materials* **23**, 3587–3589, 2011.

[274] M. P. O'Callaghan, A. S. Powell, J. J. Titman, G. Z. Chen and E. J. Cussen, Switching on Fast Lithium Ion Conductivity in Garnets: The Structure and Transport Properties of $Li_{3+x}Nd_3Te_{2-x}Sb_xO_{12}$, *Chemistry of Materials* **20**, 2360–2369, 2008.

[275] M. P. O'Callaghan and E. J. Cussen, Lithium dimer formation in the Li-conducting garnets $Li_{5+x}Ba_xLa_{3-x}Ta_2O_{12}$ ($0 < x \leq 1.6$), *Chemical Communications* **0**, 2048–2050, 2007.

[276] V. Thangadurai, S. Narayanan and D. Pinzaru, Garnet-type solid-state fast Li ion conductors for Li batteries: critical review, *Chemical Society Reviews* **43**, 4714–4727, 2014.

[277] M. Ceriotti, G. Bussi and M. Parrinello, Langevin Equation with Colored Noise for Constant-Temperature Molecular Dynamics Simulations, *Physical Review Letters* **102**, 020601, 2009.

[278] S. Plimpton, Fast Parallel Algorithms for Short-Range Molecular Dynamics, *Journal of Computational Physics* **117**, 1–19, 1995.

[279] M. Mottet, A. Marcolongo, T. Laino and I. Tavernelli, Doping in garnet-type electrolytes: Kinetic and thermodynamic effects from molecular dynamics simulations, *Physical Review Materials* **3**, 035403, 2019.

[280] R. Jalem *et al.*, Concerted Migration Mechanism in the Li Ion Dynamics of Garnet-Type $Li_7La_3Zr_2O_{12}$, *Chemistry of Materials* **25**, 425–430, 2013.

[281] Morgan Benjamin J., Lattice-geometry effects in garnet solid electrolytes: a lattice-gas Monte Carlo simulation study, *Royal Society Open Science* **4**, 170824, 2017.

[282] R. Murugan, V. Thangadurai and W. Weppner, Fast Lithium Ion Conduction in Garnet-Type $Li_7La_3Zr_2O_{12}$, *Angewandte Chemie International Edition* **46**, 7778–7781, 2007.

[283] L. J. Miara *et al.*, Effect of Rb and Ta Doping on the Ionic Conductivity and Stability of the Garnet $Li_{7+2x-y}(La_{3-x}Rb_x)(Zr_{2-y}Ta_y)O_{12}$ ($0 \leq x \leq 0.375$, $0 \leq y \leq 1$) Superionic Conductor: A First Principles Investigation, *Chemistry of Materials* **25**, 3048–3055, 2013.

[284] William W. Pillars and Donald R. Peacor, The Crystal Structure of Beta Eucryptite as a Function of Temperature, *American Mineralogist* **58**, 681–690, 1973.

[285] S. Gražulis *et al.*, Crystallography Open Database (COD): an open-access collection of crystal structures and platform for world-wide collaboration, *Nucleic Acids Research* **40**, D420–D427, 2012.

[286] A. I. Lichtenstein, R. O. Jones, H. Xu and P. J. Heaney, Anisotropic thermal expansion in the silicate β-eucryptite: A neutron diffraction and density functional study, *Physical Review B* **58**, 6219–6223, 1998.

[287] A. I. Lichtenstein, R. O. Jones, S. de Gironcoli and S. Baroni, Anisotropic thermal expansion in silicates: A density functional study of β-eucryptite and related materials, *Physical Review B* **62**, 11487–11493, 2000.

[288] H. J. Schink and H. v. Löhneysen, Vacancy-induced low-energy excitations in the one-dimensional ionic conductor β-eucryptite, *Solid State Communications* **47**, 131–135, 1983.

[289] V. Donduft, R. Dimitrijević and N. Petranović, Li^+ ion mobility in eucryptite phases, *Journal of Materials Science* **23**, 4081–4084, 1988.

[290] A. Sartbaeva, S. A. Wells, S. A. T. Redfern, R. W. Hinton and S. J. B. Reed, Ionic diffusion in quartz studied by transport measurements, SIMS and atomistic simulations, *Journal of Physics: Condensed Matter* **17**, 1099, 2005.

[291] Y. Chen, S. Manna, C. V. Ciobanu and I. E. Reimanis, Thermal regimes of Li-ion conductivity in β-eucryptite, *Journal of the American Ceramic Society* **101**, 347–355, 2018.

[292] H. G. F. Winkler, Synthese und Kristallstruktur des Eukryptits, $LiAlSiO_4$, *Acta Crystallographica* **1**, 27–34, 1948.

[293] See Supplemental Material at http://link.aps.org/supplemental/10.1103/PhysRevMaterials.3.055404 for a description of the location of additional data and analysis scripts (Sec. S I), and

additional plots on mean-square displacements, particle trajectories and SOAP descriptor clusters (Sec. S II).

[294] W. Press, B. Renker, H. Schulz and H. Böhm, Neutron scattering study of the one-dimensional ionic conductor β-eucryptite, *Physical Review B* **21**, 1250–1257, 1980.

[295] A. Kuhn, J. Köhler and B. V. Lotsch, Single-crystal X-ray structure analysis of the superionic conductor $Li_{10}GeP_2S_{12}$, *Physical Chemistry Chemical Physics* **15**, 11620, 2013.

[296] A. Kuhn, V. Duppel and B. V. Lotsch, Tetragonal $Li_{10}GeP_2S_{12}$ and Li_7GePS_8 – exploring the Li ion dynamics in LGPS Li electrolytes, *Energy & Environmental Science* **6**, 3548–3552, 2013.

[297] A. Musaelian and L. Kahle, `SITATOR`, https://github.com/Linux-cpp-lisp/sitator, 2018.

[298] T. F. Willems, C. H. Rycroft, M. Kazi, J. C. Meza and M. Haranczyk, Algorithms and tools for high-throughput geometry-based analysis of crystalline porous materials, *Microporous and Mesoporous Materials* **149**, 134–141, 2012.

[299] R. L. Martin, B. Smit and M. Haranczyk, Addressing Challenges of Identifying Geometrically Diverse Sets of Crystalline Porous Materials, *Journal of Chemical Information and Modeling* **52**, 308–318, 2012.

[300] V. Satopaa, J. Albrecht, D. Irwin and B. Raghavan, 31st International Conference on Distributed Computing Systems Workshops, 2011, pp. 166–171.

[301] A. Belsky, M. Hellenbrandt, V. L. Karen and P. Luksch, New developments in the Inorganic Crystal Structure Database (ICSD): accessibility in support of materials research and design, *Acta Crystallographica Section B Structural Science* **58**, 364–369, 2002.

[302] A. D. Robertson, A. R. West and A. G. Ritchie, Review of crystalline lithium-ion conductors suitable for high temperature battery applications, *Solid State Ionics* **104**, 1–11, 1997.

[303] J. B. Boyce and B. A. Huberman, Superionic conductors: Transitions, structures, dynamics, *Physics Reports* **51**, 189–265, 1979.

[304] S. Hull, Superionics: crystal structures and conduction processes, *Reports on Progress in Physics* **67**, 1233, 2004.

[305] W. Weppner, Engineering of solid state ionic devices, *Ionics* **9**, 444–464, 2003.

[306] M. D. Tikekar, S. Choudhury, Z. Tu and L. A. Archer, Design principles for electrolytes and interfaces for stable lithium-metal batteries, *Nature Energy* **1**, 16114, 2016.

[307] J. Nanda, C. Wang and P. Liu, Frontiers of solid-state batteries, *MRS Bulletin* **43**, 740–745, 2018.

[308] H.-J. Deiseroth *et al.*, Li_6PS_5X: A Class of Crystalline Li-Rich Solids With an Unusually High Li^+ Mobility, *Angewandte Chemie International Edition* **47**, 755–758, 2008.

[309] S.-T. Kong, H.-J. Deiseroth, J. Maier, V. Nickel, K. Weichert and C. Reiner, Li_6PO_5Br and Li_6PO_5Cl: The first Lithium-Oxide-Argyrodites, *Zeitschrift für anorganische und allgemeine Chemie* **636**, 1920–1924, 2010.

[310] N. Anantharamulu, K. K. Rao, G. Rambabu, B. V. Kumar, V. Radha and M. Vithal, A wide-ranging review on Nasicon type materials, *Journal of Materials Science* **46**, 2821–2837, 2011.

[311] H. Y.-P. Hong, Crystal structures and crystal chemistry in the system $Na_{1+x}Zr_2Si_xP_{3-x}O_{12}$, *Materials Research Bulletin* **11**, 173–182, 1976.

[312] D. Petit, P. Colomban, G. Collin and J. P. Boilot, Fast ion transport in $LiZr_2(PO_4)_3$: Structure and

conductivity, *Materials Research Bulletin* **21**, 365–371, 1986.

[313] I. S. Pronin, S. E. Sigaryov and A. A. Vashman, Ionic motion in $Li_3In_2(PO_4)_3$, *Solid State Ionics* **38**, 9–23, 1990.

[314] H. Aono, E. Sugimoto, Y. Sadaoka, N. Imanaka and G. Adachi, Ionic Conductivity of the Lithium Titanium Phosphate ($Li_{1+X}M_XTi_{2-X}(PO_4)_3$, M = Al, Sc, Y, and La) Systems, *Journal of The Electrochemical Society* **136**, 590–591, 1989.

[315] H. Aono, E. Sugimoto, Y. Sadaoka, N. Imanaka and G.-y. Adachi, Ionic Conductivity of Solid Electrolytes Based on Lithium Titanium Phosphate, *Journal of The Electrochemical Society* **137**, 1023–1027, 1990.

[316] Y.-W. Hu, I. D. Raistrick and R. A. Huggins, Ionic Conductivity of Lithium Orthosilicate–Lithium Phosphate Solid Solutions, *Journal of The Electrochemical Society* **124**, 1240–1242, 1977.

[317] R. D. Shannon, B. E. Taylor, A. D. English and T. Berzins, New Li solid electrolytes, *Electrochimica Acta* **22**, 783–796, 1977.

[318] A. R. Rodger, J. Kuwano and A. R. West, Li^+ ion conducting γ solid solutions in the systems Li_4XO_4–Li_3YO_4: X=Si, Ge, Ti; Y=P, As, V; Li_4XO_4–$LiZO_2$: Z=Al, Ga, Cr and Li_4GeO_4–Li_2CaGeO_4, *Solid State Ionics* **15**, 185–198, 1985.

[319] S. Muy *et al.*, High-Throughput Screening of Solid-State Li-Ion Conductors Using Lattice-Dynamics Descriptors, *iScience* **16**, 270–282, 2019.

[320] A. D. Sendek, Q. Yang, E. D. Cubuk, K.-A. N. Duerloo, Y. Cui and E. J. Reed, Holistic computational structure screening of more than 12000 candidates for solid lithium-ion conductor materials, *Energy & Environmental Science* **10**, 306–320, 2017.

[321] W. D. Richards, L. J. Miara, Y. Wang, J. C. Kim and G. Ceder, Interface Stability in Solid-State Batteries, *Chemistry of Materials* **28**, 266–273, 2016.

[322] M. Aykol, S. Kim, V. I. Hegde, S. Kirklin and C. Wolverton, Computational evaluation of new lithium-3 garnets for lithium-ion battery applications as anodes, cathodes, and solid-state electrolytes, *Physical Review Materials* **3**, 025402, 2019.

[323] Y. Zhu, X. He and Y. Mo, Origin of Outstanding Stability in the Lithium Solid Electrolyte Materials: Insights from Thermodynamic Analyses Based on First-Principles Calculations, *ACS Applied Materials & Interfaces* **7**, 23685–23693, 2015.

[324] C. Monroe and J. Newman, The Effect of Interfacial Deformation on Electrodeposition Kinetics, *Journal of The Electrochemical Society* **151**, A880–A886, 2004.

[325] Z. Deng, Z. Wang, I.-H. Chu, J. Luo and S. P. Ong, Elastic Properties of Alkali Superionic Conductor Electrolytes from First Principles Calculations, *Journal of The Electrochemical Society* **163**, A67–A74, 2016.

[326] S. Baroni, P. Giannozzi and E. Isaev, Density-Functional Perturbation Theory for Quasi-Harmonic Calculations, *Reviews in Mineralogy and Geochemistry* **71**, 39–57, 2010.

[327] D. Dragoni, D. Ceresoli and N. Marzari, Thermoelastic properties of $\ensuremath{\alpha}$-iron from first-principles, *Physical Review B* **91**, 104105, 2015.

[328] M. Parrinello and A. Rahman, Strain fluctuations and elastic constants, *The Journal of Chemical Physics* **76**, 2662–2666, 1982.

[329] M. Bernasconi, G. L. Chiarotti, P. Focher, S. Scandolo, E. Tosatti and M. Parrinello, First-principle-constant pressure molecular dynamics, *Journal of Physics and Chemistry of Solids* **56**, 501–505, 1995.

[330] Y. Ren, Y. Shen, Y. Lin and C.-W. Nan, Direct observation of lithium dendrites inside garnet-type lithium-ion solid electrolyte, *Electrochemistry Communications* **57**, 27–30, 2015.

[331] E. J. Cheng, A. Sharafi and J. Sakamoto, Intergranular Li metal propagation through polycrystalline Li6.25Al0.25La3Zr2O12 ceramic electrolyte, *Electrochimica Acta* **223**, 85–91, 2017.

[332] L. Porz *et al.*, Mechanism of Lithium Metal Penetration through Inorganic Solid Electrolytes, *Advanced Energy Materials* **7**, 1701003, 2017.

[333] B. J. Alder and T. E. Wainwright, Studies in Molecular Dynamics. I. General Method, *The Journal of Chemical Physics* **31**, 459–466, 1959.

[334] Y. A. Du and N. a. W. Holzwarth, Li Ion Diffusion Mechanisms in the Crystalline Electrolyte γ-Li_3PO_4, *Journal of The Electrochemical Society* **154**, A999–A1004, 2007.

[335] A. Mace, S. Barthel and B. Smit, Automated Multiscale Approach To Predict Self-Diffusion from a Potential Energy Field, *Journal of Chemical Theory and Computation* **15**, 2127–2141, 2019.

[336] L. Kahle, A. Musaelian, N. Marzari and B. Kozinsky, Unsupervised landmark analysis for jump detection in molecular dynamics simulations, *Physical Review Materials* **3**, 055404, 2019.

[337] M. Aniya and K. Wakamura, Phonons and the mechanism of ion transport in some superionic conductors, *Physica B: Condensed Matter* **219**, 463–465, 1996.

[338] S. Muy *et al.*, Tuning mobility and stability of lithium ion conductors based on lattice dynamics, *Energy & Environmental Science* **11**, 850–859, 2018.

[339] A. van de Walle, M. Asta and G. Ceder, The alloy theoretic automated toolkit: A user guide, *Calphad* **26**, 539–553, 2002.

[340] G. L. W. Hart and R. W. Forcade, Algorithm for generating derivative structures, *Physical Review B* **77**, 224115, 2008.

[341] A. Merkys, A. Vaitkus, J. Butkus, M. Okulič-Kazarinas, V. Kairys and S. Gražulis, *COD::CIF::Parser*: an error-correcting CIF parser for the Perl language, *Journal of Applied Crystallography* **49**, 292–301, 2016.

[342] S. P. Ong *et al.*, Python Materials Genomics (pymatgen): A robust, open-source python library for materials analysis, *Computational Materials Science* **68**, 314–319, 2013.

[343] R. Hundt, J. C. Schön and M. Jansen, CMPZ – an algorithm for the efficient comparison of periodic structures, *Journal of Applied Crystallography* **39**, 6–16, 2006.

[344] P. J. Hasnip, K. Refson, M. I. J. Probert, J. R. Yates, S. J. Clark and C. J. Pickard, Density functional theory in the solid state, *Philosophical Transactions of the Royal Society A: Mathematical, Physical and Engineering Sciences* **372**, 20130270, 2014.

[345] J. Ma and L.-W. Wang, Using Wannier functions to improve solid band gap predictions in density functional theory, *Scientific Reports* **6**, 24924, 2016.

[346] F. Giustino, *Materials Modelling Using Density Functional Theory: Properties and Predictions*, Oxford University Press, 2014.

[347] A. Willand *et al.*, Norm-conserving pseudopotentials with chemical accuracy compared to

all-electron calculations, *The Journal of Chemical Physics* **138**, 104109, 2013.

[348] A. Dal Corso, Pseudopotentials periodic table: From H to Pu, *Computational Materials Science* **95**, 337–350, 2014.

[349] K. F. Garrity, J. W. Bennett, K. M. Rabe and D. Vanderbilt, Pseudopotentials for high-throughput DFT calculations, *Computational Materials Science* **81**, 446–452, 2014.

[350] M. Topsakal and R. M. Wentzcovitch, Accurate projected augmented wave (PAW) datasets for rare-earth elements (RE=La–Lu), *Computational Materials Science* **95**, 263–270, 2014.

[351] M. Schlipf and F. Gygi, Optimization algorithm for the generation of ONCV pseudopotentials, *Computer Physics Communications* **196**, 36–44, 2015.

[352] M. J. van Setten *et al.*, The PseudoDojo: Training and grading a 85 element optimized norm-conserving pseudopotential table, *Computer Physics Communications* **226**, 39–54, 2018.

[353] N. Marzari, D. Vanderbilt, A. De Vita and M. C. Payne, Thermal Contraction and Disordering of the Al(110) Surface, *Physical Review Letters* **82**, 3296–3299, 1999.

[354] X. He, Y. Zhu, A. Epstein and Y. Mo, Statistical variances of diffusional properties from ab initio molecular dynamics simulations, *npj Computational Materials* **4**, 1–9, 2018.

[355] L. Kahle, *Suite for Analysis of Molecular Simulations (SAMOS)*, https://github.com/lekah/samos, 2019.

[356] M. Murayama, R. Kanno, Y. Kawamoto and T. Kamiyama, Structure of the thio-LISICON, Li_4GeS_4, *Solid State Ionics* **154**, 789–794, 2002.

[357] Y. E. Choi *et al.*, Coatable Li_4SnS_4 Solid Electrolytes Prepared from Aqueous Solutions for All-Solid-State Lithium-Ion Batteries, *ChemSusChem* **10**, 2605–2611, 2017.

[358] J. L. Allen, J. Wolfenstine, E. Rangasamy and J. Sakamoto, Effect of substitution (Ta, Al, Ga) on the conductivity of $Li_7La_3Zr_2O_{12}$, *Journal of Power Sources* **206**, 315–319, 2012.

[359] A. Logéat *et al.*, From order to disorder: The structure of lithium-conducting garnets $Li_{7-x}La_3Ta_xZr_{2-x}O_12$ (x = 0–2), *Solid State Ionics* **206**, 33–38, 2012.

[360] A. Novoselov, M. Zhuravleva, R. Zakalyukin, V. Fomichev and G. Zimina, Phase Stability and Ionic Conductivity of Solid Solutions with NASICON Structure, *Journal of the American Ceramic Society* **91**, 1377–1379, 2008.

[361] A. Aatiq, M. Ménétrier, L. Croguennec, E. Suard and C. Delmas, On the structure of $Li_3Ti_2(PO_4)_3$, *Journal of Materials Chemistry* **12**, 2971–2978, 2002.

[362] S. Saha, G. Rousse, I. B. Alcover, M. Courty, D. A. Dalla Corte and J.-M. Tarascon, Polymorphism in $Li_4Zn(PO_4)_2$ and Stabilization of its Structural Disorder to Improve Ionic Conductivity, *Chemistry of Materials* **30**, 1379–1390, 2018.

[363] S.-T. Kong *et al.*, Lithium Argyrodites with Phosphorus and Arsenic: Order and Disorder of Lithium Atoms, Crystal Chemistry, and Phase Transitions, *Chemistry – A European Journal* **16**, 2198–2206, 2010.

[364] D. A. Weber *et al.*, Structural Insights and 3D Diffusion Pathways within the Lithium Superionic Conductor Li10GeP2S12, *Chemistry of Materials* **28**, 5905–5915, 2016.

[365] O. Reckeweg, B. Blaschkowski and T. Schleid, Li_5OCl_3 and Li_3OCl: Two Remarkably Different Lithium Oxide Chlorides, *Zeitschrift für anorganische und allgemeine Chemie* **638**, 2081–2086,

2012.

[366] C. Delmas, A. Maazaz, F. Guillen, C. Fouassier, J. M. Réau and P. Hagenmuller, Des conducteurs ioniques pseudo-bidimensionnels: Li_8MO_6 (M = Zr, Sn), Li_7LO_6 (L = Nb, Ta) et $Li_6In_2O_6$, *Materials Research Bulletin* **14**, 619–625, 1979.

[367] E. Nomura and M. Greenblatt, Ionic conductivity of substituted Li_7TaO_6 phases, *Solid State Ionics* **13**, 249–254, 1984.

[368] C. Mühle, R. E. Dinnebier, L. van Wüllen, G. Schwering and M. Jansen, New Insights into the Structural and Dynamical Features of Lithium Hexaoxometalates Li_7MO_6 (M = Nb, Ta, Sb, Bi), *Inorganic Chemistry* **43**, 874–881, 2004.

[369] W. Hönle and A. Simon, Darstellung und Kristallstrukturen von $LiGaBr_4$ und $LiGaBr_3$, *Zeitschrift für Naturforschung B* **41**, 1391–1398, 2014.

[370] W. Hönle, B. Hettich and A. Simon, Darstellung und Kristallstrukturen von $LiGaCl_4$ und $LiGaI_4$, *Zeitschrift für Naturforschung B* **42**, 248–250, 2014.

[371] S. Grimme, Semiempirical GGA-type density functional constructed with a long-range dispersion correction, *Journal of Computational Chemistry* **27**, 1787–1799, 2006.

[372] G. Meyer and H.-C. Gaebell, Synthesis and crystal structure of the inter-alkali metal iodide $Cs_2Li_3I_5$, *Materials Research Bulletin* **18**, 1353–1360, 1983.

[373] W. Bronger, H.-J. Miessen, P. Müller and R. Neugröschel, Darstellung und Kristallstruktur von $Li_4Re_6S_{11}$, *Journal of the Less Common Metals* **105**, 303–310, 1985.

[374] I. N. Gejfman, N. G. Furmanova, P. G. Nagornyj and L. D. Yun, Crystal structure and B^{4+}ESR in double lithium-titanium oxyorthophosphate, alpha-$LiTiOPO_4$, *Kristallografiya* **38**, 88–94, 1993.

[375] O. Pecher *et al.*, Atomistic Characterisation of Li^+ Mobility and Conductivity in $Li_{7-x}PS_{6-x}I_x$ Argyrodites from Molecular Dynamics Simulations, Solid-State NMR, and Impedance Spectroscopy, *Chemistry – A European Journal* **16**, 8347–8354, 2010.

[376] M. Daub, H. A. Höppe and H. Hillebrecht, Further New Borosulfates: Synthesis, Crystal Structure, and Vibrational Spectra of $A[B(SO_4)_2]$ (A = Na, K, NH_4) and the Crystal Structures of $Li_5[B(SO_4)_4]$ and $NH_4[B(S_2O_7)_2]$, *Zeitschrift für anorganische und allgemeine Chemie* **640**, 2914–2921, 2014.

[377] T. Malcherek, Structure and phase transitions of $LiTaOGeO_4$, *Acta Crystallographica Section B: Structural Science* **58**, 607–612, 2002.

[378] B. Singh *et al.*, Superionic conduction in β-eucryptite: inelastic neutron scattering and computational studies, *Physical Chemistry Chemical Physics* **19**, 15512–15520, 2017.

[379] M. Touboul, M. Quarton, J. Lokaj and V. Kettmann, Structure of dilithium dimagnesium trisulfate, *Acta Crystallographica Section C* **44**, 1887–1889, 1988.

[380] D. Morgan *et al.*, Experimental and Computational Study of the Structure and Electrochemical Properties of $Li_xM_2(PO_4)_3$ Compounds with the Monoclinic and Rhombohedral Structure, *Chemistry of Materials* **14**, 4684–4693, 2002.

[381] C. Jansen, J. Küper and B. Krebs, $Na_2B_2S_5$ and $Li_2B_2S_5$: Two Novel Perthioborates with Planar 1,2,4-Trithia-3,5-Diborolane Rings, *Zeitschrift für anorganische und allgemeine Chemie* **621**,

1322–1329, 1995.

[382] Z. D. Luo *et al.*, Study of $Li_6Y(BO_3)_3$:Nd^{3+} Crystal - A New Laser Crystal, *Crystal Research and Technology* **26**, K5–K8, 1991.

[383] B. Lopez-Bermudez *et al.*, Lithium-ion conductivity in Li6Y(BO3)3: a thermally and electrochemically robust solid electrolyte, *Journal of Materials Chemistry A* **4**, 6972–6979, 2016.

[384] I. V. Pentin, V. Saltykov, J. Nuss, J. C. Schön and M. Jansen, Theoretical and Experimental Exploration of the Energy Landscape of the Quasi-Binary Cesium Chloride/Lithium Chloride System, *Chemistry – A European Journal* **18**, 3559–3565, 2012.

[385] X.-X. Liu, C.-X. Wang, S.-M. Luo and J.-X. Mi, The layered monodiphosphate $Li_9Ga_3(P_2O_7)_3(PO_4)_2$ refined from X-ray powder data, *Acta Crystallographica Section E: Structure Reports Online* **62**, i112–i113, 2006.

[386] P. Balasubramanian, M. Mancini, P. Axmann and M. Wohlfahrt-Mehrens, Facile Synthesis and Electrochemical Investigation of $Li_9V_3(P_2O_7)_3(PO_4)_2$ as High Voltage Cathode for Li-Ion Batteries, *Journal of The Electrochemical Society* **164**, A6047–A6053, 2017.

[387] K. Bernet and R. Hoppe, Ein "Lithosilicat" mit Kolumnareinheiten: $RbLi_5Li[SiO_4]_2$, *Zeitschrift für anorganische und allgemeine Chemie* **592**, 93–105, 1991.

[388] C. Logemann, J. Witt and M. S. Wickleder, Crystal structure of lithium disulfate, $Li_2[S_2O_7]$, $Li_2O_7S_2$, *Zeitschrift für Kristallographie - New Crystal Structures* **228**, 159–160, 2014.

[389] W. Yin, K. Feng, W. Hao, J. Yao and Y. Wu, Synthesis, Structure, and Properties of $Li_2In_2MQ_6$ (M = Si, Ge; Q = S, Se): A New Series of IR Nonlinear Optical Materials, *Inorganic Chemistry* **51**, 5839–5843, 2012.

[390] J.-H. Zhang *et al.*, Infrared nonlinear optical properties of lithium-containing diamond-like semiconductors $Li_2ZnGeSe_4$ and $Li_2ZnSnSe_4$, *Dalton Transactions* **44**, 11212–11222, 2015.

[391] W. Hönle, G. Miller and A. Simon, Preparation, crystal structures, and electronic properties of $LiGaCl_3$ and $LiGaI_3$, *Journal of Solid State Chemistry* **75**, 147–155, 1988.

[392] M. Schneider, P. Kuske and H. D. Lutz, Kristallstrukturen von Li_6MgBr_8 und Li_2MgBr_4, *Zeitschrift für Naturforschung B* **48**, 1–6, 2014.

[393] U. Engelmann and B. G. Müller, Darstellung und Struktur der Tetrafluoroaurate(III) MI[AuF4] mit MI = Li, Rb, *Zeitschrift für anorganische und allgemeine Chemie* **598**, 103–110, 1991.

[394] V. Manriquez, W. Hönle and H. G. v. Schnering, Trilithiumheptaphosphid Li_3P_7: Darstellung, Struktur und Eigenschaften, *Zeitschrift für anorganische und allgemeine Chemie* **539**, 95–109, 1986.

[395] H. G. v. Schnering and W. Wichelhaus, Die Lithiumphosphide LiP_5 und LiP_7, *Naturwissenschaften* **59**, 78–79, 1972.

[396] D.-Y. Seung, P. Gravereau, L. Trut and A. Levasseur, Li_3AsS_3, *Acta Crystallographica Section C: Crystal Structure Communications* **54**, 900–902, 1998.

[397] F. Q. Huang, B. Deng and J. A. Ibers, Syntheses and structures of six compounds in the A_2LiMS_4 (A=K, Rb, Cs; M=V, Nb, Ta) family, *Journal of Solid State Chemistry* **178**, 194–199, 2005.

[398] J. Kim and T. Hughbanks, Synthesis and Structures of New Ternary Aluminum Chalcogenides: $LiAlSe_2$, α-$LiAlTe_2$, and β-$LiAlTe_2$, *Inorganic Chemistry* **39**, 3092–3097, 2000.

[399] G. Mairesse and M. Drache, Lithium tetrakis(chlorosulfato)borate, *Acta Crystallographica Section B: Structural Crystallography and Crystal Chemistry* **36**, 2767–2768, 1980.

[400] E. Morin, J. Angenault, J. Couturier, M. Quarton, H. He and J. Klinowski, Phase Transition and Crystal Structures of $LiSn_2(PO_4)_3$, *ChemInform* **29**, no–no, 1998.

[401] H. Völlenkle, A. Wittmann and H. Nowotny, The crystal structure of lithium enneagermanate $Li_4[Ge_9O_{20}]$, *Monatshefte für Chemie / Chemical Monthly* **102**, 361–372, 1971.

[402] G. J. Redhammer and G. Tippelt, The polar phase of $Li_2Ge_4O_9$ at 298, 150 and 90 K, *Acta Crystallographica Section C: Crystal Structure Communications* **69**, 1091–1095, 2013.

[403] T. Kraft and M. Jansen, Die Kristallstruktur von Lithiummetaperiodat, $LiIO_4$, *Zeitschrift für anorganische und allgemeine Chemie* **621**, 484–487, 1995.

[404] A. Daidouh, M. L. Veiga, C. Pico and M. Martinez-Ripoll, A New Polymorph of $Li_4P_2O_7$, *Acta Crystallographica Section C: Crystal Structure Communications* **53**, 167–169, 1997.

[405] D. Tran Qui, S. Hamdoune and Y. Le Page, Synthèse et structure cristalline de $LiInP_2O_7$, *Acta Crystallographica Section C: Crystal Structure Communications* **43**, 201–202, 1987.

[406] P. Hartman, A uniform description of phenakite type structures as superstructures of β-Si_3N_4, *Zeitschrift für Kristallographie - Crystalline Materials* **187**, 139–144, 2015.

[407] R. P. Gunawardane, J. G. Fletcher, M. A. K. L. Dissanayake, R. A. Howie and A. R. West, Crystal Structure Refinement of Li_4TiO_4 Containing Tetrahedrally Coordinated Ti^{4+} and Tetragonally Packed Oxide Ions, *Journal of Solid State Chemistry* **112**, 70–72, 1994.

[408] H. Völlenkle, A. Wittmann and H. Nowotny, Die Kristallstruktur der Verbindung $Li_6[Si_2O_7]$, *Monatshefte für Chemie / Chemical Monthly* **100**, 295–303, 1969.

[409] M. Daub, K. Kazmierczak, P. Gross, H. Höppe and H. Hillebrecht, Exploring a New Structure Family: Alkali Borosulfates $Na_5[B(SO_4)_4]$, $A_3[B(SO_4)_3]$ (A = K, Rb), $Li[B(SO_4)_2]$, and $Li[B(S_2O_7)_2]$, *Inorganic Chemistry* **52**, 6011–6020, 2013.

[410] A. Chaushli, H. Jacobs, U. Weisser and J. Strähle, Li_5ReN_4, ein Lithium–Nitridorhenat(VII) mit anti-Flußspat-Überstruktur, *Zeitschrift für anorganische und allgemeine Chemie* **626**, 1909–1914, 2000.

[411] R. Niewa, D. A. Zherebtsov and S. Leoni, $Li_3[ScN_2]$: The First Nitridoscandate(III)–Tetrahedral Sc Coordination and Unusual MX_2 Framework, *Chemistry – A European Journal* **9**, 4255–4259, 2003.

[412] D. A. Vennos and F. J. DiSalvo, Structure of lithium niobium nitride, *Acta Crystallographica Section C: Crystal Structure Communications* **48**, 610–612, 1992.

[413] R. Juza and F. Hund, Die ternären Nitride Li_3AlN_2 und Li_3GaN_2, *Zeitschrift für anorganische Chemie* **257**, 13–25, 1948.

[414] W. X. Yuan, J. W. Hu, Y. T. Song, W. J. Wang and Y. P. Xu, Synthesis and structure of the ternary nitride Li_6WN_4, *Powder Diffraction* **20**, 18–21, 2005.

[415] R. Niewa, D. A. Zherebtsov, H. Borrmann and R. Kniep, Preparation and Crystal Structure of $Li_4[TaN_3]$, *Zeitschrift für anorganische und allgemeine Chemie* **628**, 2505–2508, 2002.

[416] J. Cabana, M. Casas-Cabanas, H. J. Santner, A. Fuertes and M. R. Palacín, Exploring order-disorder structural transitions in the Li–Nb–N–O system: The new antifluorite oxynitride

$Li_{11}NbN_4O_2$, *Journal of Solid State Chemistry* **183**, 1609–1614, 2010.

[417] R. Hoppe and R. Homann, Neue Untersuchungen an Fluorkomplexen mit dreiwertigem Silber und Gold, *Zeitschrift für anorganische und allgemeine Chemie* **379**, 193–198, 1970.

[418] A. Lachgar and H. J. Meyer, Synthesis, Crystal Structure, and Electronic Structure of $In_2Li_2Nb_6Cl_{18}$, *Journal of Solid State Chemistry* **110**, 15–19, 1994.

[419] M. He, H. Li, X.-L. Chen, Y.-P. Xu and T. Xu, $Li_2AlB_5O_{10}$, *Acta Crystallographica Section C: Crystal Structure Communications* **57**, 1010–1011, 2001.

[420] L. Mao, T. Zhou and N. Ye, Trilithium scandium bis(orthoborate), *Acta Crystallographica Section E: Structure Reports Online* **64**, i38–i38, 2008.

[421] R. W. Smith, D. Holman and E. M. Villa, Crystal structure of $Li_3Ga(BO_3)_2$, *Acta Crystallographica Section E: Crystallographic Communications* **73**, 456–458, 2017.

[422] V. Psycharis, I. A. Kapoutsis and G. D. Chryssikos, Crystal Structure and Vibrational Spectra of Li_2BAlO_4, *Journal of Solid State Chemistry* **142**, 214–219, 1999.

[423] S. Wang, N. Ye and G. Zou, Three New Alkaline Beryllium Borates $LiBeBO_3$, $Li_6Be_3B_4O_{12}$, and $Li_8Be_5B_6O_{18}$ in the Ternary Phase Diagrams Li_2O–BeO–B_2O_3, *Inorganic Chemistry* **53**, 2742–2748, 2014.

[424] T. Hasegawa and H. Yamane, Synthesis and crystal structure analysis of $Li_2NaBP_2O_8$ and $LiNa_2B_5P_2O_{14}$, *Journal of Solid State Chemistry* **225**, 65–71, 2015.

[425] M. T. Averbuch-Pouchot, I. Tordjman and J. C. Guitel, Structures cristallines des polyphosphates de cadmium–lithium et de mercurelithium, $CdLi_2(PO_3)_4$ et $HgLi_2(PO_3)_4$, *Acta Crystallographica Section B: Structural Crystallography and Crystal Chemistry* **32**, 2953–2956, 1976.

[426] T. Ben-Chaabane, L. Smiri-Dogguy, Y. Laligant and A. Le Bail, $Li_6P_6O_{18}$: X-ray powder structure determination of lithium cyclohexaphosphate, *European Journal of Solid State and Inorganic Chemistry* **35**, 255–264, 1998.

[427] T. R. Jensen, R. G. Hazell, A. Nø rlund Christensen and J. C. Hanson, Hydrothermal Synthesis of Lithium Zinc Phosphates: Structural Investigation of Twinned α-$Li_4Zn(PO_4)_2$ and a High Temperature Polymorph β-$Li_4Zn(PO_4)_2$, *Journal of Solid State Chemistry* **166**, 341–351, 2002.

[428] H. B. Yahia, M. Shikano, T. Takeuchi, H. Kobayashi and M. Itoh, Crystal structures of the new fluorophosphates $Li_9Mg_3[PO_4]_4F_3$ and $Li_2Mg[PO_4]F$ and ionic conductivities of selected compositions, *Journal of Materials Chemistry A* **2**, 5858–5869, 2014.

[429] Y. Dong and F. J. DiSalvo, Synthesis and single crystal structures of ternary phosphides Li_4SrP_2 and *AAe*P (*A*=Li, Na; *Ae*=Sr, Ba), *Journal of Solid State Chemistry* **180**, 432–439, 2007.

[430] J. B. Parise and T. E. Gier, Hydrothermal synthesis and structure of $Li_4B_4Si_8O_{24}$, *International Journal of Inorganic Materials* **2**, 81–86, 2000.

[431] H. Krüger, V. Kahlenberg and R. Kaindl, $Li_2Si_3O_7$: Crystal structure and Raman spectroscopy, *Journal of Solid State Chemistry* **180**, 922–928, 2007.

[432] X. Chen *et al.*, Li_3AlSiO_5: the first aluminosilicate as a potential deep-ultraviolet nonlinear optical crystal with the quaternary diamond-like structure, *Physical Chemistry Chemical Physics* **18**, 4362–4369, 2016.

[433] B. H. W. S. de Jong, H. T. J. Supèr, A. L. Spek, N. Veldman, G. Nachtegaal and J. C. Fischer, Mixed

Alkali Systems: Structure and ^{29}Si MASNMR of $Li_2Si_2O_5$ and $K_2Si_2O_5$, *Acta Crystallographica Section B: Structural Science* **54**, 568–577, 1998.

[434] F. Folger, Die Kristallstruktur von Li_2TeO_3, *Zeitschrift für anorganische und allgemeine Chemie* **411**, 103–110, 1975.

[435] H. Untenecker and R. Hoppe, Ein neues Oxotellurat, Na_4TeO_5, und eine Revision der Struktur von Li_4TeO_5, *Journal of the Less Common Metals* **132**, 79–92, 1987.

[436] T. Wisser and R. Hoppe, Neues über Oxotellurate(VI) der Alkalimetalle – Zur Existenz und Konstitution von Li_6TeO_6, *Zeitschrift für anorganische und allgemeine Chemie* **573**, 133–142, 1989.

[437] M. Bharathy, V. A. Rassolov, S. Park and H.-C. zur Loye, Crystal Growth of Two New Photoluminescent Oxides: $Sr_3Li_6Nb_2O_{11}$ and $Sr_3Li_6Ta_2O_{11}$, *Inorganic Chemistry* **47**, 9941–9945, 2008.

[438] J. Glaser and H.-J. Meyer, An Improved Synthesis of Ternary Carbonates: The Examples $LiLa(CO_3)_2$ and $La(CO_3)F$, *Zeitschrift für anorganische und allgemeine Chemie* **636**, 2622–2625, 2010.

[439] J.-J. Grebe, H. Stoll and R. Hoppe, Ein Oxid neuen Typs: $KLi_4[AlO_4]$, *Zeitschrift für anorganische und allgemeine Chemie* **559**, 17–26, 1988.

[440] T. W. S. Yip, E. J. Cussen and C. Wilson, Spontaneous formation of crystalline lithium molybdate from solid reagents at room temperature, *Dalton Transactions* **39**, 411–417, 2010.

[441] T. R. Jensen *et al.*, Hydrothermal synthesis and crystal structure of α-$LiZnAsO_4$, *Journal of Materials Chemistry* **8**, 969–975, 1998.

[442] M. Hajji, M. F. Zid and A. Driss, $Li_3Al(MoO_2)_2O_2(AsO_4)_2$, *Acta Crystallographica Section E: Structure Reports Online* **65**, i21, 2009.

[443] R. Baier and R. Hoppe, Zur Kenntnis von $KLiZnO_2$, *Zeitschrift für anorganische und allgemeine Chemie* **522**, 23–32, 1985.

[444] H. Untenecker and R. Hoppe, Ein neues Oxozincat: $Li_6[ZnO_4]$, *Zeitschrift für anorganische und allgemeine Chemie* **551**, 147–150, 1987.

[445] V. V. Konovalova, V. V. Fomichev, D. V. Drobot, R. M. Zakalyukin and S. Y. Stefanovich, New conducting phase in the Li_2O–ZnO–Nb_2O_5 system: Existence conditions, *Russian Journal of Inorganic Chemistry* **54**, 1650–1654, 2009.

[446] B. L. Greenberg and G. M. Loiacono, Structure of $Li_4Ge_5O_{12}$ – a new compound in the Li_2O–GeO_2 system, *Acta Crystallographica Section C: Crystal Structure Communications* **46**, 2021–2026, 1990.

[447] H.-D. Wasel-Nielen and R. Hoppe, Zur Kristallstruktur von Li_3AuO_3, Li_5AuO_4, $KAuO_2$ und $RbAuO_2$, *Zeitschrift für anorganische und allgemeine Chemie* **375**, 43–54, 1970.

[448] M. Ø. Filsø, M. J. Turner, G. V. Gibbs, S. Adams, M. A. Spackman and B. B. Iversen, Visualizing Lithium-Ion Migration Pathways in Battery Materials, *Chemistry – A European Journal* **19**, 15535–15544, 2013.

[449] G. Wehrum and R. Hoppe, Das erste Diniobat mit 'isolierten' Anionen: $KLi_4[NbO_5]$ = $K_2Li_8[Nb_2O_{10}]$, *Zeitschrift für anorganische und allgemeine Chemie* **619**, 149–157, 1993.

[450] R. Wolf and R. Hoppe, Notiz über Li_2PdO_2, *Zeitschrift für anorganische und allgemeine Chemie* **536**, 77–80, 1986.

[451] P. Kroeschell, R. Wolf and R. Hoppe, Neue Vertreter der Li_8SnO_6-Familie: Li_8IrO_6, Li_8PtO_6 und Li_8CeO_6, *Zeitschrift für anorganische und allgemeine Chemie* **536**, 81–91, 1986.

[452] E. A. Genkina and B. V. Mill', Crystal structures of sphenes $NaSbGeO_5$, $NaTaGeO_5$ and $LiTaSiO_5$, *Kristallografiya* **37**, 1424–1428, 1992.

[453] S. Chen, S. Pan, W. Zhao, Z. Yang, H. Wu and Y. Yang, Synthesis, crystal structure and characterization of a new compound, $Li_3NaBaB_6O_{12}$, *Solid State Sciences* **14**, 1186–1190, 2012.

[454] M. Mączka *et al.*, Crystal structure and phonon properties of noncentrosymmetric $LiNaB_4O_7$, *Journal of Solid State Chemistry* **180**, 410–419, 2007.

[455] M. Miessen and R. Hoppe, Neue Oxoborate der Alkalimetalle: $NaLi_2[BO_3]$, *Zeitschrift für anorganische und allgemeine Chemie* **545**, 157–168, 1987.

[456] M. Vlasse, A. Levasseur and P. Hagenmuller, Crystal structure of $Li_5B_7O_{12.5}Cl$ at 296 and 425 K, *Solid State Ionics* **2**, 33–37, 1981.

[457] E. S. Lang, U. Abram and J. Strähle, Synthese, Eigenschaften und Struktur von $LiAuI_4$ und $KAuI_4$ mit einer Diskussion der kristallchemischen Verwandtschaft zwischen den Halogenoauraten $RbAuCl_4$, $AgAuCl_4$, $RbAuBr_4$ und $LiAuI_4$, *Zeitschrift für anorganische und allgemeine Chemie* **623**, 1791–1795, 1997.

[458] A. K. Tyagi, J. Köhler, P. Balog and J. Weber, Syntheses and structures of Li_3ScF_6 and high pressure $LiScF_{4-}$, luminescence properties of $LiScF_4$, a new phase in the system LiF–ScF_3, *Journal of Solid State Chemistry* **178**, 2620–2625, 2005.

[459] B. Baján and H.-J. Meyer, Two-Dimensional Networks in the Structure of $Li_2[Nb_6Cl_{16}]$, *Zeitschrift für anorganische und allgemeine Chemie* **623**, 791–795, 1997.

[460] C. Logemann and M. S. Wickleder, The Unique bis-(Disulfato)-aurate Anion $[Au(S_2O_7)_2]^-$: Synthesis and Characterization of $Li[Au(S_2O_7)_2]$ and $Na[Au(S_2O_7)_2]$, *Inorganic Chemistry* **50**, 11111–11116, 2011.

[461] V. I. Pet'kov *et al.*, Synthesis and properties of $LiZr_2(AsO_4)_3$ and $LiZr_2(AsO_4)_x(PO_4)_{3-x}$, *Inorganic Materials* **50**, 263–272, 2014.

[462] A. Tripathi, S. J. Kim, G. M. Johnson and J. B. Parise, Synthesis and single-crystal structure of a lithium aluminogermanate with the zeolite ABW topology, *Microporous and Mesoporous Materials* **34**, 273–279, 2000.

[463] C. Ceriani, E. Fois and A. Gamba, The role of extra-framework cations on the structure of dehydrated Li-ABW. A computer simulation study, *Microporous and Mesoporous Materials* **57**, 73–81, 2003.

[464] A. Khorassani and A. R. West, Li^+ ion conductivity in the system Li_4SiO_4–Li_3VO_4, *Journal of Solid State Chemistry* **53**, 369–375, 1984.

[465] L. Kahle, A. Marcolongo and N. Marzari, Dataset for "High-throughput computational screening for solid-state Li-ion conductors", 2019.

[466] L. Kahle, *The supercell creator*, https://github.com/lekah/supercellor, 2019.

[467] A. Pérez, M. E. Tuckerman and M. H. Müser, A comparative study of the centroid and ring-

polymer molecular dynamics methods for approximating quantum time correlation functions from path integrals, *The Journal of Chemical Physics* **130**, 184105, 2009.

[468] G. Ceder, S. P. Ong and Y. Wang, Predictive modeling and design rules for solid electrolytes, *MRS Bulletin* **43**, 746–751, 2018.

[469] G. Ferraresi, M. El Kazzi, L. Czornomaz, C.-L. Tsai, S. Uhlenbruck and C. Villevieille, Electrochemical Performance of All-Solid-State Li-Ion Batteries Based on Garnet Electrolyte Using Silicon as a Model Electrode, *ACS Energy Letters* **3**, 1006–1012, 2018.

[470] V. Thangadurai, D. Pinzaru, S. Narayanan and A. K. Baral, Fast Solid-State Li Ion Conducting Garnet-Type Structure Metal Oxides for Energy Storage, *The Journal of Physical Chemistry Letters* **6**, 292–299, 2015.

[471] R. Sudo *et al.*, Interface behavior between garnet-type lithium-conducting solid electrolyte and lithium metal, *Solid State Ionics* **262**, 151–154, 2014.

[472] J. v. d. Broek, S. Afyon and J. L. M. Rupp, Interface-Engineered All-Solid-State Li-Ion Batteries Based on Garnet-Type Fast Li^+ Conductors, *Advanced Energy Materials* **6**, 1600736, 2016.

[473] F. Han *et al.*, Interphase Engineering Enabled All-Ceramic Lithium Battery, *Joule* **2**, 497–508, 2018.

[474] R. Kanno, T. Hata, Y. Kawamoto and M. Irie, Synthesis of a new lithium ionic conductor, thio-LISICON–lithium germanium sulfide system, *Solid State Ionics* **130**, 97–104, 2000.

[475] M. Murayama, Synthesis of New Lithium Ionic Conductor Thio-LISICON–Lithium Silicon Sulfides System, *Journal of Solid State Chemistry* **168**, 140–148, 2002.

[476] M. Murayama, N. Sonoyama, A. Yamada and R. Kanno, Material design of new lithium ionic conductor, thio-LISICON, in the Li_2S–P_2S_5 system, *Solid State Ionics* **170**, 173–180, 2004.

[477] X. Wu, M. El Kazzi and C. Villevieille, Surface and morphological investigation of the electrode/electrolyte properties in an all-solid-state battery using a Li_2S-P_2S_5 solid electrolyte, *Journal of Electroceramics* **38**, 207–214, 2017.

[478] J. B. Bates *et al.*, Fabrication and characterization of amorphous lithium electrolyte thin films and rechargeable thin-film batteries, *Journal of power sources* **43**, 103–110, 1993.

[479] X. Yu, A Stable Thin-Film Lithium Electrolyte: Lithium Phosphorus Oxynitride, *Journal of The Electrochemical Society* **144**, 524, 1997.

[480] Y. Wang, Z. Liu, X. Zhu, Y. Tang and F. Huang, Highly lithium-ion conductive thio-LISICON thin film processed by low-temperature solution method, *Journal of Power Sources* **224**, 225–229, 2013.

[481] M. Rawlence, I. Garbayo, S. Buecheler and J. L. M. Rupp, On the chemical stability of post-lithiated garnet Al-stabilized $Li_7La_3Zr_2O_{12}$ solid state electrolyte thin films, *Nanoscale* **8**, 14746–14753, 2016.

[482] R. Pfenninger, M. Struzik, I. Garbayo, E. Stilp and J. L. M. Rupp, A low ride on processing temperature for fast lithium conduction in garnet solid-state battery films, *Nature Energy* **4**, 475–483, 2019.

[483] R. Scholder, Über Orthosalze und maximale Sauerstoff-Koordination, *Angewandte Chemie* **70**, 583–594, 1958.

[484] R. Scholder and H. Gläser, Über Lithium- und Natriumuranate(V) und über strukturelle Beziehungen zwischen den Verbindungstypen Li_7AO_6 und Li_8AO_6, *Zeitschrift für anorganische und allgemeine Chemie* **327**, 15–27, 1964.

[485] G. Wehrum and R. Hoppe, Zur Kenntnis 'Kationen-reicher' Tantalate: Über $Li_7[TaO_6]$, *Zeitschrift für anorganische und allgemeine Chemie* **620**, 659–664, 1994.

[486] E. Kuçukbenli *et al.*, Projector augmented-wave and all-electron calculations across the periodic table: a comparison of structural and energetic properties, *arXiv:1404.3015 [cond-mat]* , 2014.

[487] I. Timrov, N. Marzari and M. Cococcioni, Hubbard parameters from density-functional perturbation theory, *Physical Review B* **98**, 085127, 2018.

[488] B. G. Dick and A. W. Overhauser, Theory of the Dielectric Constants of Alkali Halide Crystals, *Phys. Rev.* **112**, 90–103, 1958.

[489] F. Zipoli and A. Curioni, Reactive potential for the study of phase-change materials: GeTe, *New Journal of Physics* **15**, 123006, 2013.

[490] S. Plimpton, Fast Parallel Algorithms for Short-Range Molecular Dynamics, *J. Comput. Phys.* **117**, 1–19, 1995.

[491] M. Hansen, S. Jespersen, L. Leigland and C. Kroenke, Using diffusion anisotropy to characterize neuronal morphology in gray matter: the orientation distribution of axons and dendrites in the NeuroMorpho.org database, *Frontiers in Integrative Neuroscience* **7**, 31, 2013.

[492] M. A. Islam, Einstein–Smoluchowski Diffusion Equation: A Discussion, *Physica Scripta* **70**, 120, 2004.

[493] R. Kubo, Statistical-Mechanical Theory of Irreversible Processes. I. General Theory and Simple Applications to Magnetic and Conduction Problems, *Journal of the Physical Society of Japan* **12**, 570–586, 1957.

[494] Y. Zhou and G. H. Miller, Green–Kubo Formulas for Mutual Diffusion Coefficients in Multicomponent Systems, *The Journal of Physical Chemistry* **100**, 5516–5524, 1996.

[495] R. Chitra and S. Yashonath, Estimation of Error in the Diffusion Coefficient from Molecular Dynamics Simulations, *The Journal of Physical Chemistry B* **101**, 5437–5445, 1997.

[496] B. C. Wood, Exploring kinetics and thermodynamics in fast-ion conductors and hydrogen-storage materials using ab-initio molecular dynamics, *PhD Thesis*, Massachussets Institute of Technology, 2007.

[497] F. Grasselli and S. Baroni, Topological quantization and gauge invariance of charge transport in liquid insulators, *Nature Physics* , 1, 2019.

[498] H. W. Schamp and E. Katz, Self-Diffusion and Ionic Conductivity in Sodium Bromide, *Physical Review* **94**, 828–836, 1954.

[499] Kieron Burke, *The ABC of DFT*, Department of Chemistry, UC Irvine, 2007.

[500] S. Baroni, S. de Gironcoli, A. Dal Corso and P. Giannozzi, Phonons and related crystal properties from density-functional perturbation theory, *Reviews of Modern Physics* **73**, 515–562, 2001.

Leonid Kahle

0041 21 69 31157
leonid.kahle@epfl.ch
Chemin des Glycines 7,
CH-1022 Chavannes-près-Renens
LinkedIn
Github
21.09.1990, Karlsruhe (D)
Germany & Greece
B & A1

Curriculum Vitæ

Education

ÉCOLE POLYTECHNIQUE FÉDÉRALE DE LAUSANNE (CH) 2015 – 2019
PhD in Materials Science

ÉCOLE POLYTECHNIQUE FÉDÉRALE DE LAUSANNE (CH) 2013 – 2015
Master of Materials Science

UNIVERSITY OF KIEL (D) 2010 – 2013
Bachelor of Materials Science

Professional experience

THEORY AND SIMULATION OF MATERIALS LABORATORY, EPFL 2015 – 2019
Doctoral assistant
I researched ceramic ionic conductors for next-generation Li-ion batteries using quantum-mechanical atomistic simulations. I developed new methods and led a high-throughput computational screening in collaboration with industry partners (IBM, Solvay).

QUANTUM SIMULATIONS GROUP, LAWRENCE LIVERMORE NATIONAL LABORATORY (USA) 02/2018
Visiting scientist
Collaborated on software project for analysis of large data structures in materials simulation.

ROBERT BOSCH RESEARCH CENTER, CAMBRIDGE (USA) 09/2014 – 04/2015
Research and development internship
Built a PostgreSQL database for the storage of high-throughput simulations and developed a new method for the geometric analysis of atomic environments.

Awards & scholarships

2019 "Distinction for a remarkable thesis", Materials Science doctoral school, EPFL
2018 Nominated for university final of "My thesis in 180 seconds", EPFL
2015 Award for best grade of finishing class as Master of Materials Science
2013 Award for best grade of finishing class as Bachelor of Materials Science
2012 "Excellence Initiative"-scholarship by German Federal Ministry of Education & Research

Software development

AiiDA materials informatics platform 2015 – 2019
Software developer
Open-source platform (Python, SQL) to automate and store high-throughput calculations in computations materials science, used internationally in academia and industry. I contributed tools for efficient database queries and organized international workshops and coding retreats.

Quantum ESPRESSO 2017 – 2019
Software developer
Open-source code (Fortran, C) for high-performance electronic-structure calculations with over 13'000 citations. I contributed to its molecular-dynamics functionality.

SAMOS (Suite for Analysis of Molecular Simulations) 2017 – 2019
Personal software project
Analysis software (Python, Fortran) for large data structures in atomistic simulations.

Languages

English, French	Full professional proficiency (C2) in writing and speaking
German, Greek	Native, bilingual proficiency
Spanish	Elementary proficiency (A2) in writing and speaking

Technical skills

Software	Python, Fortran, Linux/UNIX, C/C++, Matlab/Octave, Mathematica, version control, unit testing
Databases	PostgreSQL, SQLAlchemy, Django
Graphics	Blender, matplotlib, mayavi, inkscape
high-perf. computing	MPI/OpenMP directives, SLURM, PBS
Atomistic simulation	Quantum ESPRESSO, LAMMPS, CP2K, GIPAW
Thin films	Spin/spray coating, physical vapor deposition, sputtering, AFM, XPS

Extracurricular

Committee member of the Club Montagne EPFL (university alpine club) 2015 – 2019
Responsible for hiking outings, courses & workshops, equipment rental & maintenance.

German Red Cross, Munich and Kiel 2006 – 2013
Honorary lifeguard, responsible for watches and physical education of new members, and honorary homework assistance to children of immigrant background.

Surfline Rhodes, Rhodes (GR) 2009, 2011, 2013
Windsurfing instructor, ~2 months per season (full time).

Mountain ranger bataillon 231, Bad Reichenhall (D) 10/2009 – 06/2010
Military service in the "Hochgebirgsjägerzug" (platoon for high alpine operations).